The University Of Sheffield.

Department Of Mechanical Engineering

Measuring lubricant viscosity at a surface and in a bearing film using shear-horizontal surface acoustic waves

Georgios Tyreas

January 2020

Supervisor: Professor Rob Dwyer-Joyce

A thesis submitted in partial fulfilment of the requirements for the degree of Doctor of Philosophy

ABSTRACT

Viscosity is an important property of lubricant oil films; in IC engines the oil film is responsible for supporting the load, keeping the components in relative motion separated and protecting them from major friction and wear. As a result, lubricant film viscosity strongly depends on the operating temperature, pressure and shear rate. Understanding the oil behaviour under real operating conditions is of great interest, for developing better lubricants. Reproducing these conditions in a laboratory viscometer, to investigate the lubricant behaviour, is a challenging task. As a result, methods that allow measuring properties of lubricant films in-situ, are preferred. In this thesis, an ultrasonic method employing shear horizontal surface acoustic waves (SH-SAWs) was developed, to measure lubricant viscosity and surface layers, at a free surface and an in-situ bearing film.

Ultrasonic methods have been widely used to measure liquid properties. Bulk acoustic waves and surface acoustic waves have been used to measure viscosity, film thickness and surface layers. Among the different types of ultrasonic waves, shear-horizontal surface acoustic waves are considered to be more suitable for measuring oil viscosity and formation of surface layers, in-situ in a running bearing application, as they present good coupling with liquids and moderate sensitivity to surface changes.

The SH-SAW response was investigated at a solid-liquid interface, for measuring lubricant properties. SH-SAWs attenuate at the solid-liquid interface, due to the liquid viscosity, and the attenuation was modelled as function of the liquid properties, material and geometry of the medium, and wave frequency. The SH-SAW attenuation-viscosity model was used to calculate the viscosity of different oils at a free surface, over a range of temperatures, which agreed with numerical models.

The SH-SAW response was further investigated for measuring the formation of viscous surface layers. Thin (h~ 10 to 30 nm) physically adsorbed surface layers were hard to detect. Further testing, has shown the successful application of SH-SAWs for detecting thick (h> 4.6 μm) surface layers, through a dry contact interface. Additionally, thick (h≥ 1.5 μm) surface layers were detected through viscosity changes at a wet contact interface, using SH-SAWs.

Finally, the SH-SAW method was utilised for measuring viscosity of oil films, in-situ in a journal bearing application. For the purpose of the study, a rotating journal and two bearing sleeves were set up in a rig, where different loading conditions were applied to create oil films of various thickness. The minimum film thickness due to loading and rig design, was expected to occur at the lower bearing sleeve, which was instrumented with two angled SH-SAW transducers to measure the changes in oil film viscosity with pressure.

In addition to the angled SH-SAW transducers, an ultrasonic shear transducer was installed inside the rotating journal, which allowed measurements of the oil film viscosity circumferentially. The two methods were found to be in good agreement. Both, successfully distinguished the different oil test samples, according to their viscosities and were able to measure changes in the oil film viscosity at the loaded region, however they were unable to measure any surface layer formation.

This thesis sets the foundation for the development of a method that potentially can bridge the gap between laboratory and in-situ testing; the SH-SAW method can be used for laboratory measurements of the oil viscosity, as well as in-situ an oil film viscosity measurements. As a result, the SH-SAW method could offer more consistent tracking of the oil properties throughout the development stages, the ability to keep tracking the properties of the fully formulated product when tested in an engine, and monitor the condition of the oil over time, for degradation. That would have significant impact on the automotive and lubricant industries, as it would significantly advance the understanding of the oil composition to help in the development of better lubricant products.

NOMENCLATURE

Roman symbols

A	Area (m^2)
b	Medium thickness (m)
c	Sound velocity (m/s)
F	Force (N)
f	Frequency (Hz)
h	Film thickness (m)
l	Liquid path length (m)
P	Power (Watt)
p	Pressure (Pa)
R	Reflection coefficient
T	Transmission coefficient
t	Temperature (°C)
u	Particle displacement (m)
V	Volume (m^3)
V_{pp}	Peak to peak voltage (V)
v	Velocity (m/s)
$\hat{x}$	Unit vector of x-axis
Z	Acoustic impedance (Rayl)

Greek symbols

α	Attenuation coefficient (m^{-1})
β_0	Wavenumber (m^{-1})
$\dot{\gamma}$	Shear rate (s^{-1})
δ	Penetration depth (m)
η	Dynamic viscosity (Pa s)
λ	Wavelength (m)

ρ	Density (kg/m^3)
τ	Shear stress (Pa)
υ	Kinematic viscosity (St)
ω	Angular frequency (rad/s)

Subscripts

i	Incident wave
r	Reflected wave
t	Transmitted wave
s	Solid
l	Liquid

ABBREVIATIONS

SAW	Surface acoustic wave
BAW	Bulk acoustic wave
VI	Viscosity index
QCM	Quartz crystal microbalance
SH-SAW	Shear horizontal surface acoustic wave
IDT	Interdigital transducer
EMAT	Electromagnetic acoustic transducer
SHo	Fundamental shear horizontal surface acoustic wave mode
FFT	Fast Fourier transform
PVM	Performance viscosity modifier
FM	Friction modifier

ACKNOWLEDGEMENTS

The author would like to acknowledge the excellent guidance, encouragement and inspiration given by Professor Rob Dwyer-Joyce throughout this project. Without his mentoring, it would not be possible to complete this work. The optimism, the scientific method for research and patience that the author has learned from him, will benefit the author for a lifetime.

The author would also like to thank Lubrizol Ltd. for the financial support and for offering this research opportunity. Special acknowledgement goes to Dr Rai Notay, John Durham, Dr David Growney and Dr Oliver Smith for their continuous support and patience throughout this project.

Thanks to all the staff, research assistants and fellow PhD students in the Tribology group for their kindness and support. Special thanks to Mr Dave Butcher and Mr Luke Callaghan for their great technical support. Without their contribution it would not be possible to complete this work. Thanks to Dr Robin Mills, Dr Michele Schirru, Dr Xiangwei Li, Dr Andrew Hunter and Dr Henry Brunskill and for their assistance and advice, especially on experimental skills. Thanks to Mr Marcello Cadeddu, Mr Tomos Brenchley, Mr Joseph Kanja, Mr Sushil Simkhada and Mr David Fort for the great discussions and help.

Thanks to all my friends for their encouragement throughout this project.

Finally, the author would like to dedicate this work to his parents, Mr Charalampos Tyreas and Mrs Spyridoula Nanou, who have always been supporting and encouraging the author.

CONTENTS

Abstract ..... **iii**

Nomenclature ..... **v**

Abbreviations ..... **vii**

Acknowledgements ..... **ix**

Contents ..... **xi**

List of Figures ..... **xvi**

List of Tables ..... **xxv**

1 Introduction **1**

1.1 Fuel economy, lubrication and viscosity 1

1.2 Statement of problem 2

1.3 Thesis aims 3

1.3.1 Thesis objectives 3

1.4 Layout of the thesis 4

2 Lubricant viscosity & additive package **6**

2.1 Viscosity 6

2.1.1 Viscosity relation with temperature 8

2.1.2 Viscosity relation with pressure 9

2.1.3 Viscosity and shear rate 10

2.2 Additive package 12

2.2.1 Viscosity modifiers 12

2.2.2 Friction modifiers 13

2.2.3 Anti-wear (AW) agents and extreme-pressure (EP) additives 14

2.2.4 Antioxidant additives (AO) 15

2.2.5 Anti-foam agents (AF) 15

2.2.6 Rust and corrosion inhibitors 16

2.3 Engine oil degradation 16

2.4 Measurement of viscosity 17

2.4.1 Capillary viscometers 17

2.4.2 Rotational viscometers 18

2.4.3 Falling body viscometers 20

2.5 Additive package measurements 23

2.5.1 Quartz crystal microbalance (QCM) 23

2.6 Conclusions 24

3 Ultrasound & surface acoustic waves **26**

3.1 The acoustic spectrum 26

3.2 Bulk acoustic wave (BAW) 26
3.3 Surface acoustic wave (SAW) 27
3.3.1 Rayleigh waves 27
3.3.2 Lamb waves 28
3.3.3 Love waves 29
3.3.4 Shear-horizontal surface acoustic wave (SH-SAW) 29
3.4 Attenuation, reflection and transmission of surface waves 30
3.4.1 Acoustic attenuation 30
3.4.2 Reflection and transmission 31
3.4.3 Dispersion 32
3.5 Surface acoustic wave generation 34
3.5.1 Surface acoustic wave device 35
3.5.2 Piezo-ceramics 37
3.5.3 Wedge method 40
3.5.4 Comb-structure method 42
3.5.5 Electromagnetic acoustic transducer (EMAT) 42
3.6 Conclusions 43
4 Ultrasound to measure viscosity, surface layers & thin films 44
4.1 Longitudinal BAWs to measure thin/thick films 44
4.2 Shear BAWs to measure liquid viscosity in films 46
4.3 SAWs to measure viscosity 50
4.4 QCM & SAW devices to measure surface layer formation 53
4.5 Conclusions 56
5 Experimental configuration for measuring lubricant properties using SH-SAWs 60
5.1 SH-SAW transducers 60
5.1.1 SH-SAW generation using piezo-ceramics 60
5.1.2 SH-SAW generation using angled transducers 60
5.2 Experimental configuration 62
5.3 Wave generation and signal acquisition 63
5.3.1 200 kHz face-shear SH-SAW transducers 63
5.3.2 400 kHz angled SH-SAW transducer 64
5.3.3 2 MHz angled SH-SAW transducers 65
5.4 Signal processing 66
5.5 Conclusions 67
6 SH-SAW propagation through a solid-liquid interface 69
6.1 SH-SAW propagation 69
6.2 SH-SAW attenuation- liquid viscosity model 70

6.3 The effect of liquid viscosity η and path length l 78
6.4 The effect of the liquid film thickness h 80
6.5 The effect of penetration depth δ 81
6.6 The effect of the solid material 84
6.7 The effect of the thickness of the medium d 85
6.8 The effect of angular frequency ω 86
6.9 Conclusions 87
7 Viscosity measurements with SH-SAWs 89
7.1 Apparatus 89
7.2 Results 91
7.2.1 The effect of shear-rate on viscosity 92
7.2.2 The effect of temperature on viscosity 95
7.3 Conclusions 99
8 SH-SAW response to surface layer formation 100
8.1 Background 100
8.2 Apparatus 104
8.3 Results 106
8.3.1 The effect of surface layer thickness on SH-SAW response 110
8.3.2 The effect of excitation frequency on the surface additives 114
8.3.3 The effect of temperature on the surface additives 115
8.4 Conclusions 116
9 Measuring viscosity of oil films in-situ in a journal bearing 118
9.1 Experimental configuration 118
9.1.1 Journal bearing rig 118
9.1.2 Ultrasonic transducers 121
9.2 Signal excitation, acquisition & processing 129
9.2.1 Signal excitation & acquisition 130
9.2.2 Signal processing 134
9.3 Determining viscosity in oil films 137
9.3.1 SH-SAW measurements of oil film viscosity 139
9.3.2 Shear BAW measurements of oil film viscosity 142
9.3.3 Comparison of shear BAW and SH-SAW methods 150
9.4 Conclusions 151
10 General discussion 153
10.1 The SH-SAW transducers 153
10.2 The attenuation-viscosity model 155
10.3 Bench-top testing of the oil viscosity and the formation of surface layers 156
10.3.1 Bench-top measurements of the oil viscosity 156

10.3.2 Bench-top measurements of surface layers 157
10.4 Oil film viscosity measurements in-situ a journal-bearing..... 158
11 Conclusions 161
11.1 Modelling the SH-SAW attenuation at a solid-liquid interface..... 161
11.2 Developing an ultrasonic method for measuring the attenuation of SH-SAW . 161
11.3 Implementing the SH-SAW method for measuring oil viscosity at a surface ... 162
11.4 Implementing the SH-SAW method for measuring oil viscosity in-situ in a bearing film 162
11.5 Future work 162
12 References 164

LIST OF FIGURES

Figure 1.1 Diagrammatic representation of workflow and linkages between the thesis objectives 4

Figure 2.1 Schematic representation of a lubricated contact with two components in relative motion 7

Figure 2.2 Three regimes of lubrication can be distinguished according to the bearing parameter; η is the dynamic viscosity, U is the sliding speed and W is the normal load [1]8

Figure 2.3 Shear stress- shear rate characteristic of a Newtonian fluid [1] 11

Figure 2.4 Shear stress- shear rate relationship of non-Newtonian fluids [7] 11

Figure 2.5 Thixotropic behaviour of fluids [1] 12

Figure 2.6 Viscosity modifiers' coil expansion with temperature to increase the oil viscosity [10] 13

Figure 2.7 Viscosity of low and high VI oils with temperature [10] 13

Figure 2.8 Schematic representation of friction modifiers [8] 14

Figure 2.9 Three commercial organic friction modifiers [13] 14

Figure 2.10 Zinc dialkylldithiophosphate (ZDDP) [8] 15

Figure 2.11 Schematic representation of a capillary viscometer; the fluid flows with speed v through the capillary [7] 18

Figure 2.12 Schematic representation of a cylindrical rotational viscometer [7] 19

Figure 2.13 Schematic representation of a cone-to-plate viscometer [7] 19

Figure 2.14 Parallel disks rotational viscometer [7] 20

Figure 2.15 a) Falling sphere viscometer, b) falling cylinder viscometer [7] 21

Figure 2.16 QCM-D schematic of electrode arrangement and coating [22] 24

Figure 2.17 QCM-D frequency and energy dissipation response to mass loading [23] 24

Figure 3.1 Sound spectrum 26

Figure 3.2 a) Particle network at rest, b) longitudinal wave, c) shear wave 27

Figure 3.3 Schematic of Rayleigh wave propagation [38] 28

Figure 3.4 a) Symmetric Lamb wave, b) anti-symmetric Lamb wave [39]..... 28

Figure 3.5 Schematic of Love wave propagation [41] 29

Figure 3.6 Schematic of shear-horizontal surface acoustic wave propagation [42] 30

Figure 3.7 Reflection and transmission of an incident wave 31

Figure 3.8 Lamb wave dispersion [44] 32

Figure 3.9 SH-SAW dispersion 33

Figure 3.10 Cross-sectional displacement of the 4 lowest SH-SAW modes [45] 34

Figure 3.11 Surface acoustic wave device (reproduction of Figure 1 [47]) 35

Figure 3.12 Single-finger three pair IDT structure [46].....36

Figure 3.13 SAW device configuration of a) Rayleigh wave, b) SH-SAW, c) Lamb wave, and d) Love wave [46] 36

Figure 3.14 a) Longitudinal, b) transverse and c) thickness-shear piezo-ceramics [48] 38

Figure 3.15 Thickness-shear piezo-ceramic (the red arrow indicates the poling direction of the particles).....38

Figure 3.16 Schematic of face-shear piezo-ceramic [49] 39

Figure 3.17 Mode conversion using the wedge method [50] 40

Figure 3.18 Wave mode change due to refraction [51].....41

Figure 3.19 Comb-structure method [50]..... 42

Figure 3.20 Schematic of EMAT structure [54] 42

Figure 4.1 Lubricant film thickness schematic 44

Figure 4.2 Schematic on an ultrasonic bean incident on a lubricated contact. *I* represents the incident wave, *F* represents the front face reflection, and *B* the back face reflections of the wave [55].....45

Figure 4.3 Mechanical analogy of spring model for Newtonian liquids 47

Figure 4.4 Mechanical equivalent of Maxwell model for viscoelastic liquids 47

Figure 4.5 Photograph of the model oil film apparatus. The circle of oil is visible as is the transducer through the transparent blocks [61] 48

Figure 4.6 Perspex plug instrumented with a shear sensor for measuring viscosity circumferentially in a journal bearing [62] 49

Figure 4.7 Addition of a polyimide layer to an ultrasonic shear probe for measuring oil viscosity circumferentially in a journal bearing [60] 50

Figure 4.8 Experimental set-up for fluid characterization using reflected Lamb waves [63] 51

Figure 4.9 Experimental set-up used for measuring liquid viscosity using S0 Lamb waves and SH0 shear-horizontal surface acoustic waves [64] 52

Figure 4.10 Experimental set-up for measuring liquid viscosity using the SH0 mode (1. angled transducer for sending/receiving waves, 2. ribbon-like medium to increase the sensitivity, 3. Vessel) [65] 53

Figure 4.11 Molecular adsorption on the electrode surface of a quartz crystal microbalance [67] 54

Figure 4.12 Schematic representation of a typical SAW device for measuring molecular adsorption [68] 54

Figure 5.1 200 kHz face-shear piezo-ceramic *(left)*, SH-SAW transmitter & receiver *(right)* 60

Figure 5.2 Angled SH-SAW transducers developed using the wedge method 61

Figure 5.3 Experimental set-up for measuring lubricant properties using SH-SAWs..... 62

Figure 5.4 Schematic of SH-SAW generation using SH-SAW transducers 63

Figure 5.5 Signal response in the time domain, using 200 kHz face-shear transducers... 64

Figure 5.6 Signal response in the time domain, using 400 kHz angled transducers 65

Figure 5.7 Signal response in the time domain, using 2 MHz angled transducers 65

Figure 5.8 2 MHz SH0 mode after being isolated from the waveform 66

Figure 5.9 Schematic representation of the fast Fourier transform (*FFT*) [72].....67

Figure 5.10 Example of the FFT of the 2 MHz SH0 mode (Figure 5.8) 67

Figure 6.1 SH-SAW propagation and particle movement [42]..... 69

Figure 6.2 SH-SAW attenuation at the solid-liquid interface 70

Figure 6.3 SH-SAW attenuation at the solid-air interface, due to the solid material properties 70

Figure 6.4 SH-SAW attenuation at the solid-liquid interface, due to the solid material properties and liquid viscosity 71

Figure 6.5 Illustration of the arrangement and the coordinates.....72

Figure 6.6 Wave power loss P_l at the solid-liquid interface.....74

Figure 6.7 Wave power in the solid 74

Figure 6.8 Power flow at the solid-air (*left*) and solid-liquid (*right*) interfaces 75

Figure 6.9 Viscosity- transmission coefficient relationship 78

Figure 6.10 Lubricant sample spreads between the Perspex and aluminium plates 79

Figure 6.11 Transmission coefficient decrease with liquid viscosity and path length..... 80

Figure 6.12 Transmission coefficient decrease for 1.0 ml and 0.5 ml of oil samples 81

Figure 6.13 SH-SAW penetration depth and liquid film thickness..... 82

Figure 6.14 SH-SAW penetration depth in a liquid film 83

Figure 6.15 Acoustic impedance effect on SH-SAW sensitivity.....85

Figure 6.16 SH-SAW amplitude on a 2 mm thick *(top),* and 0.4 mm thick *(bottom)* steel plates..... 86

Figure 6.17 SH-SAW attenuation due to PAO 4 viscosity at 400 kHz and 2 MHz 87

Figure 7.1 Experimental configuration for measuring the viscosity of lubricant oil from the attenuation of SH-SAWs through the solid-liquid interface 89

Figure 7.2 Transmission coefficient of Cannon viscosity standard lubricants at 400 kHz & 2 MHz.....91

Figure 7.3 Viscosity of Cannon viscosity standard lubricants as measured with a Brookfield viscometer and SH-SAWs 92

Figure 7.4 Transmission coefficient of PAO lubricants at 400 kHz & 2 MHz 94

Figure 7.5 Viscosity of PAO lubricants as measured with a Brookfield viscometer and SH-SAWs 94

Figure 7.6 High temperature viscosity measurement test set-up 96

Figure 7.7 Air reference calibration curve of the 0.2 mm thick steel plate 97

Figure 7.8 Viscosities of PAOs over temperature, as measured using SH-SAWs *(data points)* and predicted using Vogel equation *(dashed lines)* 98

Figure 8.1 Molecular adsorption of friction modifiers on the interacting surfaces to prevent friction and wear [1] 102

Figure 8.2. Schematic of a multifunctional polymer; a) at low speeds the surfaces are separated through an extremely viscous adsorbed polymer layer, b) at higher speeds the viscosity is based on the viscosity of the bulk lubricant [82] 102

Figure 8.3. Adsorbed polymer arrangements; a) "pancake", b) "mushroom" and c) "brushes" [13] 103

Figure 8.4. Behaviour of various lubricants with temperature and the effect on friction; paraffins (A), fatty acids (B), extreme-pressure additives (C), and fatty acids+extreme-pressure additives (D) [78] 104

Figure 8.5 SH-SAW transmission coefficient *(top)* and dynamic viscosity *(bottom)* responses to surface film formation over time 107

Figure 8.6 SH-SAW frequency responses to surface film formation over time 108

Figure 8.7 Schematic of surface layer formation through physical adsorption *(top)*, expected viscosity response over time *(middle)*, expected frequency response to molecular adsorption *(bottom)* 109

Figure 8.8 Comparison between theoretical viscosities *(dashed lines)* and measured viscosities with SH-SAWs *(solid lines)* 110

Figure 8.9 Surface layer thickness and SH-SAW penetration depth 111

Figure 8.10 Deposition of the solution (*left*), evaporation of the solvent (*middle*), and residual PVM layer (*right*) 112

Figure 8.11 SH-SAW transmission coefficient change to PVM layer formation of various thicknesses 112

Figure 8.12 SH-SAW response to PAO 4 on a 1.55 um PVM layer (*top*), and a 4.6 um PVM layer (*bottom*) 113

Figure 8.13 The effect of frequency on the FMs and PVMs 114

Figure 8.14 Temperature effect on the PVMs and FMs 115

Figure 9.1 Journal bearing rig for measuring oil viscosity in a dynamic system 119

Figure 9.2 Journal-bearing assembly component description 120

Figure 9.3 System lubrication *(top)*, oil container *(bottom right)*, oil pump *(bottom left)* 121

Figure 9.4 Journal & bearing instrumentation with shear and SH-SAW transducers, respectively 122

Figure 9.5 Bearing sleeve instrumentation with SH-SAW angled transducers 123

Figure 9.6 Bearing clamped between the two housings 124

Figure 9.7 Top and bottom housing designs for bearing sleeve installation 124

Figure 9.8 Comparison of the SH-SAW signal before and after installing in the housings 125

Figure 9.9 Temperature calibration of the bearing & housing 125

Figure 9.10 Temperature calibration curve for the bearing sleeve 126

Figure 9.11 Aluminium plug schematic *(left)* and shear wave propagation *(right)* 126

Figure 9.12 Ultrasonic shear transducer 127

Figure 9.13 Shear plug installation on the journal 127

Figure 9.14 The miniaturised ultrasonic shear transducer installed in the journal 128

Figure 9.15 Shear transducer temperature calibration curve 129

Figure 9.16 SH-SAW signal response in the time domain, as acquired with the picoscope 131

Figure 9.17 Shear wave signal response in the time domain, as acquired with the picoscope 132

Figure 9.18 Optical encoder model installed on the journal for measuring the number of revolutions 133

Figure 9.19 Encoder index pulses indicating two complete journal cycles, as they were acquired using the picoscope 133

Figure 9.20 Signal excitation & data acquisition schematic 134

Figure 9.21 SH-SAW signal processing; SH0 mode extraction *(left)* and FFT of the signal *(right)*. The black lines represent the reference signal at the solid-air interface, while the red lines represent the test signal at the solid-liquid interface..... 135

Figure 9.22 Shear signal processing; shear mode extraction *(left)* and FFT of the signal *(right)*. The black lines represent the reference signal at the solid-air interface, while the red lines represent the test signal at the solid-liquid interface..... 135

Figure 9.23 Transmission coefficient of the SH0 mode at the solid-liquid interface 136

Figure 9.24 Shear wave reflection coefficient, at the solid-liquid boundary of a rotating journal 136

Figure 9.25 Circumferential shear reflection coefficient for a complete journal rotation137

Figure 9.26 Viscosity of the PAO 4 blends, at 540 rpm and different loading conditions 140

Figure 9.27 a) Lower bearing sleeve wear marks, due to b) misalignment between the journal-bearing centres 141

Figure 9.28 Circumferential viscosity profile of the PAO 4 blends, at 540 rpm and no load 142

Figure 9.29 Raimondi-Boyd chart of the eccentricity ratio ε according to Sommerfeld number S, for 360° journal bearings of various L/D ratios [78] 145

Figure 9.30 Circumferential oil film thickness and pressure distribution along the bearing length for a) 0.5 kN, b) 1.0 kN and c) 1.5 kN load 146

Figure 9.31 Circumferential viscosity profiles of the PAO 4 blends, at 540 rpm and different loading conditions 147

Figure 9.32 Oil film regions due to loading 149

Figure 9.33 Comparison between shear BAW and SH-SAW methods for measuring oil film viscosity at the high pressure region (300° to 60°) 150

Figure 10.1 a) Schematic of the aluminium curved wedge for bearing sleeve installation, and b) the creation of multiple refraction angles, due to the curved face 154

Figure 10.2 Moulded heel to allow the flat wedge to be mounted on the bearing sleeve 155

Figure 10.3 Multi-frequency set-up using different frequency piezo-ceramics bonded a) on individual wedges, and b) on one common wedge 156

LIST OF TABLES

Table 2.1 Viscosity-temperature models [1] 9

Table 2.2 Advantages and disadvantages of conventional viscometers [7] 22

Table 2.3 Various causes that lead viscometer to erroneous results [7] 22

Table 3.1 Comparison of performance of different SAW devices..... 37

Table 4.1 Advantages and disadvantages of ultrasonic methods for measuring liquid film thickness, viscosity and the formation of surface layers 57

Table 5.1 Incident angle of Perspex wedge for aluminium and steel application 61

Table 6.1 Cannon viscosity standard lubricant properties at 25 ℃ [75] 79

Table 6.2 200 kHz SH-SAW penetration depth in the Cannon standard lubricants..... 82

Table 6.3 Oil film thickness for 1.0 ml and 0.5 ml oil samples over different path lengths82

Table 6.4 Acoustic impedance of materials [77]..... 84

Table 6.5 Number of SH-SAW modes on 0.4 and 2.0 mm thick plates 86

Table 7.1 Number of generated SH-SAW modes on a 0.2 mm thick steel plate..... 90

Table 7.2 Cannon viscosity standard lubricants properties at 25 ℃ [75]..... 90

Table 7.3 PAO lubricant properties at 25 ℃ 93

Table 7.4. The three known viscosity values at three temperatures (provided by Lubrizol Ltd.), which were used to calculate the Vogel constants, to predict the viscosities of the PAOs over temperature.....97

Table 8.1 PAO blends' properties at 25 ℃.....105

Table 8.2 PAO blends SH-SAW penetration depth..... 111

Table 9.1 Journal-bearing specifications.....123

Table 9.2 Acoustic impedances of oil, polyimide and aluminium.....128

Table 9.3 Excitation parameters for SH-SAW & shear transducers.....130

Table 9.4 Equation parameters for measuring oil viscosity, from the transmission and reflection of SH-SAWs and shear BAWs, respectively 138

Table 9.5. Oil film pressure due to load 139

Table 9.6. Viscosity-pressure coefficient α for medium VI spindle oil [1] 139

Table 9.7 Three known viscosity values at three temperatures (provided by Lubrizol Ltd.), which were used to calculate the Vogel constants, to predict the viscosities of the PAO 4 blends over temperature 140

Table 9.8 Comparison between viscosities as measured with shear BAWs in-situ in a journal bearing film and predicted by Vogel equation 143

Table 9.9 Oil film viscosity regions due to loading (*in the case of PAO 4 and 1.5 kN load) 150

1 INTRODUCTION

This chapter presents a brief description of lubrication, the impact the lubricant industry has made over time and the current trends. The problem this thesis was focussed on is also introduced, along with the thesis aim and objectives, and the thesis structure.

1.1 Fuel economy, lubrication and viscosity

Lubrication is the main process or technique used to reduce friction and wear between two components in relative motion, close to each other (almost in contact), by introducing a substance called lubricant between them. The lubricant can be a solid, a semi-solid such as grease, a liquid such as oil or water, or even a gas. In an internal combustion engine, which is the primary focus of this work, oil is used to provide lubrication between the piston rings and cylinder, the main bearings & big end bearings of the connecting rods and the crankshaft, the small end bearings of the connecting rods and the piston-pin, the bearings and the camshaft, and the timing chain or gears on the camshaft.

A good engine oil is generally characterised by low freezing and high boiling points, in order to maintain its liquid form in a wide range of temperatures. It possesses high viscosity index, it is thermally stable and presents good hydrolytic stability. It is resistive to degradation, it prevents corrosion, and it is highly resistive to oxidation [1].

Engine oils perform several critical functions, including lubrication, cleaning, cooling, suspending and protecting metal surfaces against corrosion, friction and wear. The lubricating oil consists of a base oil and an additive package. The base oil is responsible for lubricating the components and carrying the additives. The additives are responsible for either adding a new property to the base oil or enhancing existing properties. Viscosity and viscosity index, pour point and resistance to oxidation are a few examples of existing properties. Suspending and cleaning abilities, protection against wear, and control over corrosion are a few examples of new properties added to the base oil. Typically, engine oils contain 95% base oil and less than 5% additives, the main families of which include antioxidants, pour point detergents, corrosion inhibitors, viscosity modifiers, anti-foaming agents, viscosity index improvers and anti-wear agents (Chapter 3 in [1]).

An engine oil is designed to protect the moving components, which operate under different conditions of temperature, pressure and speed, against friction and wear, thus extending their life. At low temperatures, the oil is expected to maintain a sufficient flow in order to deliver enough lubrication to the moving parts. At higher temperatures, it is expected to reduce the friction between the moving components, by keeping them separated, in order to minimise wear. Contaminants cause an additional problem, as they

form in the engine during operation. These include sludge, acids, wear debris and soot particles. The lubricant oil is responsible for preventing the contaminants from damaging the components.

Some of the current trends in the lubricant industry include [2]:

- **Correction of viscosity:** more precise selection of viscosity, as it affects the fuel consumption, wear and tolerance to contamination.
- **Judicious use of premium and synthetic lubricants:** for a long time these lubricants were considered to be the solution to every problem and they were promoted to replace old lubricants in every application. After better understanding them, they are being used in applications they are best suited for.
- **Energy conserving and environmentally friendly lubricants:** huge efforts have been made for more energy conserving and environmentally friendly lubricants over the past years, however that is just the tip of the iceberg.
- **Additive reconstruction:** some oil additives can be replaced after degrading instead of changing the entire oil in a car engine, which leads to less disposal concerns.
- **Headspace management:** to prevent contamination of the lubricant inside the oil tank or the sump oil level.
- **Smart filter carts:** apart from filtering the oil, these carts are equipped with oil analysis sensors and computers to monitor the condition of the lubricant.
- **Online sensors and real-time monitoring:** for oil analysis under real operating conditions.

1.2 Statement of problem

Lubricant oil properties, e.g. viscosity, compressibility, etc. strongly depend on the operating temperature, pressure and shear rate. Modern engine lubricants comprise an additive package to enhance existing properties or add new ones, in order to improve the lubricant performance under the conditions of high temperature, high pressure and high shear. Reproducing the operating conditions of an engine in a laboratory viscometer, to investigate the lubricant behaviour, is a challenging task. As a result, methods that allow the measurement of lubricant properties in-situ in a lubricant film, are always preferred.

The two main mechanisms to reduce the friction and wear of the moving parts, are the formation of a lubricant film, thicker than the combined surface roughness of the moving parts, and the formation of protective layers on the component surfaces. Viscosity is

responsible for maintaining a thick oil film under a range of temperatures, extreme pressure and shear. When the film thickness is reduced and the components in relative motion come closer to their asperities, surface layers protect the moving parts from metal to metal contact. As a result, measuring lubricant viscosity and formation of protective layers on the metal surfaces (boundary additives, viscosity modifiers, etc.) in-situ in an engine is of great importance, as it will provide useful information about the lubricant performance which will contribute to the development of better lubricants. Currently, the development of lubricants depends on the predictions of models and lab measurements, as there are limited tools to measure and monitor lubricants' performance in-situ in an engine.

The extreme conditions of high pressure, temperature and shear, the limited space, inaccessibility and corrosive environment of an engine make in-situ condition monitoring of lubricants a challenging task. Ultrasonic methods can tackle most of these limitations as they utilise small, easy to bond transducers, robust enough to withstand the extreme engine conditions. Furthermore, ultrasonic methods do not require the transducer to be in direct contact with the lubricant, as ultrasound travels through both solids and liquids. As a result, the transducers can be bonded on an accessible place, while measuring lubricant properties in the area of interest.

Two main families of ultrasound can be distinguished according to the propagation properties; bulk acoustic waves (BAWs) and surface acoustic waves (SAWs). BAWs propagate through the bulk of a medium, while SAWs propagate along the surface of the medium. The main difference is that the measuring area of bulk waves is limited to the transducer size, whereas surface waves occupy larger area as they travel longer distances, thus increasing the measuring area. As a result, SAWs are preferred over BAWs when measuring surface changes.

1.3 Thesis aims

The aim of this thesis was to develop an ultrasonic method to measure lubricant properties in a running bearing. The output will be ultrasonic transducers that can be used to measure oil viscosity and the formation of surface layers in-situ in a running bearing.

1.3.1 Thesis objectives

- Research the effect of engine lubricants on the propagation of surface acoustic waves (SAWs)
- Research the capabilities of transmitting and receiving SAWs to build a bench top device that can be used to measure lubricant properties

- Research the effect of viscosity on the SAW propagation through a wet contact interface
- Research the potential of functionalising the SAW transducers to measure additives and surface layer formation
- Explore the SAW capabilities for in-situ in an engine viscosity measurements and detection of surface layer formation

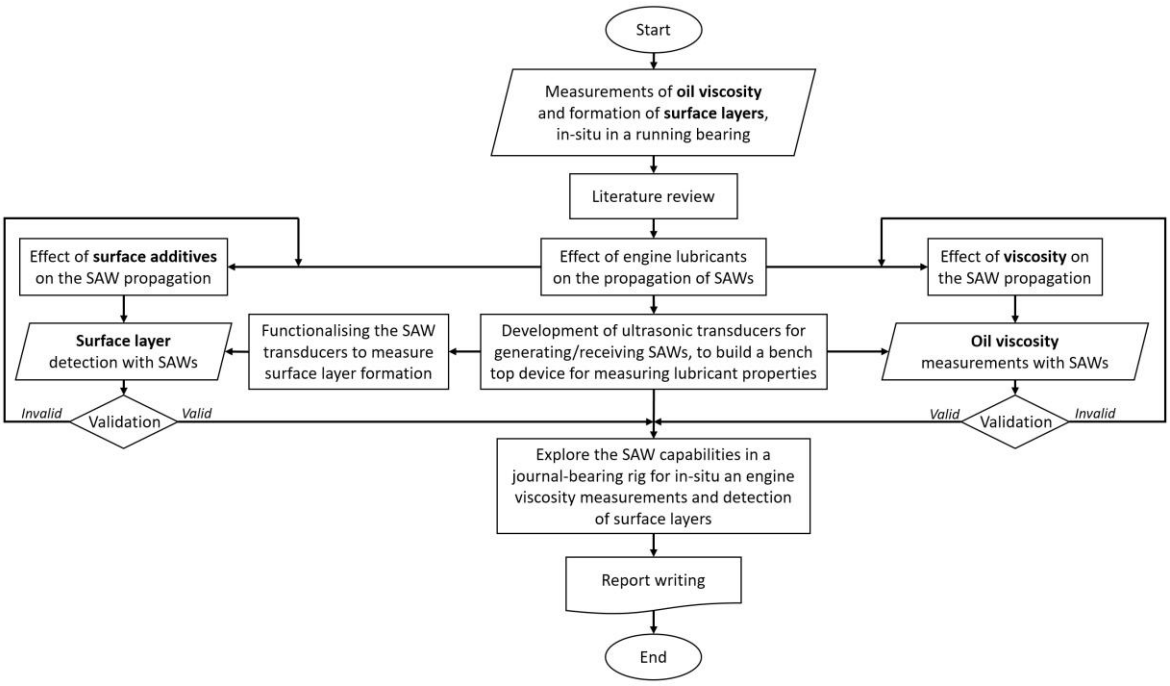

Figure 1.1 Diagrammatic representation of workflow and linkages between the thesis objectives

1.4 Layout of the thesis

In Chapter 2, a brief description of lubricant viscosity and composition is presented, including different additive packages blended with the base oil and the lubricant properties they add or enhance. Finally, methods for measuring both viscosity and different additive packages are also reported.

In Chapter 3, the theory of ultrasound and surface acoustic waves is presented, with more attention given to surface acoustic waves, as they are the primary method used throughout this work. The propagating properties of SAWs are also reported, followed by different methods for generating them.

Chapter 4 briefly reports different ultrasonic methods currently used for measuring lubricant properties, including lubricant film thickness, viscosity and additives. The findings and limitations of each method are also reported.

In Chapter 5, the experimental apparatus used in the ultrasonic technique is introduced, including the hardware for generating and receiving ultrasound, as well as the means for acquiring the ultrasonic signal and processing it.

Chapter 6 presents the results from the investigation of propagating SAWs through a solid-liquid interface. A model was used to relate the attenuation of SAWs to the viscosity of the liquid, followed by a thorough experimental study.

Chapter 7 focusses on the application of the attenuation model for measuring the viscosity of lubricant oil. The viscosity of different oils was measured using the attenuation model and a rotational viscometer, for comparison. The effect of temperature and shear rate on the lubricant viscosity was also studied experimentally and compared with analytical models.

Chapter 8 focusses on the detection of adsorbed surface additive layers on metallic surfaces with ultrasonic means. A method for detecting surface films is presented, based on the viscosity difference close to the surface and in the bulk of the oil, due to surface layer formation. Physically adsorbed surface layers were studied experimentally along with model deposited surface layers to explore the limitations of the method.

In Chapter 9, the methods previously developed were implemented in a journal bearing rig for measuring oil film viscosity and surface layers in-situ in a running bearing. A combination of SH-SAW and shear BAW sensors were employed to study the lubrication mechanisms.

Chapter 10 presents an overall discussion of the SH-SAW transducers, the attenuation-viscosity model, the bench-top measurements of the oil viscosity and the formation of surface layers, the oil film viscosity measurements in-situ a journal-bearing rig, as well as advantages and disadvantages of the SH-SAW method.

Finally, Chapter 11 summarises the findings from this work and presents the future actions.

2 LUBRICANT VISCOSITY & ADDITIVE PACKAGE

This chapter reviews the properties and composition of a lubricant oil. The viscosity of the lubricant and the additive package blended with the base oil are the primary focus of this chapter. Methods for measuring both viscosity and the presence and activity of different additives are also listed.

2.1 Viscosity

Viscosity is the most important characteristic of a lubricant oil. In simple words, viscosity of a fluid is a measure of its resistance to flow. However, this definition is oversimplified and in reality, the laws that govern viscosity are more complex.

When a fluid flows, neighbouring fluid layers move at different velocities, thus friction is developed between the fluid molecules and heat is generated. Viscosity describes the force that is required to overcome the friction between the molecules to allow the fluid to flow. Newton first noticed that when a fluid is forced between two components in relative motion, the fluid molecules generally move faster near the moving component and slower away from it. Therefore, some force is required to overcome the friction between the fluid molecules, in order to allow the fluid to flow.

Figure 2.1 shows schematically a stationary (Component 1) and a moving component (Component 2), separated by a fluid layer. Newton described the relationship between the shear force F applied to "Component 2", the relative velocity v of the fluid and the fluid layer thickness h as:

$$F = \eta A \frac{\partial v}{\partial h} \tag{2.1}$$

In Equation 2.1, A is the wet surface area, the proportionality constant η is called dynamic viscosity, v is the fluid layer velocity and $\partial v/\partial h$ is the local shear velocity or shear rate $\dot{\gamma}$. Shear viscosity therefore represents the resistance offered by a fluid to an applied shear stress.

Perhaps a more suitable definition for the viscosity, results from Eyring's equation [3] who considered the flow of a viscous fluid as a chemical reaction. Similar to Newton, Eyring considered the fluid flow as layers moving at different velocities and sliding past each other. According to Eyring, each fluid layer is one molecule thick, and the motion is assumed to take place by an individual molecule, which occasionally acquires the activation energy to pass to the next equilibrium position in the layer. In this context, viscosity represents the energy that is consumed for the passing of a single molecule from

one equilibrium position to another, by squeezing against its neighbouring molecules, and is expressed by Eyring's general equation:

$$\eta = \frac{\lambda_1 h}{\kappa \lambda^2 \lambda_2 \lambda_3} \frac{F_n}{F_a^*} e^{\frac{E_0}{kT}} \tag{2.2}$$

In Equation 2.2, λ is the distance between equilibrium positions in the direction of flow, λ_1 is the perpendicular distance between adjacent layers, λ_2 is the distance between adjacent molecules in the direction of flow, λ_3 is the distance between molecules in the plane of flow and normal to the direction of flow, κ is the transmission coefficient (κ=1 for chemical reactions), h is the Planck constant, F_n is the partition function of normal molecule, F_a^* is the partition function of the activated molecule, E_0 is the activation energy of the flow process, k is the Boltzmann constant, and T is the absolute temperature.

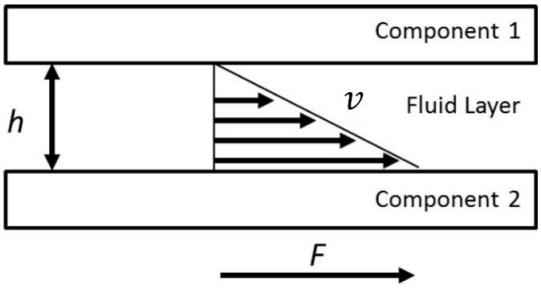

Figure 2.1 Schematic representation of a lubricated contact with two components in relative motion

Viscosity is expressed in Pa s, and it is referred to as dynamic viscosity. Another unit to express the dynamic viscosity is in P (Poise), where 1 cP= 1 mPa s. When the dynamic viscosity is divided by the density of the oil it is called the kinematic viscosity.

$$\upsilon = \frac{\eta}{\rho} \tag{2.3}$$

In Equation 2.3, υ is the kinematic viscosity and ρ is the density of the oil. The kinematic viscosity is measured in St (Stokes). The kinematic viscosity is used to quantify the resistance to the fluid flow.

The oil viscosity is responsible for supporting a thick oil film formed by the hydrodynamic action, capable of carrying the load and protecting the interacting components from friction and wear at high relative velocities between them, as the Stribeck curve indicates in Figure 2.2 (*hydrodynamic lubrication*).

As the relative velocity decreases the oil film becomes thinner, the two interacting components come closer together and the load is partially carried by asperities contacting and partially by a thin oil film formed by the hydrodynamic action (*mixed lubrication*).

As the relative velocity further decreases, the oil film becomes very thin and is no longer capable of supporting the load. As a result, the interacting components come into contact at their asperities and major friction and wear can be prevented through thin surface layers formed by additives blended with the oil (*boundary lubrication*).

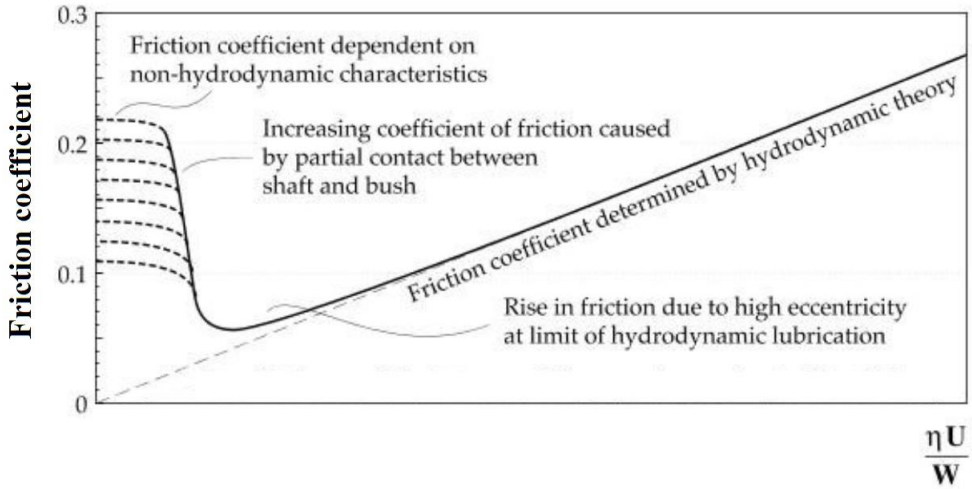

Figure 2.2 Three regimes of lubrication can be distinguished according to the bearing parameter; η is the dynamic viscosity, U is the sliding speed and W is the normal load [1]

2.1.1 Viscosity relation with temperature

The viscosity of the oil changes with temperature; as the temperature increases the viscosity of the oil decreases. With the increase of temperature, the bonds between the liquid molecules become weaker, thus less activation energy is required for the passing of one molecule from one equilibrium position to another, as the bonds present less resistance to the applied motion, and viscosity decreases [4]. The relationship between viscosity and temperature can be described very accurately using the Vogel equation, as described by Stachowiak and Bachelor in Section 2.3 [1]:

$$\eta = ae^{\frac{b}{(t-c)}} \tag{2.4}$$

In Equation 2.4, a, b, c are constants defined by fitting three known values of viscosity at three temperatures, and t is the temperature at which the viscosity is measured. There are several other models to describe the viscosity-temperature relationship, a few of which are listed in Table 2.1.

Table 2.1 Viscosity-temperature models [1]

Model	Equation	Comments
Reynolds	$\eta = be^{-at}$	Early equation; accurate only for very limited temperature range
Slotte	$\eta = a/(b+t)^c$	Reasonable; useful in numerical analysis
Walther	$(v+a) = bd^{1/t^c}$	Forms the basis of ASTM viscosity-temperature chart

In Table 2.1, v refers to the kinematic viscosity, t is the temperature viscosity is measured at and a, b, c, d are constants.

2.1.2 Viscosity relation with pressure

The viscosity of the oil is proportional to its pressure; as the pressure rises the viscosity of the oil increases. According to Eyring's theory [4], a molecule has to overcome both the internal and external pressures applied to it, in order to pass from one equilibrium position to another, thus the activation energy required for the reaction becomesE_0= E_{int}+E_{ext}. At small pressures, the energy E_{int} required to overcome the internal pressure is greater than the energy E_{ext} required to overcome the external pressure, thus $E_0 \sim E_{\text{int}}$. When the external pressure rises though, the parameter E_{ext} becomes considerable and more energy E_0 is required to overcome both internal and external pressures, thus leading to an increase in the viscosity. The relationship between the pressure and viscosity can be described by the Barus equation [5]:

$$\eta = \eta_0 e^{\alpha p} \tag{2.5}$$

In Equation 2.5, η is the viscosity at pressure p, η_0 is the viscosity at ambient pressure and α is the pressure coefficient. Barus equation can estimate the viscosity of a lubricant accurately up to 0.5 GPa pressure. Above that pressure, the equation becomes unreliable and leads to serious errors, especially when the ambient temperature is very high [1]. This occurs due to the dependency of the pressure-viscosity coefficient α on the molecular structure of the lubricant, its physical characteristics, and the temperature-viscosity relationship, which can be different among the oils. A good approximation of the pressure-viscosity coefficient α in Barus equation, was proposed by Roelands [6] and can be expressed as:

$$\alpha^* = p^{-1}(ln\eta_0 + 9.67)\left[\left(\frac{t-138}{t_0-138}\right)^{-S_0}(1+5.1\times10^{-9}p)^Z - 1\right] \tag{2.6}$$

In Equation 2.6, α^* is the Roelands pressure-viscosity coefficient, which is a function of both the pressure p and the temperature t, t_0 is the reference or ambient temperature in [K], and Z, S_0 are constants, different for each oil, independent of temperature and pressure, and they are calculated using Equations 2.7 and 2.8, respectively:

$$Z = \frac{\alpha}{5.1\times10^{-9}(ln\eta_0+9.67)} \tag{2.7}$$

$$S_0 = \frac{\beta(t_0-138)}{(ln\eta_0+9.67)} \tag{2.8}$$

In Equations 2.7 and 2.8, α is the pressure-viscosity coefficient similar to Equation 2.5, and $\beta = (ln\eta_0 + 9.67)(1 + 5.1 \times 10^{-9}p)^Z \left(\frac{S_0}{t_0-138}\right)$.

2.1.3 Viscosity and shear rate

The shear rate is a measure of the fluid particle velocity and strongly affects the fluid viscosity. Depending on the nature of the fluid, the shear rate has different effect on viscosity (Section 2.6 in [1]). Fluids can be classified into two main categories; Newtonian and non-Newtonian fluids.

2.1.3.1 Newtonian fluids

In Newtonian fluids, the applied shear stress is linearly related to the shear rate, as shown in Figure 2.3. The relationship between shear stress τ and shear rate $\dot{\gamma}$ is described by Equation 2.9:

$$\eta = \frac{\tau}{\dot{\gamma}} \tag{2.9}$$

This means that the viscosity of purely Newtonian fluids is independent of the shear rate. In reality, most fluids are exhibiting a non-Newtonian behaviour where viscosity changes with the shear rate. Most engines operate at high velocities, thus subjecting the oil to high shear rates, and the oil behaves as a non-Newtonian fluid. This occurs due to the addition of additives in the oil or its molecular structure. For these lubricants the relationship between shear stress and viscosity is non-linear.

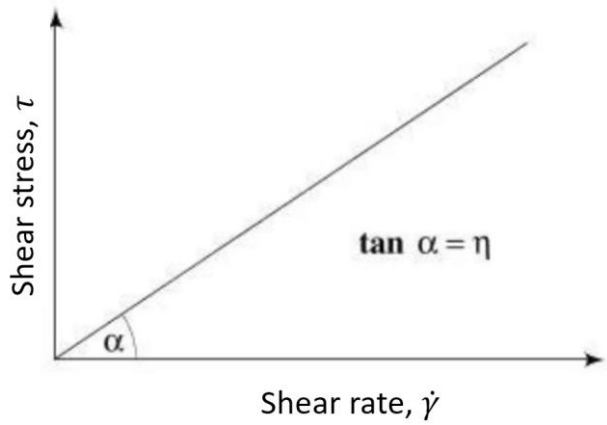

Figure 2.3 Shear stress- shear rate characteristic of a Newtonian fluid [1]

2.1.3.2 Non- Newtonian fluids

Non-Newtonian fluids are divided in two main types depending on the behaviour they exhibit; *pseudoplastic* and *thixotropic*.

Pseudoplastic refers to fluids which exhibit a *shear-thinning* or *shear-thickening* behaviour. In shear-thinning fluids, viscosity decreases with increased shear rate. The opposite is shear-thickening, also known as **dilatancy**, where the fluid viscosity increases with increased shear rate. The pseudoplastic and dilatant behaviour of fluids are shown in Figure 2.4, in comparison with the purely Newtonian behaviour.

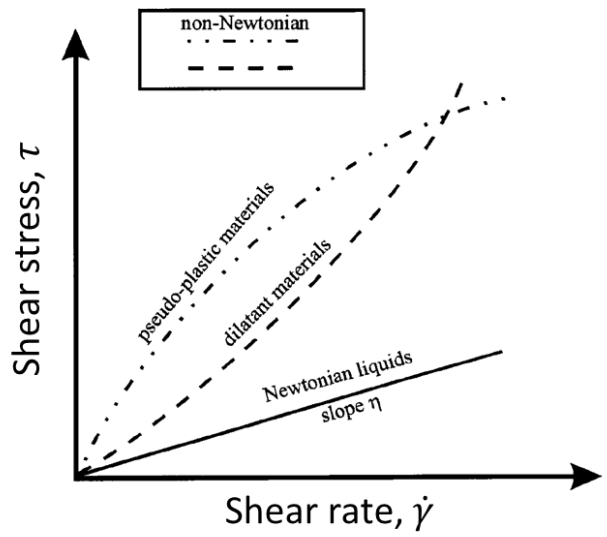

Figure 2.4 Shear stress- shear rate relationship of non-Newtonian fluids [7]

Thixotropic behaviour is characterised by the *shear duration thinning* behaviour of a fluid, in response to an increase in the **duration** of shear the fluid is subjected to. In this case, the

fluid apparent viscosity reduces with time the fluid is subjected to a constant shear, until balance is reached and the apparent viscosity attains a steady value, as shown in Figure 2.5.

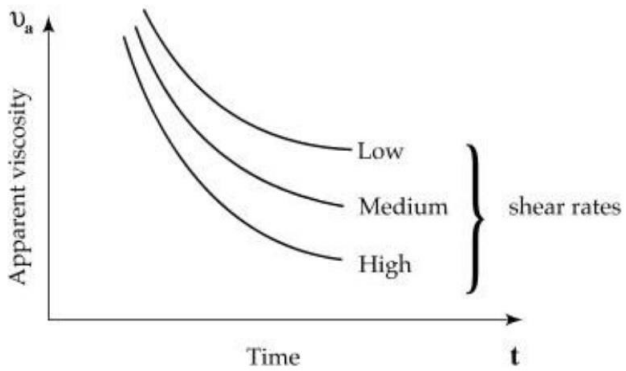

Figure 2.5 Thixotropic behaviour of fluids [1]

2.2 Additive package

Additives are chemical compounds added to the base oil to provide specific properties to the finished oil. Some additives add new and useful properties to the base oil, some enhance existing properties, while others reduce the rate at which undesirable effects take place in the oil during its service life. The most used additives in terms of their primary function, as they are described by Nassar et al. [8], are discussed in the following sections.

2.2.1 Viscosity modifiers

Viscosity modifiers are polymers with high molecular weight (>10,000 gr/mol) and are being used to increase the viscosity of the base oil (Figure 2.6) and to improve the viscosity index (Figure 2.7). Viscosity index (VI) is an arbitrary measure to characterise the change of oil viscosity with temperature variations. Higher VI indicates less change in viscosity with temperature and vice versa. At lower temperatures the viscosity modifiers change the viscosity of the lubricant oil as little as possible, whereas at higher temperatures the polymer solubility increases, leading to "coil expansion", which results in higher viscosity than expected for untreated oil [9]. Common viscosity improvers include polymethacrylate (PMA) and mixed polymethacrylate/olefin copolymer (PMA-O), olefin copolymers (OCP) and dispersant polyethylene propylene copolymer (OCP-D), polyalkylmethacrylate (PAMA), hydrogenated styrene–diene (HSD), polyisobutene (PIB), polystyrene-b-isoprene block polymer (PSB) and hydrogenated isoprene star copolymer (HIP-S).

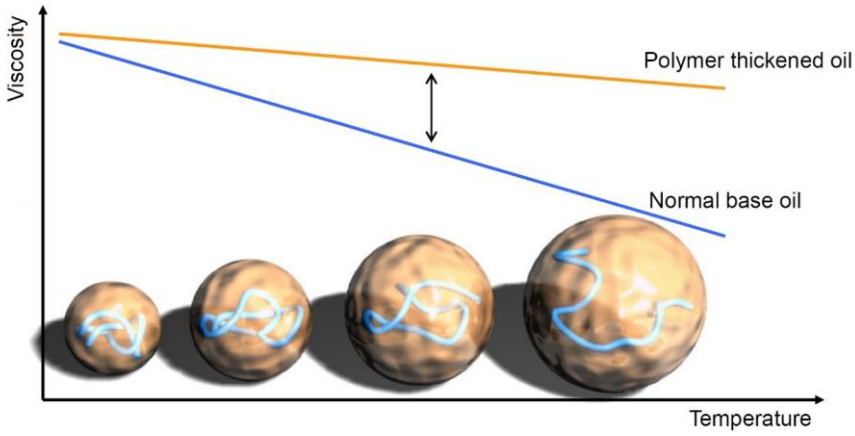

Figure 2.6 Viscosity modifiers' coil expansion with temperature to increase the oil viscosity [10]

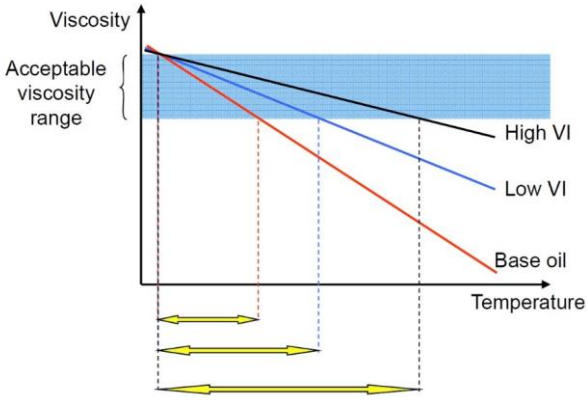

Figure 2.7 Viscosity of low and high VI oils with temperature [10]

The primary focus of viscosity modifiers is to improve the oil flow and its lubricating properties at the hydrodynamic regime, producing products that meet the multigrade specifications [11]. A secondary function of the VMs is the formation of thick (10-30 um) boundary films [12], through physical adsorption of molecules on the metal surfaces, able to withstand high temperatures (>120 °C), which results in reduced friction in sliding contacts. Reduced friction has also been noticed in rolling contacts due to the formation of boundary VM films, which has led contacts to operate at lower friction (mixed or elastohydrodynamic regimes) than they normally do at low speeds (boundary regime) [11]. Typical example of VMs forming boundary films is that of the polymethacrylate (PMA) and polyalkylmethacrylate (PAMA).

2.2.2 Friction modifiers

These are additives that usually reduce friction, by forming surfactant monolayers adsorbed from the solution or self-assembled on the solid surfaces [8]. Friction modifiers consist of a polar head group and a hydrocarbon chain, as shown in Figure 2.8; the

amphiphilic polar heads self-assemble on metal surfaces with the hydrocarbon chains vertically oriented in the bulk of the oil, to form dense monolayers [13]. These monolayers are durable enough to keep the surfaces separated and reduce the friction between them, due to the cumulative van der Waals forces between the closely packed hydrocarbon chains. The polar head serves to locate the molecule on the metal surface and its bonding can be reversible. A few examples of organic friction modifiers in use today include oleylamide, glyceryl monooleate and bis (2-hydroxyethyl) alkyl amine, schematics of which can be seen in Figure 2.9.

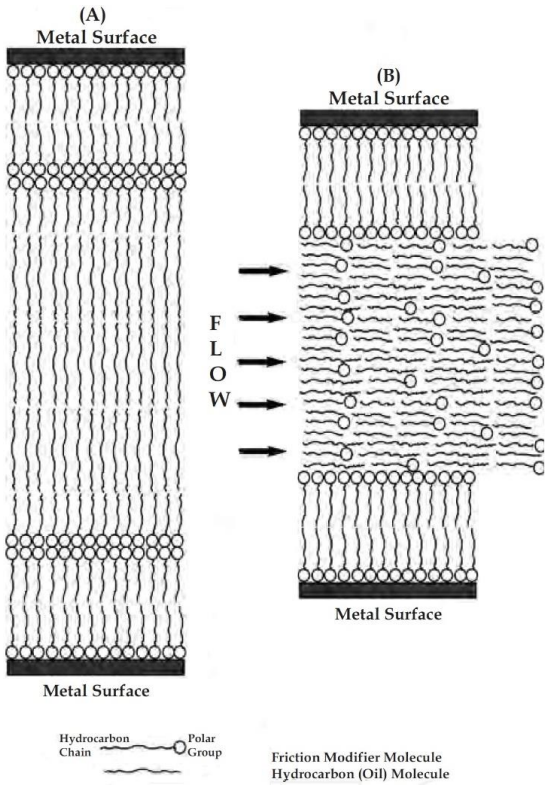

Figure 2.8 Schematic representation of friction modifiers [8]

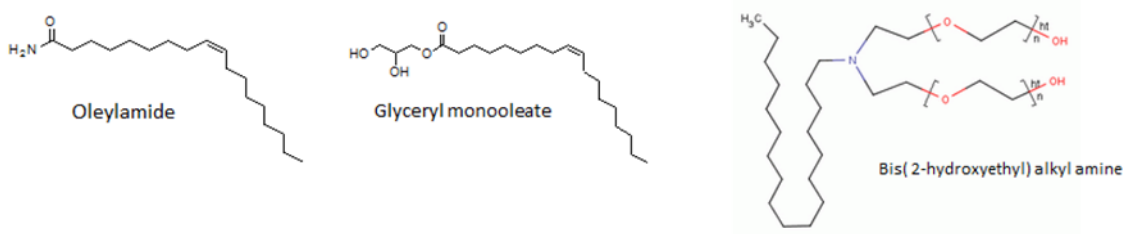

Figure 2.9 Three commercial organic friction modifiers [13]

2.2.3 Anti-wear (AW) agents and extreme-pressure (EP) additives

The anti-wear (AW) agents and extreme-pressure (EP) additives are chemical compounds that prevent wear in the moving parts. They both are thermally activated; they decompose

to release compounds that react with the metal surfaces. These surface-additives form thin sacrificial layers to protect the surfaces against shear by the wearing of the layer instead of the surfaces, under boundary lubrication conditions [8].

Anti-wear agents have a lower activation temperature in comparison with the extreme-pressure (EP) additives. The latter form extremely viscous surface layers through thermo-chemical reaction with the metal surfaces. These films can withstand the extreme temperatures and mechanical pressures encountered in an engine during operation, they prevent direct contact between surfaces, hence protecting them from scoring and seizing. Phosphates, polysulphides, dithiocarbamates and dithiophosphates are a few anti-wear and extreme pressure additives blended with engine oils. Zinc dialkyldithiophosphate or ZDDP, shown in Figure 2.10, is the most widely used anti-wear additive in the lubricant industry due to its anti-wear and antioxidant properties.

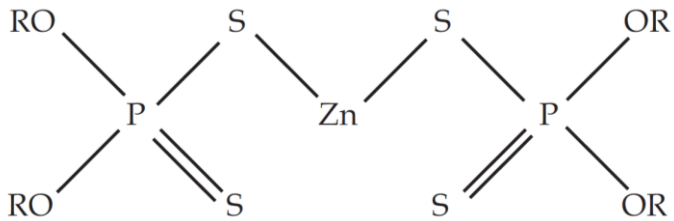

Figure 2.10 Zinc dialkylldithiophosphate (ZDDP) [8]

2.2.4 Antioxidant additives (AO)

One of the most important properties of a lubricant oil is the stability against oxidation. Hydrocarbons exposed to oxygen and heat, will accelerate the oxidation process. The conditions encountered in an internal combustion engine are ideal for catalysing oxidation. In addition, some metal parts in the engine such as copper and iron, increase the rate of oxidation. Thus, lubricant oils designed for engine machinery are subjected to oxidation more than any other lubricant application.

The lubricant oils consist of hydrocarbons with (C_{20} – C_{70}) carbon atoms. At high temperatures these hydrocarbons are oxidised to form fatty peroxides, fatty aldehydes, fatty acids, ketones, fatty alcohols and fatty esters. All these oxidants form solid asphaltic materials. As a result, antioxidants are blended to all lubricant oils in order to prevent the formation of such compounds [8].

2.2.5 Anti-foam agents (AF)

Another cause of oil oxidation is the foaming of the lubricant oil. It is a very undesirable effect that leads to air bubble formations (cavitation) and insufficient oil supply in the system that can lead to starvation. The foaming effect depends very much on the lubricant

oil itself. The presence of surface additives such as corrosion inhibitors and detergents, and the surface tension of the base oil strongly affect the foaming process.

In some applications, foaming may be a desirable effect, while in other applications can be extremely troublesome, as even small amounts of foam may cause issues. The anti-foam additives attach to the air gaps leading them to grow or form bridges between them. That leads the bubbles to merge into larger bubbles, which rise to the surface of the foam layer and collapse, thus releasing the trapped air.

2.2.6 Rust and corrosion inhibitors

Rust inhibitors are usually substances that are attracted to the metal surfaces. They either physically or chemically adsorbed to the metal surfaces, forming a robust, continuous surface layer that prevents water from reaching the metal surfaces. Alkaline earth sulfonates and mine succinates and are two examples of the most used rust inhibitors.

The corrosion inhibitors prevent the corrosive substances from attacking the metal surfaces, by forming protective layers on the metal surfaces. The formation of the surface layer is achieved through physical or chemical adsorption of the inhibitors on the metal surface.

2.3 Engine oil degradation

The engine oil is designed to lubricate various engine components; the crankshaft and the engine bearings, the small end bearings and the gudgeon pin, the engine cylinders and the piston liner, the camshaft (tappets) and push rods, and the valves and cylinder head. As a result, the engine oils are manufactured to perform under various conditions of pressure, temperature and shear. With continuous exposure to such extreme conditions though, engine oils degrade with time and require replacement. The main factors that cause the degradation of engine oils are [14]:

- **Oxidation:** occurs when air trapped in the form of bubbles and/or water get inside the oil film leading the oil molecules to react with oxygen.
- **Thermal breakdown:** occurs either due to poor cooling of the lubricant that results in higher operating temperature than the recommended which leads viscosity to decrease, or due to air bubbles trapped in the oil the temperature of which increases as they pass from the low pressure region to the high, resulting in the oxidation of the neighbouring oil molecules.

- **Contamination:** occurs when dirt, water, air, etc. are trapped in the oil. Both air and water, are sources of oxygen that reacts with the oil molecules and oxidises them. Dirt contains metal particles that act as catalyst which accelerates degradation.

Various methods are being employed to study the oil degradation, by measuring the progress of antioxidants, base reserve, anti-wear agents and the presence of contaminants in the oil including water, soot particles, wear, fuel dilution, and identifying oil degradation products including oxidation, nitration, sulfation, acids [15]. High resolution mass spectroscopy [15] has been used to measure intact ZDDP (main anti-wear additive in engine oil composition) and its degradation products; dialkyl thiophosphate, dialkyl phosphates, phosphoric acid, and sulfuric acid. Fourier transform infrared spectroscopy has been used to measure residual amounts of antioxidant and anti-wear additives in the oil used in an engine [16]. Impedance spectroscopy and potentiometric sensors have been used to measure the conductivity and acidity of the oil, respectively [17]. Optical method (laser) has been used to measure the effect of oil degradation on the oil film thickness between piston ring and cylinder wall in a fired engine [18]. Capacitance [19] and conductance [20] methods have also been used to measure oil degradation and/or oxidation products.

2.4 Measurement of viscosity

Viscosity is measured with instruments called viscometers [7]. Viscometers can be mechanical, when a body shears the fluid or vibrational, when the fluid is sheared by vibration. Viscosity is commonly measured with capillary or rotational viscometers, which shear the fluid mechanically. The viscosity in these devices is measured by correlating the geometry of the viscometer to the torque and the shear applied to the fluid.

2.4.1 Capillary viscometers

Capillary viscometers measure the kinematic viscosity of a fluid by correlating the time a fluid takes to flow through a capillary. The higher the fluid kinematic viscosity, the longer the time that is required by the fluid to travel through the capillary. Figure 2.11 shows the schematic of a capillary viscometer. The main advantages of capillary viscometers compared to rotational include high accuracy, the ability to achieve high shear rates and their low cost. On the other hand, high residence time and variation of shear across the flow, can affect the structure of the test liquid, especially in the case of complex liquids and can lead to shear heating in the case of highly viscous samples.

The kinematic viscosity in capillary viscometers is measured as:

$$\upsilon = \left(\frac{4n(\Delta p D^4 \pi)}{(3n+1)(128QL)}\right) \tag{2.10}$$

Where Δp is the difference in pressure at the inlet and outlet of the viscometer, n is the slope of the measured $\log(\Delta \mathrm{p}\, \pi\, \mathrm{D}^4/128\mathrm{QL})$ curve, D is the diameter of the capillary, Q is the fluid volume flow rate, and L is the length of the capillary.

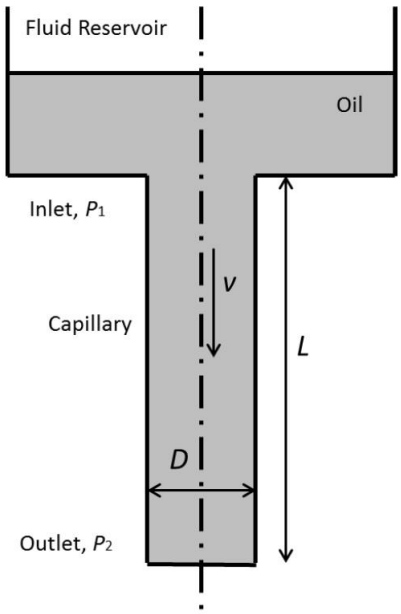

Figure 2.11 Schematic representation of a capillary viscometer; the fluid flows with speed v through the capillary [7]

2.4.2 Rotational viscometers

Rotational viscometers are employed to measure dynamic viscosity. In this type of viscometer, the liquid is interleaved between two surfaces; one stationary, while the second one rotates. The viscosity is measured either by measuring the change in rotational speed given a fixed torque or by measuring the torque change given a constant rotational speed. The main rotational viscometers are cylindrical or cone-to-plate.

Compared to other viscometers, rotational viscometers can operate continuously at a given shear rate, that allows steady-state measurements to be easily performed. As a result, possible thixotropic behaviour of liquids can be detected and measured. In addition, further measurements of the samples can be performed at a range of temperatures and different shear rates, offering a better understanding of the liquid behaviour.

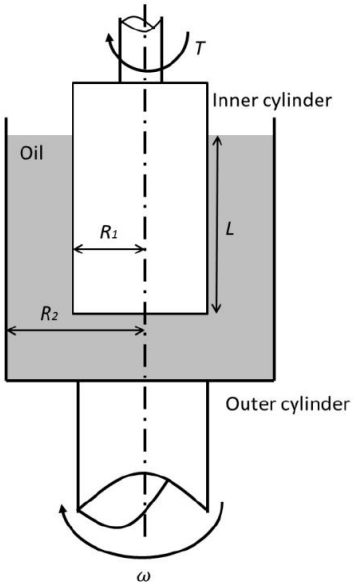

Figure 2.12 Schematic representation of a cylindrical rotational viscometer [7]

Cylindrical rotational viscometers (Figure 2.12) are being used to determine the absolute viscosity of a liquid, which requires a well-defined shear rate and shear stress. These instruments are available in different configurations, including models for low and high shear rates, which allows measurements of almost any liquid. The dynamic viscosity in cylindrical viscometers is determined using Equation2.11:

$$\eta = \left(\frac{\beta^2-1}{4\pi\beta^2 R_1^2 L}\right)\frac{T}{\omega} \tag{2.11}$$

Where $\beta = R_2/R_1$ is a parameter dependent on the cylinder geometry, ω is the rotational speed, T is the applied torque and L is the effective length of the cylinder at which the torque is measured.

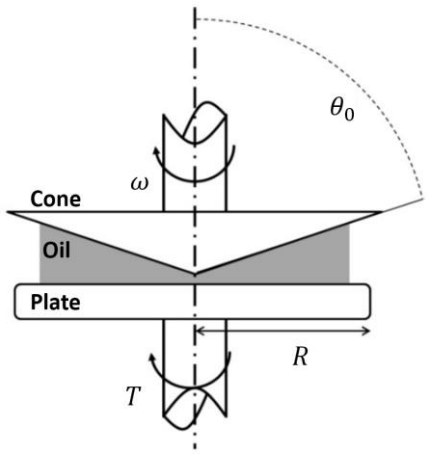

Figure 2.13 Schematic representation of a cone-to-plate viscometer [7]

Another type of rotational viscometers is the cone-to-plate viscometers (Figure 2.13). Due to the geometry of the cone, cone-to-plate viscometers provide uniform shear rate throughout, which makes them a very popular tool for measuring non-Newtonian behaviour in liquids. The dynamic viscosity in cone-to-plate viscometers is derived from:

$$\eta = \frac{3T\theta_0}{2\pi\omega R^3} \tag{2.12}$$

In Equation 2.12, θ_0 is the cone angle of incidence and R is the plate radius, T is the applied torque and ω is the rotational speed. As it can be seen from Equation 2.12, the applied shear stress and shear rate increase by reducing the diameter and angle of the cone, respectively.

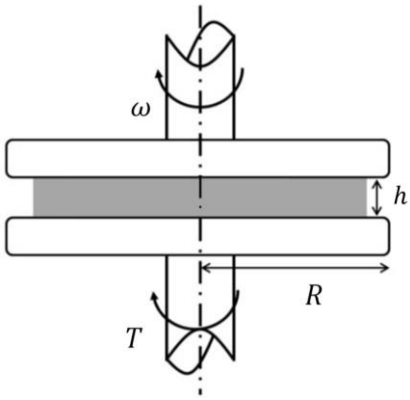

Figure 2.14 Parallel disks rotational viscometer [7]

Another configuration, is the parallel disks rotational viscometer, which is shown in Figure 2.14. Due to the geometry, the shear rate is not uniform throughout, but it depends on the radial distance from the axis of rotation and the distance between the disks, h. Parallel disks viscometers are being used with non-Newtonian liquids, the viscosity of which depends on the shear rate. The viscosity in parallel disks rotational viscometers is determined using Equation 2.13:

$$\eta = \frac{2Th}{\pi\omega R^4} \tag{2.13}$$

In Equation 2.13, T is the applied torque, h is the distance between the two disks, R is the radius of the disks and ω is the rotational speed.

2.4.3 Falling body viscometers

Falling body viscometers measure viscosity by correlating the time a body takes to travel through a capillary, with the resistance offered by the fluid, and hence its viscosity. Figure 2.15 reports two examples of falling body viscometers. Falling body viscometers offer

measurements of a wide viscosity range and due to the simplicity of their design, they are suitable for high pressure and high temperature viscosity measurements [7].

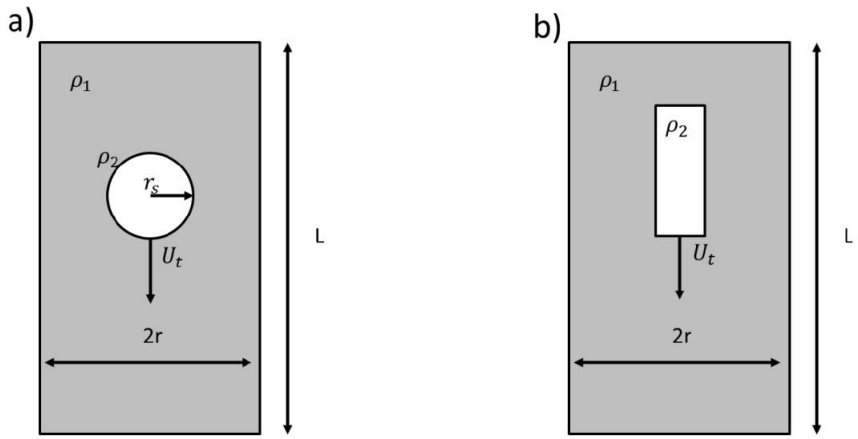

Figure 2.15 a) Falling sphere viscometer, b) falling cylinder viscometer [7]

Figure 2.15 a) shows the schematic of a falling sphere viscometer, while Figure 2.15 b) shows a falling cylinder viscometer. In this section, only the case of the falling sphere is analysed, but similar considerations can be made to obtain the value of viscosity from the falling cylinder viscometer type. The opposing force F, that results from the viscous drag in a fluid as a sphere travels through the capillary, is calculated from Stokes' law as:

$$F = 6\pi\eta r_s U_t \tag{2.14}$$

where r_s is the radius of the sphere, η is the dynamic viscosity, and U_t is the terminal velocity of the falling body. By balancing Equation 2.14 with the force applied on the sphere by the fluid, viscosity can be calculated as:

$$\eta = 2gr_s^2 \frac{(\rho_2 - \rho_1)}{9U_t} \tag{2.15}$$

where ρ_1, ρ_2 are the densities of the fluid and the sphere, respectively. More accurate equations can be obtained by taking into consideration the wall effect and the finite length of the capillary.

Table 2.2 Advantages and disadvantages of conventional viscometers [7]

Viscometer	Advantages	Disadvantages
Capillary	Simple to use, very high shears and shear range	Very inhomogeneous shear, bad for time dependency, time consuming
Cylindrical rotational	Good for low viscosity, high shear rates	Hard to clean thick liquids
Rotational cone-to-plate	Homogenous shear, best for non-Newtonian liquids and normal stresses	Requires good alignment, problems with loading and evaporation
Rotational parallel disks	Non-Newtonian liquids and normal stresses; easy sample loading	Inhomogeneous shear
Falling body	Very simple to use, good for high temperature and pressure	Requires fluid density to be known and special sensors for opaque fluids, unreliable with viscoelastic fluids

Table 2.3 Various causes that lead viscometer to erroneous results [7]

Error/effect	***Cause/comment***
End/edge effect	Energy losses at the fluid entrance and exit of main geometry
Kinetic energy losses	Pressure loss to kinetic energy
Secondary flow	Energy loss due to undesirable secondary flow, vortices, etc.
Non-ideal geometry	Deviations from ideal shape, alignment and finish
Non-uniform shear rate	Important for non-Newtonian liquids
Temperature variation and viscous heating	Temperature variations in time and space, which can influence viscosity measurements
Miscellaneous effects	Test specimen, thixotropy, rheopexy, etc.

Table 2.2 summarises the advantages and disadvantages of different viscometers as they were presented in sub-Sections 2.4.1 to 2.4.3, and Table 2.3 presents a number of different causes that can lead viscometers to erroneous results. As it can be seen, there is no single tool to cover completely the various conditions (temperature, pressure and shear) the engine oils are subjected to, nor the oil's nature (Newtonian, dilatant, thixotropic, pseudoplastic, etc.), in order to determine viscosity more accurately. Hence, the combination of different tools is required to determine viscosity and the liquid behaviour, at different operating conditions.

2.5 Additive package measurements

To the author's best knowledge, there is no available method for measuring the presence and activity of the different additives in a fully formulated lubricant in-situ in a running engine. Since the additives are blended with the carrier, it is very hard to isolate and detect only one additive at a time in the end mixture. Any characterisation or measurement of the additives is currently being made according to the effect/property they add to the oil.

Additive and lubricant test are designed to measure wear and surface damage prevention, deposit control, friction control, lubricant degradation, contaminants and lubricant rheology [21]. Tests include both laboratory, complex rig/engine tests and field tests. This process takes a very long time given the number of additives blended in the oil, the behaviour they exhibit towards one another and the end product, their performance and concentration they best perform at.

Field tests are performed on actual vehicles to test the performance of the additives through the performance of the fully formulated oil. These tests depend on the fuel consumption and condition of the lubricated components to derive any conclusions about the product, however the cost and time involved are considerable, given that any signs of friction and wear on the interacting components will take time to show and that the lubricants have to be tested under different environmental conditions and terrains, in order to be precise.

2.5.1 Quartz crystal microbalance (QCM)

In recent years, the quartz crystal microbalance with dissipation monitoring (QCM-D) has been used for measuring the presence of additives in the oil. The QCM-D is an extremely sensitive mass balance that utilises a quartz crystal which vibrates at specific frequencies.

A functional coating is applied on the surface of the quartz crystal that allows adsorption of certain additives, as shown in Figure 2.16 [22].

Figure 2.16 QCM-D schematic of electrode arrangement and coating [22]

The adsorption of molecules on the coating leads to change in the resonant frequency of the crystal and energy loss at the solid-liquid interface, due to mass deposition or film formation (Figure 2.17). Employing both the frequency change and energy dissipation, returns more accurate results of the deposited mass [23]. As a result, the QCM-D is limited to measure additives that get adsorbed on a metal surface, however there are more additives inside the lubricant left undetected by the QCM-D.

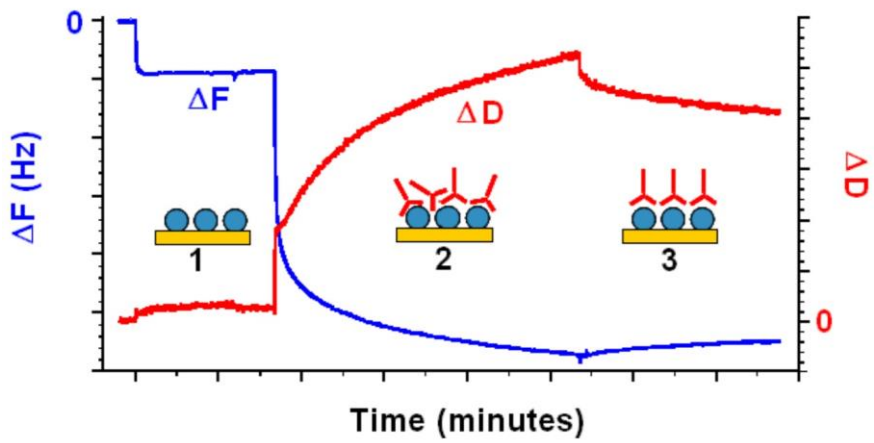

Figure 2.17 QCM-D frequency and energy dissipation response to mass loading [23]

2.6 Conclusions

Fully formulated engine lubricants are blended with an additive package either to add new properties to the oil or enhance existing ones. These lubricants are subjected to extreme conditions of high temperature, high pressure and increased shear, which have a

significant effect on the lubricant performance. As a result, measuring lubricant properties under real operating conditions is of great interest, for developing better products capable of performing in these conditions.

Currently, oil analysis is being made using a combination of methods, where each method is measuring individual properties of the oil or the presence and activity of molecular species. The oil is tested in every stage of its development and combining the results from all the testing, provides most information about the end product. However, this process takes a very long time to complete considering the number of different additives blended in the oil.

As a result, there is a great interest for developing new tools, like the QCM-D, that can be used for *in lab* and *in-situ in an engine* lubricant measurements respectively, quicker than the current test processes, while providing more information about the efficiency and performance of the oil product.

3 ULTRASOUND & SURFACE ACOUSTIC WAVES

This chapter introduces the concept of ultrasound and helps with the familiarisation of the two main families of ultrasound, *bulk acoustic waves* or *BAWs* and *surface acoustic waves* or *SAWs*, with more attention given on the latter.

3.1 The acoustic spectrum

Ultrasound is a sound wave with frequencies higher than the upper audible limit of human hearing (Figure 3.1). Ultrasound is no different from audible sound in its physical properties, except in that humans cannot hear it. Ultrasound devices operate with frequencies from 20 kHz up to several gigahertz. As in the case of the sound, the ultrasound is a vibration that propagates as a mechanical wave of pressure and displacement through a medium.

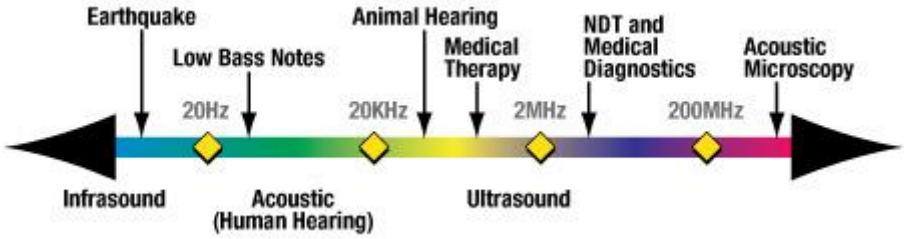

Figure 3.1 Sound spectrum

Ultrasound propagates in different modes, depending on the sound wave type and source. When a wave is propagating through a material or in the bulk of a material, it is characterised as a *bulk* or *plane acoustic wave*, whereas when a wave is propagating along the surface of a material is characterised as a *surface acoustic wave*.

3.2 Bulk acoustic wave (BAW)

There are two types of bulk acoustic waves, *longitudinal waves* and *transverse* or *shear waves*. In the case of the longitudinal wave, the particle displacement is parallel to the wave propagation when a longitudinal or compressional wave interacts with the particles network, forming areas of rarefaction and compression, as it is shown in Figure 3.2b).

In the case of the transverse or shear wave, the displacement of the particle is normal to the wave propagation. When a shear or transverse wave interacts with the particle network, it forms crests and troughs, as it can be seen in Figure 3.2c).

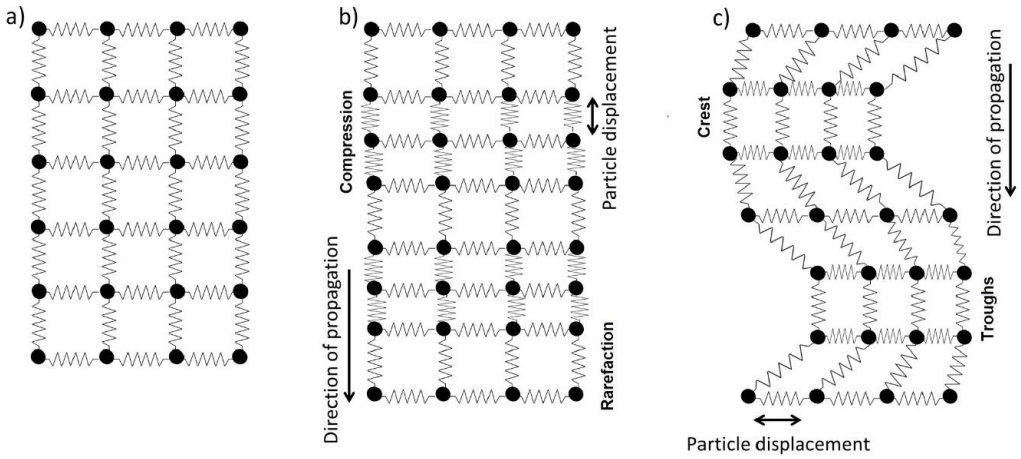

Figure 3.2 a) Particle network at rest, b) longitudinal wave, c) shear wave

3.3 Surface acoustic wave (SAW)

A surface acoustic wave is an acoustic wave travelling along the surface of an elastic material, with particle oscillation that decays exponentially with depth into the substrate. SAWs were first explained in 1885 by Lord Rayleigh, who described the surface acoustic mode of propagation and predicted its properties [24]. Since then, SAW devices have found application in different fields [25].

They have been used in electronic components to provide a number of different functions, including filters [26], correlators [27] [28] and DC to DC converters [29]. SAWs have found application in different industrial sectors including telecommunications [30], chemistry and medical applications [31], characterisation of materials [32] [33] [34], and as a non-destructive testing (NDT) method in a variety of applications [35] [36].

There are different modes of surface acoustic waves, depending on the wave type and source, as it is stated by Ferrari and Lucklum [37], and they are analysed in detail in the following sections.

3.3.1 Rayleigh waves

These waves are named after Lord Rayleigh for his discovery in 1885 [24]. Rayleigh waves consist of a *longitudinal* and a *vertical/shear* component that can couple with any media in contact with the surface. This surface coupling strongly affects the particle oscillation and wave velocity, allowing SAW sensors to detect mass deposition on the surface and mechanical properties. The particles of the material move elliptically, and their movement is more intense on the surface of the material, and becomes weaker with depth into the substrate, as it is shown in Figure 3.3.

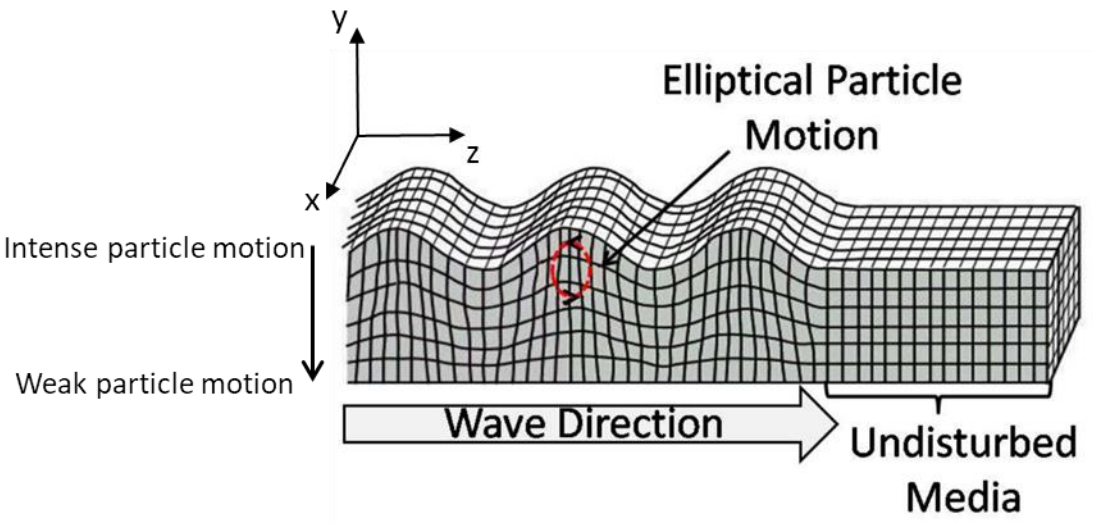

Figure 3.3 Schematic of Rayleigh wave propagation [38]

3.3.2 Lamb waves

A special case of the Rayleigh waves is that of the Lamb waves. When the thickness of the medium, in which a Rayleigh wave propagates, is of the order of the wavelength, Lamb waves are generated. These waves have the ability to propagate on both the sides of the medium, in either symmetric or anti-symmetric modes, as it is shown in Figure 3.4 a), b) respectively, creating two waves of different velocities and amplitudes. In general, the propagation velocity of Lamb waves is quite different from that of Rayleigh waves, allowing lower frequencies of operation.

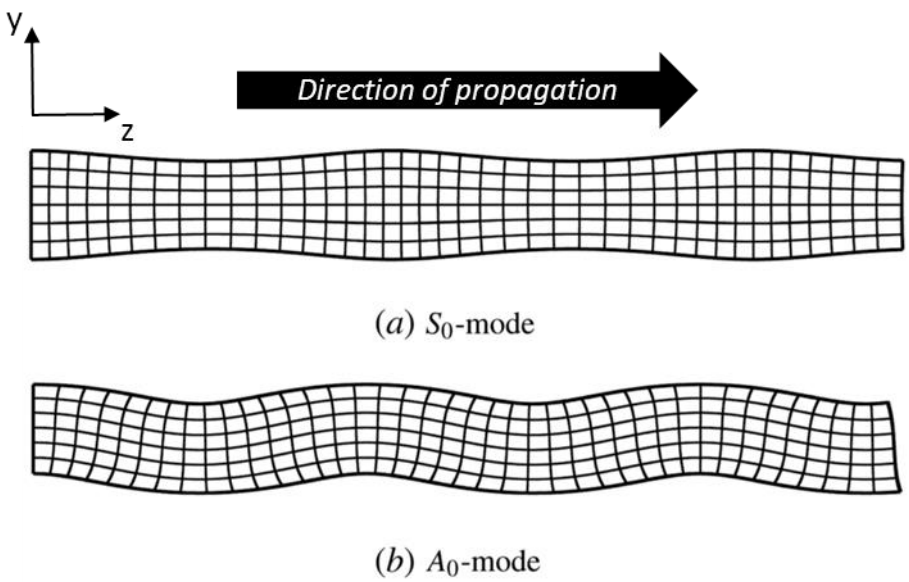

Figure 3.4 a) Symmetric Lamb wave, b) anti-symmetric Lamb wave [39]

3.3.3 Love waves

Love waves were named after Augustus Edward Hough Love [40], and they are also known as surface-skimming bulk waves. In Love waves the particles move horizontally, perpendicularly polarized to the direction of propagation, offering a shear effect. This type of surface waves is generated when the wave is trapped in a thin layer of lower acoustic velocity than the substrate. As a result, the wave energy is confined in a small area near the surface of the substrate offering an increased sensitivity in mass changes. Figure 3.5 represents the propagation of a Love wave. As it can be seen, the upper particles move more than the lower particles, indicating that the amplitude of Love waves decreases with depth into the substrate.

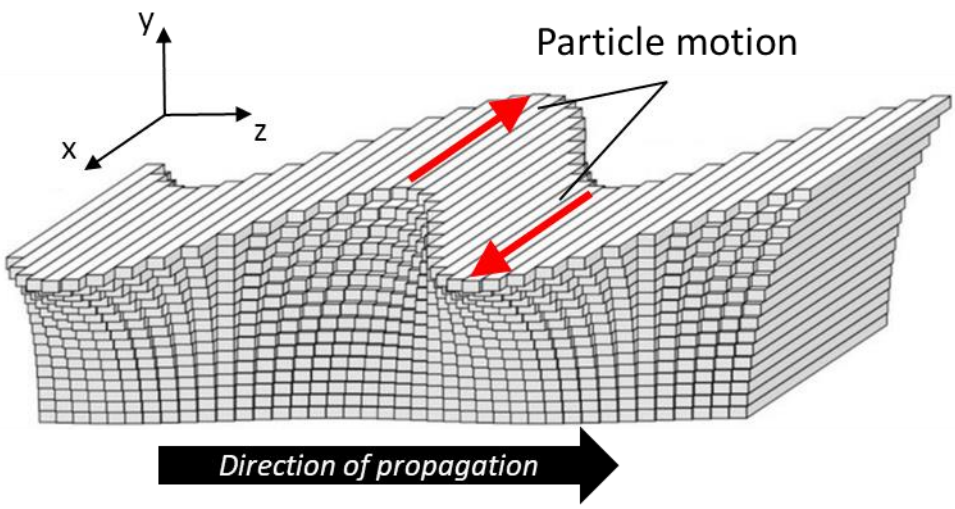

Figure 3.5 Schematic of Love wave propagation [41]

3.3.4 Shear-horizontal surface acoustic wave (SH-SAW)

Shear-horizontal surface acoustic waves are pseudo surface waves, with horizontally polarized bulk shear component. As in the case of Love waves, in SH-SAW the particles move horizontally, perpendicularly polarized to the direction of propagation, with the only difference that the wave is not trapped in a thin layer, but moving freely in the bulk of the substrate, as it is shown in Figure 3.6. When the thickness of the substrate is comparable to the wavelength, the whole substrate becomes sensitive. As in all other cases, the SH-SAW is subject to the same principle that the amplitude is decreasing with depth into the substrate.

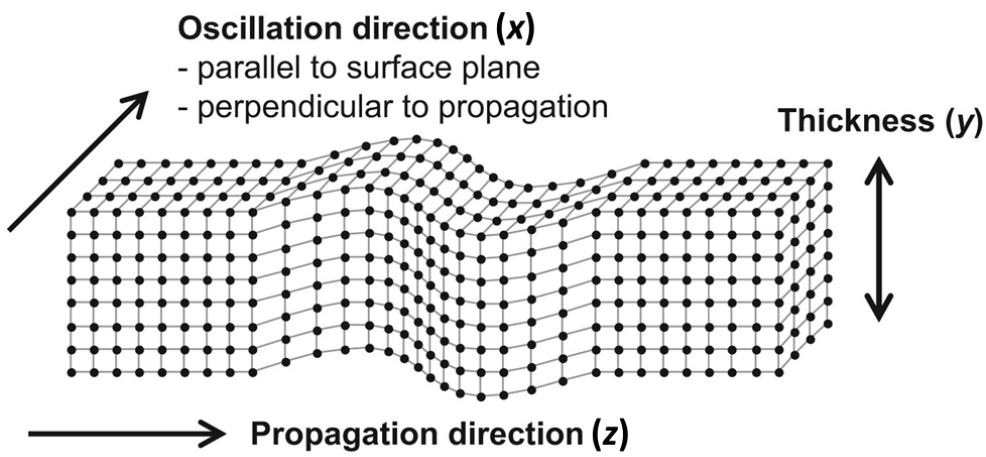

Figure 3.6 Schematic of shear-horizontal surface acoustic wave propagation [42]

3.4 Attenuation, reflection and transmission of surface waves

Surface acoustic waves, regardless of the type, are subjected to *attenuation, reflection* and *transmission*. Acoustic attenuation in a medium and the reflection and transmission of the wave at the boundaries, play an important role in many scientific researches and engineering fields, such as in non-destructive testing methods, characterisation of materials, oil-film thickness measurements, viscosity measurements, etc.

3.4.1 Acoustic attenuation

When a SAW is generated, it has an initial amplitude u_0 and after travelling a distance d along the surface of the medium, the amplitude decreases and it will be u. This is described by the attenuation equation (Equation 3.1).

$$u = u_0 e^{-\alpha d} \tag{3.1}$$

The parameter α is dimensionally the reciprocal of length, and it is known as the *attenuation coefficient*. It is a measure that is material depended and in the international system of units (SI), it is expressed in nepers per meter or simply the reciprocal of meter (m^{-1}) that is, if α= 1 m^{-1} the wave amplitude decreases by a factor 1/*e* for each meter travelled.

Basically, Equation 3.1 is a measure of the **energy loss** of sound propagation in media. Most media have **viscosity**, and are therefore not ideal media. When sound propagates in such media, there is always energy loss in the form of heat due to friction between the particles of the medium, leading to attenuation of the sound wave.

3.4.2 Reflection and transmission

Surface acoustic waves are subjected to the laws of transmission and reflection, as the bulk waves or the electromagnetic waves do, as it is stated in Krautkramer [43]. When a surface wave meets a boundary, it is partly reflected back and partly transmitted through, as Figure 3.7 indicates.

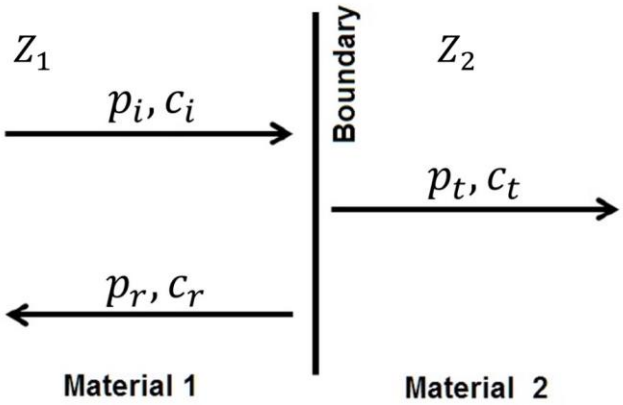

Figure 3.7 Reflection and transmission of an incident wave

In Figure 3.7, p is the acoustic pressure of the wave, and c is the sound velocity in the medium. The subscripts i, r, t represent the incident wave, the reflected and the transmitted one, respectively. The coefficients of reflection and transmission can therefore be calculated as:

$$\frac{p_r}{p_i} = R \quad and \quad \frac{p_t}{p_i} = T$$

The reflection coefficient R and transmission coefficient T, are dimensionless numerical values and the relationship between them is given by Equation 3.2.

$$T = 1 + R \tag{3.2}$$

The amount of the reflected and transmitted wave depends on the acoustic impedance of the material and the geometry at the boundary. The acoustic impedance Z is a measure of the resistance a material presents in the wave propagation, and it is the product of the material density ρ and longitudinal speed of sound c inside that material.

$$Z = \rho c \tag{3.3}$$

Materials with high acoustic impedance are characterised acoustically hard and with low acoustic impedance, soft. When two materials are coupled together, the acoustic mismatch is used to describe the quality of the coupling at the boundary. Materials with low acoustic mismatch ($Z_1 \geq Z_2$) are coupled very well (greater wave transmittance from one material to the other, $R < T$), while high acoustic mismatch ($Z_1 \gg Z_2$) leads to poor

coupling (less energy is transferred in the second material, $R > T$). The reflection coefficient R is expressed in terms of the acoustic impedance using Equation 3.4.

$$R = \frac{Z_2 - Z_1}{Z_2 + Z_1} \tag{3.4}$$

A surface wave is subjected to reflection and transmission not only at the boundaries of the propagating medium, such as edges, but when it is changing medium or a crack or discontinuity is present. For this reason, surface acoustic waves are very important and widely used in non-destructive testing, and more specifically in the testing of very complex geometries where other methods fail. Surface waves not only indicate where a discontinuity or a crack is present, but due to their nature they can return information about the depth of the crack, offering a better image of the damaged material.

3.4.3 Dispersion

Lamb waves and SH-SAWs, when propagating in thin media ($b \leq \lambda$, where λ is the wavelength and b is the thickness of the medium), they travel through the thickness and along both surfaces of the medium, making it sensitive on both sides.

Lamb waves propagate either symmetrically (S- modes) or anti-symmetrically (A- modes), as explained in the previous section. The fundamental symmetric and anti-symmetric modes are commonly referred to as So and Ao, respectively. Depending on the thickness of the medium and the frequency of the waves, higher S- and A- modes may appear. These modes can be calculated using the Matlab based program, "Mode shape" [44], which was designed to calculate the velocity of the higher S- and A- modes, depending on the thickness of the medium and frequency. The results are shown in Figure 3.8.

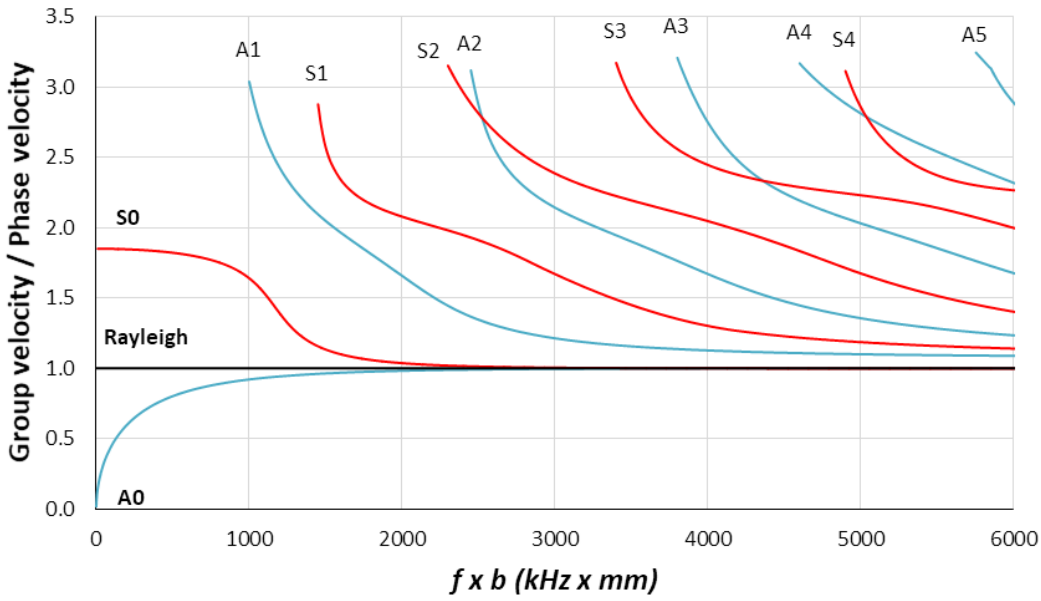

Figure 3.8 Lamb wave dispersion [44]

SH-SAWs exhibit similar behaviour to Lamb waves when propagating in thin media ($b \leq \lambda$) at high frequencies. Higher modes appear depending on the wave frequency and thickness of the medium. Figure 3.9 presents the SH-SAW dispersion as calculated using Equation 3.5, as described by Martin et al. [45].

$$v_{group} = v_{phase}\sqrt{1 - \left(\frac{n\lambda}{2b}\right)^2} \tag{3.5}$$

Where v_{group} is the velocity the particles travel through space (perpendicularly to the direction of propagation), v_{phase} is the velocity the wave propagates as a whole, and n is the mode number (n = 0, 1, 2, 3, ...). According to Equation 3.5, for the fundamental mode SHo (n= 0), $v_{group} = v_{phase}$ and the wave travels undistorted through space regardless of the wave frequency or thickness of the medium. For this reason, the fundamental SHo mode has attracted great attention in the non-destructive methods.

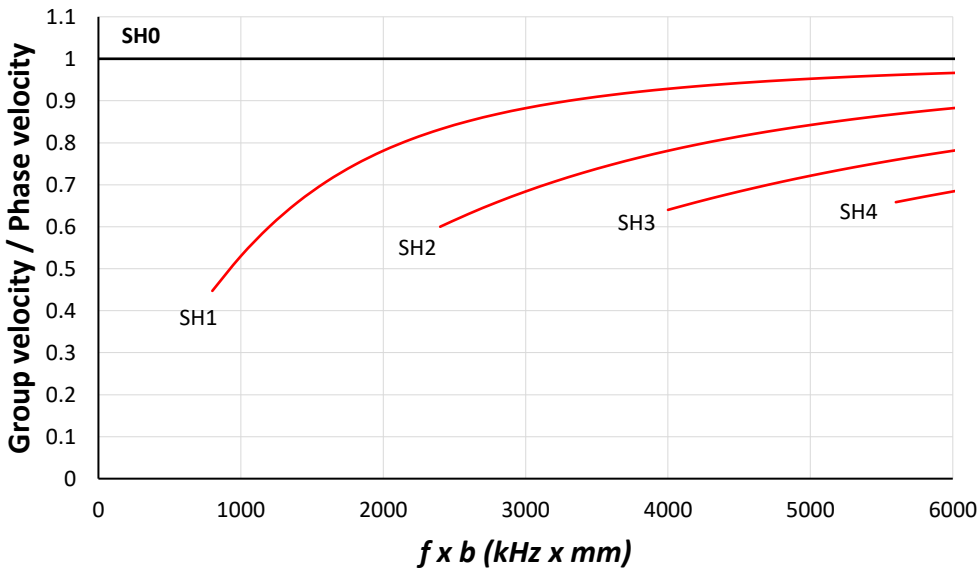

Figure 3.9 SH-SAW dispersion

The cross-sectional displacement for the first 4 SH-SAW modes is presented in Figure 3.10. The difference in the particle displacement is clear for each case. As it can be seen, only the fundamental mode SHo travels in space as a whole.

In Figure 3.10, the particles move parallel to the surface of the medium along the x-direction, travelling through the thickness of the medium (along y-axis), while the wave propagates along z-direction (normal to the page).

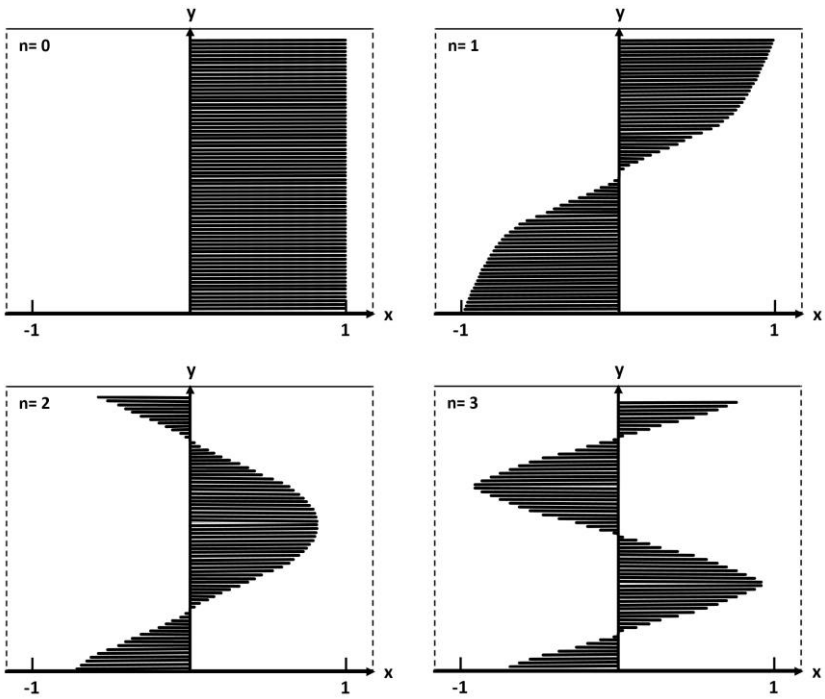

Figure 3.10 Cross-sectional displacement of the 4 lowest SH-SAW modes [45]

As it was seen, both Lamb waves and SH-SAWs exhibit dispersion when propagating in thin media at high frequencies. As a result, in most applications low frequencies are preferred to excite either the fundamental So, Ao or SHo modes, respectively and avoid exciting the higher, more complex modes.

3.5 Surface acoustic wave generation

Surface acoustic waves can be excited by various means such as mechanical impact, pulsed thermal energy, electromagnetism or the inverse piezoelectric effect. The last is by far the most important for acoustic devices, and the most efficient.

Piezoelectricity is the ability certain solid materials possess, such as crystals and certain ceramics, to convert mechanical stress to electric charge. When mechanical stress is applied on a piezoelectric material it generates an electric charge, and when an electric charge is applied on a piezoelectric material it produces a mechanical stress. Naturally occurring crystals that possess piezoelectricity include topaz, berlinite, lead titanate, and the most widely used, the quartz. The most used synthetic crystals include lithium niobate and lithium tantalate, and the most common piezoelectric synthetic ceramic in use today is lead zirconate titanate, more commonly known as PZT.

3.5.1 Surface acoustic wave device

In most applications, surface acoustic waves are generated with SAW devices. As it is stated by Vellekoop [46], these devices employ a piezoelectric substrate, two interdigital transducers (IDTs) deposited on top of the substrate, one acting as a transmitter and the other as a receiver, and a protective coating, as it is shown in Figure 3.11.

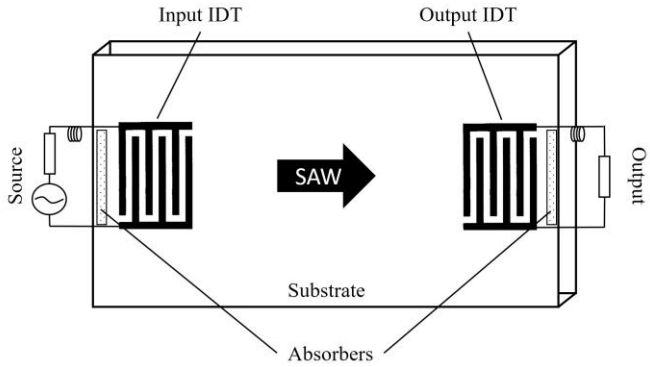

Figure 3.11 Surface acoustic wave device (reproduction of Figure 1 [47])

When electric current is applied on the input IDT, due to the inverse piezoelectric effect, the substrate starts vibrating and it creates a surface wave that propagates along the surface of the substrate until it is received by the output IDT. When the surface wave reaches the output IDT the piezoelectric effect takes place. The substrate vibrates due to the presence of the surface wave and generates an electric charge that travels through the output IDT.

The IDTs' structure depends on the frequency of the generated wave and its sensitivity. The IDTs consist of stripes/combs called fingers. One positively excited finger and a negatively excited one form a finger pair. The IDTs consist of *N* number of finger pairs and that number depends on the application and the strength of the generated wave. Usually, the number of finger pairs do not exceed 100. Figure 3.12 shows the structure of a single-finger three pair IDT. The distance between two consecutive finger pairs is called period p, and it is equal to the wavelength of the generated wave. The width of each finger is equal to the gap between them. The length A is called acoustic aperture which represents how narrow the generated wave will be, and usually is set to be equal to seven times the wavelength. In most cases, the IDTs are made out of aluminium, due to its low cost and good electric conductivity. The thickness of the IDTs is usually between 100 and 200 nanometres.

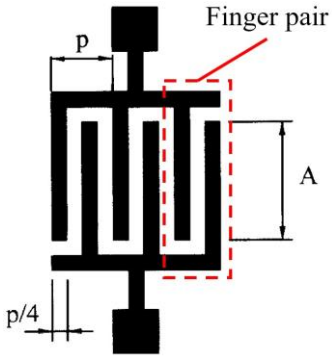

Figure 3.12 Single-finger three pair IDT structure [46]

Different modes of surface waves can be excited depending on the selected piezoelectric material. It is the piezoelectric substrate's structure and particle movement that generate different types of surface waves.

The IDTs are deposited on the piezoelectric substrate through the process of photolithography, a chemical process that includes several baths in different solutions and a UV light drying process. After the SAW device is finished, it can be coated so the IDTs can be protected when the device is used in contact with a liquid. In many applications, after the deposition of the coating, another layer between the input and output IDT is added that acts as a sensing area which increases the sensitivity of the device in mass changes, by attracting certain substances.

Figure 3.13 shows the different types of SAW devices according to the type of the generated wave, while Table 3.1 compares the different SAW devices according to the sensitivity, operating frequency, propagating medium, and the field of application.

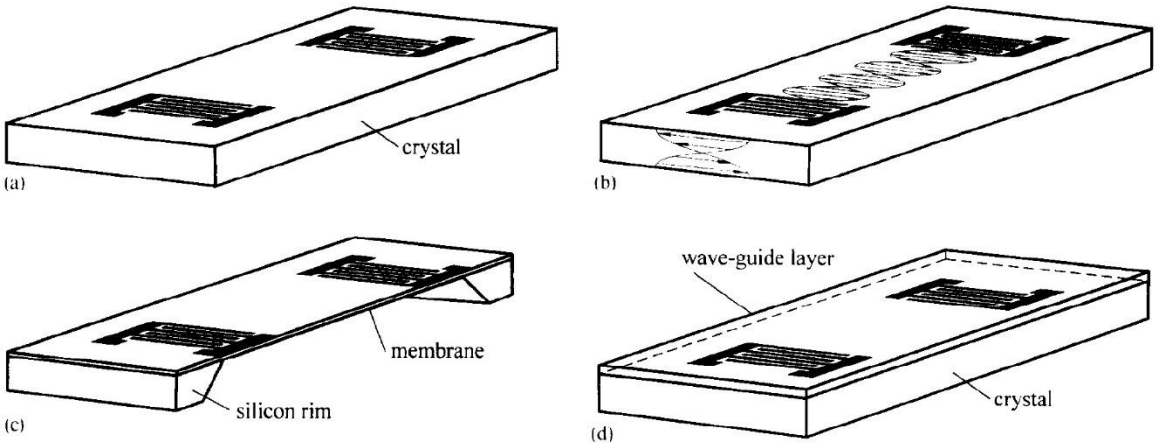

Figure 3.13 SAW device configuration of a) Rayleigh wave, b) SH-SAW, c) Lamb wave, and d) Love wave [46]

SAW devices are considered to be the most efficient way to generate surface waves of different modes, and they are easy to use. However, these devices are very fragile, they can be used only in lab measurements, are quite big in size depending on the sensing area and the application, and more importantly they are difficult and very expensive to manufacture.

Table 3.1 Comparison of performance of different SAW devices

Wave Type	Sensitivity/Noise	Gas(g) or liquid(l) operation	Operating frequency (MHz)	Mass sensitivity (gr/m²)	Applications
Rayleigh	High/ Low	g	30-500	0.005-0.01	gas, voltage
Lamb	High/ Moderate	g+ l	1-10	0.001-0.005	gas, biochemical, density, sound speed
SH-SAW	Moderate/ Low	g+ l	25-200	0.025-0.05	gas, biochemical, viscosity
Love	High/ Low	g+ l	50-500	0.002-0.0067	gas, biochemical, viscosity

3.5.2 Piezo-ceramics

Piezo-ceramics bonded on a substrate (metallic, plastic, ceramic) can be used to generate SAWs, using the inverse piezoelectric effect. When excited by electric current piezo-elements start to vibrate, generating mechanical waves. And vice versa, when they vibrate due to mechanical waves, they produce electric current. Piezo-ceramics exhibit the exact same properties as piezo-electric materials do, and they can withstand high temperatures, are more resistant to harsh conditions and less expensive to manufacture, than most piezo-elements are.

Piezo-ceramics come into different sizes and shapes, depending on the type of the generated wave and its frequency. There are a lot of detailed information regarding the shape and size of piezo-ceramics which can be found on the product catalogue of most suppliers. In general,

- Bigger in size piezo-ceramics produce low frequency waves, and smaller piezo-ceramics higher frequency waves
- Three main type of piezo-ceramics can be found depending on the particle oscillation, as it can be seen in Figure 3.14. When they elongate and compress, they generate strong longitudinal waves (Figure 3.14 a) followed by a weak transverse wave, as during elongation/compression a weak transverse motion (Figure 3.14 b) occurs.

  When the transverse motion is more dominant (Figure 3.14 b), a strong transverse wave is generated, following a weak (almost negligible) longitudinal wave, as the transverse motion creates elongations/compressions of the piezo-ceramic.

  Lastly, when the piezo-ceramic motion is somewhat elliptical, strong shear waves are generated. This type of shear piezo-ceramic is known as the thickness shear piezo-ceramic (Figure 3.15).

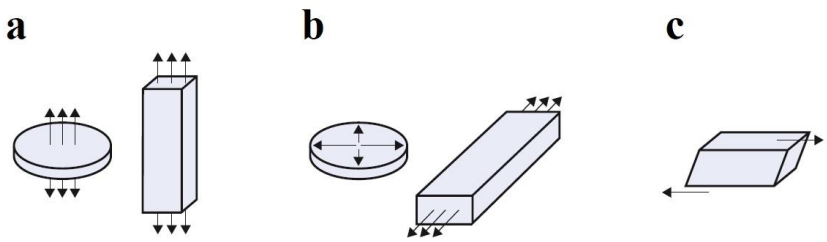

Figure 3.14 a) Longitudinal, b) transverse and c) thickness-shear piezo-ceramics [48]

Apart from a strong shear wave normal to the surface (along y-axis), the thickness shear piezo-ceramic generates a weak Lamb wave along z-axis, and a weak SH-SAW along x-axis.

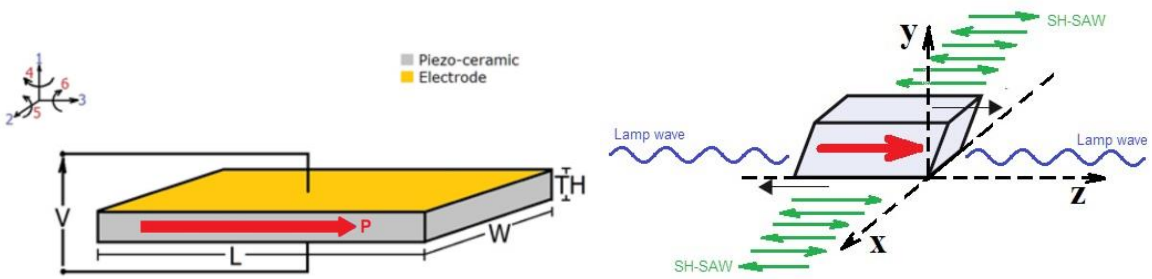

Figure 3.15 Thickness-shear piezo-ceramic (the red arrow indicates the poling direction of the particles)

The following conditions have to be taken into consideration when selecting a thickness-shear piezo-ceramic for generating SAWs and Lamb waves:

- The thickness of the piezo-ceramic defines the operating frequency; thinner the piezo-ceramic higher the operating frequency, and vice-versa.
- The length should be greater or equal to the width of the piezo-ceramic. When the length is greater than the width, strong SH-SAWs are generated along the *x* direction, and weaker Lamb waves along the *z* direction. When equal, equally strong SH-SAWs and Lamb waves are generated along *x* and *z* directions, respectively.
- The thickness of the piezo-ceramic should be 5 times smaller than its length, to allow uniform particle oscillation inside the piezo-ceramic.

Thickness-shear piezo-ceramics can generate strong shear waves between 0.5 – 10 MHz of frequency, but they are limited to a few kHz when they are used for generating SAWs. Most likely, this is due to the design of the piezo-ceramics, as they are mainly used for generating shear waves, whereas the SH-SAW and Lamb wave generation is merely a happy coincidence.

A more effective geometry for piezo-ceramics has been developed by Li et al. [49], that allows pure SH-SAW generation along both the *x* and *z* directions, free of Lamb waves. The face-shear piezo-ceramic, as it is called, can be seen in Figure 3.16. Compared to the thickness-shear, in the face-shear the electrodes are located on the side surfaces of the piezo-ceramic, parallel to its poling direction (pointed with the red arrow). When excited by electric current, it creates symmetric elongation and compression on the edges, thus generating SH-SAWs in all directions.

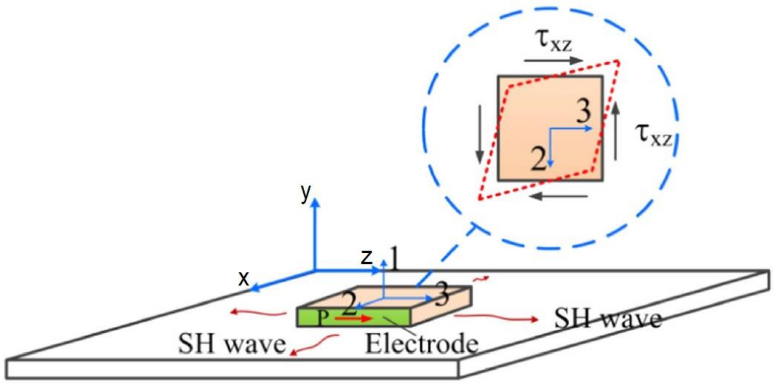

Figure 3.16 Schematic of face-shear piezo-ceramic [49]

The conditions that have to be met in order to allow SH-SAW generation, are:

- The length of the piezo-ceramic (along its poling direction) should be greater or equal to its width (perpendicular to its poling direction). When equal, equally strong SH-SAWs are generated along both *x* and *z* directions.

- The width defines the frequency; higher the frequency smaller the width, and vice-versa.
- The thickness of the piezo-ceramic should be 5 times smaller than its width and hence its length, to allow uniform particle oscillation inside the piezo-ceramic.

According to the aforementioned, clearly there are geometrical restrictions in generating high frequency SH-SAWs (> 600 kHz), so this method is limited to generating low frequency waves (100- 600 kHz). As the frequency increases, the width of the ceramic must be decreased. However, the thickness should always be 5 times smaller than the width, and that leads to very small and fragile piezo-ceramics, which are very difficult to manufacture.

3.5.3 Wedge method

Another way to excite SAWs is by exploiting the changing mode effect. A wave is changing mode, when the material it propagates along is coupled to a different material. The most commonly used methods is the wedge method, as it is referred by Viktorov [50].

The wedge method uses a wedge made out of a material with lower acoustic velocity than the substrate, to generate SAWs. The selected material for the wedge is usually made out of Perspex because the wave velocity is lower than most of the other materials, specifically metals such as steel and aluminium. The wedge is instrumented with a piezoelectric transducer, bonded on the sloping surface of the wedge, as shown in Figure 3.17. When the projection of the transducer coincides with the edge of the wedge, the generation of the wave maximizes.

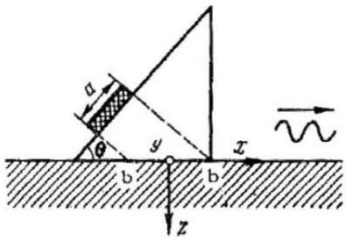

Figure 3.17 Mode conversion using the wedge method [50]

The angle of the wedge depends on the type of the generated wave, and can be calculated using Snell's law of refraction:

$$\frac{c_1}{c_2} = \frac{sin\theta_1}{sin\theta_2} \tag{3.6}$$

Where c_1 is the velocity of the incident wave inside the medium 1, c_2 is the wave velocity of the refracted wave inside the medium 2, θ_1 is the incident angle, and θ_2 is the refracted angle.

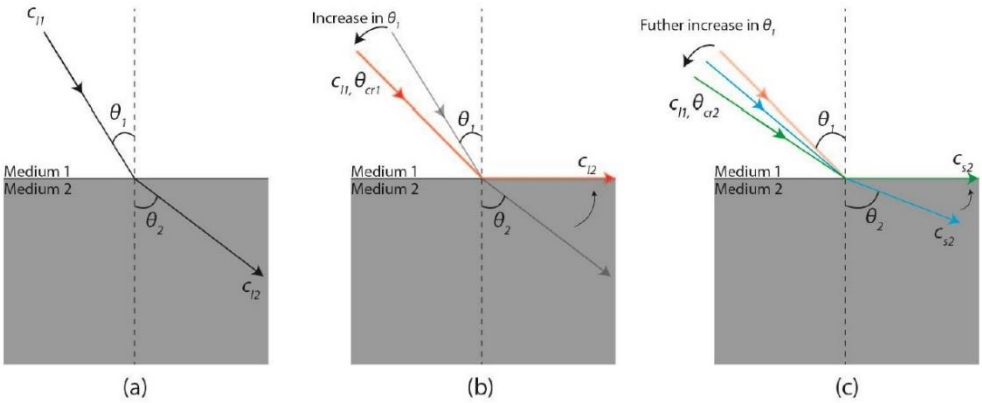

Figure 3.18 Wave mode change due to refraction [51]

When a longitudinal piezo-ceramic is bonded on the wedge, Rayleigh waves can be generated on the surface of the propagating medium, depending on the incident angle θ_1, as shown in Figure 3.18 a). As the angle θ_1 increases, the refracted longitudinal component of the wave moves to the surface of the propagating medium. There is a first critical point θ_{cr1} where the refracted longitudinal component inside the material becomes parallel to the surface, as it is shown in Figure 3.18 b). By increasing further the angle θ_1 the refracted longitudinal component vanishes and a refracted shear component is created. There is a second critical point θ_{cr2} of the incident angle where the refracted shear component inside the material becomes parallel to the surface of the propagating medium, as it can be seen in Figure 3.18 c). Further increase of the incident angle over the second critical point creates a Rayleigh wave that propagates along the surface of the propagating medium.

The same principles can be used to generate SH-SAWs using the wedge method. Instead of using a longitudinal piezo-ceramic, a thickness-shear piezo-ceramic is bonded on the wedge to create the shear motion that will be guided to propagate parallel to the surface of the medium, using Snell's law.

The wedge method presents some advantages over other methods for generating SAWs, including low cost transducers, easy to bond to a variety of media, as there are plenty of material options for the wedges. The geometry of the wedge solely depends on the acoustic velocities in the medium and wedge, which allows SAW generation of different frequencies using the same wedge geometry.

3.5.4 Comb-structure method

Another way to generate Rayleigh waves is the comb-structure method [50]. This method employs a comb like structure and a longitudinal transducer bonded on top of the structure, as it is shown in Figure 3.19.

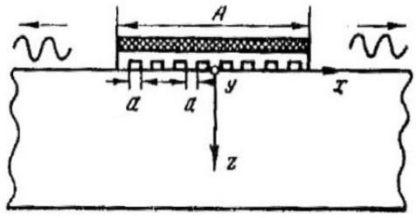

Figure 3.19 Comb-structure method [50]

The size of the combs is equal to the size of the gaps between them, and both are equal to half the wavelength of the generated wave. So, this method is frequency depended because the maximum generation of a Rayleigh wave is available only at one certain frequency. In order to generate Rayleigh waves at different operating frequencies, a new comb structure is required.

3.5.5 Electromagnetic acoustic transducer (EMAT)

EMATs are a relatively new technology for generating surface acoustic waves. This method has already been used to generate Rayleigh waves [52] and SH-SAWs [53]. These transducers employ electromagnetism to excite surface waves near the surface of the test piece. EMATs consist of a permanent magnet placed on top of a coil circuit excited by alternating current, as it is shown in Figure 3.20.

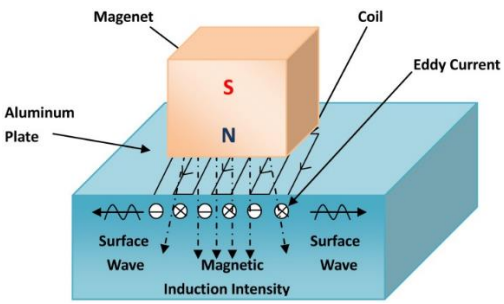

Figure 3.20 Schematic of EMAT structure [54]

The structure of the coil depends on the application and the type of the generated wave. The coil is deposited near the surface of the test piece leaving an air gap between them, and it is excited by alternate current which creates an electromagnetic field around it. This magnetic field creates an induced current on the surface of the test piece. The magnet is

then deposited near the coil and interferes with the magnetic field created by the coil. This interference creates eddy currents and Lorenz forces inside the test piece, which excites the particle structure into movement, generating a surface wave.

The electromagnetic acoustic transducers as a method to generate surface acoustic waves is less efficient, compared to methods that employ the piezoelectric effect, like SAW devices or the wedge and comb-structure methods. EMATs are quite big in size due to the size of the permanent magnet, thus difficult to apply to in-situ measurements. The manufacturing cost of these sensors is very expensive, less expensive though than the fabrication of a SAW device. On the other hand, EMATs are more resistant to extreme temperatures due to the materials they are made of, and the non-contact application of the sensors with the test piece.

3.6 Conclusions

Ultrasound is a mechanical wave with the same properties as sound, but of higher frequencies that exceed the hearing capabilities. Two families of ultrasound can be distinguished, the bulk acoustic waves and surface acoustic waves. BAWs propagate through a medium, while SAWs propagate along the surface of a medium. Different types of BAWs and SAWs exist, depending on the source and the propagating medium.

Among the different types of surface acoustic waves, SH-SAWs seem to be more suitable for the current application. They present good coupling with liquids, moderate sensitivity to surface changes and can be used for measuring liquid viscosity.

There are different methods for exciting surface acoustic waves including methods that employ piezo-electricity as a mean for generating SAWs, wave-mode changing methods that convert BAWs in to SAWs using wedges or comb-structures and methods that use electro-magnetism to excite particles of the medium in to oscillating and thus generating SAWs.

Considering the purchasing or manufacturing cost, the working conditions, available space for installation and the thesis objectives, generating SH-SAWs using piezo-ceramics or the wedge method seems to be more suitable as all three methods are very flexible when it comes to the transducer size that allows installation to the most confined spaces and present a working frequency range from 100 kHz to 10 MHz. Transducers, using any of the three methods, are cheap to manufacture and robust enough to withstand high temperatures and corrosive environments.

4 ULTRASOUND TO MEASURE VISCOSITY, SURFACE LAYERS & THIN FILMS

Both bulk acoustic waves and surface acoustic waves have been widely used to measure liquid properties, including viscosity, film thickness and surface layers. This chapter focusses on some relevant work that has been done in the field of ultrasound, providing new tools for measuring liquid properties including in lab measurements and in-situ measurements.

4.1 Longitudinal BAWs to measure thin/thick films

The film thickness is a very important parameter in lubricant applications, as it prevents direct contact of the interacting components and protects against friction and wear (Figure 4.1). The lubricant film thickness varies during operation, depending on the load and speed, as it can be seen from the Stribeck curve in Section 2.1 (Figure 2.2). As a result, measuring the thickness of the lubricant film under real operating conditions is of great importance, in order to ensure proper operation of the moving parts. Longitudinal BAWs have been used to measure liquid film thickness, as demonstrated by various authors.

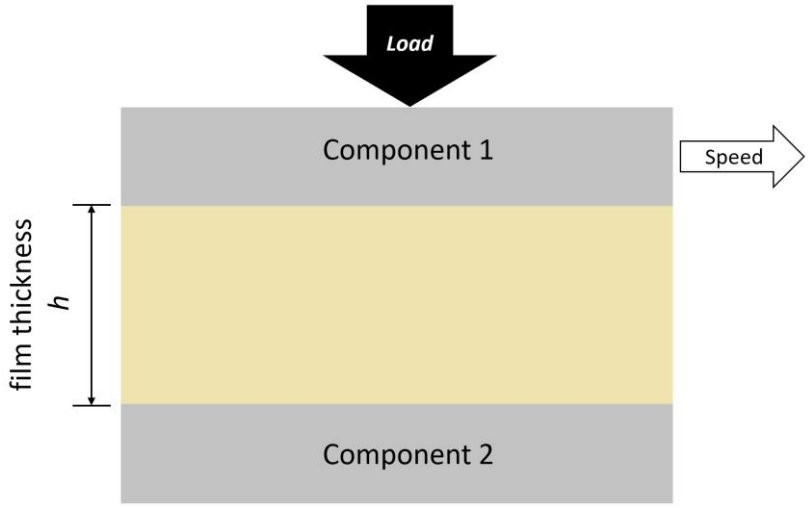

Figure 4.1 Lubricant film thickness schematic

Reflected longitudinal BAWs were used by Dwyer-Joyce et al. to measure the oil film thickness in-situ in a rolling bearing, between the raceway and a sphere [55]. Measuring the oil film thickness in-situ in a rolling bearing provides information on whether there is adequate lubrication to prevent wear of the moving parts. In this study, a focussed wide-band transducer was positioned on the outer surface of the raceway to send and receive longitudinal waves through the raceway and into the oil film. Two methods were used to calculate the film thickness, the *spring model* and *film resonance.*

The *spring model* utilises the reflection coefficient R to calculate the thickness of a film. At the solid-liquid interface the longitudinal wave loses energy, as it is partly transmitted through the liquid and partly reflected back (Figure 4.2), which is indicated by a decrease in the reflection coefficient values. The spring model treats the film as a spring of negligible mass and damping and of stiffness K, thus the energy transmitted into the liquid is related to the film stiffness which is linked to the film thickness. The results from the measurements of both stationary liquid films and dynamic lubricating films, have shown that accurate measurements of thin films (<10 µm) can be performed using the spring model. For thicker films, the mass starts to have an effect on the wave response and resonances appear, which are not accounted for by the spring model.

As the thickness of the film increases the system starts resonating at different frequencies, and these frequencies are directly related to the film thickness. This method is known as the *film resonance* method. According to Dwyer-Joyce et al. the resonance method can be used to measure film thicknesses up to 40 µm.

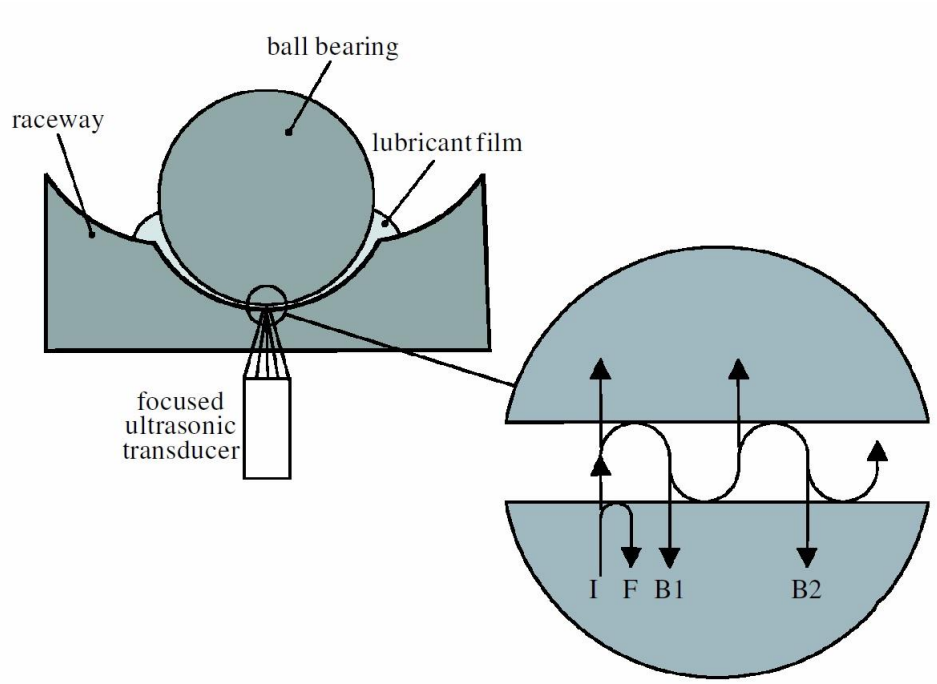

Figure 4.2 Schematic on an ultrasonic bean incident on a lubricated contact. *I* represents the incident wave, *F* represents the front face reflection, and *B* the back face reflections of the wave [55]

A very thorough comparative study between the two methods was made by Hunter et al., where oil films of various thicknesses were measured by both ultrasonic reflection and an independent method [56]. In the experiments, the film thickness was measured ultrasonically and the results were compared to both the thickness inferred from the geometry of the surfaces constraining the liquid film and measurements taken using

capacitive and verified laser interferometer techniques. Excellent correlation was observed between the measurement methods and estimated thicknesses in all experiments.

Dwyer-Joyce et al. have used the spring model method to also measure the oil film thickness in the liner-piston skirt [57], using a single cylinder 4-stroke engine on a dyno test platform for evaluation. For this application a piezo-electric transducer was bonded to the outside surface of the cylinder liner for transmitting and receiving high frequency short duration ultrasonic pulses. The wave reflections were used to determine the oil film thickness as the piston skirt passed over the sensor location. Oil films in the range of 2 to 21 μm were recorded, varying with engine speeds and the results were found to be in agreement with detailed numerical predictions.

Both the spring model and film resonance methods were used by Geng et al. to measure the lubricant film thickness of a hydrodynamic bearing [58]. A piezo-electric transducer was bonded to the outer surface of the bearing to send and receive pulses perpendicular to a water film inside. An algorithm was developed to automatically choose between the spring model and film resonance methods, according to the film thickness. As the results have shown, the spring model method was more accurate for films thickness less than a wavelength, whereas the film resonance method was found to be more precise for film thicknesses greater than a few microns.

4.2 Shear BAWs to measure liquid viscosity in films

Apart from the film thickness, viscosity is equally important in lubricating applications, as explained in Section 2.1. Viscosity is strongly affected by the operating conditions and more specifically temperature, pressure and speed. However, reproducing these conditions in a laboratory viscometer to investigate the lubricant behaviour is hard, as shown in Table 2.2, and as a result, measuring viscosity in the film itself is preferred.

Shear bulk acoustic waves have been used for measuring liquid viscosity in thin films. When a shear wave is incident on a solid-liquid boundary, it is partly transmitted inside the liquid, and partly is reflected back. Due to the engagement with the liquid, wave energy is lost at the solid-liquid interface in the attempt to shear the liquid particles. The energy loss is shown in the reflected portion of the wave and is directly related to the liquid viscosity. There are different models that relate the shear reflection to the liquid viscosity, but the most commonly used are the *spring model* for *Newtonian* liquids and *Maxwell model* for *viscoelastic* liquids.

The *spring model* assumes the liquid to behave as a Newtonian fluid and considers a linear relationship between shear stress τ and strain rate $\dot{\gamma}$ (Equation 2.9). The mechanical

equivalent is a spring of stiffness *K*, as shown in Figure 4.3. The viscosity of Newtonian liquids can be calculated using Equation 4.1 [59], as function of the shear wave reflection from a solid-liquid boundary.

$$\eta_l = 2\frac{(c_s\rho_s)^2}{\omega\rho_l}\frac{cos^2(\theta_l)}{cos^2(\theta_s)}\frac{R(1-R^2)sin\varphi}{(1+R^2+2Rcos\varphi)^2} \tag{4.1}$$

In Equation 4.1, the subscripts s and l refer to the solid and liquid, respectively, η is the viscosity, ρ is the density, ω is the wave angular frequency, θ is incident (θ_s) and refraction (θ_l) angles, respectively, R is the reflection coefficient ($0 \leq R \leq 1$), which can be determined using Equation 3.4 and φ is the phase of the wave ($0 \leq \varphi \leq 2\pi$). In Equation 3.4, $Z_1 = \rho_s c_s$ is the acoustic impedance of the solid and $Z_2 = \sqrt{\eta_l \rho_l \omega}$ is the acoustic impedance of the liquid.

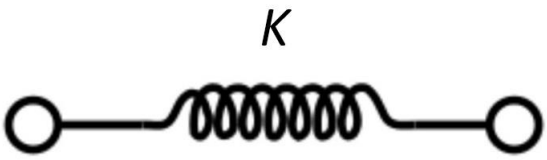

Figure 4.3 Mechanical analogy of spring model for Newtonian liquids

The Maxwell model takes into consideration both the viscous and elastic behaviour of a liquid and Equation 4.2 shows the relationship between shear stress and strain, where $\dot{\tau}$ is the rate of shear and t_r is the relaxation time of the liquid. The mechanical equivalent of the Maxwell model is a spring in series with a dashpot and it is shown in Figure 4.4. Viscosity can be calculated then using Equation 4.3 [60], as a function of reflected shear waves from a solid-liquid boundary.

$$\eta = \frac{\tau}{\dot{\gamma}} + t_r\frac{\dot{\tau}}{\dot{\gamma}} \tag{4.2}$$

$$\eta_l = 2\frac{(c_s\rho_s)^2}{\omega\rho_l}\frac{cos^2(\theta_l)}{cos^2(\theta_s)}\frac{R(1-R^2)sin\varphi}{(1+R^2+2Rcos\varphi)^2}(1+\omega^2{t_r}^2) \tag{4.3}$$

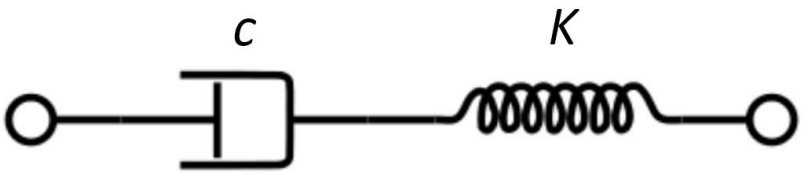

Figure 4.4 Mechanical equivalent of Maxwell model for viscoelastic liquids

Kasolang and Dwyer-Joyce investigated shear BAW reflections from thin lubricant films for measuring viscosity [61]. The proportion of a shear BAW reflected at a thin film depends on the film stiffness. This stiffness was incorporated by the authors into the

spring model of shear ultrasonic reflection, in order to determine the viscosity of thin oil films, as a function of the film thickness. The approach was experimentally evaluated on static oil films between Perspex plates (Figure 4.5). Oil films in the range of 4 to 22 μm were formed by depositing a drop of engine oil of known volume between the plates. The shear reflection data was used firstly to determine the viscosity, if the film thickness is known and secondly to determine the film thickness, if the datasheet value of viscosity is used. In both cases, good agreement was achieved for thin films (<15 μm). For thicker films, the shear stiffness reduces to such an extent that almost all the wave is reflected and the difference associated with the film response is hard to distinguish from background noise.

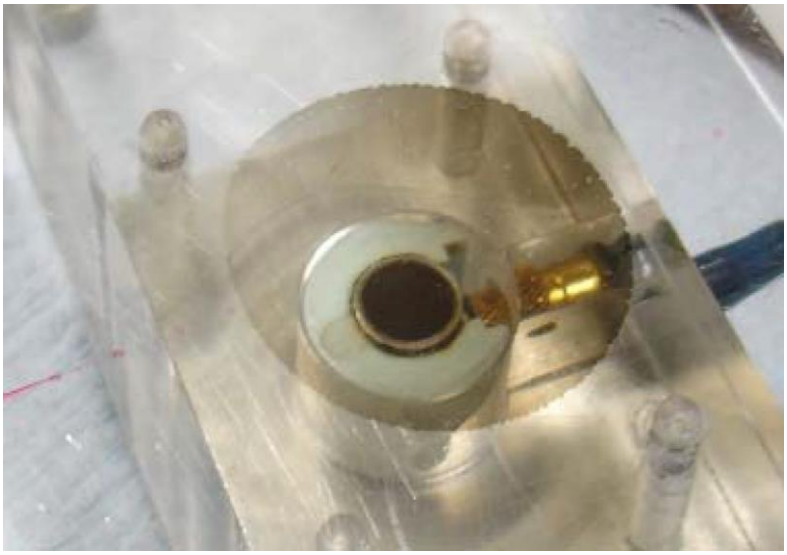

Figure 4.5 Photograph of the model oil film apparatus. The circle of oil is visible as is the transducer through the transparent blocks [61]

Kasolang et al. also used shear BAW reflections to measure the circumferential viscosity profile in a stationary journal bearing [62]. In this preliminary study, the reflection coefficient of an ultrasonic shear wave from an oil film was predicted for different materials (metallic and non-metallic). As it was found, the shear wave reflection from a Perspex-oil-solid interface presents the highest sensitivity for any combination of solid materials on the other side of the oil film. This occurs due to the fact that the acoustic impedance of Perspex is closer to the acoustic impedance of the oil, thus reducing the *acoustic mismatch* between them, allowing more wave energy to transmit through the Perspex-oil interface. On the contrary, metallic materials present greater acoustic impedance than oil, thus increasing the acoustic mismatch and most of the wave energy is reflected back at the metal-oil boundary.

For the purpose of measuring the circumferential viscosity profile in a stationary journal bearing, a Perspex plug was instrumented with a shear transducer, as shown in Figure 4.6 and was press fitted inside a journal, which was then ground so the plug follows the contour of the journal. Load was applied on the bearings in order to vary the oil film pressure circumferentially and thus the oil viscosity and film thickness. The spring model was used to determine the oil viscosity as a function of the shear reflection coefficient and oil film thickness. As it was found experimentally, viscosity measurements were poor for thick films (>20 μm), especially in the region near the oil supply hole. In the case of thinner films though (<20 μm), around the loaded region, viscosity measurements were found to be within reasonable agreement with the expected values and consistent.

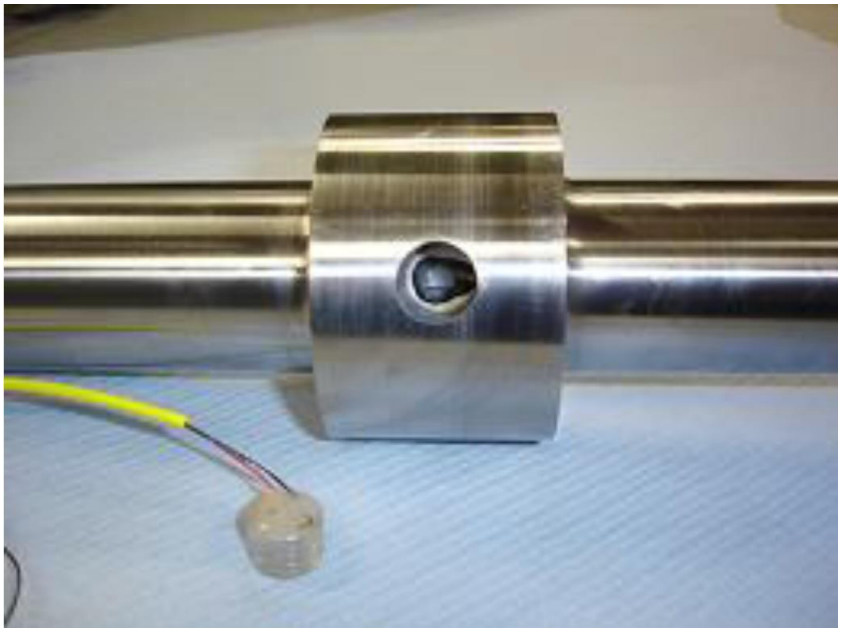

Figure 4.6 Perspex plug instrumented with a shear sensor for measuring viscosity circumferentially in a journal bearing [62]

As the author states, this occurs due to the shear stiffness which is higher in thin films than in thicker films, currently limiting the method to measuring viscosity of thin films. In addition, Perspex is unsuitable for high temperature applications as it has a low melting point, thus testing a lubricant oil under real operating conditions may be a challenging task. Metallic materials are preferred to manufacture the plug, but they present high acoustic mismatch with oil.

Schirru et al. has developed a novel shear ultrasonic measurement technique to measure lubricant viscosity circumferentially in-situ in an operating journal bearing [60]. The technique utilises a miniaturised ultrasonic viscometer, using a metallic plug instrumented with a shear transducer on the one side and a *matching layer* on the opposite side (in contact with liquid), as shown in Figure 4.7.

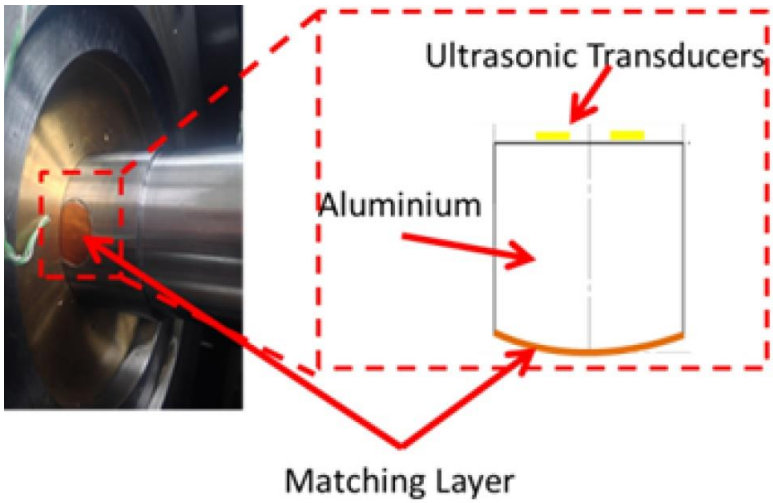

Figure 4.7 Addition of a polyimide layer to an ultrasonic shear probe for measuring oil viscosity circumferentially in a journal bearing [60]

The addition of the matching layer improved the acoustic mismatch between metal and oil, as the low acoustic mismatch between metal-layer allows more wave energy to be transmitted inside the layer. Then the low acoustic mismatch between layer-oil allows more wave energy to be transmitted inside the oil, thus improving the shear reflection response to thin viscous films. When the thickness of the matching layer is equal to ¼ the wavelength, the matching layer resonates, thus increasing the sensitivity of the method.

The miniaturized ultrasonic viscometer was placed inside a journal to obtain the circumferential viscosity profile, under different loading conditions, temperature and rotational speeds. The Maxwell model was used to calculate the viscosity of different oils, as a function of the shear BAW reflection coefficient and relaxation time of the oil. Four viscosity regions were identified due to the variations in localized temperatures and loads. The results were compared with the isothermal solution of the Reynolds equations for hydrodynamic lubricated bearings, and it was found that the ultrasonic viscometer located the angle the maximum load occurs and the length of loaded contact, with good accuracy.

4.3 SAWs to measure viscosity

Surface acoustic waves have been also used to measure viscosity of liquids in many applications. Compared to shear bulk acoustic waves, surface acoustic waves do not require a matching layer and metallic media can be used in direct contact with liquids for measuring viscosity.

Reflected Lamb waves from a solid-liquid boundary interface have been used to characterise liquid viscosity, as described by Wilkie-Chancellier et al. [63]. In their work, they used a wedge transducer for sending and receiving Lamb waves along a stainless steel

plate in contact with a viscous liquid, as shown in Figure 4.8. The reflected 1st anti-symmetric A1 mode was used to measure the acoustic impedance of different water-glycerol mixtures, as a function of the acoustic impedance of the solid and the reflection coefficient (Equation 4.4). Viscosity was calculated then using Equation 4.5 and assuming Newtonian behaviour. For Newtonian liquids the measured dynamic viscosity was found to be in good agreement with that obtained by other techniques in the literature, for small values less than 7 mPas as the shear component of the wave highly dissipates in more viscous liquids. As a result, the method is limited to measuring viscosity of very thin liquids and other methods are required for more viscous liquids.

$$z_l = z_s \frac{1-R}{1+R} \tag{4.4}$$

$$z_l = \sqrt{i\rho_l \eta_l \omega} \tag{4.5}$$

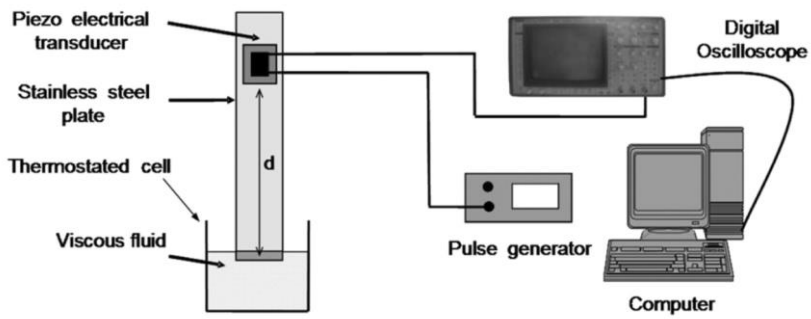

Figure 4.8 Experimental set-up for fluid characterization using reflected Lamb waves [63]

The fundamental symmetric Lamb wave mode S0 along with the fundamental SH-SAW mode SH0 were used to measure the viscosity of highly viscous non-Newtonian liquids, as described by Kazys et al. [64]. Two aluminium plates were instrumented with Lamb wave and SH-SAW transducers, respectively. Two transducers were bonded on each plate, one for transmitting and the other for receiving waves. The aluminium plates were placed between the two halves of a cylindrical vessel in such way that both faces on the plate were in contact with the sample when the vessel was filled, as shown in Figure 4.9. The wave attenuation due to the liquid viscosity was measured between 30 and 60 °C. The feasibility to measure variations of viscosities in the range of 20 to 25000 Pa s was theoretically and experimentally proved. The results has shown that the SH0 mode was able to measure a wider range of viscosities up to 25000 Pa s, compared to the S0 mode which was limited to ~3500- 4000 Pa s. The experiments also revealed that the measured dynamic viscosity of the N2700000 standard was frequency dependent and much lower than the one indicated by the manufacturer, which is a characteristic feature of non-Newtonian liquids. And lastly, according to the results, the proposed ultrasonic method was found to be more

mechanically robust and better fitted for measuring the viscosity of highly viscous substances during manufacturing process in extreme conditions, compared to other known methods.

Although this work has reported a wider measuring viscosity range, there is a large viscosity range from 10mPas to 20 Pas, which is of great interest to the lubricant industry, that the current methods are unable to measure or there is lack of experimental data to support the contrary.

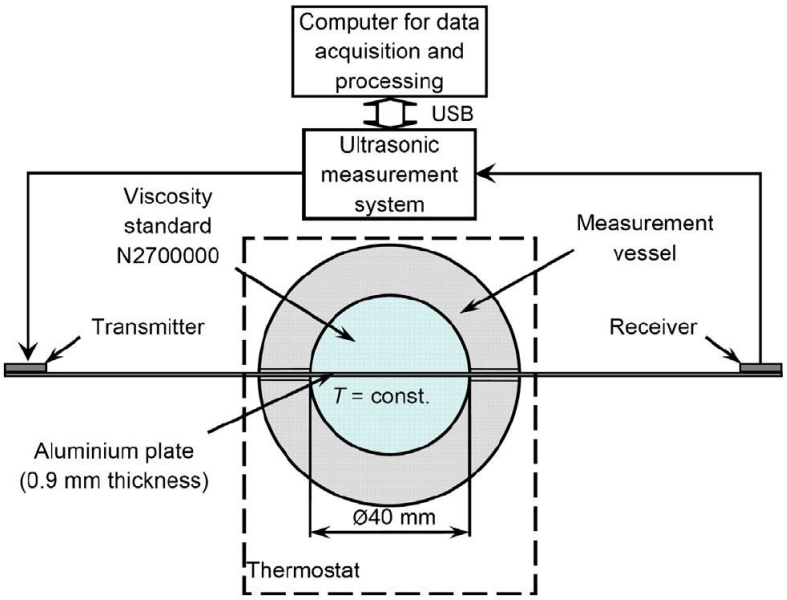

Figure 4.9 Experimental set-up used for measuring liquid viscosity using So Lamb waves and SHo shear-horizontal surface acoustic waves [64]

Gitis et al. studied the effect of liquid viscosity on the propagation of the zero mode of a shear horizontal surface acoustic wave (SHo mode) in a thin waveguide immersed in the liquid [65]. It was shown that the wave amplitude decayed exponentially as a function of the distance, at a damping coefficient proportional to the square root of the shear viscosity of the liquid. The amplitude decay due to the viscous properties of the liquid was numerically estimated from the ratio of the liquid shear impedance to the shear impedance of the waveguide and the results were found to be encouraging for developing a method to measure viscosity at high accuracy. The method was developed and tested on an aluminium waveguide, at a frequency of 2 MHz. An angled transducer was used to generate and receive the wave that travelled along the waveguide, was reflected at the waveguide boundary and travelled back to the transducer (Figure 4.10). The decrease in the signal amplitude when the waveguide was immersed in distilled water compared to the amplitude in the unloaded (air) waveguide was measured and considered to be a

measure of the sensitivity of the method. Viscosities from 6 to 60 mPas were measured using different solutions of sucrose in distilled water and the experimental results were found to be in good agreement with the theoretical estimates.

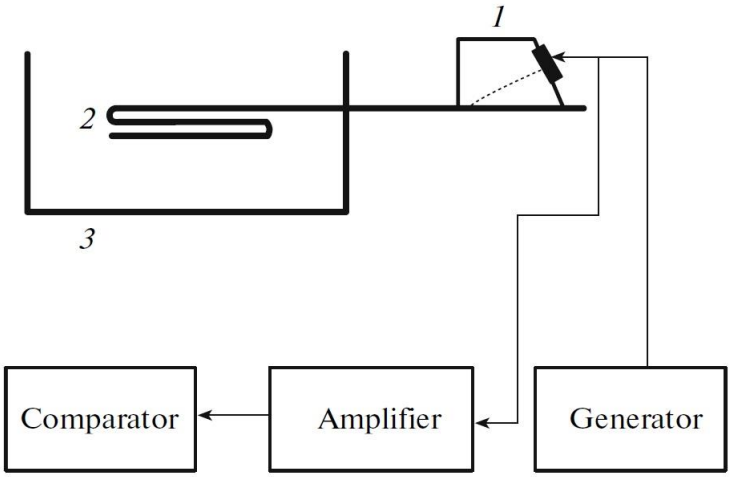

Figure 4.10 Experimental set-up for measuring liquid viscosity using the SH0 mode (1. angled transducer for sending/receiving waves, 2. ribbon-like medium to increase the sensitivity, 3. Vessel) [65]

The viscosity and shear modulus of liquids were measured by Kielczynski et al. [66], using SH-SAWs. The viscosity and shear modulus sensor they proposed, consisted of a piezoelectric substrate with a metallic waveguide on top of it. A transducer for sending and receiving SH-SAWs was bonded on the boundary of the piezoelectric substrate in such way so it was in contact with both the substrate and the waveguide. Direct proportionality of the change on the complex propagation constant of the wave to the shear impedance of a liquid, was established. The shear impedance of the liquid was evaluated by measuring the change in the time of flight between two wave impulses and the change in their amplitude. Viscosity and shear modulus were then calculated using the Maxwell model for three different samples, with viscosities varying from 220 mPas to 2230 mPas, and the results were found to be in reasonable agreement with the values obtained from a capillary viscometer. According to the authors, the proposed method for determining the rheological parameters of a viscoelastic liquid was found to be more sensitive compared to bulk waves or Love waves, and more specifically the sensitivity increased linearly with frequency.

4.4 QCM & SAW devices to measure surface layer formation

Both the quartz crystal microbalance (QCM) and surface acoustic wave (SAW) devices have been used to measure the formation of surface layers. The QCM utilizes a quartz

crystal, with printed electrodes on the two surfaces of the crystal, as shown in Figure 4.11. The crystal is free to vibrate at its resonant frequency when voltage is applied on the electrodes. Usually, the crystal surface is coated with a functional layer that allows molecular adsorption. Different coatings are being used depending on the molecules under testing. The adsorption of molecules on the crystal coating changes the mass of the coating, which has two effects; it changes the resonant frequency of the crystal and dissipates the wave amplitude (similar to the reflection coefficient in the case of BAWs), thus indicating surface layer formation on the coating surface. The resonant frequency of a typical QCM is between 4-6 MHz, but odd harmonics can be used to achieve higher frequencies up to 30 MHz.

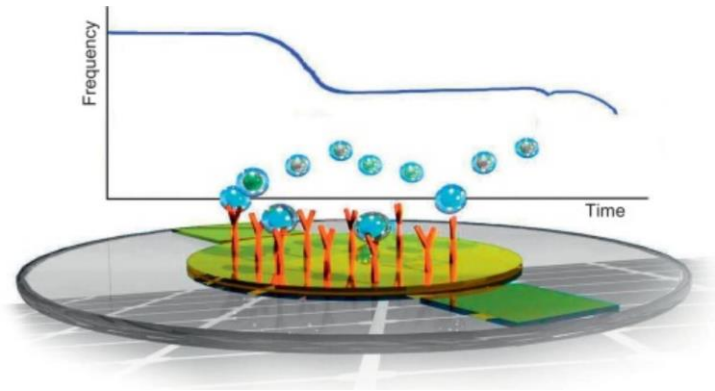

Figure 4.11 Molecular adsorption on the electrode surface of a quartz crystal microbalance [67]

SAW devices employ a piezoelectric substrate with two interdigital transducers (IDTs) printed on it. As in the case of the QCM, SAW devices are coated with different layers to increase the sensitivity of the device and allow molecular adsorption of the surface of the coating (Figure 4.12). Molecular adsorption leads to change in the mass of the coating, which similarly to the QCM changes the resonance frequency of the piezo-substrate and wave amplitude along the coating-layer interface, which is related to a surface layer formation. The resonant frequency of typical SAW devices is a few hundreds of MHz, which improves the sensitivity of these microbalances to measure smaller molecular species than the QCM.

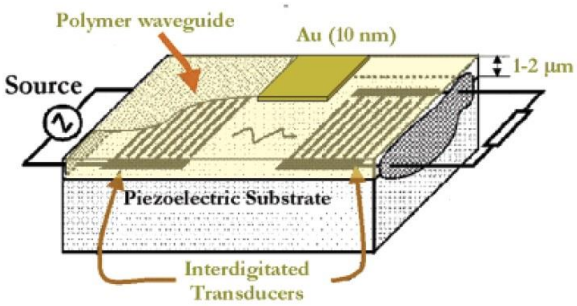

Figure 4.12 Schematic representation of a typical SAW device for measuring molecular adsorption [68]

Qin et al. have used the quartz crystal resonator technique to measure differences in the viscoelastic behaviour of the bulk of a solution and a solution boundary layer at a solid-liquid interface, due to molecular adsorption of macromolecules at the interface [69]. A 5 MHz quartz crystal was coated with a gold layer to allow molecular adsorption and changes in resonant frequency of the crystal were monitored. The wave penetrated the liquid up to a certain depth, which was a function of the wave frequency, liquid density and viscosity. Measurements were taken for different poly-ethylene-glycol (PEG) solutions inside the bulk of the solution and close to the solid-liquid interface for comparison. According to the results, there has been a clear difference in the resonant frequencies and the wave amplitude between the two, indicating that physisorption or physical adsorption has taken place at the Au-water interface for different PEG solutions. The results has shown that adsorption occurred for PEGs with molecular weights above a few thousands g/mol, but no adsorption occurred at the interface for smaller PEG molecules. As for PEGs with modest molecular weight, the results agreed with the theory that they do not adsorb on hydrophilic surfaces on aqueous solutions.

The acoustic responses of molecular films with continuous concentration profiles adsorbed on solid-liquid interfaces probed by QCM, were numerically analysed using a continuum model by Zhu et al. [70]. Numerically calculated results has shown that the change in the electrode resonant frequency and wave amplitude of a QCM were determined mostly by the change of viscoelastic profile of the layers in the solution adjacent to the solid-liquid interface, due to the adsorbed molecular films on the QCM electrode surface. It was found that for films with the same amount of adsorbed mass, the changes on the resonant frequency and wave amplitude varied approximately linearly with the width of the film-solution interface in the profiles.

Combined surface acoustic wave and surface plasmon resonance (SPR) techniques were used by Friedt and Francis for measuring water content in collagen and fibrinogen protein layers [71]. SAWs resonate the surface coating using mechanical waves, while SPR resonates the electrons at the interface between negative and positive permittivity materials stimulated by light. In their work, they have shown how a two-step measurement, first using copper electrodeposition for instrument calibration, followed by a measurement on the actual biological layer under investigation, on a combined SAW/SPR instrument leads to an estimate of the water content and layer thickness. While each individual technique could not achieve such identification, both common parameters (water content ratio and layer thickness) could be identified with the combination of the two methods. The results from the combination of SAW/SPR were validated with a QCM. In both cases, change of the resonant frequency due to mass deposition on the coating surface was measured and attributed to a surface layer formation. Although, the two

techniques have a different acoustoelastic effect on the liquid, they presented the same trend. Such results are especially useful for protein layers with high water content for which the hydrodynamic interaction can become predominant over rigid adsorbed mass.

Shear-horizontal surface acoustic waves have also been used by Saha et al. to quantify the viscoelastic properties and calculate the density of a protein layer deposited on a solid-liquid interface [68]. They used SH-SAWs propagating in a waveguide configuration at 108 and 155 MHz for the detection of specific binding and adsorption of IgG antibodies to protein modified surfaces and gold, respectively. The viscoelasticity of surface protein layers was quantified in real time during the formation of the layer. The formation of the layer due to molecular adsorption on the device coating surface was measured from changes in the resonant frequency of the coating and wave amplitude. Via a self-calibrating technique, the viscoelastic response of biological layers as glycerol-equivalent surface viscosity was quantified. This viscosity yielded comprehensive information about the regime where relaxation processes in the biological layer with relaxation times up to half the device period (~5 nm) were taking place.

4.5 Conclusions

The studies in the previous sections very well report the range of applications ultrasonic methods have been used for measuring liquid properties. Table 4.1 highlights a few of the advantages and disadvantages of the methods that were presented in Sections 4.1 to 4.4.

According to the results, films of various thicknesses can be accurately measured with ultrasonic means, using different models to relate ultrasonic properties to the film thickness. In applications where the film thickness varies a lot and combination of models is required for the calculations, additional time may be required for testing and data processing, as a single sensor may not cover all models.

The findings of the work with reflected shear BAWs for measuring lubricant film viscosity, have significant impact in the automotive and lubricant industries. They significantly advance the understanding of the complex lubrication conditions found in engine contacts and further validate the existing lubrication models. However, the requirement for a matching layer to improve the acoustic mismatch between metals and oil, makes the method difficult to implement in actual engineering components. SAWs overcome this limitation and offer viscosity measurements at a metal-liquid interface.

Table 4.1 Advantages and disadvantages of ultrasonic methods for measuring liquid film thickness, viscosity and the formation of surface layers

Measurement	Method	Advantages	Disadvantages
Film thickness	Longitudinal BAWs	Large measurable range, in-situ a film measurements	Combination of methods is required to obtain both thin and thick films, frequency dependent method
Viscosity	Shear BAWs	In-situ a film measurements, non-Newtonian behaviour identification	A matching layer is required when used with metals, frequency dependent method
	Lamb waves	No requirement for a matching layer	Limited measurable viscosity range
	SH-SAWs	No requirement for a matching layer, in-situ measurements, large measurable viscosity range, non-Newtonian behaviour identification	Returns the average viscosity of a liquid interfering with the ultrasonic path length, frequency dependent method
Surface layer formation	QCM	High frequency range for measuring layer formations down to 1 nm	Limited to bench-top measurements, sensitive to certain molecular species that get adsorbed on the electrode surface
	SAWs	Various coatings can be used to attract the adsorption of different molecular species, high frequency range for measuring layer formations <1 nm	Limited to bench-top measurements

Lamb waves, both symmetric and antisymmetric, and SH-SAWs have been used to measure viscosity of different liquids. According to the results reported by various authors, SH-SAWs seem to be more suitable for measuring viscosity of liquids than Lamb waves, as the measuring viscosity range is considerably greater. The method can be used in either *pulsed-echo* mode (one sensor transmitting/receiving) or *pitch-catch* mode (one transmitter and one receiver), offering more flexibility depending on the application. Finally, the propagating medium or waveguide (as it is most commonly known) can be installed inside an extreme environment while the sensors can be safely installed outside. SH-SAWs look promising for measuring viscosity at a metal-liquid interface, but they have yet to be implemented in engine components to measure oil viscosity in-situ a film. In this thesis engine bearing sleeves, a key component in every engine, will be explored as a SH-SAW waveguide for measuring oil viscosity in-situ a rotating journal bearing.

QCM and SAW devices can be successfully used to measure the adsorption of molecules and formation of surface layers in laboratory based testing, but they cannot be used in-situ in an engine for measuring the oil additives' presence and activity, due the fragile nature of the quartz crystal and piezo-electric substrate they use, respectively. As a result, developing ultrasonic methods that employ metallic media but with the capabilities of a QCM or SAW device present great interest for measuring surface layer formation and additive activity in-situ in lubricated engines. In this thesis, SH-SAWs generated on a metal waveguide will be used to measure the adsorption of viscosity modifiers and friction modifiers, both very important additions in the engine oil as described in sub-Sections 2.2.1 and 2.2.2, for forming boundary layers.

In order to develop a SH-SAW method for measuring engine oil viscosity in-situ the film and the formation of surface layers on engine components, there are a number of parameters that need to be taken into consideration. Firstly, the method needs to meet the requirements for the end goal, which is the application in engine bearings. As a result, the method should be robust to withstand the vibrations of the engine, thermally stable to withstand the high temperature of the engine, and chemically resistant to the oily environment of the engine. These parameters need to be taken into consideration when sourcing or manufacturing sensors for generating SH-SAWs, as well as the frequency range capabilities of each method. Frequency is important for characterising a liquid as Newtonian or non-Newtonian, since it defines the rate of shear the liquid is subjected to. A suitable couplant is also required to bond the sensors to the metal medium, which must not lose its composition at high temperatures, be chemically resistant to oxidation and the engine oil and offer good coupling. It is suggested then, the various sensors are tested on flat metal plates first, similar to engine bearing metals, to investigate the SH-SAW propagation through a metal-oil interface and their capabilities for measuring oil viscosity

and formation of surface layers, before moving to a more complex system as the engine bearing. It is suggested to test the sensors in pitch-catch mode throughout, as two sensors will be required in the final application, because after the half-bearing sleeves are installed there will be no reflective edge for the SH-SAWs to return back to the sensor.

The SH-SAW should meet some standards in order to be considered reliable and accurate method for measuring oil viscosity and formation of surface layers. In this thesis, the acceptance criteria are the repeatability of results and small error <5%. To investigate those two criteria, all tests will be repeated 5 times under the exact same conditions in order to exclude unwanted parameters that may affect the measurements and focus only on the method itself. The method will be validated throughout the development procedure using the oil manufacturer's viscosity datasheets and a Brookfield rotational viscometer, and using an ultrasonic shear BAW sensor in the final application; in-situ a journal-bearing film viscosity measurements.

5 EXPERIMENTAL CONFIGURATION FOR MEASURING LUBRICANT PROPERTIES USING SH-SAWS

According to the conclusions from Sections 4.3 and 4.4, SH-SAWs have been successfully used for measuring viscosity of various liquids and the formation of adsorbed surface layers. As a result, they present great interest for the aim of this project, which is to measure viscosity of oil and the formation of surface additive layers in-situ in a running journal bearing.

This chapter introduces the experimental set-up for sending/receiving SH-SAWs and the signal processing techniques that were developed for measuring lubricant properties. The transducers for generating SH-SAWs, the hardware for signal excitation and acquisition and the signal processing techniques, are explained in detail in the following sections.

5.1 SH-SAW transducers

In this work, transducers were manufactured using face-shear piezo-ceramics and piezo-ceramics bonded on wedges, for generating SH-SAWs on metallic surfaces.

5.1.1 SH-SAW generation using piezo-ceramics

According to the technique outlined in Section 3.5.2, 200 kHz face-shear piezo-ceramics were used to make transducers for generating low frequency SH-SAWs on a metallic medium, which can be seen in Figure 5.1. The piezo-ceramics were wired up with coaxial cable and potted with protective epoxy to secure the cable connections and make them more robust.

Figure 5.1 200 kHz face-shear piezo-ceramic *(left)*, SH-SAW transmitter & receiver *(right)*

5.1.2 SH-SAW generation using angled transducers

According to technique outlined in Section 3.5.3, two pairs of angled SH-SAW transducers were built (Figure 5.2), using 400 kHz and 2 MHz thickness-shear piezo-ceramics, respectively. The material of the wedge was selected to be Perspex, as the shear velocity in Perspex is much lower than the SH-SAW velocity in either aluminium or steel (which are

the two metallic media that were investigated in this work). The piezo-ceramics were bonded on the Perspex wedges with a cyanoacrylate and wired with coaxial cable. After, they were potted with epoxy to protect the piezo-ceramics and the cable connections. In Figure 5.2, the piezo-ceramic can be seen through the wedge, placed in such way that its projection pointed straight to the edge of the wedge, offering maximum SH-SAW generation.

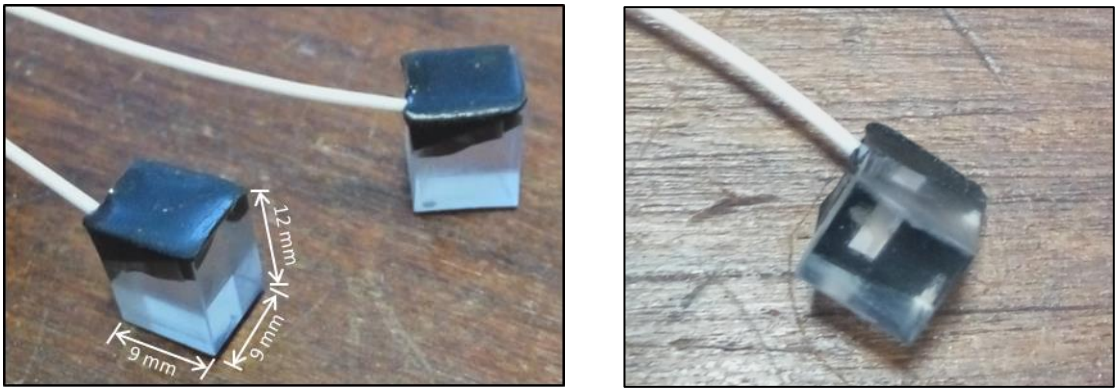

Figure 5.2 Angled SH-SAW transducers developed using the wedge method

Table 5.1 presents the corresponding incident angle for both materials, as well as their shear acoustic velocities. Clearly, the shear acoustic velocity in Perspex is much lower than the shear acoustic velocities in either aluminium or steel, which makes it suitable for generating SH-SAWs on both material.

Table 5.1 Incident angle of Perspex wedge for aluminium and steel application

Material	Shear acoustic velocity	Incident angle
Perspex	1330 m/s	-
Steel	3200 m/s	24.55°
Aluminium	3100 m/s	25.4°

More detailed description for the selection of the 400 kHz and 2 MHz frequency for generating SH-SAWs with angled transducers, follows in the next chapters.

When angled transducers are used, there is a time delay in the SH-SAW propagation, due the time it takes for the shear wave to propagate inside the wedges.

In the case of the Perspex wedges, the distance inside each wedge was 11 mm (22 mm in total) and the speed of shear BAWs in Perspex is ~1330 m/s, which led to ~16.5 μs time delay.

5.2 Experimental configuration

The general experimental ultrasonic apparatus is shown schematically in Figure 5.3. Two transducers were bonded directly on a steel plate using an adhesive couplant, in order to ensure good coupling between them and the plate. One transducer was acting as the transmitter and the other as the receiver. This pulsing/receiving set-up is commonly known as pitch-catch mode and was selected over the pulsed-echo mode for two reasons. Firstly, the sensors can be placed closer together or further apart to vary the sensing area. Secondly, the incident wave can be directly received instead of receiving a distorted reflected wave from a boundary. As a result, the pitch-catch mode does not require a boundary to be present and the distance between the sensors can be adjusted depending on the requirements of each application.

A function generator (TTI TG5011A) was used to produce a burst sine pulse (sinusoidal pulse of finite duration) that excited the transmitter to generate the wave. The selection of a sine pulse was made due to the better response of the piezo-ceramics to sine pulses compared to square or ramp pulses [43]. The burst mode (finite duration of the pulse) was selected over the continuous mode (that QCM uses), as it allows co-existing wave modes to be distinguished in the time-domain according to their speed and each of them to be investigated individually.

The wave was received using a second transducer connected to a digitizer (picoscope 5444D model) for signal acquisition.

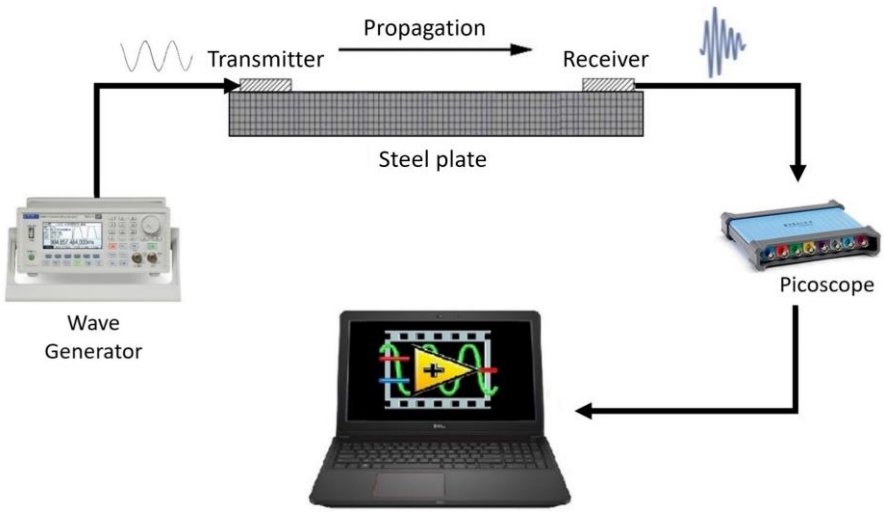

Figure 5.3 Experimental set-up for measuring lubricant properties using SH-SAWs

The same hardware was used in all experiments; two SH-SAW transducers, a function generator and a picoscope. The material of the medium, its dimensions, the bonding and type of transducers were slightly modified between the experiments. More details about the medium properties and transducers bonding, will be given for each experimental case.

5.3 Wave generation and signal acquisition

In this section, the face-shear and angled SH-SAW transducers were tested for generating SH-SAWs on a 1000mm x 700mm x 2mm steel plate, as shown in Figure 5.4. The different transducer pairs were coupled on the plate with Olympus shear couplant and held in position with two magnetic clamps. This set-up was selected to temporarily attach the transducers on to the steel plate to explore the generation of SH-SAWs using different pairs. The Olympus shear couplant was selected due to its good coupling properties when shear waves are used. The magnetic clamps were used to prevent the transducers from detaching and to ensure the continuous coupling of the transducers with the plate, in order to obtain comparative results. The distance between the transducers and number of burst cycles was adjusted depending on the operating frequency, to prevent waves from overlapping. In order to reduce noise, 30 captures were taken which then averaged, in order to obtain reduced noise signals.

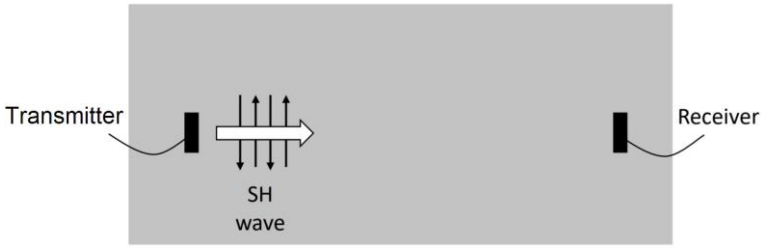

Figure 5.4 Schematic of SH-SAW generation using SH-SAW transducers

5.3.1 200 kHz face-shear SH-SAW transducers

The face- shear SH-SAW transducers were placed 650mm apart on the steel plate and excited by a 200 kHz, 10 Vpp, 3-cycle sinusoidal pulse using the function generator. The raw signal from the receiver, as it was acquired with the picoscope, can be seen in Figure 5.5.

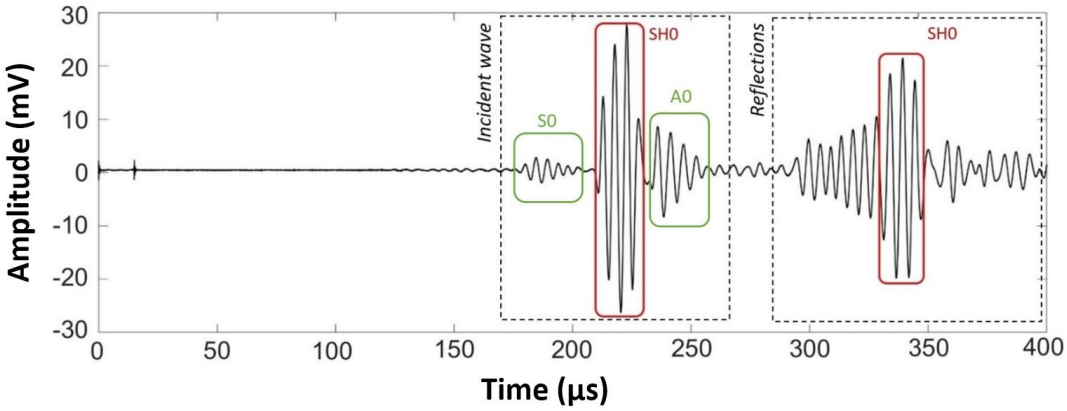

Figure 5.5 Signal response in the time domain, using 200 kHz face-shear transducers

According to the waveform graph, a strong incident and reflective fundamental SH-SAW mode (SH0) was successfully generated among other waveforms, as indicated by the time-of-flight measurements (*speed= distance/ time-of-flight*). No higher SH-SAW modes were generated, which agrees with the dispersion theory of SH-SAWs for frequency-thickness product of 400 kHz mm, as shown in Figure 3.9. Other waveforms as identified include a reflected SH0 mode, a weak S0 Lamb wave and a weak A0 Lamb wave, which agrees with the dispersion theory of Lamb waves for frequency-thickness product of 400 kHz mm, as shown in Figure 3.8.

5.3.2 400 kHz angled SH-SAW transducer

The 400 kHz angled SH-SAW transducers were placed 220mm apart on the steel plate and excited by a 400 kHz, 10 Vpp, 2-cycle sinusoidal pulse using the function generator. The raw signal as it was acquired in the time domain can be seen in Figure 5.6.

The 16.5 µs time delay inside the wedges was taken into consideration in the time-of-flight measurements, in order to obtain the velocity for each wave. According to the waveform graph and time-of-flight, a dominant SH0 mode was generated along with a weak S0 Lamb wave, an A0 lamb wave and the first higher SH1 mode, according to the dispersion theory for frequency-thickness product of 800 kHz mm, as shown in Figure 3.8 and Figure 3.9.

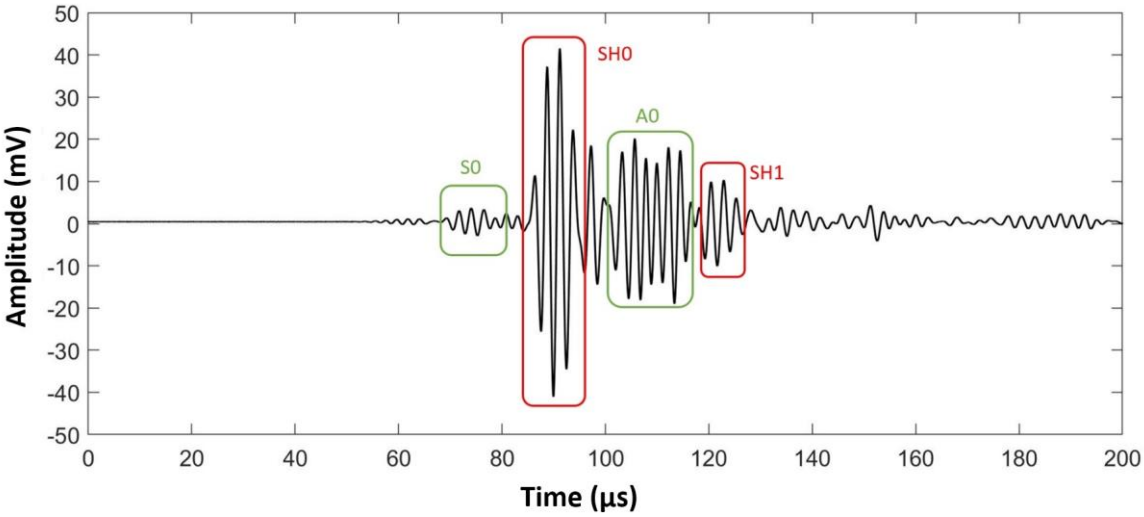

Figure 5.6 Signal response in the time domain, using 400 kHz angled transducers

5.3.3 2 MHz angled SH-SAW transducers

The 2 MHz angled SH-SAW transducers were placed 110 mm apart on the steel plate and excited by a 2 MHz, 10 Vpp, 3-cycle sinusoidal pulse using the function generator. The raw signal as it was acquired in the time domain can be seen in Figure 5.7.

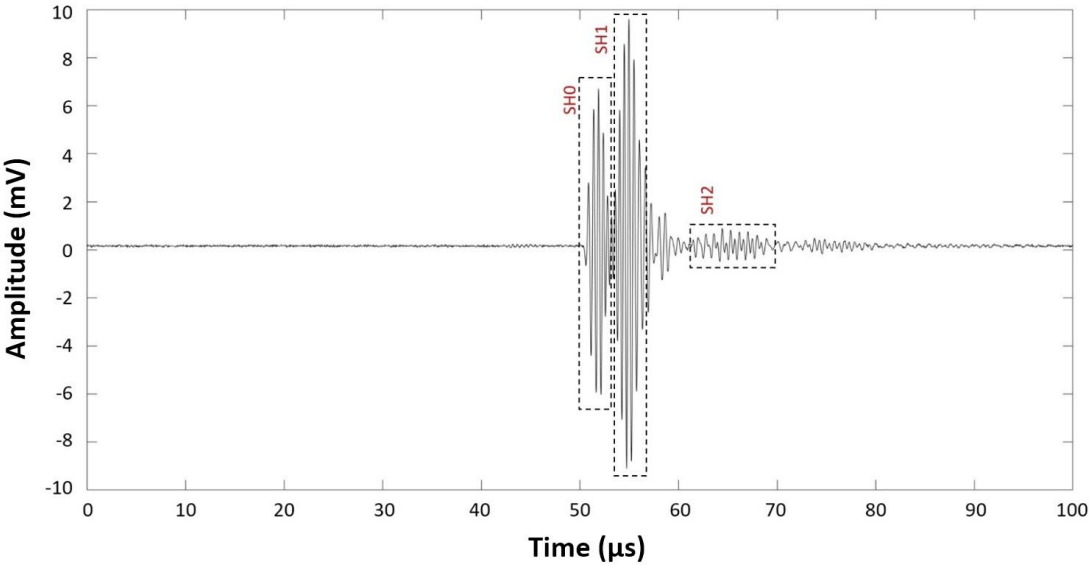

Figure 5.7 Signal response in the time domain, using 2 MHz angled transducers

According to the waveform graph, 3 SH-SAW modes were distinguished according to the wave speed, that agree with the dispersion theory in Figure 3.9, for frequency-thickness product of 4000 kHz mm. Similarly to the 400 kHz angled transducers, the 16.5 µs time delay in the wedges was taken into consideration in the time-of-flight measurements.

5.4 Signal processing

As was seen in the previous section, the signal was acquired with a picoscope or digitizer in the time domain, but further signal processing is required to isolate the SH0 mode from the other waveforms in order to investigate its response through a solid-liquid interface.

After acquisition, the signal was imported in Matlab for processing using customized scripts. As it was seen in the previous sections, the wave speed was obtained from the time domain signal by measuring the time-of-flight. However, the wave amplitude and frequency require further processing to obtain.

Depending on the excitation frequency, number of cycles and time-of-flight, the SH0 mode was extracted from the waveform, as shown in Figure 5.8 for the 2 MHz SH0 mode (from Figure 5.7), generated using the angled transducers. The window was selected to be large enough to include the wave and equal number of points before and after the wave (whenever possible), in order to improve the resolution of the post-processing method.

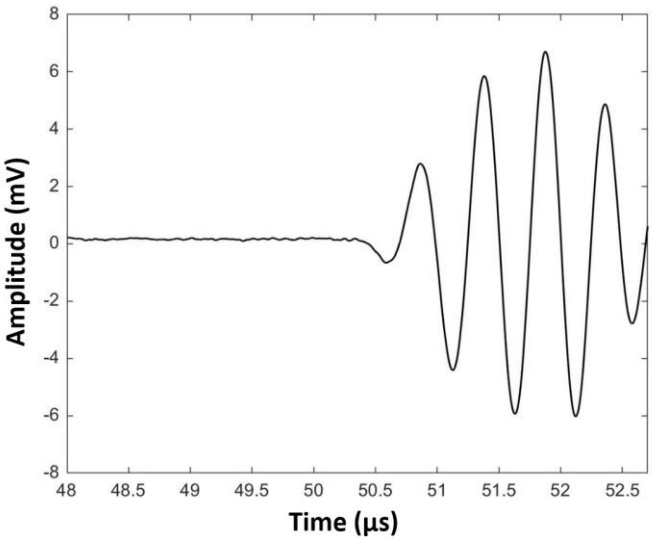

Figure 5.8 2 MHz SH0 mode after being isolated from the waveform

The fast Fourier transform (FFT) was applied after extracting the SH0 mode, to obtain the signal in the frequency domain, as shown in Figure 5.9. From the FFT of the signal, the maximum amplitude of the signal was obtained, along with the frequency it occurred (resonant frequency). Obtaining the wave amplitude and resonant frequency is essential for investigating the attenuation of SH-SAWs at a solid-liquid interface.

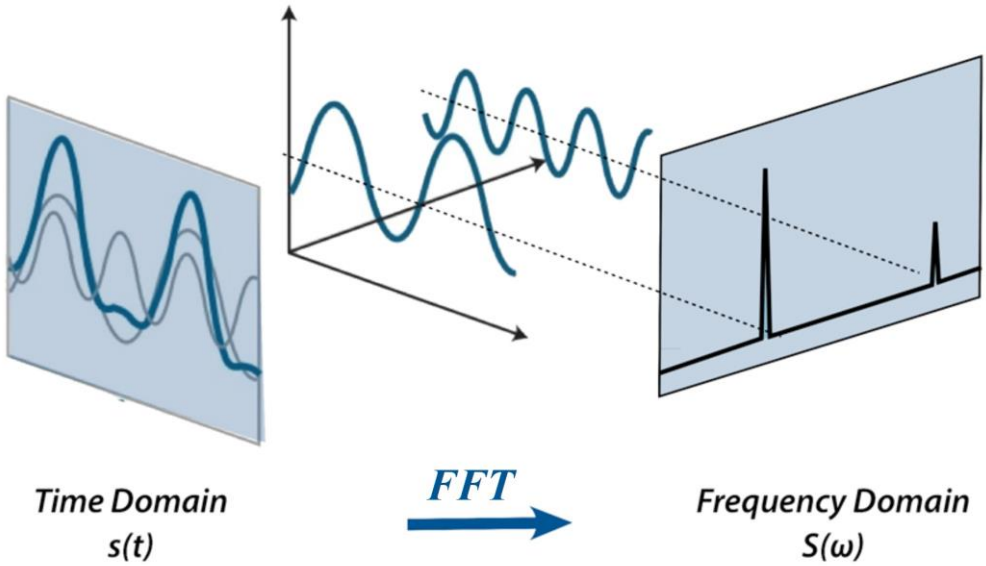

Figure 5.9 Schematic representation of the fast Fourier transform (*FFT*) [72]

An example of the FFT is shown in Figure 5.10, for the 2 MHz SH0 mode. The maximum amplitude and centre frequency of the wave were obtained using custom Matlab scripts.

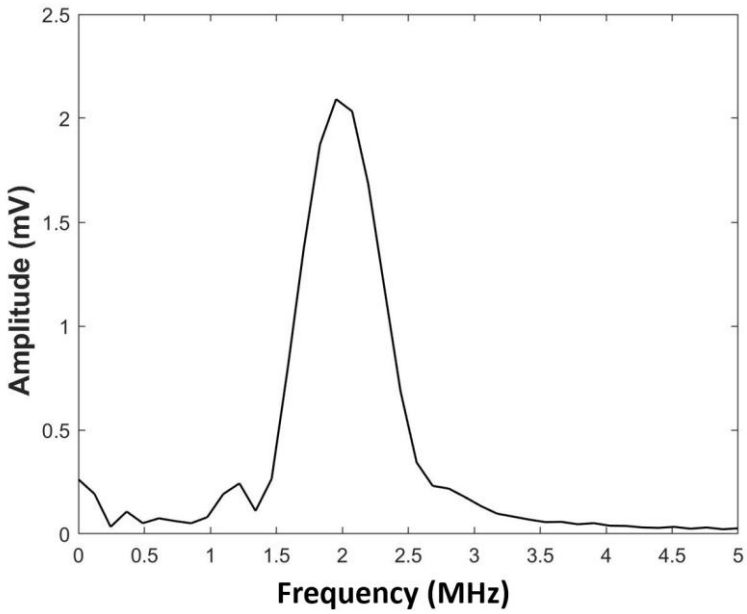

Figure 5.10 Example of the FFT of the 2 MHz SH0 mode (Figure 5.8)

5.5 Conclusions

This chapter has demonstrated the successful generation of SH-SAWs on a steel plate, using face-shear piezo-ceramics and angled transducers. One transducer acting as a

transmitter and a second as a receiver, operating in the pitch-catch mode, were used for sending and receiving SH-SAWs.

According to the results in Section 5.3, the fundamental SH0 mode was always excited, regardless of the type of transducer or the operating frequency. However, the frequency seemed to affect the generation of secondary modes, including higher SH-SAW modes and Lamb wave modes, which found to be in good agreement with the dispersion theory in sub-Section 3.4.3.

Using post-processing tools, the fundamental SH0 mode was extract from the waveform graph, in order to study its propagation properties at a solid-liquid interface, for measuring viscosity of lubricant oil and formation of surface layers. The fast Fourier transform was used on the isolated SH0 mode, to extract its propagation properties, including the wave amplitude and centre frequency.

6 SH-SAW PROPAGATION THROUGH A SOLID-LIQUID INTERFACE

In this chapter, the propagation of SH-SAWs through a solid-liquid interface was investigated both experimentally and numerically, for measuring oil properties.

6.1 SH-SAW propagation

SH-SAWs are free to propagate on the surface of solids, and their amplitude maximizes when the surface is open in the air. Only then, the particles of the medium are free to oscillate back and forth, perpendicularly to the direction the wave propagates (Figure 6.1).

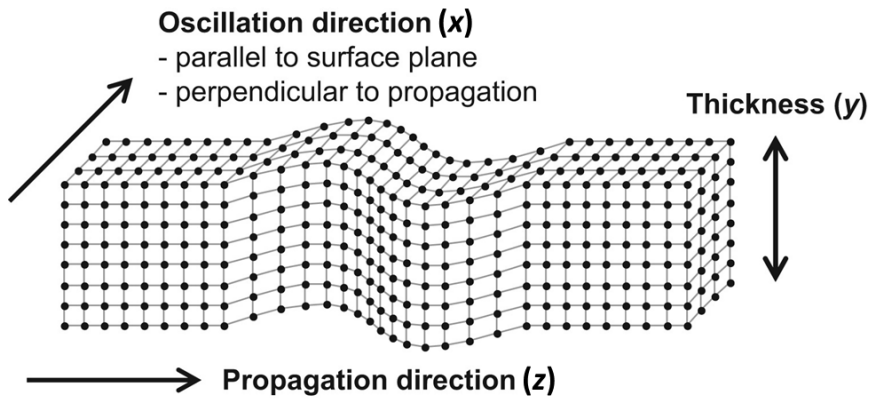

Figure 6.1 SH-SAW propagation and particle movement [42]

When a liquid is deposited on the propagating surface, it acts as a resistor to the shear particle movement, energy is lost, and thus the amplitude of the wave decreases (Figure 6.2). That is called *attenuation due to the viscous properties of a liquid*, and was explored in this work for measuring lubricant viscosity and the formation of surface layers.

Apart from the amplitude decrease at the solid-liquid interface, the wave velocity decreases as the liquid particles resist the wave propagation. In SH-SAW devices when loaded with a liquid, changes in the resonant frequency have been reported, corresponding to the deposited mass on top of the device. However, the velocity decrease and frequency shift may not always occur, as the tested liquid may be too inviscous to reduce the wave velocity or the tested quantity may be insignificant compared to the size of the system, with negligible effect on the resonant frequency. On the other hand, the liquid loading seems to have a more significant effect on the wave attenuation rather than on the velocity or resonant frequency. For this reason more attention was given to the wave attenuation for measuring lubricant properties.

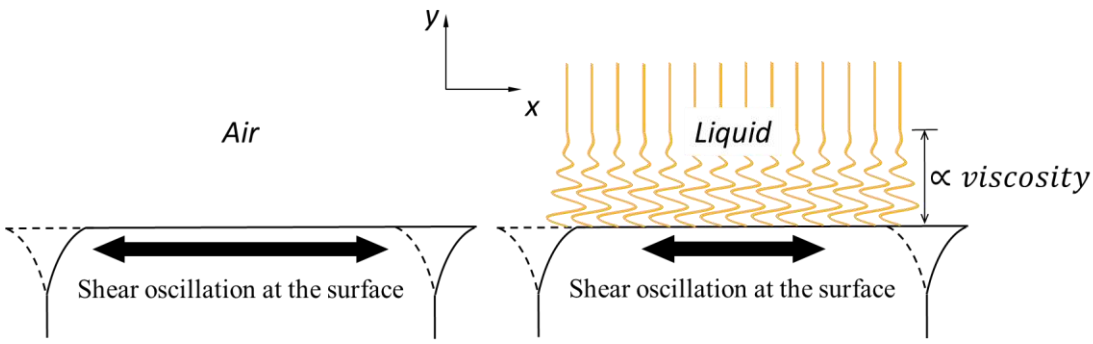

Figure 6.2 SH-SAW attenuation at the solid-liquid interface

6.2 SH-SAW attenuation- liquid viscosity model

By definition, *wave attenuation* is the decrease in the particle oscillation of a wave after it has propagated a distance l in a medium, and it is expressed by Equation 3.1.

$$u_x\,(l) = u_{x_0} e^{-\alpha l} \tag{3.1}$$

According to the attenuation equation, the wave loses energy in the attempt of the medium particles to move their neighbouring particles, hence the amplitude of the particle oscillation decays with distance from the source. For a SH-SAW travelling distance l along the surface of a medium, the particle oscillation is depicted in Figure 6.3.

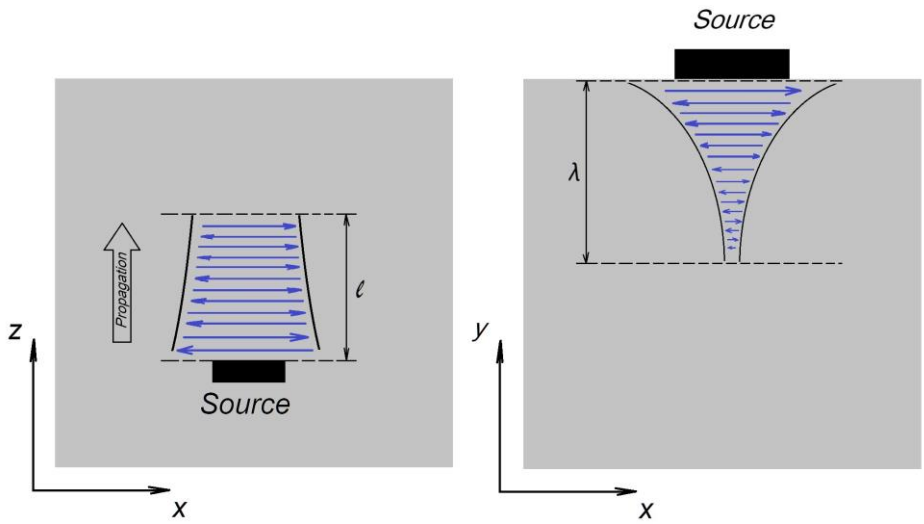

Figure 6.3 SH-SAW attenuation at the solid-air interface, due to the solid material properties

When the medium is coupled with air, the wave attenuates only due to the medium material properties after travelling a distance l, since the resistance offered by air to the solid particle movement can be considered negligible. In this case, the transmission coefficient $T = 1$ as the wave is fully transmitted through the solid-air interface, with negligible energy loss due to the low viscosity of air. However, when a liquid is coupled

with the medium, the wave loses energy due to the liquid viscosity (which is considerably greater than the viscosity of air) and attenuates, which can be seen in Figure 6.4.

In this case, the solid particles at the surface of the medium are no longer free to oscillate, but they lose energy due to the viscous loading. The liquid particles close to the surface follow the solid particle oscillation and transfer the motion to their neighbouring liquid particles up to a certain depth, which is called the penetration depth δ. Due to the viscous coupling, energy is lost and the amplitude of the solid particle oscillation further reduces after travelling the same distance l. The amplitude of the solid particle oscillation reduces in both the z-direction (direction of propagation) and y-direction (thickness of the medium), and the transmission coefficient $T < 1$ since the energy that previously was responsible for moving the solid particles is now consumed in the liquid. This property is very important when the thickness of the medium d is equal or smaller than the wavelength λ ($d \leq \lambda$). In this case, the wave propagates along both surfaces of the medium and changes on one surface can be perceived on the opposite surface. Potentially, SH-SAW transducers could be bonded on the outer surface of an engine bearing, while measuring viscosity at the bearing-oil interface on the opposite surface.

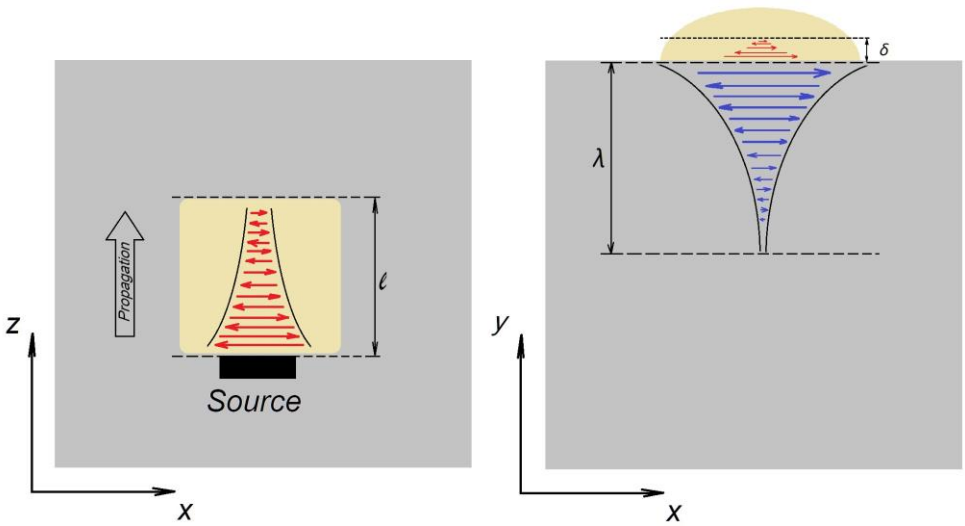

Figure 6.4 SH-SAW attenuation at the solid-liquid interface, due to the solid material properties and liquid viscosity

For the purpose of this study, the medium is considered to be a plate of length l, width b and thickness d which is assumed to be bounded by a viscous liquid in the y-direction only on one side ($\mathrm{y} = d$), while waves are generated on the opposite side ($y = 0$), as shown in Figure 6.5. The waves propagate along z-direction, while the particles oscillate along x-direction which develops shear stresses τ_{xy} inside the liquid.

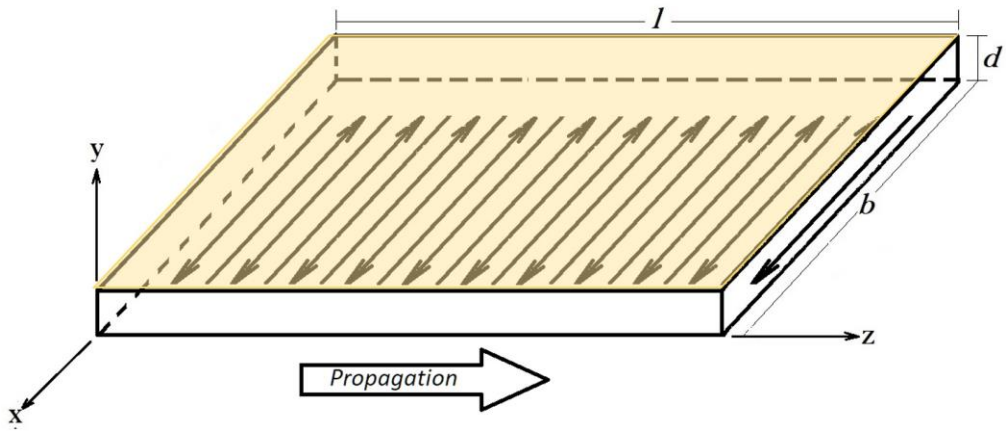

Figure 6.5 Illustration of the arrangement and the coordinates

It is assumed that the liquid is in contact with one face of the plate (xz-plane), and behaves as an incompressible, Newtonian liquid. As such, the constitutive relationship between shear stresses and strains is given by:

$$\tau_{xy} = \eta\, \dot{\gamma}_{xy} \tag{6.1}$$

where τ_{xy} is the shear stress and $\dot{\gamma}_{xy}$ is the shear strain acting in the x-direction on the xz-plane, and η is the liquid dynamic viscosity.

When the particle velocity on the surface (xz-plane) is sufficient that a flow is generated in the liquid, the velocity field in the liquid can be described by $v = v_x(y, z, t)\hat{x}$. This relation, in addition to Equation 6.1 and the Navier-Stokes conservation of momentum $\nabla \cdot \tau = \rho_l\, \dot{v}$ [45], leads to:

$$\nabla \cdot (\eta\, \dot{\gamma}_{xy}) = \rho_l\, \dot{v}_x$$

where ρ_l is the liquid density and $\dot{\gamma}_{xy} = \nabla v_x$ is the velocity gradient.

$$\eta(\nabla \cdot \nabla v_x) = \rho_l\, \dot{v}_x$$

Replacing the divergence ($\nabla \cdot$) of the gradient (∇v_x) with the Laplace operator Δ, leads to:

$$\eta(\Delta v_x) = \rho_l\, \dot{v}_x$$

Expanding the term $\Delta v_x = \frac{\partial^2 v_x}{\partial y^2} + \frac{\partial^2 v_x}{\partial z^2}$ gives:

$$\eta\left(\frac{\partial^2 v_x}{\partial y^2} + \frac{\partial^2 v_x}{\partial z^2}\right) = \rho_l \dot{v}_x \tag{6.2}$$

Invoking non-slip boundary condition at the solid-liquid interface, the wave solution to Equation 6.2 has the form [73] [74]:

$$v_x(y, z, t) = v_{x0} e^{-\alpha y} e^{i(\omega t - \beta_0 z)} \tag{6.3}$$

where v_{x0} is the maximum particle velocity, $\beta_0 = \omega/c$ is the wavenumber, ω is the angular frequency of the SH-SAW, c is the wave velocity and α is the attenuation coefficient. Substituting Equation 6.3 in 6.2, returns:

$$\eta\left[\frac{\partial^2}{\partial y^2}\left(v_{x0}e^{-\alpha y}e^{i(\omega t-\beta_0 z)}\right)+\frac{\partial^2}{\partial z^2}\left(v_{x0}e^{-\alpha y}e^{i(\omega t-\beta_0 z)}\right)\right]=\rho_l\frac{\partial}{\partial t}\left(v_{x0}e^{-\alpha y}e^{i(\omega t-\beta_0 z)}\right)$$

Which simplifies to:

$$\eta\left(\alpha^2-{\beta_0}^2\right)v_x = i\rho_l\omega v_x \tag{6.4}$$

Rearranging, gives the attenuation coefficient:

$$\alpha^2 = \left(\frac{\omega}{c}\right)^2 + i\frac{\rho_l\omega}{\eta} \tag{6.5}$$

For a Newtonian regime, $\left(\frac{\omega}{c}\right)^2 \ll \frac{\rho_l\omega}{\eta}$ so that the imaginary component dominates in Equation 6.5, giving:

$$\alpha^2 = i\frac{\rho_l}{\eta}\omega \tag{6.6}$$

Solving Equation 6.6, results in the following expression for the attenuation coefficient α:

$$\alpha = \sqrt{i\frac{\rho_l\omega}{\eta}} = \sqrt{i}\sqrt{\frac{\rho_l\omega}{\eta}} = \pm\left(\frac{1}{\sqrt{2}}+i\frac{1}{\sqrt{2}}\right)\sqrt{\frac{\rho_l\omega}{\eta}}$$

$$\alpha = \pm\left(\sqrt{\frac{\rho_l\omega}{2\eta}}+i\sqrt{\frac{\rho_l\omega}{2\eta}}\right)$$

$$\alpha = -\sqrt{\frac{\rho_l\omega}{2\eta}}-i\sqrt{\frac{\rho_l\omega}{2\eta}} \tag{6.7}$$

In Equation 6.7, the negative sign is used, to represent the effect of attenuation (wave amplitude decrease, thus energy loss).

Noting that the shear strain can be expressed as the ratio of the liquid speed in the direction normal to the plate:

$$\dot{\gamma}_{xy} = \frac{\partial v_x}{\partial y} = \frac{\partial}{\partial y}\left(v_{x0}e^{-\alpha y}e^{i(\omega t-\beta_0 z)}\right) = -\alpha v_x \tag{6.8}$$

Substituting Equation 6.8 into 6.1, the shear stresses applied by the solid in driving the liquid to oscillate, can be found by:

$$\tau_{xy} = -\eta\alpha v_x \tag{6.9}$$

The coupling between the solid and the viscous liquid leads to wave power loss across the interface as can be seen in Figure 6.6, which can be defined as:

$$P_l = v_x\, F_{xy} = v_x\, \tau_{xy}\, bl \tag{6.10}$$

After replacing τ_{xy} with the expression from Equation 6.9, becomes:

$$P_l = -\eta\alpha {v_x}^2 bl \tag{6.11}$$

where P_l is the *wave power loss* in the liquid due to the viscosity and bl is the area of contact (*solid-liquid interface*).

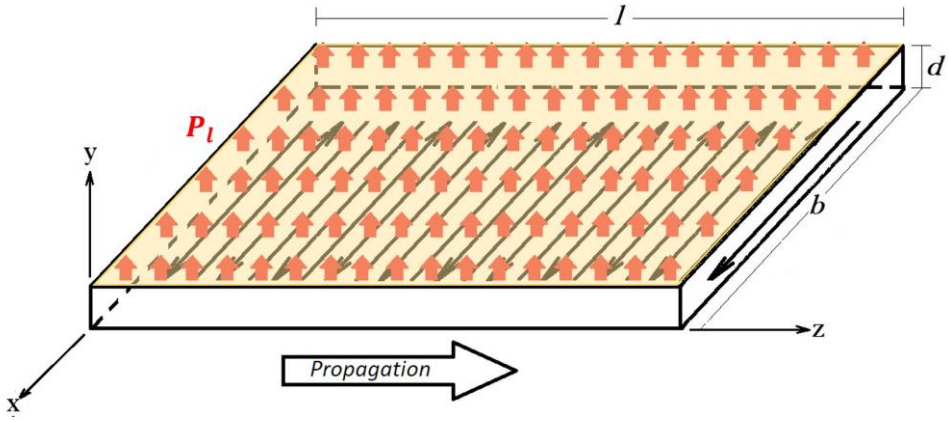

Figure 6.6 Wave power loss P_l at the solid-liquid interface

Similarly, the wave power in the solid is given by Equation 6.12:

$$P_s = v_x\, F_{xy} = v_x\, \tau_{xy}\, bd = Z_s v_x^2\, bd \tag{6.12}$$

Where $Z_s = \rho_s c_s$ is the acoustic impedance of the solid, ρ_s is the density of the solid, c_s is the fundamental SHo mode velocity in the solid and bd is the plane normal to the power flow (Figure 6.7).

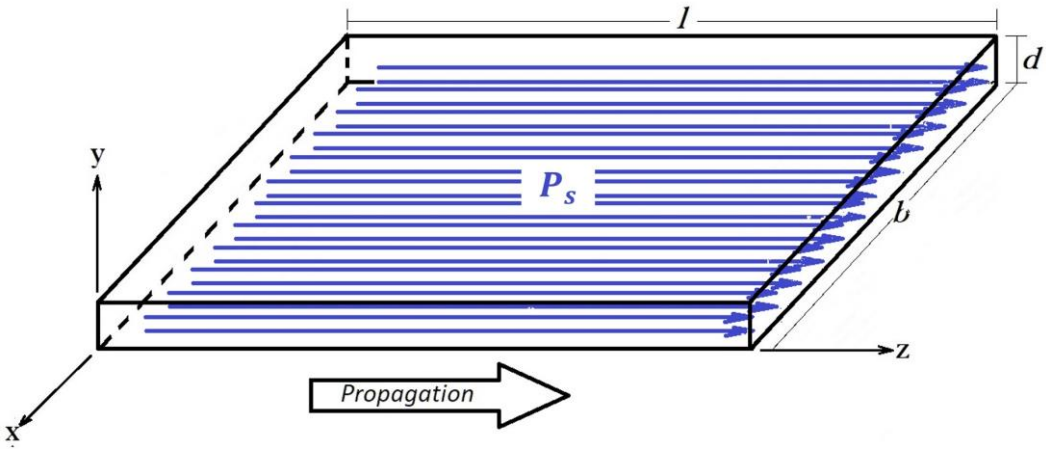

Figure 6.7 Wave power in the solid

Conservation of energy requires the wave power lost in the liquid P_l, to be balanced by a change in the wave power inside the solid ΔP_s (Figure 6.8):

$$P_l = P_s^{air} - P_s^{liquid} \tag{6.13}$$

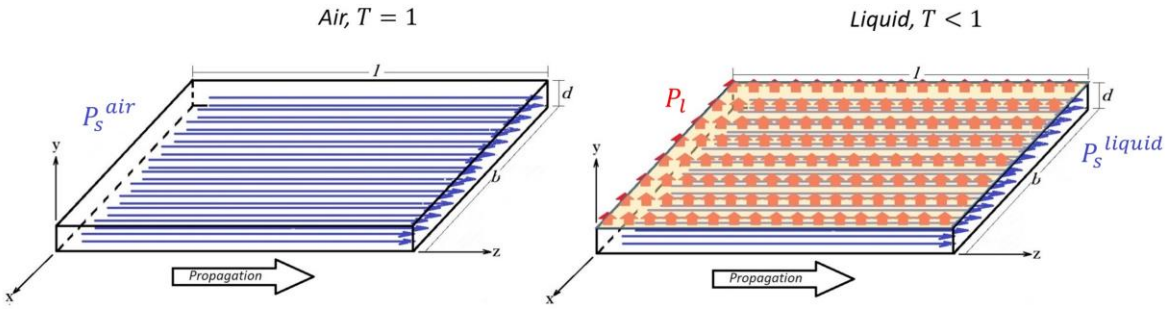

Figure 6.8 Power flow at the solid-air (*left*) and solid-liquid (*right*) interfaces

where P_s^{air}, $P_s^{liquid}$is the *wave power* in the solid when coupled with air and a liquid, respectively. Considering that the wave power in the solid P_s flows along both z-direction and y-direction, Equation 6.13 can be written as:

$$P_l = \left(\frac{\partial P_s^{air}}{\partial z} + \frac{\partial P_s^{air}}{\partial y}\right) - \left(\frac{\partial P_s^{liquid}}{\partial z} + \frac{\partial P_s^{liquid}}{\partial y}\right) \tag{6.14}$$

Replacing Equation 6.12 in 6.14 leads to:

$$P_l = \left(\frac{\partial}{\partial z}(\rho_s c_s v_x^2\ bd)^{air} + \frac{\partial}{\partial y}(\rho_s c_s v_x^2\ bd)^{air}\right)$$
$$- \left(\frac{\partial}{\partial z}(\rho_s c_s v_x^2\ bd)^{liquid} + \frac{\partial}{\partial y}(\rho_s c_s v_x^2\ bd)^{liquid}\right) \tag{6.15}$$

Only the particle velocity v_x is a function of z and y, so Equation 6.15 can be written:

$$P_l = \rho_s c_s bd\left[\left(\frac{\partial}{\partial z}(v_x^2)^{air} + \frac{\partial}{\partial y}(v_x^2)^{air}\right) - \left(\frac{\partial}{\partial z}(v_x^2)^{liquid} + \frac{\partial}{\partial y}(v_x^2)^{liquid}\right)\right]$$

Substituting v_x with Equation 6.3, leads to:

$$P_l = \rho_s c_s bd\left[\left(\frac{\partial}{\partial z}\left({v_{x0}}^2 e^{-2\alpha y} e^{2i(\omega t - \beta_0 z)}\right)^{air} + \frac{\partial}{\partial y}\left({v_{x0}}^2 e^{-2\alpha y} e^{2i(\omega t - \beta_0 z)}\right)^{air}\right)\right.$$
$$\left. - \left(\frac{\partial}{\partial z}\left({v_{x0}}^2 e^{-2\alpha y} e^{2i(\omega t - \beta_0 z)}\right)^{liquid} + \frac{\partial}{\partial y}\left({v_{x0}}^2 e^{-2\alpha y} e^{2i(\omega t - \beta_0 z)}\right)^{liquid}\right)\right]$$

Differentiating with respect to z and y, leads to:

$$P_l = \rho_s c_s bd\left[\left(-i2\beta_0^{air} v_x^2 - 2\alpha^{air} v_x^2\right) - \left(-i2\beta_0^{liquid} v_x^2 - 2\alpha^{liquid} v_x^2\right)\right]$$

Which simplifies to:

$$P_l = \rho_s c_s v_x^2 bd\left[\left(i2\beta_0^{liquid} - i2\beta_0^{air}\right) - \left(2\alpha^{air} - 2\alpha^{liquid}\right)\right]$$

Replacing $\beta_0 = \omega/c$ and $P_s = \rho_s c_s v_x^2\ bd$, leads to:

$$P_l = P_s\left[2i\left(\frac{\omega}{c_s^{liquid}} - \frac{\omega}{c_s^{air}}\right) + \left(2\alpha^{liquid} - 2\alpha^{air}\right)\right]$$

Rearranging the imaginary term in the equation, returns:

$$P_l = P_s\left(2\Delta\alpha + i2\frac{\omega\Delta c_s}{c_s^{air}c_s^{liquid}}\right) \tag{6.16}$$

where $\Delta\alpha$ reflects the decrease in the solid particle displacement and $\frac{\omega\Delta c_s}{c_s^{air}c_s^{liquid}}$ the decrease of the wave velocity, due to the viscous coupling, respectively.

Substituting Equation 6.11 in 6.16, the expression for the wave power loss at the solid-liquid interface becomes:

$$P_s\left(2\Delta\alpha + i2\frac{\omega\Delta c_s}{c_s^{air}c_s^{liquid}}\right) = -\eta\alpha {v_x}^2 bl$$

Expanding the term P_s and replacing α from Equation 6.7, leads to:

$$\left(2\Delta\alpha + i2\frac{\omega\Delta c_s}{c_s^{air}c_s^{liquid}}\right)\rho_s c_s v_x^2\, bd = -\eta {v_x}^2 bl\left(-\sqrt{\frac{\rho_l\omega}{2\eta}} - i\sqrt{\frac{\rho_l\omega}{2\eta}}\right)$$

Which simplifies to:

$$\left(2\Delta\alpha + i2\frac{\omega\Delta c_s}{c_s^{air}c_s^{liquid}}\right) = \frac{l}{2d}\frac{1}{\rho_s c_s^{air}}\left(\sqrt{\frac{\rho_l\omega}{2\eta}} + i\sqrt{\frac{\rho_l\omega}{2\eta}}\right) \tag{6.17}$$

Separating the real and imaginary components in Equation 6.17, leads to the following two expressions:

$$\Delta\alpha = \frac{1}{2d}\frac{\sqrt{\frac{\eta\rho_l\omega}{2}}}{Z_s} \tag{6.18}$$

$$\frac{c_s^{air} - c_s^{liquid}}{c_s^{liquid}} = \frac{1}{2d}\frac{\sqrt{\frac{\eta\rho_l\omega}{2}}}{\omega\rho_s} \tag{6.19}$$

where $\Delta\alpha$ and $\Delta c_s/c_s^{liquid}$ are the *attenuation coefficient* measured in (m^{-1}) and *velocity change coefficient* due to the viscous coupling, respectively.

On the other hand, the attenuation of an SH-SAW travelling distance $z = l$, for the solid-air and solid-liquid interfaces, is given by:

$${u_x}^{air}(z = l) = u_{x_0}e^{-a_{air}l} \tag{6.20}$$

$${u_x}^{liquid}(z = l) = u_{x_0}e^{-a_{liquid}l} \tag{6.21}$$

where u_{x_0} is the amplitude at zero distance from the source (z= 0) and l is the liquid path-length.

Dividing Equations 6.20 and6.21, leads to:

$$\frac{u_x{}^{liquid}}{u_x{}^{air}} = e^{-(a_{liquid}-a_{air})l}$$

Which simplifies to:

$$\ln(T) = -\Delta\alpha\, l$$

And leads to the following expression for the attenuation $\Delta\alpha$:

$$\Delta\alpha = \frac{1}{l} ln\left(\frac{1}{T}\right) \tag{6.22}$$

where $T = \frac{u_x{}^{liquid}}{u_x{}^{air}}$ is the transmission coefficient and can be determined experimentally.

Combining Equation 6.18 and 6.22, the attenuation of SH-SAWs over a distance l due to the viscous properties of a liquid, is given by:

$$ln\left(\frac{1}{T}\right) = \frac{l}{2d}\frac{\sqrt{\frac{\eta\rho_l\omega}{2}}}{Z_s} \tag{6.23}$$

Solving the Equation 6.23 with respect to the viscosity η, becomes:

$$\eta = 2\frac{\left[ln\left(\frac{1}{T}\right)2d_sZ_s\right]^2}{\rho_l\omega\, l^2} \tag{6.24}$$

where the subscripts l and s represent the liquid and the solid, respectively. The relationship between transmission coefficient T and viscosity η can be visualised in Figure 6.9, for different solid media Z_s, wave frequency ω, liquid path length l and medium thickness d_s, while the liquid density ρ_l= 900 kg/m^3 remained constant.

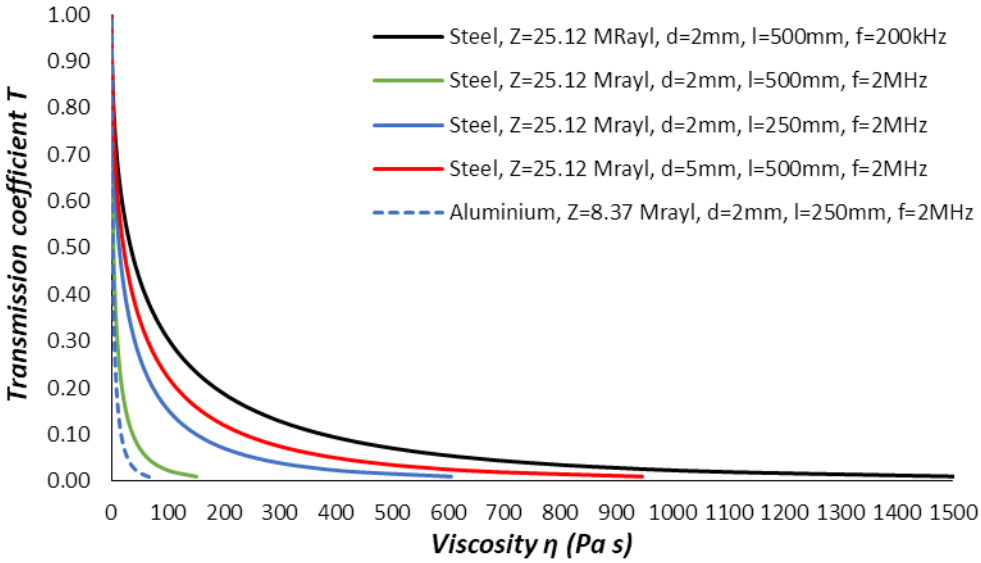

Figure 6.9 Viscosity- transmission coefficient relationship

The transmission coefficient can be calculated from Equation 6.24, after solving with respect to T.

$$T = e^{-\frac{l}{2d}\frac{\sqrt{\frac{\eta\rho_l\omega}{2}}}{Z_s}} \tag{6.25}$$

Each term in Equation 6.25 was studied individually, to investigate their effect on the transmission coefficient. The transmission coefficient was determined both experimentally, $T = {u_x}^{liquid}/{u_x}^{air}$ and using Equation 6.25. The results from this investigation are presented in the following sections.

6.3 The effect of liquid viscosity η and path length l

To investigate the effect of viscous loading on the free surface where a SH-SAW propagates, three Cannon viscosity standard lubricants were tested, the properties of which are given on Table 6.1 [75]. The Cannon viscosity standards are hydrocarbon oils and most them are Newtonian liquids. However, high shear rates may cause "viscous heating" which lowers the oils' viscosities and thus may appear as non-Newtonian liquids.

The 200 kHz SH-SAW transducers were used for the purpose of this study, bonded on a 1000 mm x 700 mm x 2 mm aluminium plate, 650 mm apart. 1.0 ml of lubricant sample was deposited with a pipette equally distant between the transducers and covered with a Perspex plate to control how the samples spread (Figure 6.10). The signal was captured after the samples have covered 80, 100, 120 and 140 mm on the aluminium plate.

The experimental values for the transmission coefficient were then compared to the transmission coefficient as it was calculated using Equation 6.25.

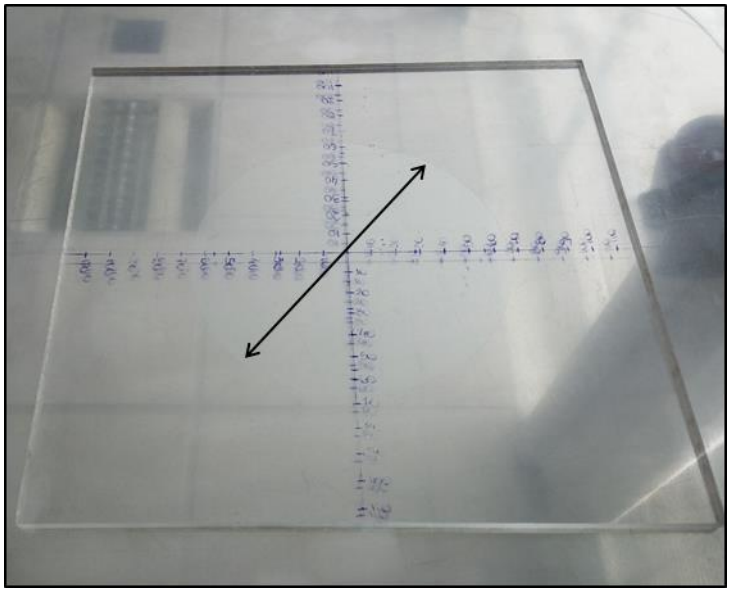

Figure 6.10 Lubricant sample spreads between the Perspex and aluminium plates

Table 6.1 Cannon viscosity standard lubricant properties at 25 °C [75]

Sample	Dynamic viscosity (cP)	Density (kg/m³)
S60	104	873
S200	340	837
S600	1100	844

Figure 6.11 shows, the transmission coefficients as they were measured experimentally, $T = {u_x}^{liquid}/{u_x}^{air}$ and using Equation 6.25. The results were found to be in good agreement for the three samples over various liquid path lengths.

SH-SAWs lose energy due to the viscosity of the liquid; the transmission coefficient decreases as the viscosity increases, at any given distance.

The transmission coefficient decreases as the liquid path length increases, for each sample. Any liquid deposited on the free surface acts as a resistor to the particle movement. Since more liquid particles engage with the free surface, this is more wave attenuation and thus the transmission coefficient will decrease.

Lastly, the results seem to be very consistent as indicated by the small error bars (+/- standard deviation).

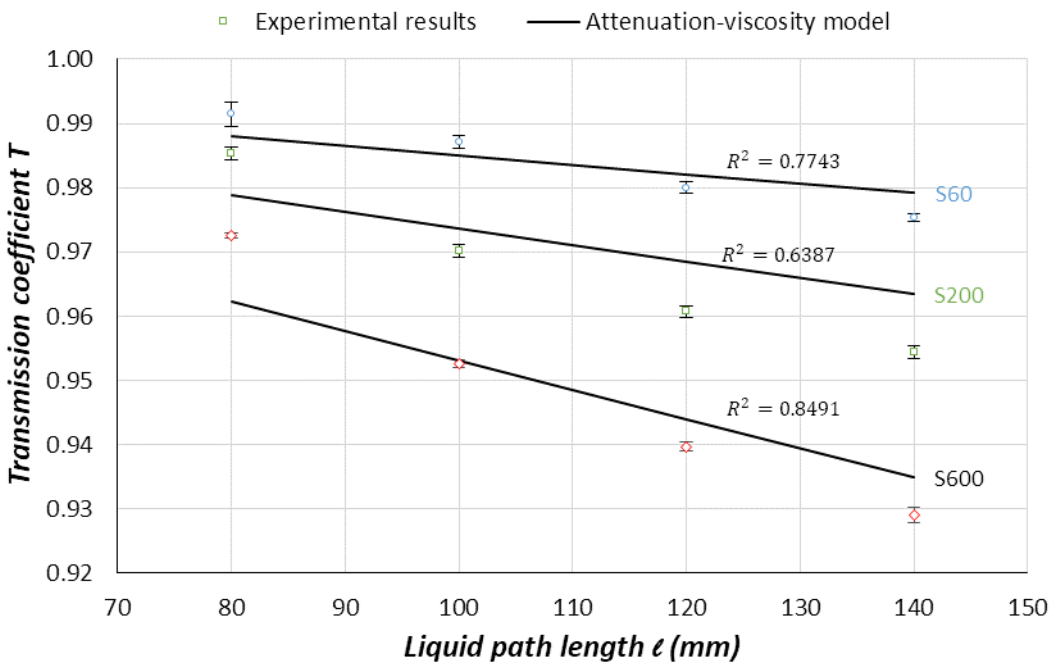

Figure 6.11 Transmission coefficient decrease with liquid viscosity and path length

The attenuation of SH-SAWs through an oil film is a function of the oil viscosity and its spreading distance or path length. However, when a certain amount of lubricant spreads, apart from occupying larger area on the free surface, it also decreases in film thickness h. The effect of the oil film thickness on the SH-SAW transmission is presented in the next section.

6.4 The effect of the liquid film thickness h

In order to investigate whether the wave attenuation was due to the increase of the lubricant path length or decrease of its film thickness h, the experiment was repeated for 0.5 ml of lubricant samples. Half the amount of sample spread over the same distance leads to half film thickness. If the wave attenuation is independent of the oil film thickness and depends only on the viscosity and path length, the values for the transmission coefficient should match the previous values.

According to Figure 6.12, there is an excellent match between the 1.0 ml and 0.5 ml of samples for the S60 and S200, for any given path length, indicating that the wave attenuation is independent of the film thickness.

However, for the S600 it seems that the transmission coefficient values for the 0.5 ml sample match those for the 1.0 ml sample, only for the 80 mm and 100 mm of liquid path length and keep decreasing as the path length increases (film thickness decreases).

Apparently, there is no clear conclusion from this experiment, and further investigation is required to answer whether the wave attenuation is independent of the film thickness, which is shown in the next section.

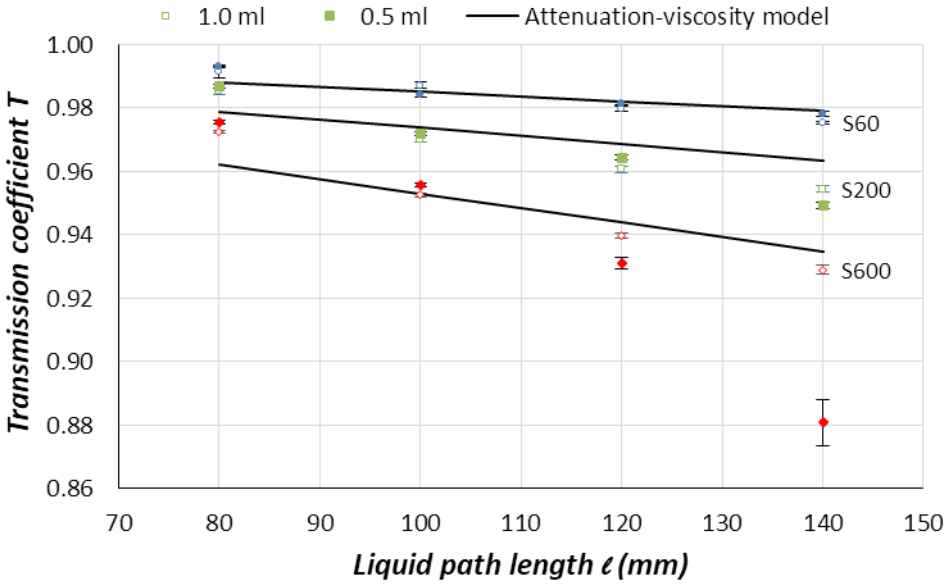

Figure 6.12 Transmission coefficient decrease for 1.0 ml and 0.5 ml of oil samples

6.5 The effect of penetration depth δ

Physically, the propagation of a wave inside a solid or along its surface, is achieved by energy transferred from one particle to its neighbouring particles and so on. In the case of a liquid in contact with the oscillating surface, the energy is transferred to the liquid particles as well, where slowly gets lost due to the liquid viscosity. The SH-SAW penetration depth, is a function of the liquid viscosity, its density and the angular frequency of the SH-SAW oscillation [76]. The penetration depth is described by Equation 6.26 and can be calculated for each sample individually.

$$\delta = \sqrt{\frac{2\eta}{\omega\rho}} \tag{6.26}$$

Table 6.2 presents the SH-SAW penetration depth δ inside each of the lubricant samples and Table 6.3 presents the oil film thickness h for the 1.0 ml and 0.5 ml samples over 80, 100, 120 and 140 mm of liquid path length l. The oil film thickness h can be calculated using the following equation:

$$h = \frac{4V}{\pi l^2} \tag{6.27}$$

where V is the volume of the deposited sample (known).

Table 6.2 200 kHz SH-SAW penetration depth in the Cannon standard lubricants

Sample	Dynamic viscosity (*cP*)	Density (kg/m^3)	Penetration depth (*μm*)
S60	104	873	13.77
S200	340	837	25.43
S600	1100	844	42.83

Table 6.3 Oil film thickness for 1.0 ml and 0.5 ml oil samples over different path lengths

Path length *ℓ*	80 mm	100 mm	120 mm	140 mm
h for 1.0 ml	198 μm	127 μm	88.4 μm	65 μm
h for 0.5 ml	99 μm	63.5 μm	44.2 μm	32.5 μm

According to Table 6.2 and Table 6.3, the oil film thicknesses are always greater than the SH-SAW penetration depth inside the samples, but for the S600 at 120 and 140 mm of path length, it looks like the SH-SAW penetration depth is equal or greater than the oil film thickness.

Physically, when the SH-SAW penetration depth is equal or greater than the liquid film thickness, the liquid is subjected to the SH-SAW oscillation throughout its thickness. When the liquid is in contact with a solid on the one end, and it is open in the air on its other end, the transmission coefficient should decrease only due to the liquid viscosity and the liquid path length. However, when the liquid is sandwiched between two solids and it is excited throughout its thickness, the liquid particles attempt to move the second solid too, which leads to the extra energy loss, as shown in Figure 6.13. In this case, the transmission coefficient should be a function of the liquid path length l, its viscosity η, as well as the resistance the second solid offers to the liquid particle movement.

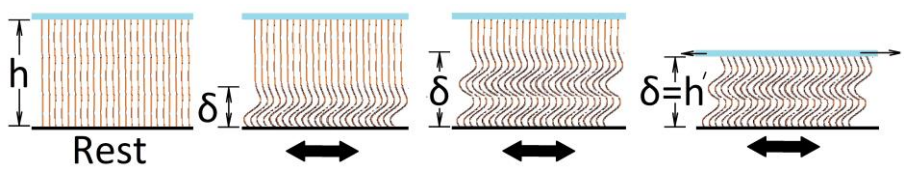

Figure 6.13 SH-SAW penetration depth and liquid film thickness

To validate this hypothesis, the S200 and S600 lubricants were tested further. In order to vary the oil film thickness, 0.2 ml, 0.5 ml, 1.0 ml and 2.0 ml of sample were covered with the Perspex plate to spread over 100 mm of path length. The oil film thickness was calculated using Equation 6.27.

The results of this experiment can be seen in Figure 6.14. According to the graph, when the oil film thickness is greater than the SH-SAW penetration depth (*dashed lines*), the wave attenuates only due to the oil viscosity; since the path length is constant, and it is independent of the oil film thickness. However, when the penetration depth is equal (*in the case of S200*) or greater (*in the case of S600*) than the oil film thickness, the wave attenuates even more, leading to the conclusion that the extra energy loss comes from the Perspex cover plate in the attempt of the oil particles to move it.

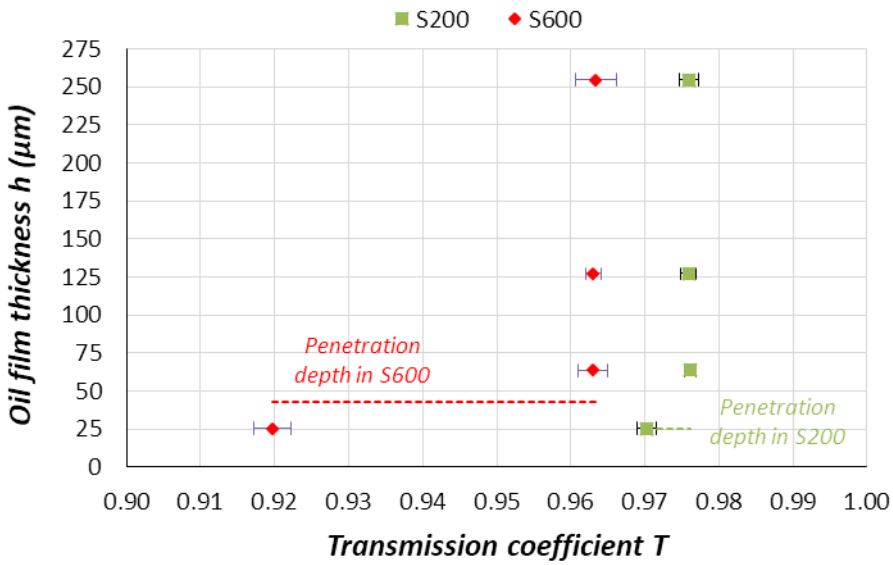

Figure 6.14 SH-SAW penetration depth in a liquid film

The SH-SAWs can transmit through an oil film, but they lose energy. The energy loss is a function of the oil viscosity and the oil path length and independent of the oil film thickness, as it was proved experimentally. However, the oil film thickness needs to be taken in to consideration when it is smaller or equal than the SH-SAW penetration depth, especially in applications where the oil is used to protect two interacting surfaces. At a *solid-liquid-solid* interface the wave loses energy due to the interaction with the second solid through the oil film, when the thickness of the latter is equal or smaller than the wave penetration depth. In any other case, the energy loss should only be a function of the liquid viscosity and the liquid path length.

6.6 The effect of the solid material

Another parameter that affects the transmission coefficient, as it is shown in Equation 6.25, is the acoustic impedance of the solid Z_s. Acoustically softer materials are preferred over harder, as they present lower acoustic mismatch with most liquids, as it was explained in Section 3.4.2.

To investigate the effect of acoustic impedance and hence the material of the medium on the SH-SAW transmittance, tests were carried out on both a 1000mm x 700 mm x 2 mm aluminium plate and a 1000mm x 700mm x 2mm steel plate in contact with a liquid, the properties of which are given on Table 6.4. The 200 kHz sensors were used to excite the fundamental SH-SAW mode on both plates, and a PAO 4 (polyalphaolefin) provided by Lubrizol Ltd., served as the test liquid.

The sample was deposited inside a rubber ring of 100 mm diameter (100 mm path length) bonded on the metal plates, to prevent the sample from leaking and allow uniform spreading. The results from the material investigation can be seen in Figure 6.15.

Table 6.4 Acoustic impedance of materials [77]

Material	**Viscosity (*cP*)**	**Density *(kg/m³)***	**Longitudinal velocity *(m/s)***	**Acoustic impedance *(MRayl)***
Aluminium	-	2700	6370	17.2
Steel	-	7850	5870	46.08
PAO 4	26.2 (25 °C)	900	1460	1.3

According to the graph, there is an excellent agreement between the experimental and predicted values for the transmission coefficient of PAO 4 on both the aluminium and steel plates. As it can be seen, aluminium presents better sensitivity than steel due to the lower acoustic mismatch with the tested liquid, as indicated through the increased transmission losses. For time < 10 sec, the transmission coefficient increased and after time > 10 sec it stabilised. This more likely occurred due to temperature difference between the metal plates and the oil sample.

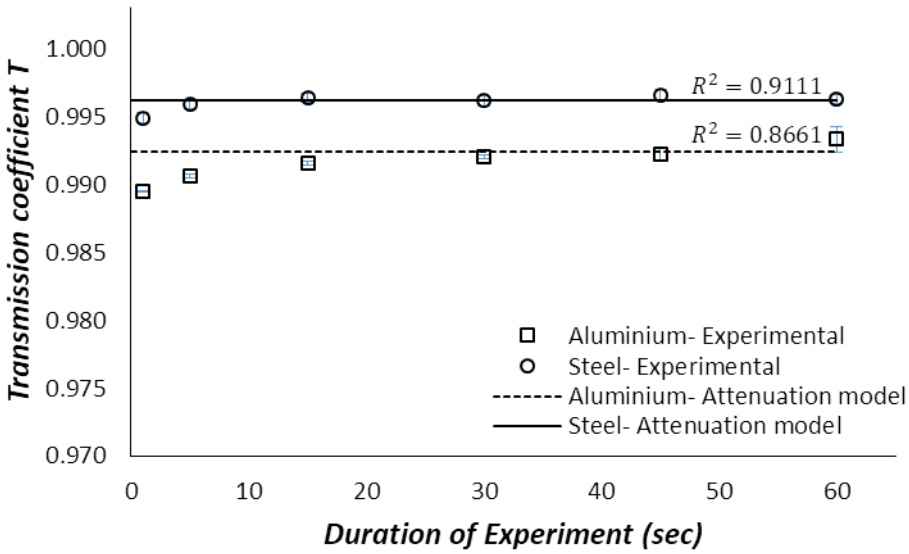

Figure 6.15 Acoustic impedance effect on SH-SAW sensitivity

6.7 The effect of the thickness of the medium d

The thickness of the propagating medium affects the propagation of SH-SAWs. In thin media $d < \lambda$, the wave energy is concentrated uniformly in more confined space, which leads to the existence of the fundamental SH0 mode that propagates along both surfaces of the medium. In any other case, the wave energy is concentrated closer to the surface of the source, and decays as it moves away from it. That often leads to perturbation of the particle movement inside the medium and other SH-SAW modes appear. These other modes can be distinguished from the fundamental mode from the velocity difference, as they propagate either faster or slower than the latter.

In order to explore the effect of the medium thickness on the SH-SAW sensitivity, two steel plates of different thicknesses were tested, a 2 mm thick steel plate and a 0.4 mm thick one, for comparison. The amplitude of the signal was monitored and captured, as an indication of the wave energy magnitude. The 2 MHz angled transducers were used for this experiment, bonded on the steel plates 140 mm apart.

As mentioned above, when the thickness of the medium exceeds the wavelength, other SH-SAW modes appear, apart from the fundamental. Table 6.5 presents the wave velocity in steel, the frequency and corresponding wavelength, along with the medium thickness and number of expected SH-SAW modes. The ratio of the medium thickness over the wavelength, after rounded up, returns the number of SH-SAW modes [45].

Table 6.5 Number of SH-SAW modes on 0.4 and 2.0 mm thick plates

Steel	Velocity c	Frequency f	Wavelength $\left(\lambda = {}^{c}/_{f}\right)$	No. of SH-SAW modes $\left(\frac{Thickness}{Wavelength}\right)$
0.4 mm	3200 m/s	2 MHz	1.6 mm	1
2.0 mm				2

The two signals can be seen in Figure 6.16. In both media, the fundamental SH0 mode was successfully generated, according to the time-of-flight measurements.

As it can be seen from the graphs, the wave amplitude and hence the energy concentration, is greater on the 0.4 mm steel plate as expected. It appears that apart from the fundamental SH0 mode, another mode appears on the 2 mm steel plate, which agrees with Table 6.5.

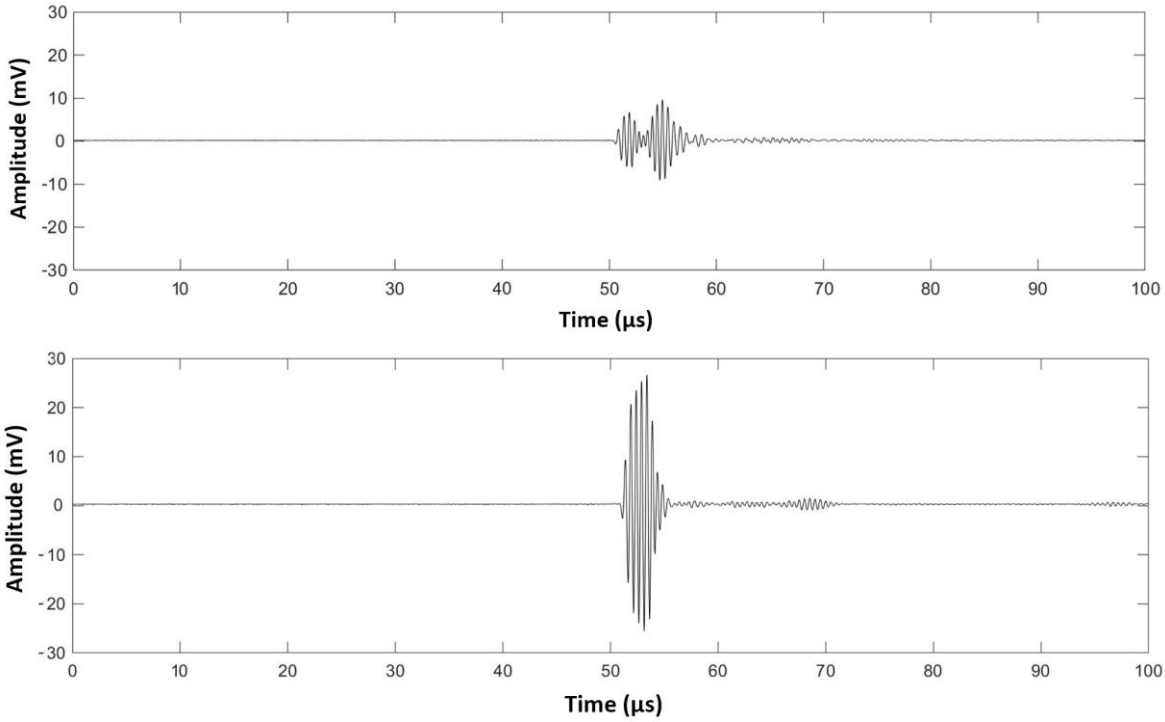

Figure 6.16 SH-SAW amplitude on a 2 mm thick *(top)*, and 0.4 mm thick *(bottom)* steel plates

6.8 The effect of angular frequency ω

Finally, to test the SH-SAW sensitivity at different frequencies, a 0.4 mm thick steel plate was used, along with the 400 kHz and 2 MHz angled transducers. The PAO 4 was used as the test liquid, to investigate where the energy loss is maximised. In Figure 6.17, at higher

frequency more energy is lost, as indicated by the drop in the transmission coefficient, as the particles oscillate faster and closer to the surface of the source.

It is worth mentioning here that the gradients that appear on the 2 MHz and 400 kHz curves represent the sample deposition and spreading, before the samples have reached equilibrium inside the container.

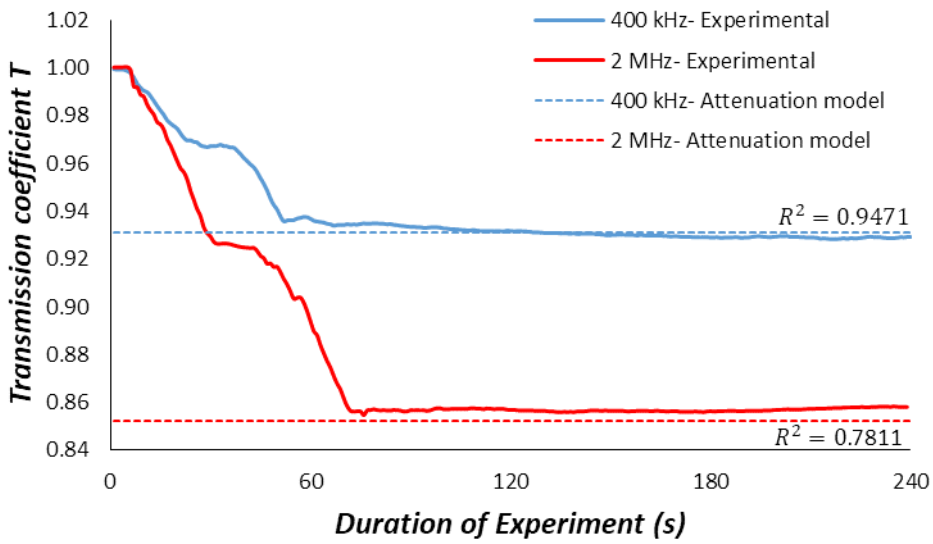

Figure 6.17 SH-SAW attenuation due to PAO 4 viscosity at 400 kHz and 2 MHz

6.9 Conclusions

The SH-SAW response was investigated at a solid-liquid interface, for measuring lubricant oil properties. SH-SAWs lose energy at the solid-liquid interface, due to the liquid viscosity. As it was found both numerically and experimentally, viscosity, the liquid path length or area of contact increases the energy loss, as more liquid particles resist the wave oscillation. The liquid film thickness does not affect the wave response, provided that the penetration depth is smaller than the film thickness.

The SH-SAW sensitivity at the solid-liquid interface is strongly dependent on the thickness and material properties of the medium, the wave frequency and the liquid path length or contact area. Thinner and acoustically softer media appear to have greater sensitivity, as the energy is concentrated in a more confined space and the particles oscillate more freely, as it was found experimentally. The higher the frequency, greater the sensitivity, as the particles oscillate faster and closer to the surface of the source. When the liquid covers a greater area on the propagating surface, the sensitivity maximises, as more liquid particles engage with the particles of the medium, and resist their movement.

To summarise, the SH-SAW sensitivity at the solid-liquid interface is a function of the liquid viscosity and path length, the frequency of the SH-SAW, the acoustic mismatch, hence the material properties of the medium, and finally its thickness.

SH-SAWs seem very promising for measuring lubricant viscosity, surface layers and boundary films, due to their good coupling at the solid-liquid interface and their increased sensitivity in any surface change.

7 VISCOSITY MEASUREMENTS WITH SH-SAWS

This chapter presents the measurement of oil viscosity from the attenuation of SH-SAWs through a metal-oil interface and a Brookfield rotational viscometer. The attenuation-viscosity model (Section 6.2) was used to relate changes in the transmission coefficient of SH-SAWs to the oil viscosities. The results were compared to the viscosities from the Brookfield viscometer.

7.1 Apparatus

In order to increase the sensitivity of the SH-SAW method for measuring lubricant viscosity and ensure accurate results, the test set-up was slightly modified; the medium was replaced with a 200mm x 200 mm x 0.2 mm thick steel plate to increase the SH-SAW sensitivity and allow only the fundamental SH0 mode to appear (Table 7.1). In order to secure the 0.2 mm thick steel plate and allow for easier handling, it was clamped on a 200mm x 200mm x 5 mm steel plate. No couplant was used between the two steel plates, to ensure that SH-SAWs would propagate only along the thin (0.2 mm) steel plate.

The 400 kHz and 2 MHz angled transducers were used for the viscosity measurements and bonded on the medium, 140 mm apart, with Olympus shear couplant and two magnetic clamps, as shown in Figure 7.1.

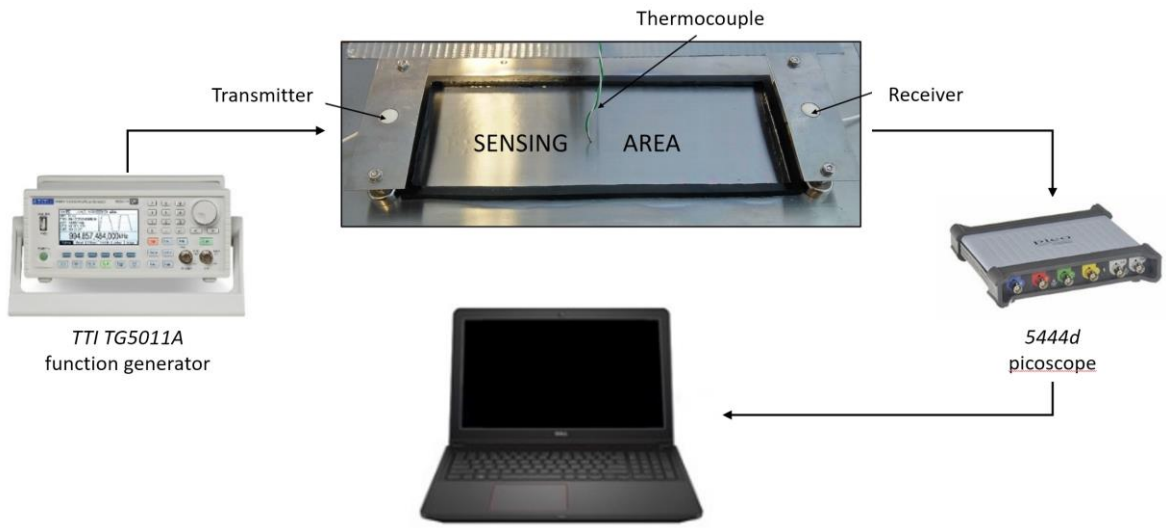

Figure 7.1 Experimental configuration for measuring the viscosity of lubricant oil from the attenuation of SH-SAWs through the solid-liquid interface

A 140 mm x 60 mm rubber container was bonded on the medium to prevent the samples from leaking and allow liquid path length equal to the distance between the sensors, for maximum sensitivity.

All viscosity tests were performed in quasi-static conditions, and to ensure consistent results, the temperature of the samples was monitored with a thermocouple. Since, the experiment was conducted at atmospheric pressure, and the shear rate was controlled by the SH-SAW frequency, temperature was the only unknown variable that could affect the viscosity measurements.

Table 7.1 Number of generated SH-SAW modes on a 0.2 mm thick steel plate

Steel	Velocity c	Frequency f	Wavelength $\left(\lambda = {}^{c}/_{f}\right)$	No. of SH-SAW modes $\left(\frac{Thickness}{Wavelength}\right)$
0.2 mm	3200 m/s	400 kHz	8 mm	1
		2 MHz	1.6 mm	1

In order to validate the SH-SAW method for measuring lubricant viscosity, a few calibration oils of different viscosities were tested first. The Cannon viscosity standard lubricants S3, N10, N35, S200 and S600 samples [75], the properties of which can be seen on Table 7.2, were tested at both 400 kHz and 2 MHz. As these lubricants are considered to be Newtonian [75], their viscosities should be independent of the shear rate and hence the wave frequency.

Table 7.2 Cannon viscosity standard lubricants properties at 25 °C [75]

Samples	Density (kg/m^3)	Datasheet dynamic viscosity (cP)
S3	864	3.3
N10	872	16
N35	864	56
S200	837	340
S600	847	1100

2.0 ml of lubricant sample was deposited each time, to cover the whole area inside the rubber container. In order to ensure that the oil would cover the whole area, the sample was deposited in the form of drops in various locations inside the container, and left to naturally spread, until there was no dry space left on the surface. The fundamental SH0 mode was then generated to measure the acoustic losses as the wave loses energy at the solid-liquid interface, due to the viscosity of the samples.

7.2 Results

In this section, the investigation of the SH-SAW method for measuring lubricant viscosity is presented, along with experimental results to support it, as well as, the effect of shear rate and temperature on the liquid viscosity.

The transmission coefficient for each sample was determined experimentally, from the ratio of the wave amplitude at the solid-liquid and solid-air interfaces, respectively, as shown in Section 6.2 and it was correlated to the viscosities of the Cannon viscosity standards. The transmission coefficient and viscosity at both 400 kHz and 2 MHz can be seen in Figure 7.2 and Figure 7.3, respectively.

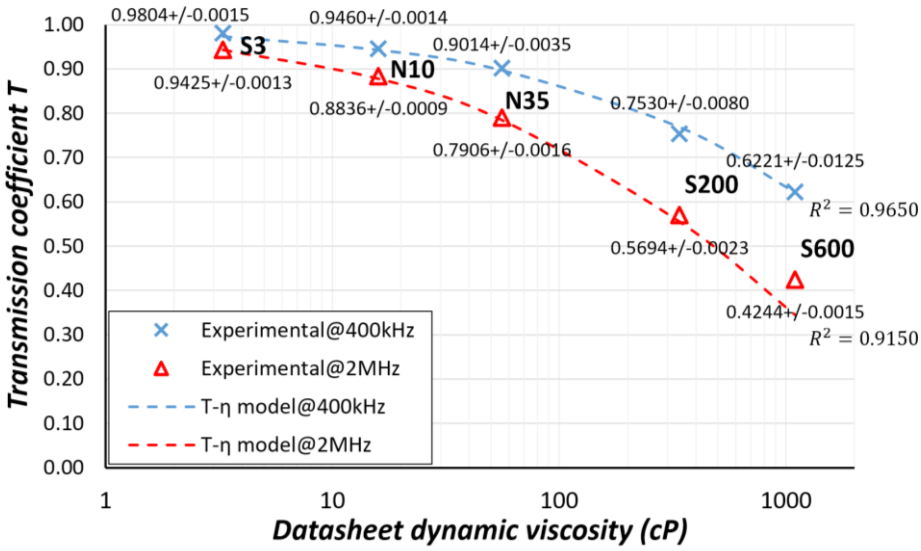

Figure 7.2 Transmission coefficient of Cannon viscosity standard lubricants at 400 kHz & 2 MHz

In Figure 7.2, the transmission coefficient decreases as the viscosity increases, at both 400 kHz and 2 MHz, indicating the energy loss at the solid-liquid interface. The transmission coefficient appears to be lower for the 2 MHz SH-SAWs compared to the 400 kHz, for the same samples, on the same medium. The transmission coefficient values were then imported in Equation 6.24 to calculate the viscosity of each sample at 400 kHz and 2 MHz.

Figure 7.3 shows the viscosities of the Cannon standard lubricants as they were measured from the transmittance of SH-SAWs at the solid-liquid interface using Equation 6.24. The temperature was monitored all time with a thermocouple for the 2 MHz and 400 KHz cases, respectively, to ensure a temperature of 25 °C (+/-1) between the tests, to allow for comparison.

As it can be seen in Figure 7.3, there is a very good agreement between the measured viscosity and the datasheet values.

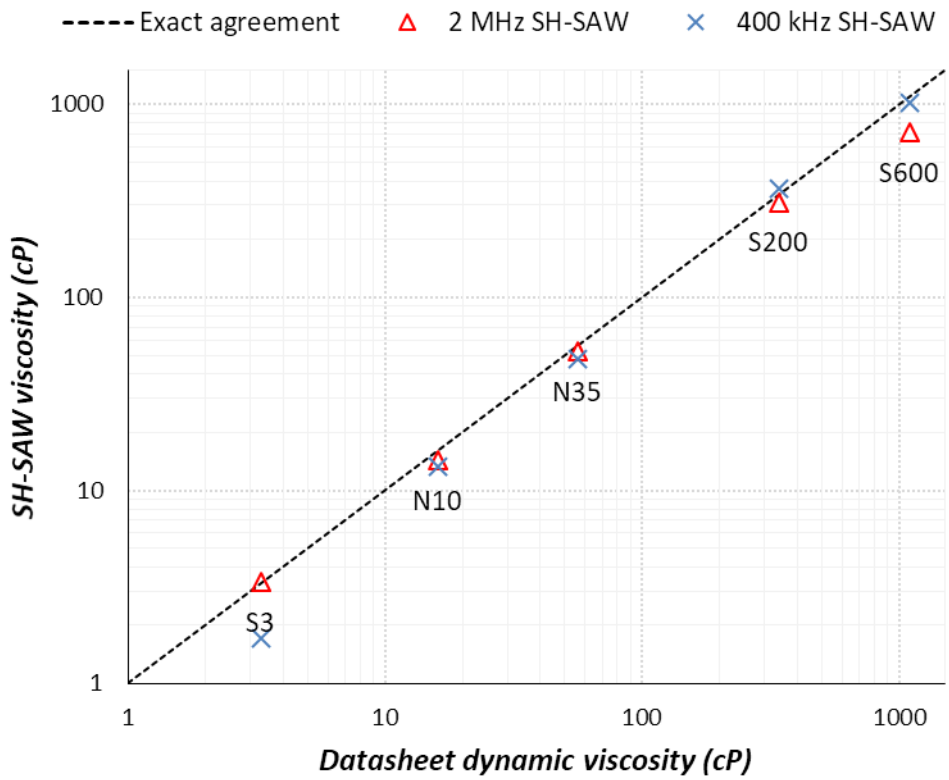

Figure 7.3 Viscosity of Cannon viscosity standard lubricants as measured with a Brookfield viscometer and SH-SAWs

A mismatch seems to appear for the viscosity of S600 sample at 2 MHz. Its viscosity was found to be lower than expected, which is an indication of a possible shear-thinning behaviour.

The S600 is considered to be a Newtonian liquid under certain shear rates. Since, the shear rate ultrasound applies is much higher than any real-life application, it is hard to conclude whether the S600 is indeed Newtonian or not, at the higher excitation frequency [75]. For the rest of the samples, the viscosities present an excellent agreement, regardless of the frequency and hence the shear rate, indicating their Newtonian nature, as expected.

7.2.1 The effect of shear-rate on viscosity

In some liquids, viscosity is a function of the shear rate and these liquids are called non-Newtonian liquids. In reality, most liquids belong in this category and their viscosity may increase or decrease with shear-rate; the former are called *shear-thickening* and the latter *shear-thinning* liquids. So, it is very important to measure the viscosity of liquids and more importantly lubricants, especially when they operate at different shear-rates and they are required to maintain their properties throughout the whole range.

Four PAOs of different viscosities, provided by Lubrizol Ltd., were tested in quasi-static conditions. PAOs' viscosity is determined from their molecular weight; the greater the molecular weight, the larger the molecule and greater the resistance against the applied shear stresses, hence higher the viscosity of the sample, and vice versa.

PAO 4 and PAO 8 molecular weights are very low and the molecule resistance is not affected by the shear-rate; they exhibit the same resistance regardless the rate of shear motion, since the molecules are very small and resonate at any frequency.

On the other hand, PAO 40 and PAO 100 molecular weights are greater, as they consist of large molecules which lead to lower resonant frequencies. When at resonance, the molecules are forced by the applied shear stresses to oscillate with maximum displacement, thus the resistance is maximised. As the difference between the molecules' resonant frequency and the frequency of the shear motion increases, the resistance of the liquid molecules to shear decreases and as a result the viscosity of the liquid.

Table 7.3 PAO lubricant properties at 25 °C

PAO	Density (kg/m^3)	Brookfield dynamic viscosity (cP)
4	900	26.2
8	900	88.6
40	900	926.6
100	900	4600

Figure 7.4 shows the decrease in the wave transmission coefficient with increase of the oil viscosity and wave frequency. Figure 7.5 presents a comparison between the viscosities as they were measured with SH-SAWs and the Brookfield viscometer.

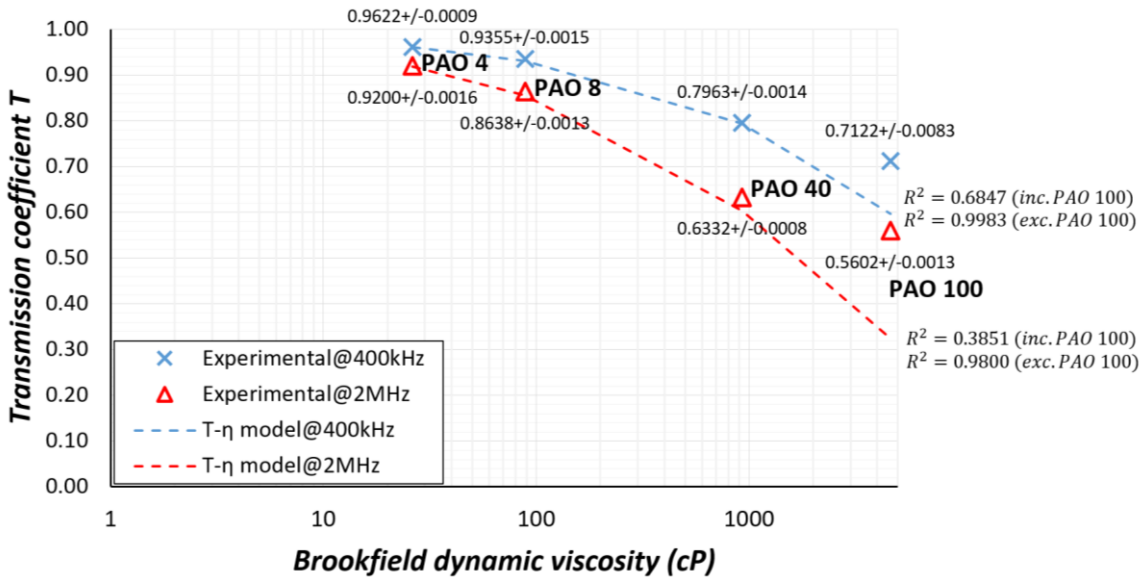

Figure 7.4 Transmission coefficient of PAO lubricants at 400 kHz & 2 MHz

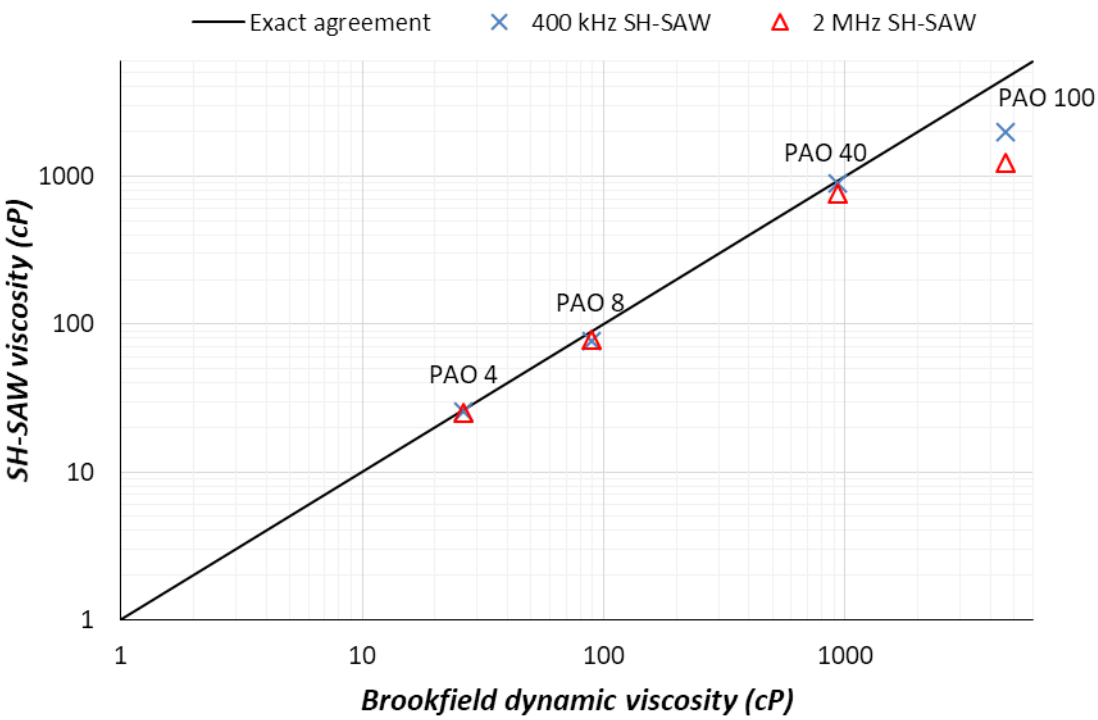

Figure 7.5 Viscosity of PAO lubricants as measured with a Brookfield viscometer and SH-SAWs

In Figure 7.5, the viscosities of the PAO 4 and 8 as measured with 400 kHz and 2 MHz SH-SAWs, match the Brookfield viscosity values, which indicates Newtonian behaviour of the samples.

PAO 40 on the other hand, appears to be harder to characterise. The viscosity as measured at 400 kHz matches the Brookfield viscosity, which indicates a Newtonian behaviour, as

viscosity remains unchanged at this shear rate. But, viscosity appears to be lower at 2 MHz, indicating non-Newtonian behaviour. Further testing is required, at higher frequencies (>2 MHz), to explore PAO 40's nature.

The viscosity of PAO 100 appears to be decreasing as the frequency and hence the shear rate increases. The viscosity at 400 kHz appears to be greater than at 2 MHz and lower than the Brookfield viscometer, which indicates a non-Newtonian behaviour. According to the results, the PAO 100 exhibits shear-thinning behaviour.

7.2.2 The effect of temperature on viscosity

Temperature affects the viscosity of the oil. As shown in sub-Section 2.1.1, with the increase of temperature, the bonds between the oil molecules become weaker, thus less activation energy is required for the passing of one molecule from one equilibrium position to another, as the bonds present less resistance to the applied motion, and viscosity decreases.

In this section, the effect of temperature on the viscosity of the PAO 4, 8, 40 and 100 was investigated. Before the start of testing, the test set-up was modified to withstand high temperatures. The Perspex wedges were replaced with aluminium wedges, as aluminium has a much higher melting point than Perspex (~ 70 ℃), and meets the requirements for a successful SH-SAW generation.

Two 2 MHz thickness-shear piezo-ceramics were bonded on the aluminium wedges with high temperature (< 230℃) strain gauge adhesive. The transducers were covered with high temperature epoxy to protect the cable connections and the piezo-ceramics from heat and any other hazards. The same high temperature epoxy was used to bond the aluminium angled transducers on the 0.2 mm thick steel plate, 140 mm apart. This selection was made due to high resistance to temperature variations of the epoxy, as well as the good coupling properties it presents in transmitting SH-SAWs. The epoxy was also used to bond a 140 mm x 60 mm rubber container on the steel plate for the sample deposition. Keeping the selection of different materials to the minimum, ensures that heat is transferred in a more controlled rate and is less likely temperature difference between the materials to occur, which may lead to unwanted errors.

Figure 7.6 High temperature viscosity measurement test set-up

After the 0.2 mm thick steel plate was instrumented with the two 2 MHz aluminium angled transducers, it was placed in the oven (Memmert UF55 plus programmable oven) for temperature calibration. The steel plate was heated up to 100 °C and left there to gradually cool down to room temperature. The temperature was monitored with a thermocouple in contact with the plate surface. The signal was acquired per 1 °C during both the warming and cooling processes, to explore the temperature effect on the wave amplitude. A temperature calibration coefficient was used to visualise the wave amplitude change with temperature, by diving the signal amplitude for each temperature with the signal amplitude at 25 °C. The temperature calibration curves for the warming and cooling cycles seem to match well, as it can be seen in Figure 7.7. This step is essential in order to calibrate out any other effect temperature has on the system, and focus on the effect on the lubricant viscosity.

In Figure 7.7, the temperature calibration coefficient seems to increase with temperatures up to 55 °C, but decreases as the temperature further increases. That most likely occurred due to the different thermal expansion coefficients of the aluminium wedge (~23 10^{-6}/K) and the steel plate (~12 10^{-6}/K), which created strains at the interface. The difference in the strain of the aluminium and steel led to shearing of the epoxy adhesive and as a result poorer coupling between the wedges and plate at elevated temperatures.

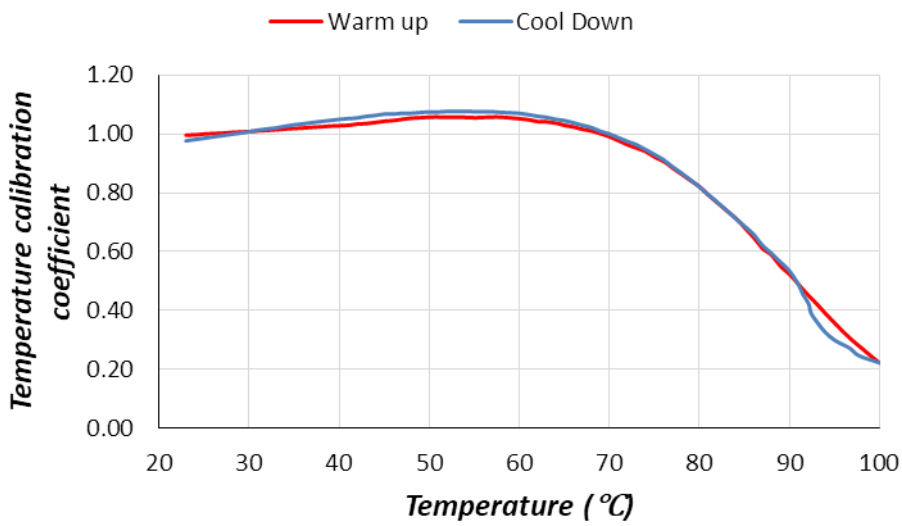

Figure 7.7 Air reference calibration curve of the 0.2 mm thick steel plate

2.0 ml of each sample was then deposited inside the rubber container and the plate was placed in the oven. The samples were heated up to 100 °C and left to gradually cool down to room temperature. Measurements were taken every 1 °C, during the cooling process, in order to make sure that all components are in thermal equilibrium.

The transmission coefficient T over temperature was calculated for each oil sample, by dividing the wave amplitude at the solid-liquid interface with the amplitude at the solid-air interface, at the corresponding temperature. It was used then to determine the viscosities of the oil samples over temperature using Equation 6.24. Using the Vogel equation (Equation 2.4), the viscosities of the PAOs were predicted from 25 to 100 °C temperature (shown by the dashed lines). The three known viscosities at three temperatures, that were used to calculate the a, b, c constants in Vogel equation, can be seen in Table 7.4 for the four PAOs. The predicted viscosity values were then compared to the experimental values, and are presented in Figure 7.8.

Table 7.4. The three known viscosity values at three temperatures (provided by Lubrizol Ltd.), which were used to calculate the Vogel constants, to predict the viscosities of the PAOs over temperature

#	*Temperature*			*Vogel constants*		
	25 °C	**40 °C**	**100 °C**	***a***	***b***	***c***
PAO 4	26.15	8	2.2	0.8705	95.5859	-3.0922
PAO 8	88.6	46.73	7.96	0.0358	1314.84	-143.2416
PAO 40	926.6	410.7	40.3	0.0165	2040.41	-161.5918
PAO 100	4600	1302	103.2	2.2418	576.85	-50.6373

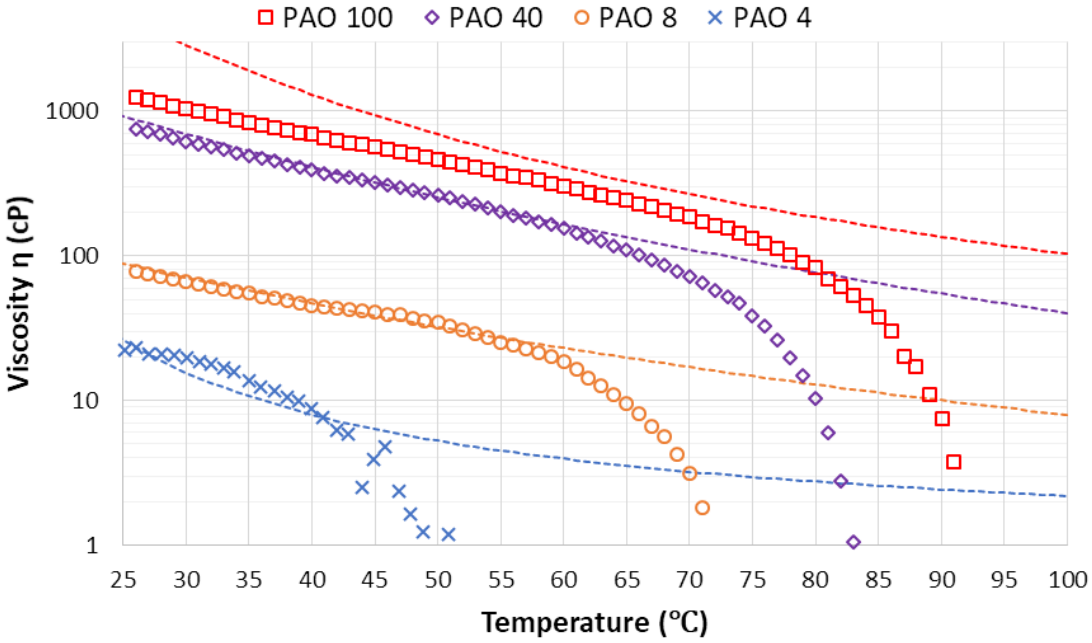

Figure 7.8 Viscosities of PAOs over temperature, as measured using SH-SAWs *(data points)* and predicted using Vogel equation *(dashed lines)*

The data points represent the viscosity values as they were measured experimentally with the SH-SAW method, at 2 MHz every 1°C.

According to the graph:

- The PAO 4 presents good agreement between the experimental values and predicted values for viscosity up to 40 °C. Above that temperature, the experimental values no longer follow the viscosity curve. That might be either due to limitations of the method, or the combination of high frequency and high temperature might lead to a thinner lubricant.
- The PAO 8 viscosity, as measured experimentally, matches the viscosity as predicted with the Vogel equation up to 60 °C. Above that temperature, viscosity suddenly decreases and reduces almost to zero.
- The same trend was noticed for the PAO 40 sample; the experimental viscosity values follow the viscosity curve up to a certain temperature and then they deviate from it.
- The PAO 100 presents a very high mismatch between the experimental and predicted viscosities, but it was somewhat expected, since it presents a non-Newtonian behaviour and Vogel equation does not take into account the effect of the shear rate.

It can be concluded then, that above a certain temperature (~55-65 °C), the shearing of the epoxy adhesive due to the different thermal expansion coefficients of steel and aluminium, affects the viscosity measurements and the experimental set-up returns unreliable measurements. This problem needs to be taken into consideration and then experimental set-up needs to be re-designed.

7.3 Conclusions

This chapter has presented the successful application of SH-SAWs for measuring lubricant viscosity in a laboratory based approach. The SH-SAW attenuation-viscosity model was used to calculate the viscosity of different oils from the transmission coefficient values and was compared to the viscosity values obtained with a Brookfield viscometer.

Tests were performed with Newtonian oils on a steel plate and the viscosities as they were measured with both methods were found to be in excellent agreement. Following good results, both Newtonian and non-Newtonian lubricants were tested with the SH-SAW method at different frequencies to investigate the effect of shear rate on the lubricant viscosity.

Different PAOs of different viscosities were tested on a steel plate at both 400 kHz and 2 MHz. According to the results, the viscosity of the Newtonian lubricants as it was measured with the SH-SAW method matched the Brookfield viscosity, and was found to be independent of the wave frequency and hence the shear rate. The viscosity of non-Newtonian lubricants on the other hand, was found to be somewhat lower than the Brookfield viscosity, and kept decreasing with the frequency and hence the shear rate, indicating a non-Newtonian behaviour.

The same PAOs were further tested up to 100 °C with the SH-SAW method, to investigate the validity of the proposed attenuation-viscosity model for measuring oil viscosity over temperature. The Vogel equation was used to predict the viscosity of the tested lubricants over the whole range of temperatures, and compared to the experimental results. As the results have shown, there was a good agreement between the experimental and predicted values for the viscosity of the Newtonian lubricants. However, there seems to be a temperature over which the model does not fit. As for the non-Newtonian lubricant, the viscosity as measured experimentally did not match the viscosity as predicted with the Vogel equation, as it does not take into consideration the non-Newtonian nature of the liquid.

SH-SAWs can be successfully used for measuring lubricant viscosity, over a range of temperatures and different shear rates, with the potential to be implemented in an actual running bearing for in-situ oil viscosity monitoring.

8 SH-SAW RESPONSE TO SURFACE LAYER FORMATION

In this chapter, the SH-SAW response to the formation of surface layers, was investigated. Surface layers are formed through molecular adsorption on metallic parts, to protect them against friction and wear, when the oil viscosity is not enough to sustain a full oil film. Both physically adsorbed surface layers and model deposited surface layers were studied, to explore the capabilities of the SH-SAW method for detecting their formations, on a solid-liquid interface.

8.1 Background

As mentioned in previous chapters, viscosity is probably the most important property of a lubricant, as it is responsible for supporting a thick lubricant film (film thickness > surface roughness), which keeps the interacting surfaces separated and protects them from major friction and wear in the hydrodynamic and elastohydrodynamic regimes of lubrication.

Viscosity is proportional to the pressure and inversely proportional to the temperature and shear rate or velocity. As a result, when the speed of the moving parts decreases, the lubricant film decreases (film thickness ≤ surface finish), which leads to an increase in the temperature of the lubricant due to the friction that develops from the contact between the two surfaces at their asperities (boundary lubrication regime). At these extreme conditions, viscosity can no longer support a lubricant film to protect the interacting surfaces and major wear is likely to occur. To overcome this problem, lubricants are blended with an additive package to enhance existing properties or add new ones. Among these additives, some form surface layers (or boundary films) on the surfaces of the components that provide enough lubrication between the surfaces' asperities to reduce friction and prevent major wear.

Boundary additives are long chain molecules with a polar head and a tail, such as fatty acids, alcohols or amines. These molecules adsorb on metal surfaces to form protective layers, with the polar heads attached to the surface and the tails free inside the carrier to form a closely packed layer through strong forces of lateral attraction between them [78] [79]. A boundary additive is considered to be effective when a strong bond between the polar head and the metal surface is achieved. The bond can be either physical (electrostatic or dipole forces) or the result of chemical reactions between the metal surface and the lubricant. The former is known as physical adsorption or physisorption and the latter as chemical adsorption or chemisorption. Physisorption is a reversible process; the adsorbed surface layer can be removed without damaging the metal surface, whereas chemisorption is an irreversible process that involves permanent modification of the metal surface. Physisorption and chemisorption strongly depend on the operating temperature,

sliding speed of the components and the reactivity of the metal surfaces with the lubricant [78]. Therefore, the formation of surface layers is the result of several, complex processes including oxidation and thermal decomposition of hydrocarbons, polymerisation, catalysis by metal surfaces, tribochemical and tribomechanical reactions [80].

Oxidation reactions are important for the formation of polar species, which react with the metal surfaces to form products that provide lubrication on the surface. Upon lubricant oxidation, the molecules tend to form either low molecular weight products through beta carbon scission or decomposition, or high molecular weight products through condensation. Phosphorous-containing organic compounds and metal dithiophosphates react with oxygen and water to form low molecular weight products such as sulphates, oxides, mineral phosphates, etc. [81]. Metals, such as chromium, nickel, copper and iron exhibit catalytic behaviour with hydrocarbons; the products from the oxidation of hydrocarbons react with the metal surfaces and form metallic soaps. Different metals exhibit different rate of lubricant oxidation [80]. Condensation reactions form high molecular weight products, which after reaching/exceeding the solubility limit, become insoluble in the oil and deposit on the surface [80]. Examples of condensation products include benzene or cetene that provide anti-wear protection, oil soluble molybdenum compounds, complex esters, etc. [81].

The mechanisms by which surface layers provide protection upon the metal surfaces include low shear interlayers, sacrificial layers, shear resistant layers, friction modifying layers and viscous polymer layers [80]. The low shear interlayer employs solid lubricant molecules that exhibit weak attraction in the direction of shear that allows the lubricating film to slide easily along the plane of motion. The sacrificial layer is bound weakly on the metal surfaces and is easily removable, thus the layer itself is being worn under shear instead of the metal surfaces. The oxide layer that is formed on steel surfaces is an example of sacrificial layers. These layers are considered to be effective for protecting the metal surfaces only if the rate of the layer formation is higher than the rate of the layer removal. Shear resistant layers strongly adhere on the metal surfaces and behave like solids. As a result they exhibit resistance against shear between the layer and the metal surface. Friction modifying layers, such as fatty acids (Figure 8.1), allow the metal surfaces to slide relative to each other, by forming weakly bonded adsorbed layers on the ordered structure that the lubricant molecules or reaction products form at the interface.

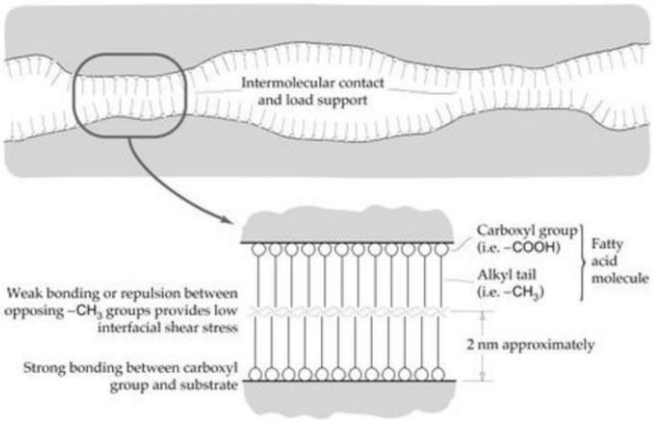

Figure 8.1 Molecular adsorption of friction modifiers on the interacting surfaces to prevent friction and wear [1]

Dissolved polymers are added to lubricants to improve the rheological properties of the end product and strongly affect its viscosity. It has also been noticed that some of these polymers form surface layers through molecular adsorption, the viscosity of which is considerably higher than the viscosity in the bulk of the lubricant (Figure 8.2). Such polymers are pour point depressants, viscosity index improvers and dispersants [82]. These polymers consist of a polar head and a non-polar chain, and their functionality strongly depends on the solubility of the non-polar chain. Therefore, depending on the solvent, polymers can adsorb on the surfaces in three configurations; "pancake", "mushroom" and "brush". In the "mushroom" arrangement, the polar head is attached to the surface while the non-polar chain is soluble in the lubricant, but somewhat unravelled. When the adsorption of the polar head at the surface becomes denser, the non-polar chain unravels to create "brushes". On the other hand, if the non-polar chain is insoluble in the solvent, both the polar head and non-polar chain will adsorb on the surface, creating a "pancake" arrangement [13]. Examples of the "pancake", "mushroom" and "brush" arrangements can be seen in Figure 8.3. Viscous polymer layers vary in thickness from 2 nm up to 30 nm, depending on the molecular weight of the polymer.

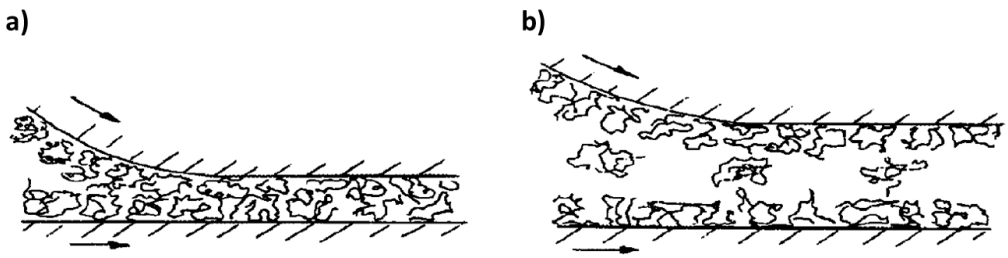

Figure 8.2. Schematic of a multifunctional polymer; a) at low speeds the surfaces are separated through an extremely viscous adsorbed polymer layer, b) at higher speeds the viscosity is based on the viscosity of the bulk lubricant [82]

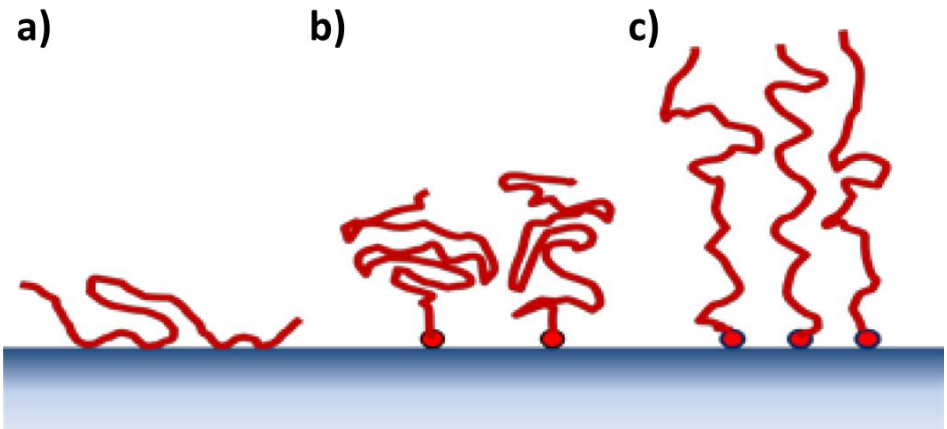

Figure 8.3. Adsorbed polymer arrangements; a) "pancake", b) "mushroom" and c) "brushes" [13]

Velocity, not much greater than the minimum velocity required to introduce rubbing between two components [78], produces heat which raises the temperature at the surface of the solids for 1 μs or less [80], due to the friction that develops between them at their asperities. The extreme asperity temperature is known as "flash temperature" [83]. Temperature affects strongly the surface layers; either promoting their formation or it is responsible for their break down. As explained by Williams [78], a physically adsorbed surface layer will gradually desorb and reduce the surface coverage, as the molecules become more mobile due to rise in temperature. As a result, the coefficient of friction will increase. When the surface temperature exceeds ~150 °C physisorption has negligible effect in surface layer formation. The behaviour of a physisorbed surface layer can be seen in Figure 8.4 and is illustrated by curve A. On the other hand, for a surface layer that chemically reacts with metals, the rise in temperature increase the rate of chemical reaction between the additive and the metal surface. This may be either assisting the layer formation or breaking an already formed surface layer. For example, fatty acids adsorb on metal surfaces to form solid-like surface layers that reduce friction and protect the surfaces up to the melting point of the surface layer. This behaviour is shown in Figure 8.4, illustrated by curve B. Extreme-pressure additives on the contrary (Figure 8.4, curve C), stay inactive at low temperatures but react with hot metal surfaces to form solid-like surface layers, such as chloride, sulphide or phosphide layers, which protect the surfaces up to 300-400 °C. Curve D in Figure 8.4, exhibits the behaviour of an oil blended with both friction modifiers and extreme-pressure additives, to improve the protection against friction over a wide range of temperatures. Even greater surface protection is possible with the use of anti-wear agents, such as zinc dialkl dithiophospate or ZDDP. Anti-wear agents form thick (50- 500 nm), viscous polymeric layers of the same order of thickness as the surface roughness, which protect from seizure and major wear but separating the two surfaces.

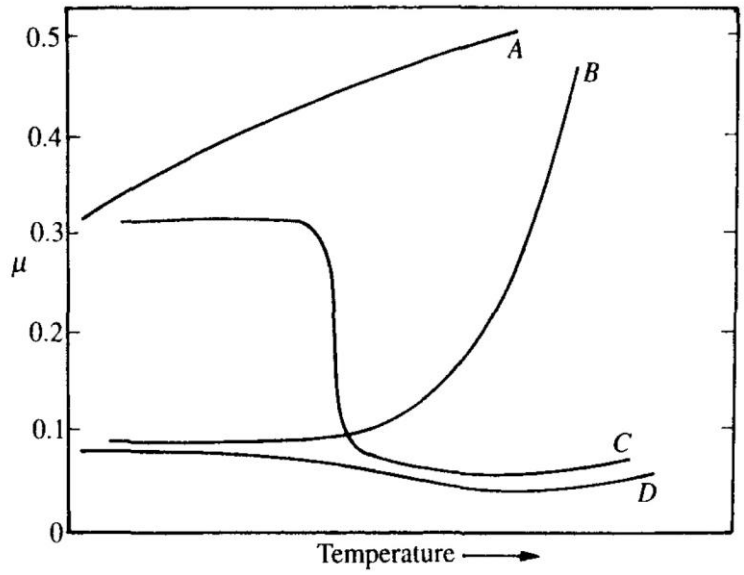

Figure 8.4. Behaviour of various lubricants with temperature and the effect on friction; paraffins (A), fatty acids (B), extreme-pressure additives (C), and fatty acids+extreme-pressure additives (D) [78]

Temperature has a more dominant role in the formation and break down of surface layers, rather than the shear or load [80]. Low shear initiates rubbing between two surfaces at their asperities, which increases the surface temperature, but it is the temperature that promotes the chemical reactions between the lubricants and the metal surfaces to either form or decompose surface layers. That explains the formulation of an engine oil, which is blended with different lubricating additives to offer surface protection at different conditions. Measuring the presence of surface additives and surface layer formation inside lubricated engine bearings is critical for the protection of the interacting surfaces and to ensure normal operation of the engine. However, there are no available techniques for measuring surface layers in-situ in engines. The QCM and SH-SAW devices have been used for measuring molecular adsorption [68] [69] [70] [71], and hence surface layer formation, but they are limited to laboratory measurements, as shown in Section 4.4.

Both the frequency change and amplitude attenuation of SH-SAWs propagating on a **non piezo-electric substrate** in contact with a lubricant blended with an additive package, were investigated in this thesis for measuring surface layer formation and lubricant viscosity, respectively.

8.2 Apparatus

To investigate the application of the SH-SAW method for detecting surface layer formations on a **metallic substrate**, four lubricants were tested, provided by Lubrizol Ltd, the properties of which can be seen in Table 8.1.

A PAO 4, which is the most commonly used engine lubricant, was blended with two different additive packages, performance viscosity modifiers (PVMs) and friction modifiers (FMs), respectively. According to the supplier, PVMs are high molecular weight (in the order of 100,000 gr/mol) polymers that expect to adsorb on a metal surface to form a thick (~30nm), viscous, surface layer. FMs are monomers that expect to adsorb on a metal surface to form a monomolecular surface layer or monolayer, approximately 1-2 nm thick. In both cases, surface layers were expected to form naturally, provided that a polar surface (such as steel) was present, as it was shown by Lundgren et al. [84] for adsorbed FMs on a steel surface, and by Qin et al. [85] for adsorbed VMs on a gold surface, using the quartz crystal microbalance with dissipation factor or QCM-D. In the QCM-D, the quartz crystal oscillates freely at its resonance frequency, but when molecules adsorb on the crystal, lead to a change in the resonance frequency which is directly related to the added mass. Slow speed ball-on-disc friction tests, in combination with optical interferometry [86] [87], have showed that in the case of FMs some degree of rubbing action is required in order to initiate friction reduction [13]. In friction tests, such as ball-on-disc, the surface layer formation is inferred from the effect it has on the friction that develops between the rubbing surfaces. As a result, sliding speed, temperature and load affect the measurements. Whereas, in the QCM-D measurements the surface layer formation is inferred through the mass deposition on the surface of the quartz crystal. As a result, with the QCM-D the measurements are independent of the load, sliding speed and temperature. The SH-SAW method that was investigated in this work, is related more to the QCM-D measurements rather than the ball-on-disc measurements. Therefore, the SH-SAW method focussed on measuring the presence of a layer on the metal surface, rather than its effect on reducing friction.

The samples were deposited on the 200mm x 200mmx 0.2 mm steel plate, inside the 140 mm x 60 mm rubber container, and tested for 30 minutes at room temperature, with no load and no shear applied, using the 2 MHz aluminium angled transducers.

Table 8.1 PAO blends' properties at 25 °C

PAO	Density (kg/m^3)	Dynamic viscosity (cP)
4	900	26.2
4+1%PVM	900	36.6
4+1%40	900	36.4
4+1%40+1%FM	900	35.9

As time passes, the molecules are expected to get adsorbed on the steel surface until it has been fully covered, forming surface layers that will increase the viscosity close to the surface, as well as the mass of the system. In order to distinguish any viscosity changes due to the formation of a surface layer, the samples were designed to have similar viscosities at room temperature, so as any change in the viscosity would be attributed to the surface layer formation. The concentrations of FMs and PVMs in the samples were selected the same as the FM and PVM concentrations in commercial products, for more representative results. The 1% concentration of PVMs in the PAO 4 though, led to a more viscous product compared to the PAO 4+1% FMs. To match the viscosity of PAO 4+1% PVMs, 1% PAO 40 was added to the PAO 4+1% FMs, to act as a viscosity modifier. As shown in Table 8.1 from the comparison between PAO 4+ 1% PAO 40 and the PAO 4+1% PAO 40+1% FMs, the addition of FMs had no effect on the viscosity of the bulk oil sample, but it was expected to change the viscosity close to the surface at the metal-oil interface.

A 2 MHz SH-SAW was generated on the unperturbed surface for the first 2 minutes of the experiment. Then, 2.0 ml of lubricant sample was deposited inside the container to cover the whole 140 mm x 60 mm sensing area, and left there for 30 minutes. After 30 minutes, the sample was removed and the surface was cleaned off any lubricant residue. The SH-SAW response was captured during the whole process, including the sample deposition, testing, removal and surface cleaning. A thermocouple was in contact with the sensing area the whole time to monitor the temperature, in order to ensure accurate results.

The transmission coefficient was determined experimentally, from the SH-SAW amplitude attenuation at the solid-liquid interface, and the values were imported in Equation 6.24 to calculate the viscosity of each sample.

8.3 Results

Figure 8.5 shows the SH-SAW transmission coefficient and dynamic viscosity over time for all samples *(amplitude response)*, after using Equation 6.24 to calculate the latter from the former. Figure 8.6 shows the frequency change over time *(frequency response)*.

The temperature (shown with the dotted lines) was similar for all the samples and remained fairly constant the whole time for each of the experiments, so any temperature effect on the lubricant viscosity can be neglected.

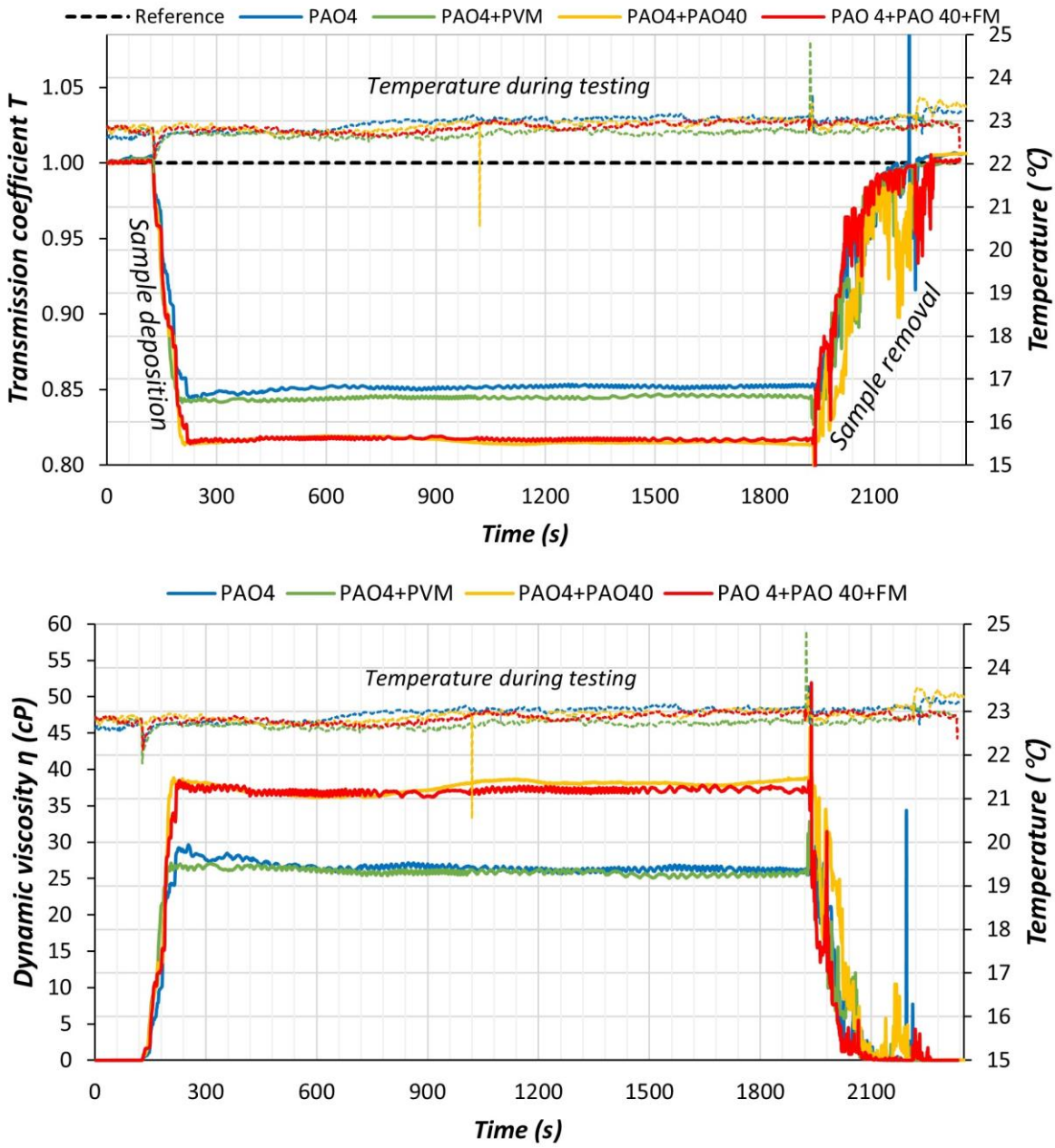

Figure 8.5 SH-SAW transmission coefficient *(top)* and dynamic viscosity *(bottom)* responses to surface film formation over time

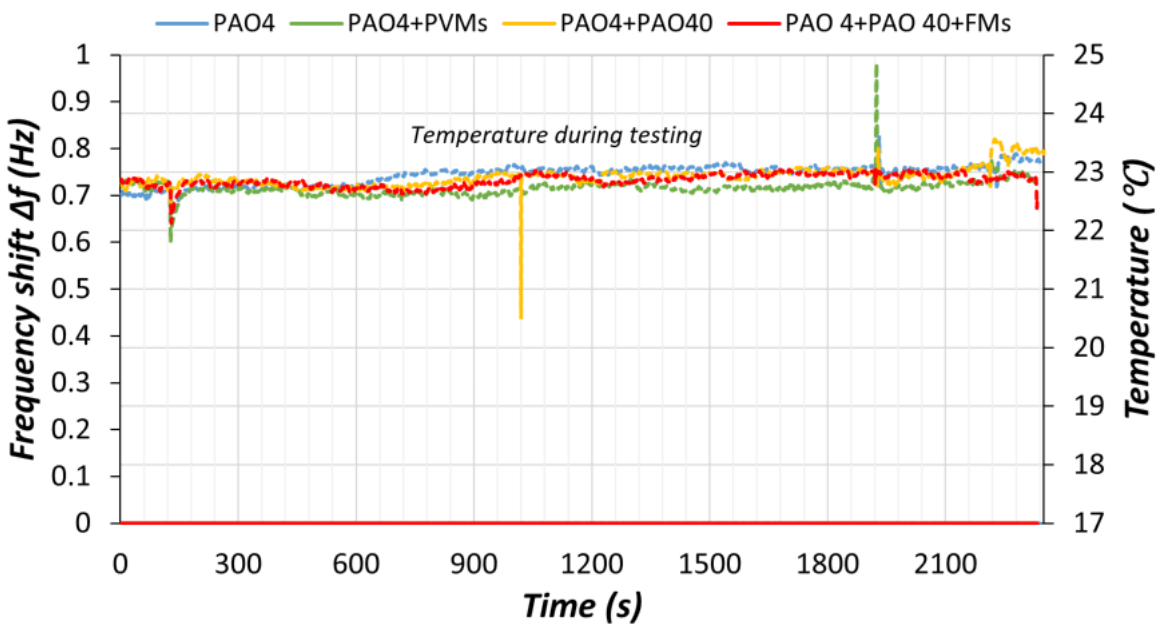

Figure 8.6 SH-SAW frequency responses to surface film formation over time

The transmission coefficient remained constant and equal to 1.0 at the unperturbed surface for the first 2 minutes of the experiments, reduced after the samples were deposited (ramp down) and returned to 1.0 after the surface was cleaned (ramp up) from any sample residue. Two main conclusions can be drawn according to the results:

1. Firstly, neither the transmission coefficient, hence the viscosity, nor the frequency changed over time for any of the samples, indicating either no surface layer formation or that a layer was indeed formed, but with no effect on the SH-SAW response.

   The PAO 4+PVMs and PAO 4+PAO 40+FMs blends were expected to decrease both the SH-SAW frequency and amplitude (Figure 8.7, bottom), as the adsorbates attach on the surface (Figure 8.7, top) increasing the viscosity close to it (Figure 8.7, middle), but their viscosities were found to be constant over time and no frequency change occurred.

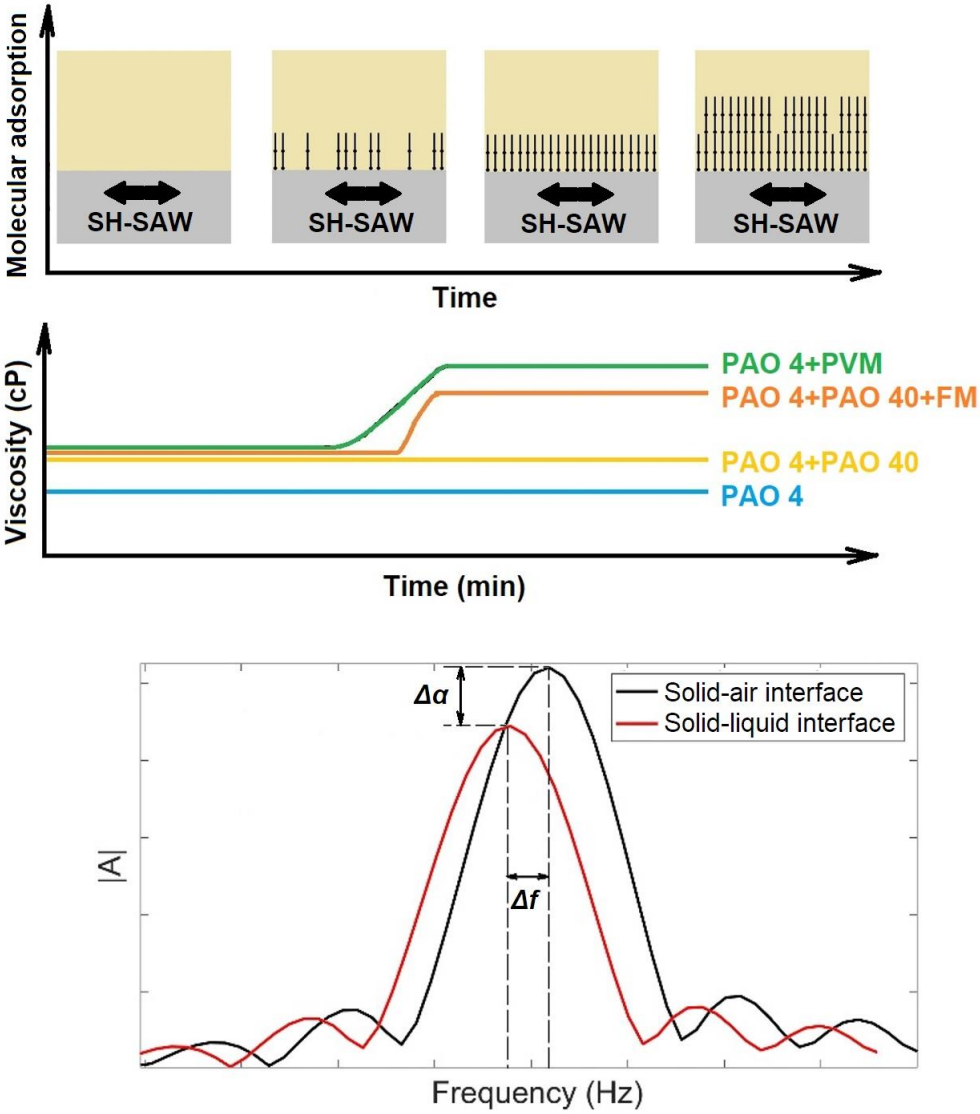

Figure 8.7 Schematic of surface layer formation through physical adsorption *(top)*, expected viscosity response over time *(middle)*, expected frequency response to molecular adsorption *(bottom)*

Frequency change was less likely to occur on a **metallic substrate** for the following reasons:

- It was not coated to allow molecular adsorption that would change the resonant frequency of the coating and thus the substrate's.
- The mass of the adsorbate was negligible compared to the mass of the metallic substrate, thus it did not affect its resonance.

Regarding the viscosity response to the surface layer formation, further investigation is required in order to understand whether a surface layer was not formed or formed, but without affecting the SH-SAW response.

2. Secondly, the experimental viscosities of the PAO blends seem to follow the values on Table 8.1 (shown by dashed lines), except for the PAO 4+ 1%PVMs, the viscosity of which appears to be equal to the viscosity of the pure PAO 4, as shown in Figure 8.8.

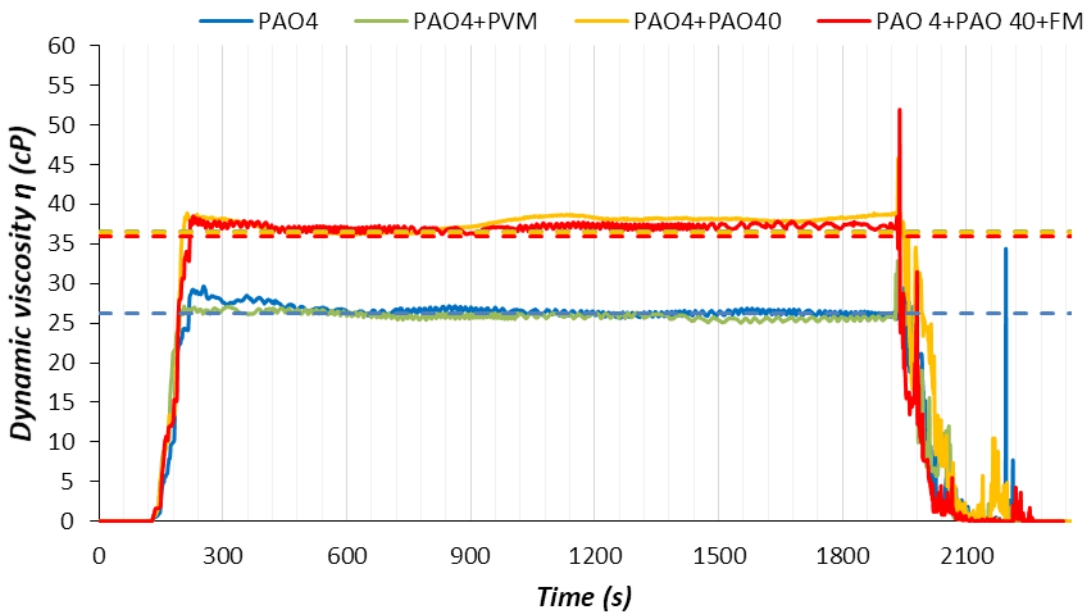

Figure 8.8 Comparison between theoretical viscosities *(dashed lines)* and measured viscosities with SH-SAWs *(solid lines)*

It seems that the PVMs either remained inactive at this temperature or that their molecular weight was too big [1], hence the 2 MHz frequency was far from their resonant frequency and as a result they were not excited, thus they showed no presence. Further testing, at different frequencies and temperatures, is required to fully understand the PVM behaviour.

8.3.1 The effect of surface layer thickness on SH-SAW response

According to Figure 8.5, viscosity did not change over time for either the PAO 4+PVMs or the PAO 4+PAO 40+FMs, leading to the conclusion that either a layer was not formed or formed but without any effect on the SH-SAW response.

Assuming that a surface layer was indeed formed, the thickness of which was expected to be ~2 to 30 nm (depending the sample) [1] and considering the penetration depth of the SH-SAW inside the lubricant samples (Table 8.2), it is clear that the thickness of the surface layer is insignificant compared to the depth the SH-SAW penetrates inside the mixture, thus the SH-SAW response to viscosity is affected more by the carrier (base oil) rather than the surface layer (Figure 8.9), which would explain the results.

Table 8.2 PAO blends SH-SAW penetration depth

PAO	Density (kg/m³)	Dynamic viscosity@25 °C (cP)	SH-SAW penetration depth (µm)
4	900	26.2	2.14
4+1%PVM	900	36.6	2.54
4+40	900	36.4	2.54
4+40+1%FM	900	35.9	2.52

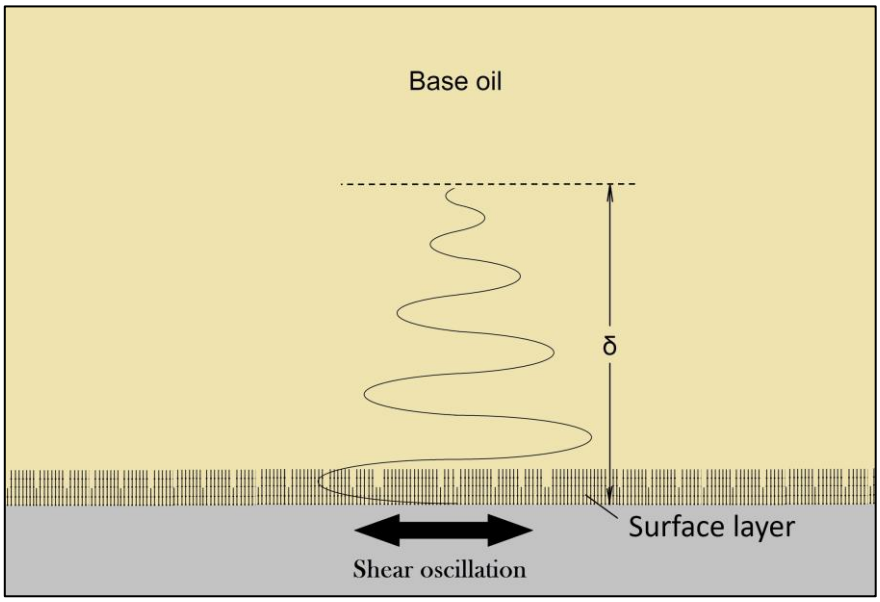

Figure 8.9 Surface layer thickness and SH-SAW penetration depth

So, either the SH-SAW penetration depth needs to be reduced closer to the surface or the surface layer thickness needs to be increased to allow its detection. In order to investigate the *surface layer thickness- penetration depth* relationship, the test was repeated for a solution of Heptane+1 % PVMs.

Since Heptane is a solvent, after deposition it will evaporate leaving a residual PVM film on the surface. Depositing a known quantity of the solution over a known area and knowing the concentration of PVMs in the solution, the thickness of the residual PVM layer can be estimated through Equation 8.1. Repeating the process over and over again will lead to thicker surface layers, as shown in Figure 8.10.

$$h_{PVM} = \frac{0.01\, V_{solution}}{A} \tag{8.1}$$

where h_{PVM} is the deposited layer thickness, $V_{solution}$ is the quantity of the solution, A is the area and 0.01 is the 1% PVM concentration in the solution.

For the purpose of the study 1ml of sample was deposited over a 132mm x 49mm sensing area, which led to a 1.55 µm thick PVM layer, estimated using Equation 8.1. The process was repeated 6 times to form thicker films up to ~ 9.27 µm. The results from this study can be seen in Figure 8.11.

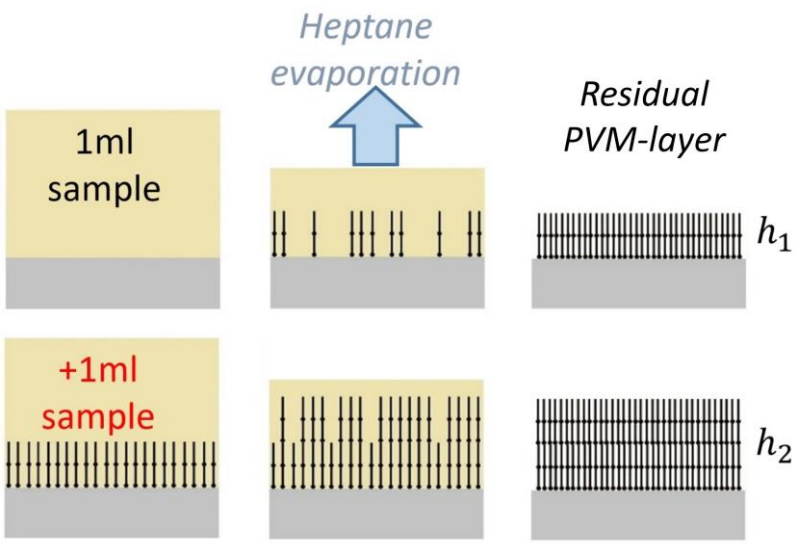

Figure 8.10 Deposition of the solution (*left*), evaporation of the solvent (*middle*), and residual PVM layer (*right*)

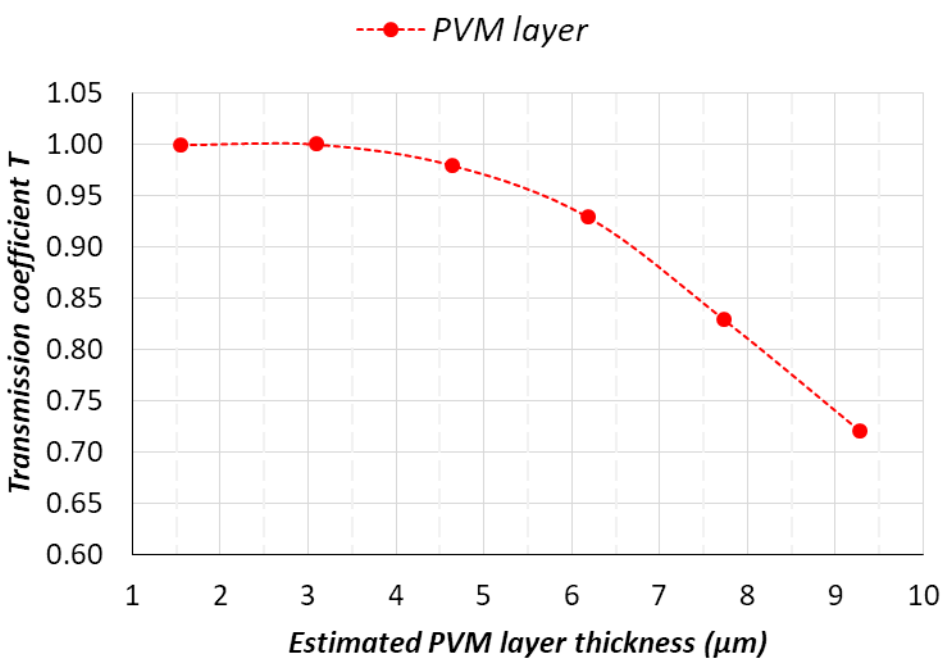

Figure 8.11 SH-SAW transmission coefficient change to PVM layer formation of various thicknesses

Figure 8.11 shows, that the transmission coefficient decreased as the PVM layer thickness increased. There is no change in the transmission coefficient for $h_{PVM} < 4.6\ \mu m$, however after a thick enough layer has formed, there is a clear change. So, the formation of thick surface layers can be detected with SH-SAWs through a dry contact interface.

However, the aim is to detect the formation of surface layers through a lubricated contact interface. In order to explore the SH-SAW response to thick surface layers through a wet interface, 2 ml of pure PAO 4 were deposited on the 1.55 and 4.6 µm thick PVM layers. The results were compared to the SH-SAW response to pure PAO 4, and they are shown in Figure 8.12.

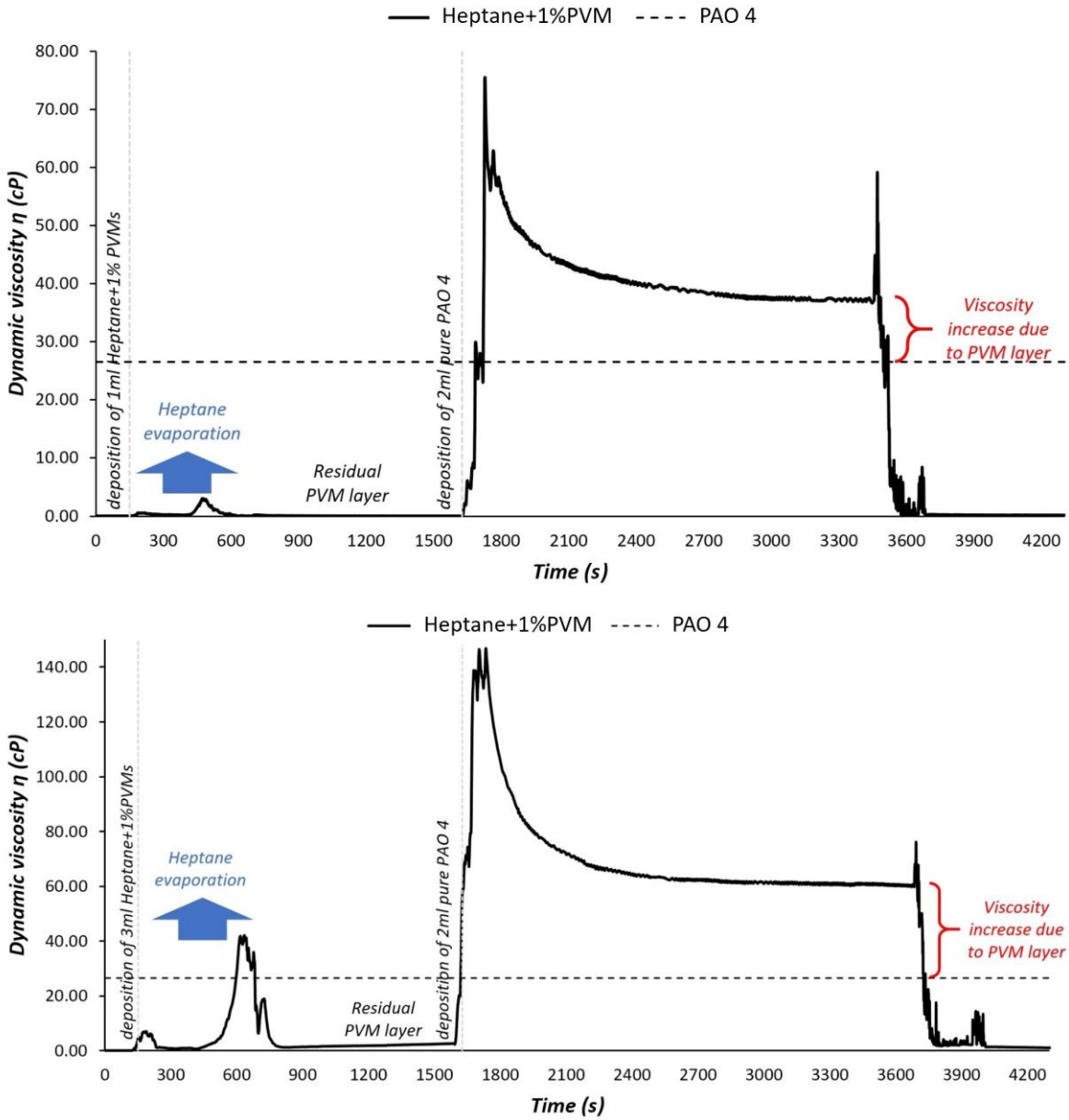

Figure 8.12 SH-SAW response to PAO 4 on a 1.55 um PVM layer (*top*), and a 4.6 um PVM layer (*bottom*)

According to Figure 8.12, the PAO 4 viscosity was affected by the presence of the PVM layers. As the surface layer thickness increased, it had a more significant effect on the PAO 4 viscosity. A 1.55 µm PVM layer was undetectable at the dry contact interface, but it was detected after PAO 4 was deposited on top of the 1.55 µm PVM layer, through an increase in the viscosity of the oil.

As a result, the formation of thick surface layers $h_{layer} > 1.5\ \mu m$ can be detected through the viscosity change, on both a dry and a wet contact interface, using SH-SAWs. For thin surface layers $h_{layer} < 30\ nm$, the penetration depth of the SH-SAW should be reduced closer to the surface, to allow their detection.

8.3.2 The effect of excitation frequency on the surface additives

In the attempt to measure the formation of PVM and FM layers (in the beginning of Section 8.3), it was noticed that the viscosity of PAO 4+1%PVMs matched the viscosity of the pure PAO 4, instead of the value provided by the supplier (Figure 8.8). This was attributed to the molecular weight of the PVMs which is considerably larger than the FMs, and the inability of high frequencies to resonate the PVM particles inside the sample to show presence.

In order to test this hypothesis and investigate the effect of frequency on different molecular weight additives, the PAO blends were tested at both 400 kHz and 2 MHz.

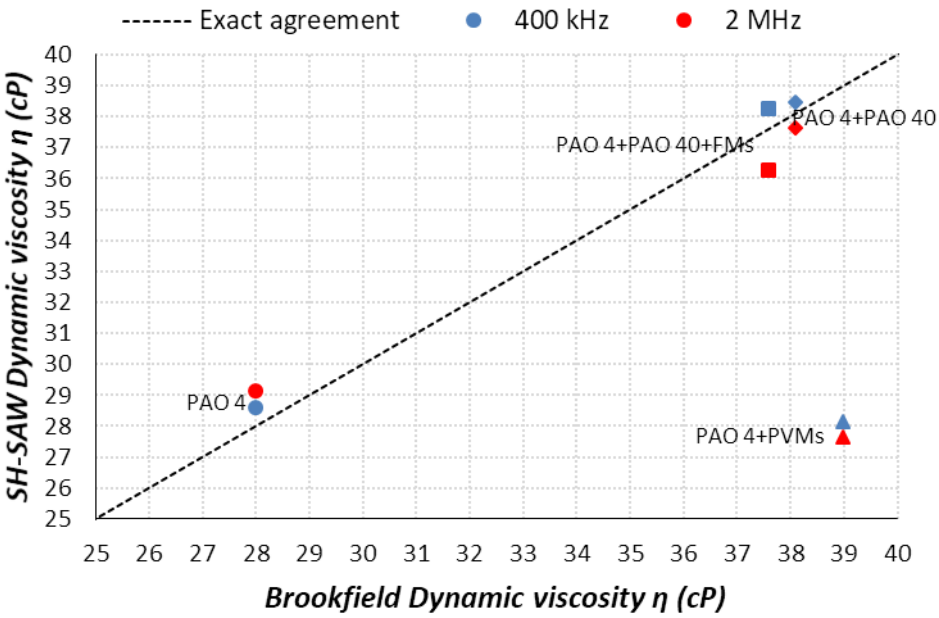

Figure 8.13 The effect of frequency on the FMs and PVMs

As it can be seen in Figure 8.13, there is a good agreement between the SH-SAW and Brookfield viscosities for all the samples, except for the PAO 4+PVMs. The viscosity of PAO 4+PVMs appears to be equal to the viscosity of pure PAO at both 400 kHz and 2 MHz. Furthermore, there is not a big difference between the viscosity values at the two frequencies, indicating that the resonant frequency of PVMs is much lower than 400 kHz. As a result, even lower frequencies are required to excite the PVM particles inside the sample to show presence.

8.3.3 The effect of temperature on the surface additives

Another parameter that may have prevented the detection of PVMs inside the sample is the temperature. The PVMs were designed to maintain the viscosity of the mixture within a certain range of temperature. As a result, at room temperature it is more likely to stay inactive and perhaps that is the reason they did not show presence in the previous tests (Section 8.3.2).

To explore the effect of temperature on the PVMs and FMs, the PAO 4 blends were tested from 25 to 60 °C at 2 MHz and the results can be seen in Figure 8.14. The Vogel equation (Equation 2.4) was used to validate the results, but only for the pure PAO 4, as Vogel equation does not take into consideration the presence of additives inside the oil. Three known viscosities at three temperatures, provided by Lubrizol Ltd., were used to calculate the a, b, c constants in Vogel equation, which can be seen in Table 7.4.

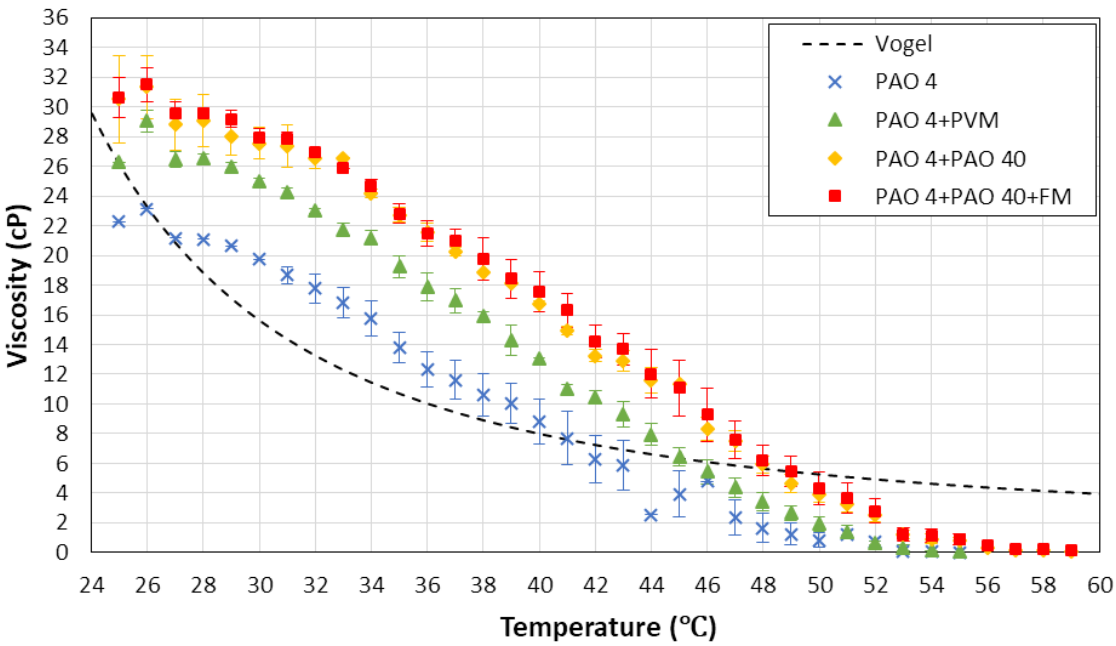

Figure 8.14 Temperature effect on the PVMs and FMs

As it can be seen in Figure 8.14, there is relatively good agreement between the measured and predicted values for the viscosity of the PAO 4. Temperature seemed to have a clear effect on the PAO 4+PVMs viscosity, which appeared to be higher than the viscosity of PAO 4. Lastly, temperature seemed to have no effect on the FMs, as it can be seen from the viscosity curves of the PAO 4+PAO 40 and PAO 4+PAO 40+FMs, which look alike. According to the viscosity curves of the four different samples in Figure 8.14, at temperatures above 45-50 ℃, viscosity decreases faster with temperature and reduces to almost zero above 55 ℃, for all oil samples. The same trend was noticed in sub-Section 7.2.2 for the PAO 8, 40 and 100, when tested from 25 to 100 ℃. It is clear that experimental set-up must be reviewed and actions need to be taken to overcome the shearing of the epoxy adhesive, due to the different thermal expansion coefficients between the steel plate and aluminium wedges.

8.4 Conclusions

In this chapter the SH-SAW response to the formation of viscous surface layers was investigated. For the purpose of the study, four lubricants were tested supplied by Lubrizol Ltd.; a pure PAO 4 and PAO 4+1% PVMs, a PAO 4+PAO 40 and PAO 4+PAO 40+ 1%FMs, for comparison. According to the supplier, the PVMs and FMs were expected to form surface layers a few nanometers thick of much higher viscosity than the viscosity of the mixture through *physisorption*.

Viscosity changes over time were monitored, for the detection of surface layer formation. According to the results, viscosity did not change for neither the PAO 4+1% PVMs, nor the PAO 4+PAO 40+1% FMs, indicating either that a surface film was not formed, or formed but was unable to be detected. Two reasons might have prevented the detection of surface layers; either the conditions for physisorption were not met so a surface film was not formed, or a few nanometers thick surface layers were insignificant compared to the SH-SAW penetration depth in the mixture.

A solution of Heptane+1% PVMs was used to investigate the surface layer thickness and penetration depth relationship. Heptane is a solvent and as such, after deposition it evaporated, leaving a residual PVM layer. Repeating this process multiple times allowed for control over the PVM layer thickness. According to the results from this investigation, a fully formed PVM layer could be detected through a **dry contact interface** with SH-SAWs, provided that the layer was sufficiently thick ($h_{PVM} > 4.6\ \mu m$). Additionally, pure PAO 4 was deposited on top of a 1.55 μm and 4.6 μm thin PVM layers to investigate whether their presence would affect the viscosity of PAO 4. Both PVM layers increased the viscosity of PAO 4 at different levels. According to the results, thin ($h_{PVM} \geq 1.5\ \mu m$)

surface layers could be detected through viscosity changes at a **wet contact interface**. There is a clear relationship between the SH-SAW penetration depth and surface layer thickness. In order to detect thin surface layers ($h_{surface\ layer} < 30\ nm$), the penetration depth of SH-SAWs needs to be reduced closer to the surface. Higher frequencies are required to allow penetration depth of a few nanometres. However, the known methods for generating SH-SAWs are currently limited to a few MHz.

In addition to the penetration depth-surface layer thickness investigation, tests were conducted over a range of temperatures for the four samples, in order to activate the PVMs and FMs to show presence. According to the results, temperature had a clear effect on the PVMs as it was expected, but it did not seem to affect the FMs. As a result, the conditions under which the samples are tested need to be taken into consideration, especially when looking at additive packages which may have different activation mechanisms.

9 MEASURING VISCOSITY OF OIL FILMS IN-SITU IN A JOURNAL BEARING

This chapter presents the implementation of the SH-SAW method in a journal bearing application for measuring viscosity of oil films in-situ. The experimental configuration for the purpose of this study is presented in detail, including the transducers for wave generation, the instrumentation of the medium and installation in a journal bearing rig, signal triggering and signal acquisition hardware. This is followed by the signal processing method to meet the requirements of the application. Different oils were tested under different loading conditions to vary the oil film profile and hence the oil viscosity, in order to study the effect of pressure on oil viscosity. The results were then compared to the viscosity as it was measured with an ultrasonic shear sensor.

9.1 Experimental configuration

This section describes the experimental configuration that was used for measuring oil viscosity in-situ in a dynamic system, as well as the equipment for triggering an ultrasonic signal, acquiring the received signal and further processing it in order to obtain the ultrasonic response to the oil film viscosity.

9.1.1 Journal bearing rig

For the purpose of this study, a journal bearing rig was designed, as shown on Figure 9.1. An electric motor was used to drive the journal, a starter to initiate the motor, an inverter to control the motor speed and direction of rotation, a guarding frame to protect the user from exposing to any moving parts, oil spillages or other potential hazards, and a journal-bearing assembly for measuring oil viscosity in a lubricant film.

Figure 9.2 shows a closer view of the journal-bearing assembly, which consisted of:

- two "lever" plates, that were used for the bearing housing installation and applying load on the journal. The load was applied on one end of the plates with a hydraulic jack , while the other end was on a pivot, hence the plates acted as a lever
- a hydraulic jack, for applying load on the journal using a hydraulic pump
- a single 2-part bearing housing, to allow installation of two bearing sleeves in order to replicate engine components. A feeding hole was designed on the upper housing to allow oil supply, while two drain holes were designed on the lower housing to allow the oil to flow inside an oil container

- a load cell, for measuring the applied load from the hydraulic jack, so it can be converted to applied load on the journal, through the "lever" plates geometry
- two self-aligning roller bearings, for supporting the journal
- a slip ring, to allow for the transducer wires coming out of rotating parts to be connected to stationary parts, without breaking
- an optical encoder, for measuring the location of the rotating journal during testing
- thermocouples, for measuring the temperature of the oil at different locations during testing
- ultrasonic transducers, for measuring oil viscosity in a running journal-bearing film

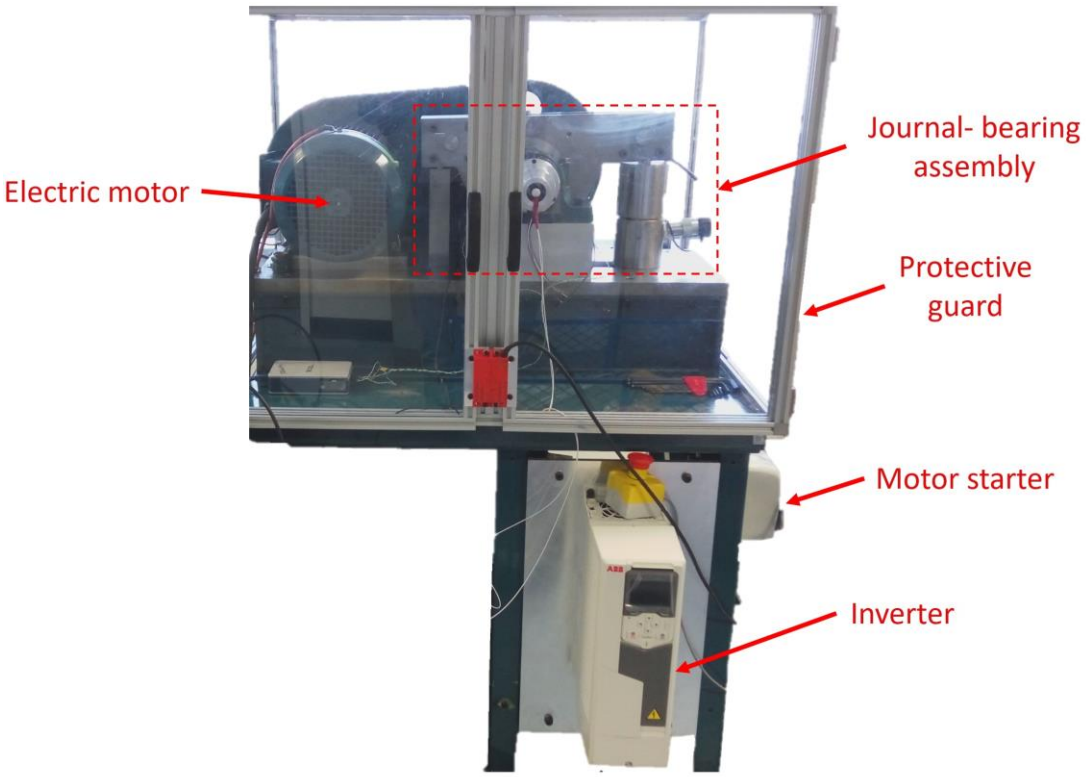

Figure 9.1 Journal bearing rig for measuring oil viscosity in a dynamic system

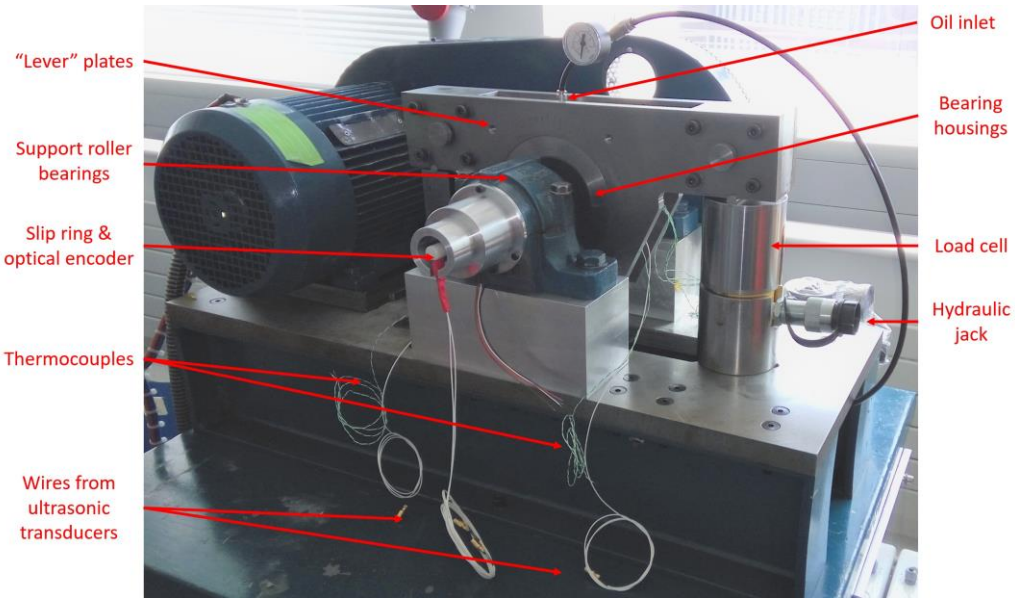

Figure 9.2 Journal-bearing assembly component description

The lubrication of the rotating journal was achieved by pumping oil through a feeding hole on the upper bearing sleeve. A tube ran through the upper housing, down to the bearing sleeve feeding hole, to allow oil to flow between the bearings and the journal. The oil supply was achieved using an oil container and an electric pump, as it can be seen in Figure 9.3.

The test sample was placed inside the oil container underneath the journal-bearing assembly, and it was supplied in the system using the electric pump. The oil was supplied continuously to ensure adequate lubrication and collected back inside the oil container through two drain holes, designed on the bottom housing. As a result, the oil was circulating in the system, similarly to a running engine.

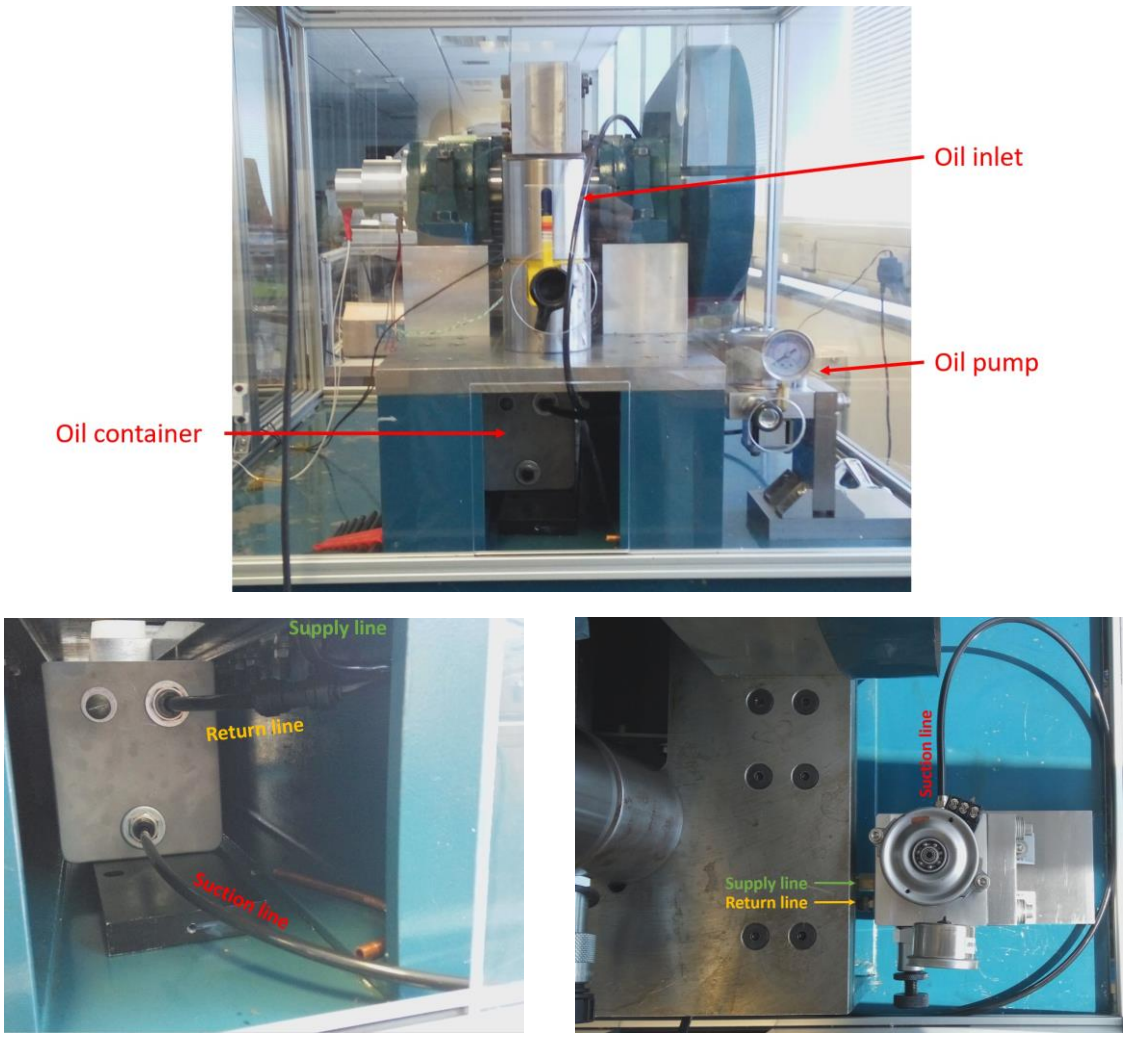

Figure 9.3 System lubrication *(top)*, oil container *(bottom right)*, oil pump *(bottom left)*

9.1.2 Ultrasonic transducers

Measurements of viscosity inside the oil film between journal and bearing, were performed using two methods. The SH-SAW attenuation at a solid-liquid interface was used to determine the SH-SAW transmission coefficient, which was used to calculate the oil viscosity, as described in the Chapter 7. Reflected shear BAWs from a solid-liquid boundary were used to determine the shear reflection coefficient, which was used to calculate the oil viscosity, as described in Section 4.2.

A bearing sleeve was instrumented with two SH-SAW angled transducers to study the attenuation of SH-SAWs along the bearing-oil interface. The journal was instrumented with an ultrasonic shear transducer to study the reflection of shear waves at the journal-oil boundary. A schematic of the bearing and journal instrumentation is shown in Figure 9.4.

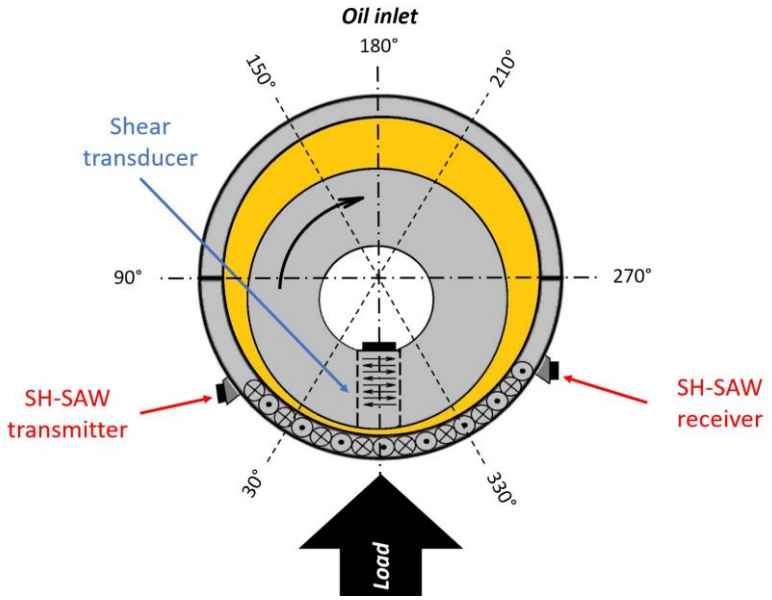

Figure 9.4 Journal & bearing instrumentation with shear and SH-SAW transducers, respectively

Four thermocouples were bonded on the bearing sleeves at 30°, 150°, 210° and 330°, to monitor the oil temperature circumferentially. According to Figure 9.4, only the bottom bearing sleeve was instrumented with SH-SAW transducers, since load was applied from below, normal to the bearing, thus decreasing the oil film thickness around that region and increasing the oil viscosity, as pressure was building up. Instrumenting the journal with an ultrasonic shear transducer allowed for circumferential measurements of viscosity to be performed around the oil film.

- ***Bearing sleeve instrumentation with SH-SAW angled transducers***

Figure 9.5 shows the instrumentation of a bearing sleeve with two SH-SAW angled transducers. Big end bearings for Audi 1.6 & 1.9 TDi passenger cars were used in this study, the properties of which can be seen in Table 9.1. The SH-SAW angled transducers were manufactured using 2 MHz shear piezo-ceramics bonded on two aluminium wedges. Aluminium was selected for this application instead of Perspex, due to its good mechanical properties, good coupling with steel and ability to withstand higher temperatures than Perspex (<60°C).

The two transducers were bonded on the bearing sleeve at 60° and 300°, with respect to Figure 9.4, using high temperature epoxy, which offered stable coupling between the transducers and the bearing sleeve, over a large range of temperatures.

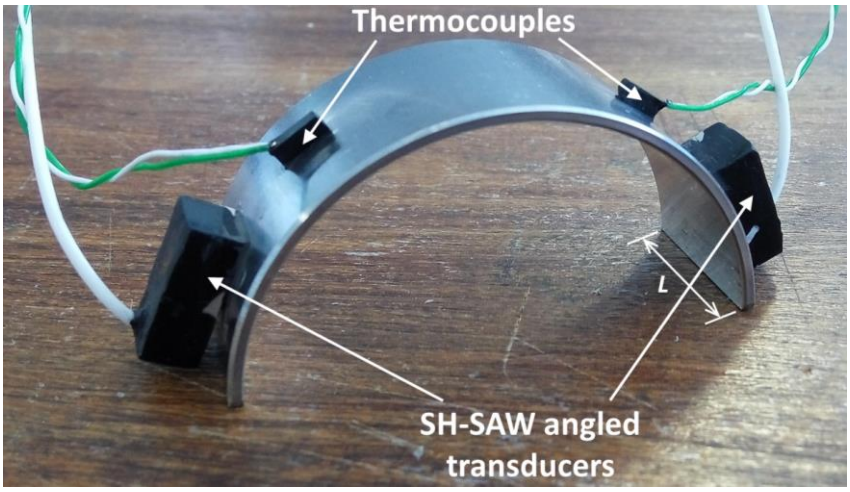

Figure 9.5 Bearing sleeve instrumentation with SH-SAW angled transducers

Table 9.1 Journal-bearing specifications

Component	*Main Material*	*Diameter D (mm)*	*Wall thickness (mm)*	*Length L (mm)*
Big end bearing	Steel	47.796	1.402	20.000
Journal	Steel	47.697 / 47.687	-	38.000
Housing	Steel	50.599 / 50.612	-	37.500

After instrumentation, the bearing sleeve was installed in the housing, as shown in Figure 9.6. The housing inner diameter was designed according to Table 9.1, in order to meet the bearing requirements for installation, and the design can be seen in Figure 9.7. Apparently the clamping between the housings led to a decrease in the amplitude of the signal, as it can be seen in Figure 9.8. This most likely occurred, due to the compression of the angled transducers between the bearing sleeve and the housing wall, which may have reduced the adherence of the epoxy and the coupling of the wedges with the bearing sleeve.

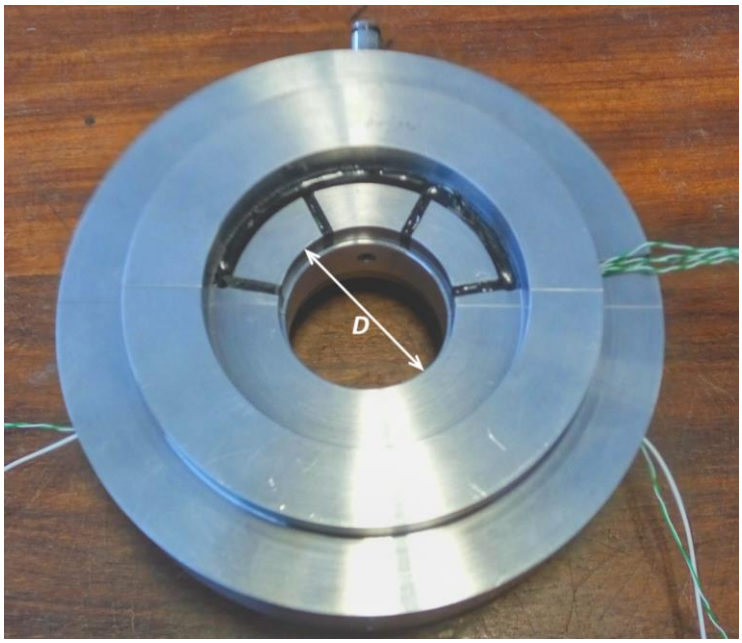

Figure 9.6 Bearing clamped between the two housings

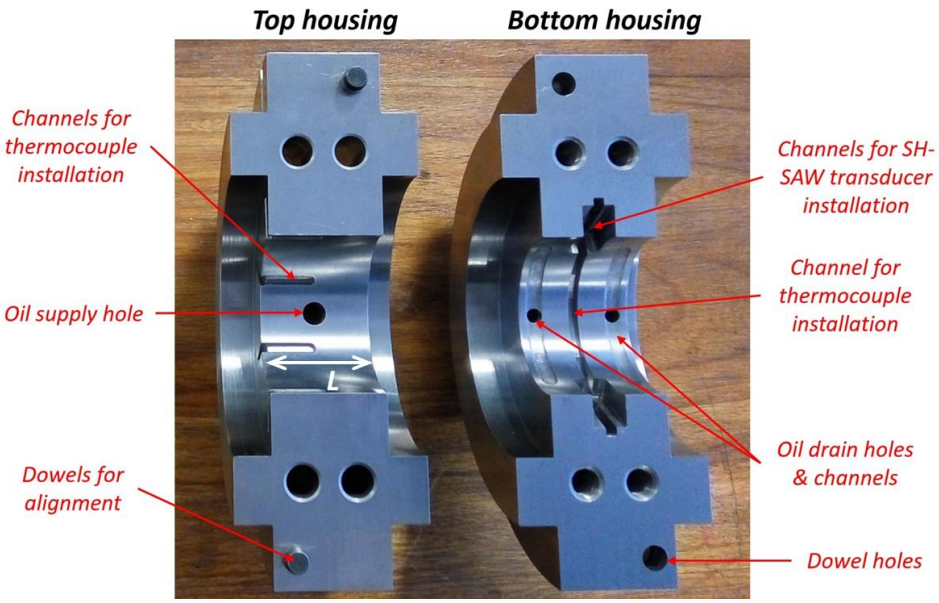

Figure 9.7 Top and bottom housing designs for bearing sleeve installation

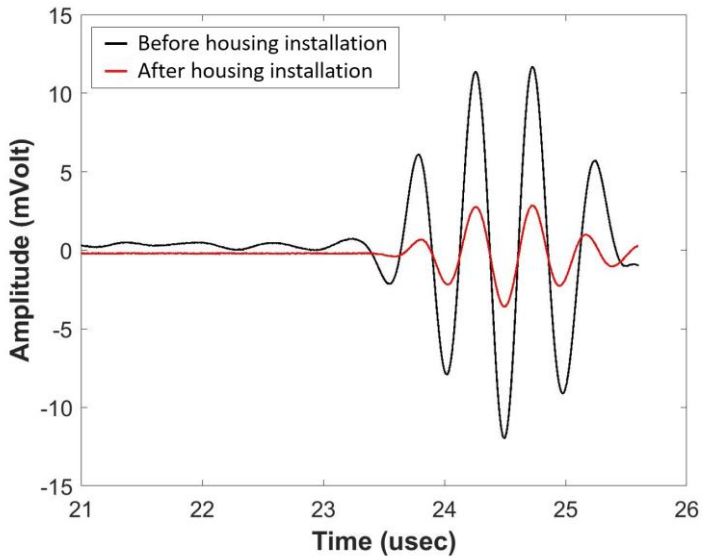

Figure 9.8 Comparison of the SH-SAW signal before and after installing in the housings

After installation inside the housing, the bearing was placed in an oven for temperature calibration, as shown in Figure 9.9. Temperature calibration was required in order to extract the effect of temperature on the bearing and transducers. The calibration process was performed three times to ensure consistent signal response to temperature change and obtain the temperature calibration curve (as shown in Figure 9.10). The amplitude of the signal was measured from 23 to 80 °C, every 1 °C and the temperature calibration coefficient was calculated by dividing the amplitude of the signal at each temperature with the amplitude of the signal at 25 °C, which served as the signal reference. Results are shown in Figure 9.10. The temperature calibration coefficient decreases with temperature (similarly to Figure 7.7), most likely due to the different thermal expansion coefficients of the steel bearing sleeve and the aluminium wedges, which led to shearing of the epoxy adhesive.

Figure 9.9 Temperature calibration of the bearing & housing

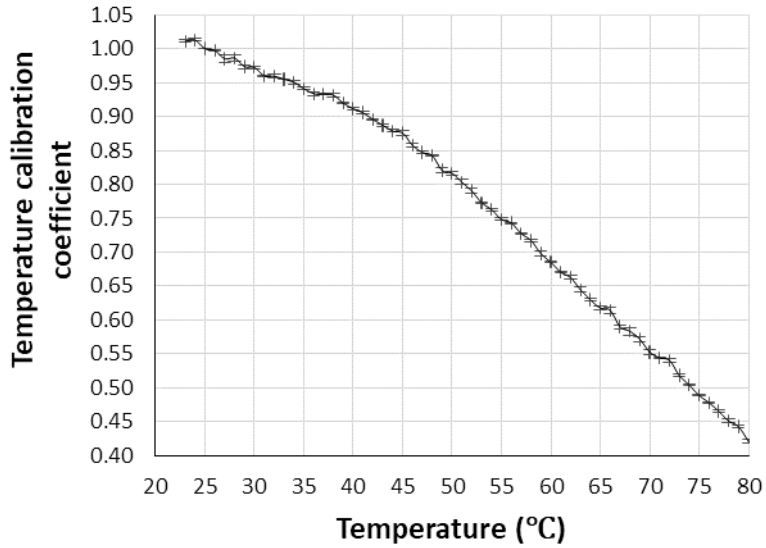

Figure 9.10 Temperature calibration curve for the bearing sleeve

- ***Journal instrumentation with a shear BAW transducer***

An ultrasonic shear transducer was manufactured and installed inside a journal, for measuring the viscosity inside the oil film. The shear BAW transducer was manufactured using an aluminium plug (Figure 9.11), instrumented with a 3 mm x 3 mm, 5 MHz thickness-shear piezo- ceramic, as shown in Figure 9.12.

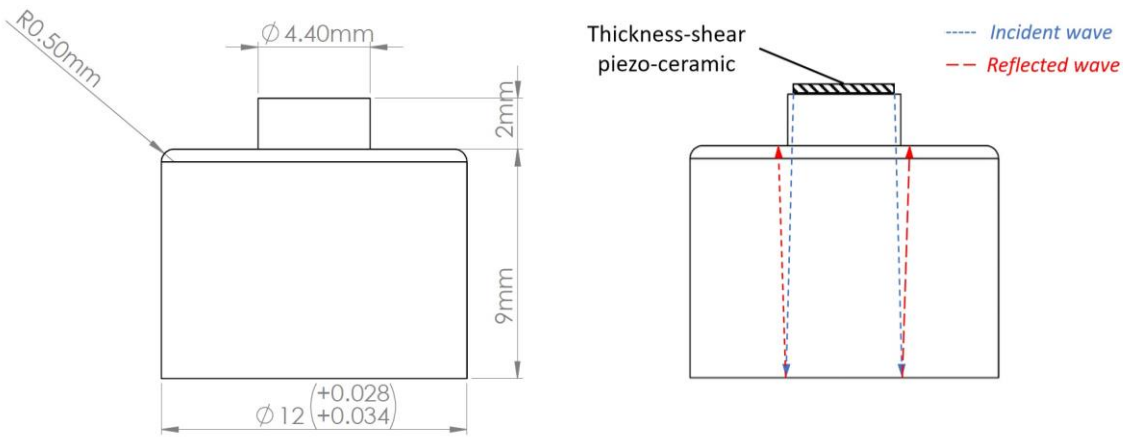

Figure 9.11 Aluminium plug schematic *(left)* and shear wave propagation *(right)*

The plug was designed with a small step for the piezo-ceramic bonding. The step ensured that the reflected waves from the boundary would be guided through a narrower path before reaching the piezo-ceramic, leading to more concentrated energy received by the piezo-ceramic, thus improving the signal resolution. After wiring the piezo-ceramic, a copper collar was installed around the step and filled with backing epoxy to secure the

connections and protect the piezo-ceramic from the harsh environment of a lubricated, rotating journal.

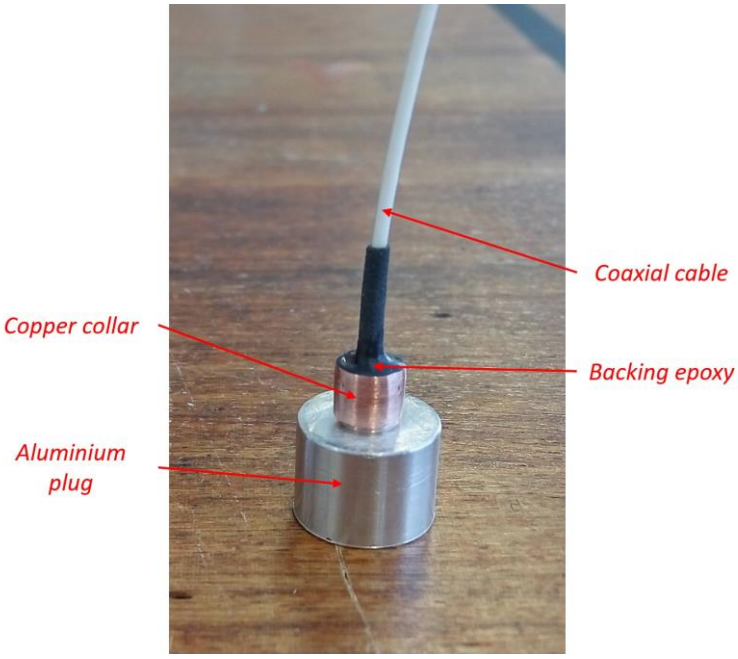

Figure 9.12 Ultrasonic shear transducer

The plug was then press fit inside the middle section of a hollow steel journal (to allow access to the transducer wire), as shown in Figure 9.13 and sent for grinding to meet the requirements for the bearing installation, according to Table 9.1. The plug was ground as well, in order to follow the contour of the journal. After grinding, the plug was further pushed inside the journal using a 50 µm shim, to account for the *matching layer* thickness.

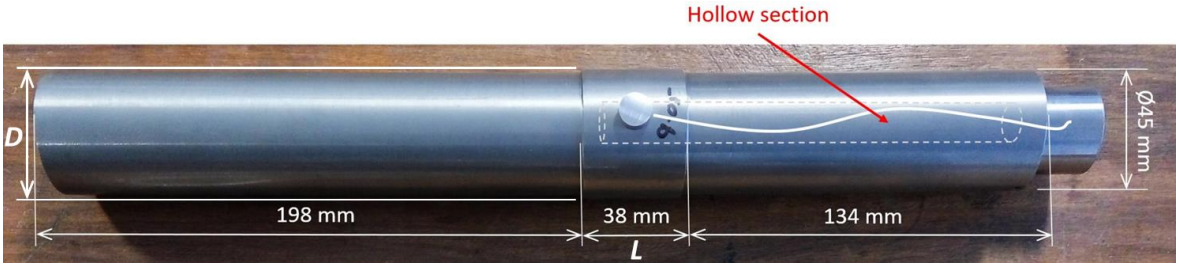

Figure 9.13 Shear plug installation on the journal

A matching layer was required as stated in Section 4.2, to improve the acoustic mismatch between the aluminium and the oil (Table 9.2), by adding a layer with acoustic impedance between the impedances of the two materials. Polyimide was selected as a matching layer due to its acoustic impedance, resistance against chemical corrosion and high melting point, which makes it suitable for measuring oil viscosity over a range of temperatures.

The thickness of the polyimide layer was selected to be equal to ¼ the shear wavelength, in order to make the layer resonate, thus increase the sensitivity of the ultrasonic shear transducer. The shear wave velocity in polyimide is 780 m/s and for a 5 MHz shear wave the corresponding wavelength is 156 μm. Then the matching layer thickness should be 39 μm according to the ¼ wavelength theory. The closest polyimide sheet to that thickness was 50 μm, which in theory corresponds to 3.9 MHz resonant frequency, but in reality was found to resonate at 4.4 MHz.

Table 9.2 Acoustic impedances of oil, polyimide and aluminium

Material	***Density ρ*** **(kg/m³)**	***Longitudinal speed of sound*** c_L **(m/s)**	***Shear speed of sound*** c_S **(m/s)**	***Acoustic impedance*** $Z = \rho c_L$ **(MRayls)**
Oil	~ 900	1490	-	1.34
Polyimide	1420	2440	780	3.46
Aluminium	2700	6370	3100	17.20

A polyimide layer was cut from the sheet to fit the dimensions of the plug, and carefully bonded on with a strain gauge adhesive. Figure 9.14 shows the ultrasonic shear transducer after the application of the matching layer. Similarly to the bearing sleeve, the journal was calibrated with temperature, to extract its effect on the journal and shear transducer, and left with its effect on viscosity. The process was repeated three times to ensure consistent signal response and the results can be seen in Figure 9.15. The temperature calibration coefficient was calculated by dividing the amplitude of signal at each temperature with the amplitude of the signal at 25 °C, which served as the reference.

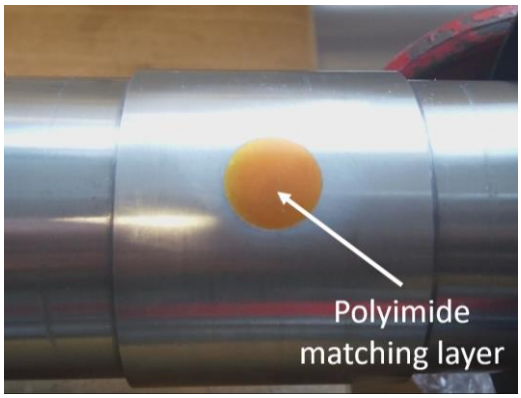

Figure 9.14 The miniaturised ultrasonic shear transducer installed in the journal

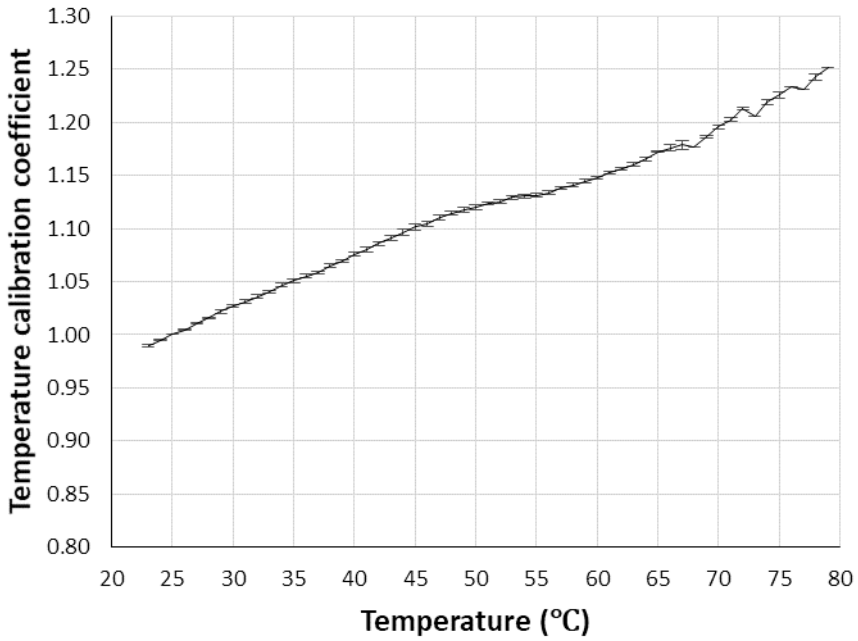

Figure 9.15 Shear transducer temperature calibration curve

In Figure 9.15, the temperature calibration coefficient increased with temperature. Possible reasons include changes in the bond-line with temperature, the backing and/or the electrical characteristics of the transducers/wiring.

After the journal and the bearing were instrumented and calibrated, they were installed carefully in the rig, for testing.

9.2 Signal excitation, acquisition & processing

For the purpose of this study, a function generator, a picoscope and an optical encoder were used to send and receive the ultrasonic signals. Matlab scripts were used to process the acquired signals, including the ultrasonic signals, the thermocouple readings and the optical encoder signal. The shear and fundamental SHo modes were isolated and the reference amplitudes were extracted from the temperature calibrations at the solid-air interface, depending on the temperature of the test at the solid-liquid interface. The reflection and transmission coefficients were calculated then from the ratio of the test amplitude over the reference amplitude, for the case of reflected shear BAWs from the journal-oil boundary and transmitted SH-SAWs along the bearing-oil interface, respectively.

9.2.1 Signal excitation & acquisition

The function generator was used to excite the angled SH-SAW transmitter, while the picoscope was used to excite the shear ultrasonic transducer. The selection was made according to the voltage capabilities of the function generator and picoscope, and the requirements of the SH-SAW and shear transducers. It is worth noting here that the picoscospe operates as both a digitiser and an arbitrary waveform generator.

As it was seen in sub-Section 9.1.2, the SH-SAW signal was distorted after the bearing was installed in the housing, due to the compression of the angled transducers between the housing and the bearing sleeve. As a result, high input voltage was required to allow for the SH0 mode to be generated. The maximum output voltage of the function generator is 10 Vpp, which was enough to generate a clear wave. Any further amplification would result in the amplification of the noise as well, and further hardware would be required to filter it out. For the shear transducer on the other hand, the 4 Vpp output from the picoscope was sufficient to generate strong shear waves.

The picoscope was used in both cases to receive the ultrasonic signals. The version of the picoscope that was used in the tests, consists of 4 input (receiving) channels and one output (4 Vpp arbitrary waveform generator), which allowed pulsing the shear transducer, while receiving the shear reflection in one channel and the SH0 mode in another. The SH-SAW and shear transducers were excited using the parameters in Table 9.3, and the signals as they were acquired with the picoscope, can be seen in Figure 9.16 and Figure 9.17.

Table 9.3 Excitation parameters for SH-SAW & shear transducers

Transducer	***Excitation method***	***Excitation mode***	***Excitation type***	***Cycles***	***Frequency***	***Input voltage***	***Acquisition method***
SH-SAW	Function generator	Burst	Sine pulse	2	2 MHz	10 Vpp	Picoscope (Channel A)
Shear	Picoscope	Burst	Sine pulse	10	4.4 MHz	4 Vpp	Picoscope (Channel B)

In both cases, sinusoidal burst pulses (finite pulse duration) were used to excite the transducers, in order to allow for coexisting waveforms to be distinguished and isolate the shear and SH0 modes, respectively. The number of cycles was selected according to the

wave period, to prevent coexisting waveforms from overlapping, while increasing the wave energy as much as possible. In the case of SH-SAWs for example, only 2 cycles were used that led to low energy waves (wave amplitude in Figure 9.16), due to the SH-SAW period and time of appearance, compared to the time the following wave was received. In the case of shear waves on the other hand, the time separation between successive waves was large enough to allow 10 cycles to be used, which allowed high energy waves to be generated (wave amplitude in Figure 9.17).

In Figure 9.16, three SH-SAW modes were distinguished according to time-of-flight measurements, the fundamental SH0 mode, SH1 and SH2 modes, for thickness-frequency product of 2800 mm Hz, which agrees with the dispersion theory in Section 3.4.3.

In Figure 9.17, the first shear reflection was generated, according to time-of-flight measurements. Apart from the 1st shear reflection, the 2nd shear reflection was also captured in the waveform graph.

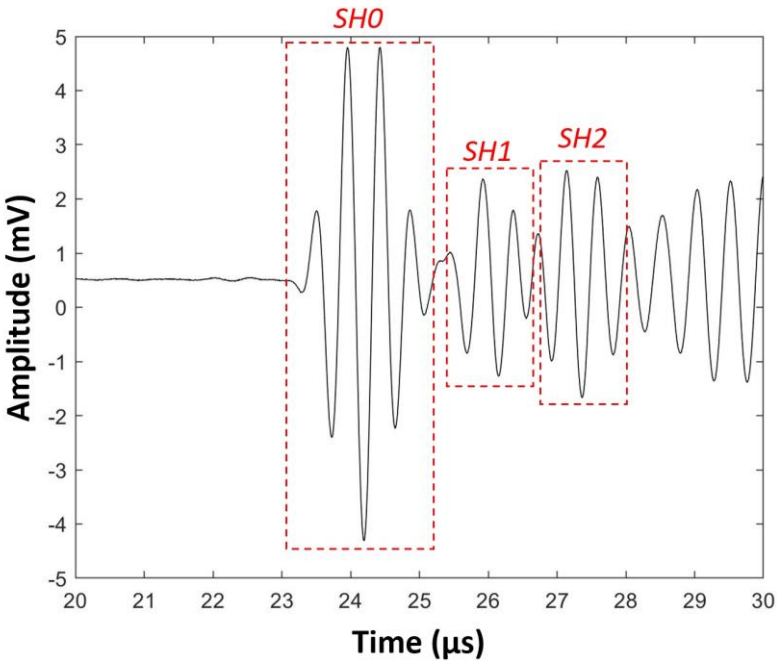

Figure 9.16 SH-SAW signal response in the time domain, as acquired with the picoscope

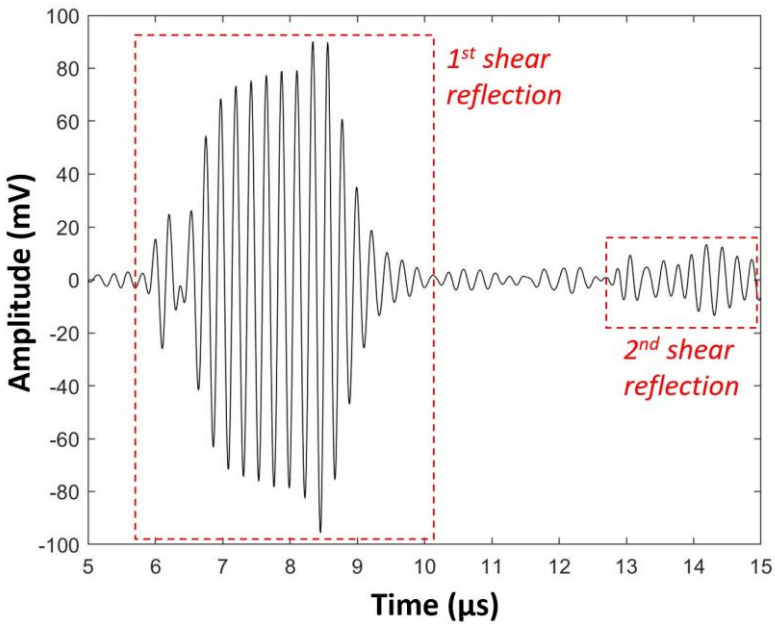

Figure 9.17 Shear wave signal response in the time domain, as acquired with the picoscope

An optical encoder was employed to measure the location of the shear transducer relative to the location of the encoder module, while the journal was rotating. Figure 9.18 shows the installation of the patterned disk on the journal and the location of the encoder module. In the signal processing, that allowed the separation of the number of cycles the journal has completed, during signal acquisition. An optical sensor was monitoring the rotation of the patterned disk, attached to the journal. Once per revolution, the optical sensor read the index pattern and the encoder module produced a 10 Vpp pulse, as shown in Figure 9.19. Two consecutive pulses indicated a full journal rotation. The 10 Vpp index pulse from the encoder module was captured using the picoscope. The encoder module pulse and shear transducer signal were acquired simultaneously, for 3 full journal rotations. The acquisition rate of the picoscope is fast enough that allowed 2 captures/1 degree and 30 waveforms/capture, to be acquired. That resulted in circumferential measurements of the shear reflection response to oil film viscosity, as the journal rotated.

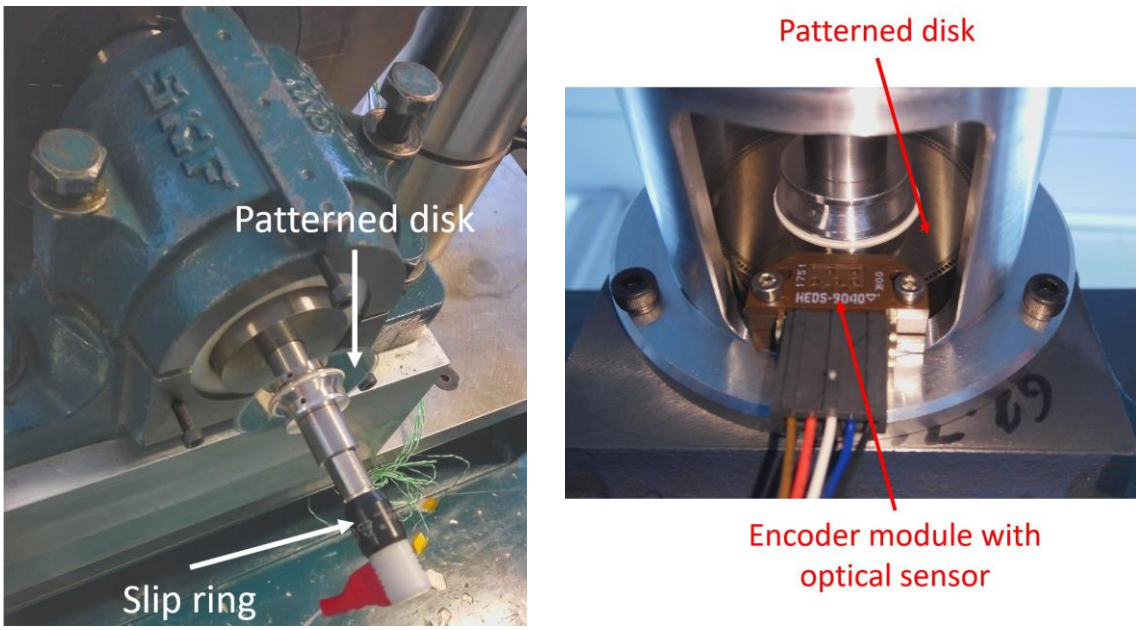

Figure 9.18 Optical encoder model installed on the journal for measuring the number of revolutions

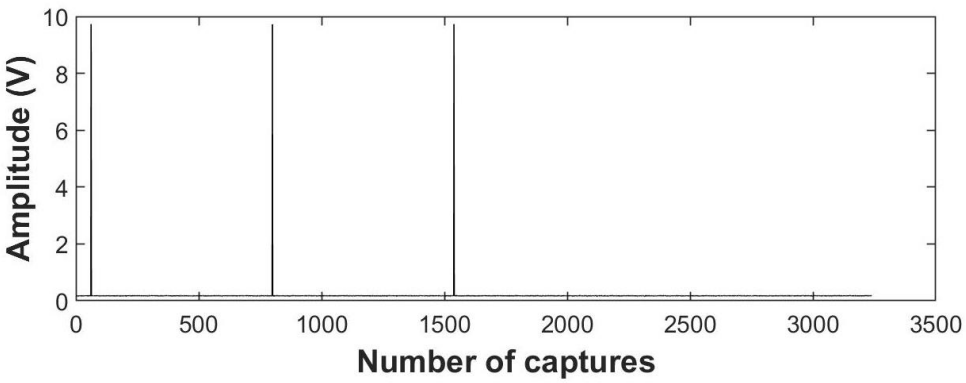

Figure 9.19 Encoder index pulses indicating two complete journal cycles, as they were acquired using the picoscope

Figure 9.20 shows a schematic of the signal excitation and data acquisition set up. The signal from the shear transducer (Channel B) and encoder module (Channel C), were acquired simultaneously, in order to locate the shear transducer as the journal rotated. The SH-SAW signal (Channel A) was captured separately, since locating the transducers was not required, as they were fixed on a stationary bearing sleeve. In order to reduce the signal noise and improve the resolution, 30 waveforms were acquired per capture and averaged in the signal processing, for the SH-SAW and shear transducers, as well as the optical encoder.

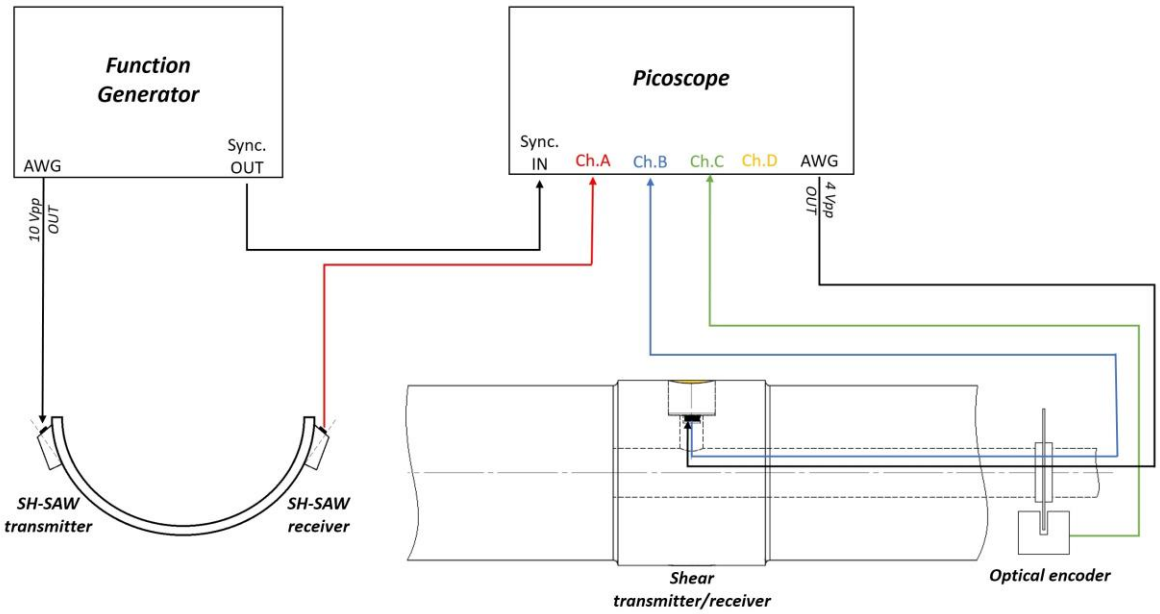

Figure 9.20 Signal excitation & data acquisition schematic

After the signals were acquired, they were imported in Matlab for processing, in order to extract the reflection and transmission coefficients, which were then used to calculate the oil viscosity.

9.2.2 Signal processing

Custom Matlab scripts were used to process the signals after acquisition. The SH-SAW and shear BAW data, along with the encoder data and the readings from the 4 thermocouples, were imported in Matlab for processing.

The data from the SH-SAW and shear BAW transducers were processed following the steps as described in Section 5.4; first they were averaged, then the shear and SH0 modes were isolated, respectively, and then the Fourier transform was applied to extract the maximum amplitude and the frequency it occurred.

According to the temperature of each capture at the solid-liquid interface, the reference amplitude of the wave was extracted automatically, from the temperature calibrations at the solid-air interface. The wave extraction process and fast Fourier transform can be seen in Figure 9.21 and Figure 9.22 for the SH-SAW and shear waves, respectively.

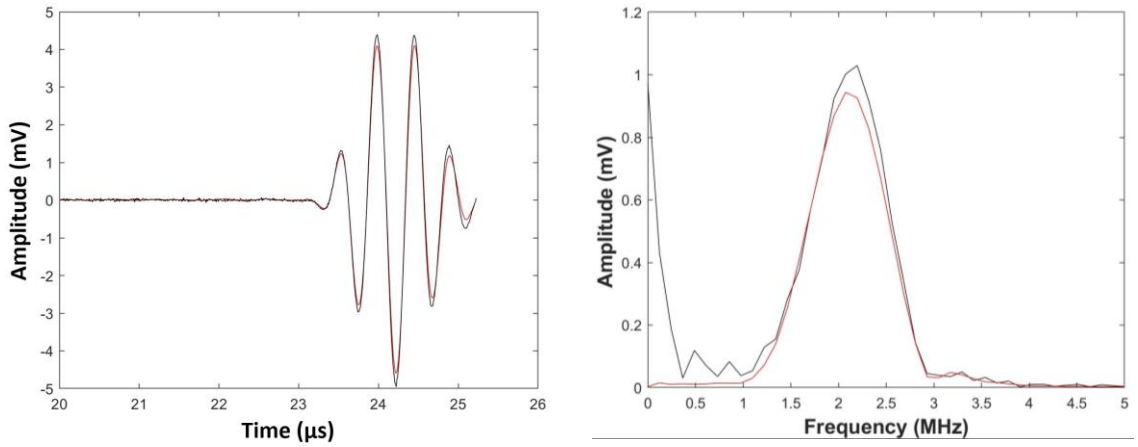

Figure 9.21 SH-SAW signal processing; SH0 mode extraction *(left)* and FFT of the signal *(right)*. The black lines represent the reference signal at the solid-air interface, while the red lines represent the test signal at the solid-liquid interface

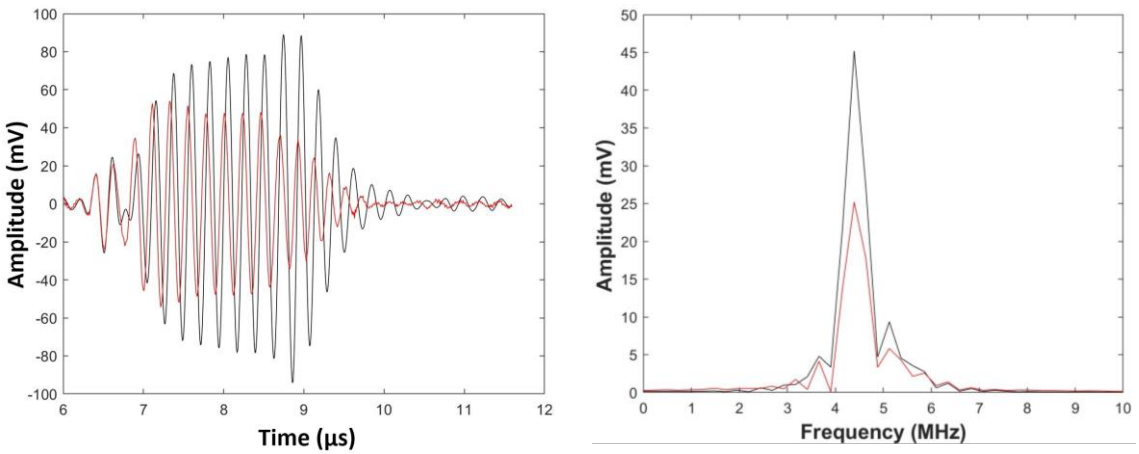

Figure 9.22 Shear signal processing; shear mode extraction *(left)* and FFT of the signal *(right)*. The black lines represent the reference signal at the solid-air interface, while the red lines represent the test signal at the solid-liquid interface

After the amplitudes at the solid-air and solid-liquid interfaces were obtained for both the SH0 and shear wave modes, the transmission and reflection coefficients were calculated, respectively, as shown in Figure 9.23 and Figure 9.24.

In the case of the SH0 mode, the transducers were in a fixed position, offering measurements over time but fixed in space. As a result, the transmission coefficient was averaged from the number of captures, since the acquisition time was negligible for the oil conditions to change. In the end, the script returned a single transmission coefficient value for each individual test.

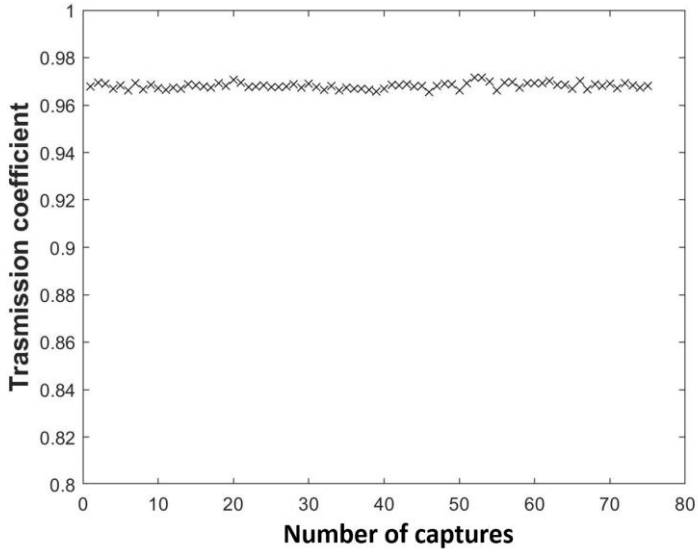

Figure 9.23 Transmission coefficient of the SHo mode at the solid-liquid interface

In the case of the shear wave mode, the shear transducer was rotating with the journal, offering measurements over both time and space. Figure 9.24 shows the shear reflection coefficient for four full journal rotations. However, it was difficult to relate the results to the journal location, since the shear transducer could be anywhere around the circumference of the journal when the signal was acquired. For this reason, the signal from the encoder was also used, to relate the shear reflection coefficient to the journal location. Two consecutive peaks in the encoder signal indicated one complete journal rotation, as shown in Figure 9.19.

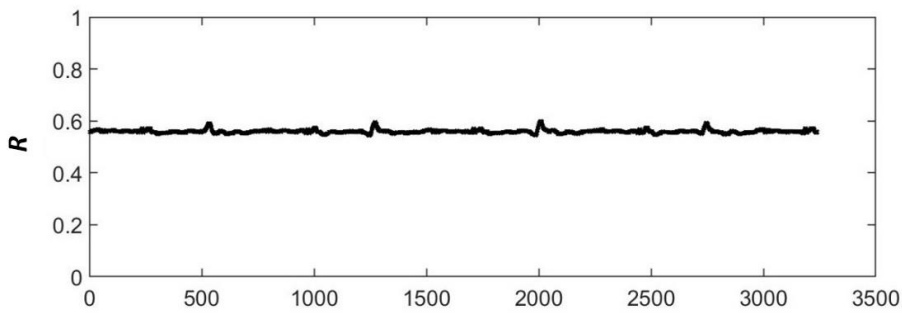

Figure 9.24 Shear wave reflection coefficient, at the solid-liquid boundary of a rotating journal

The reflection coefficient was then extracted within the boundaries of these peaks, in order to obtain its circumferential profile for a full journal rotation, as shown in Figure 9.25.

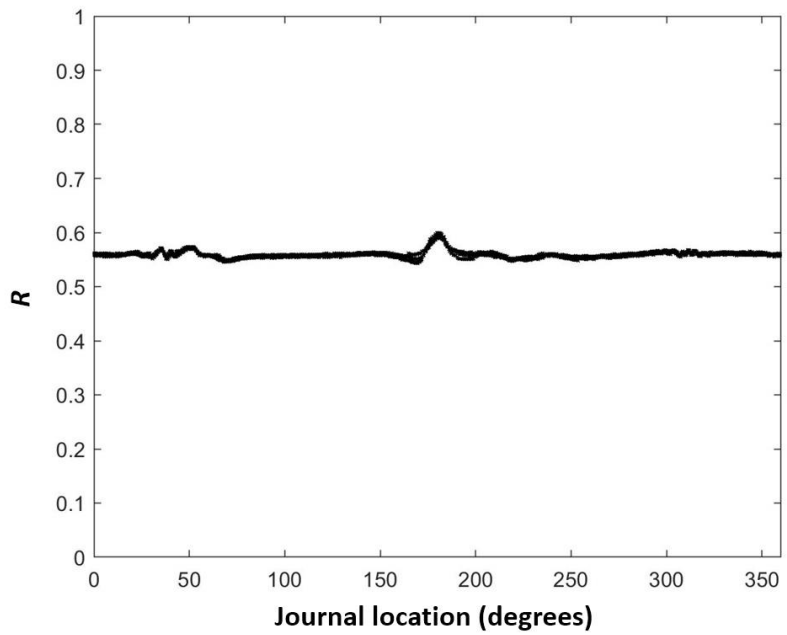

Figure 9.25 Circumferential shear reflection coefficient for a complete journal rotation

After the reflection and transmission coefficients were obtained, they were imported in Equations 4.1 and 6.24, respectively to calculate the oil film viscosity, as explained in the following section.

9.3 Determining viscosity in oil films

This section presents the viscosity results of different lubricant oils, as they were measured with the SH-SAW angled transducers and the ultrasonic shear BAW transducer, respectively.

The SH-SAW transmission coefficient T was imported in Equation 6.24 to obtain the average oil viscosity in the lower bearing sleeve:

$$\eta = 2\frac{\left[ln\left(\frac{1}{T}\right)2d_s\rho_s c_s^{air}\right]^2}{\rho_l\omega\, l^2} \tag{6.24}$$

The bulk shear reflection coefficient R was imported in Equation 4.1, to obtain the oil viscosity profile:

$$\eta_l = 2\frac{{Z_s}^2}{\omega\rho_l}\frac{cos^2(\theta_l)}{cos^2(\theta_s)}\frac{R\left(1-R^2\right)sin\varphi}{(1+R^2+2Rcos\varphi)^2} \tag{4.1}$$

where, θ_l= θ_s= 0° for normal incident shear waves and φ= 90°, for reflected waves from a solid-liquid boundary [43], which leads to:

$$\eta_l = 2\frac{{Z_s}^2}{\omega\rho_l}\frac{R\left(1-R^2\right)}{(1+R^2)^2} \tag{9.1}$$

According to Schirru et al. [60], the acoustic impedance of the solid for a layered system is given by:

$$Z_S = \frac{{Z_P}^2}{Z_A} \tag{9.2}$$

where Z_P is the acoustic impedance of the polyimide layer, and Z_A is the acoustic impedance of the aluminium plug.

Table 9.4 shows the parameters that were used in Equations 6.24 and 9.1, to measure oil film viscosity.

The four PAO 4 blends (Section 8.2), provided by Lubrizol Ltd., were used for the purpose of this study. The samples were tested at a journal speed of 540 rpm, without any load and with 0.5 kN, 1.0 kN and 1.5 kN of load, in order to vary the oil film thickness, and as a result the pressure, and hence the oil film viscosity. The low speed (540 rpm) and low loads (0-1.5 kN) were selected for the safety of the user and the surroundings, and safe operation of the rig. These conditions should be sufficient to vary the oil film thickness enough, to increase the oil film pressure and as a result, the oil film viscosity to increase. Measuring the viscosity changes with both shear BAWs and SH-SAWs would provide encouraging evidence for use in actual engine bearings.

The results from the shear BAW and SH-SAW measurements of oil film viscosity, are presented in the following sub-sections.

Table 9.4 Equation parameters for measuring oil viscosity, from the transmission and reflection of SH-SAWs and shear BAWs, respectively

Method	Medium thickness d_s (m)	Path length l (m)	Medium speed of sound c_s (m/s)	Medium density ρ_s (kg/m³)	Oil density ρ_l (kg/m³)	Wave angular frequency ω (rad/s)
Equation 6.24	0.0014	0.054	3200	7850	900	$4\pi\ 10^6$
Equation 9.1	-	-	c_A = 3100	ρ_A = 2700	900	$8.8\pi\ 10^6$
			c_P = 780	ρ_p = 1420		

9.3.1 SH-SAW measurements of oil film viscosity

In the case of the SH-SAWs, viscosity was measured for the region between 300° to 60° (Figure 9.4), where the two SH-SAW transducers were located and the results were compared with numerical models for validation.

The Vogel equation (Equation 2.4) was used to predict the viscosity of the four oils, over a range of temperatures. Then the predicted viscosity values were used in Barus equation (Equation 2.5) to predict the viscosity over temperature and the pressure which developed due to the 0.5, 1.0 and 1.5 kN load. For simplicity, it was assumed that the load, F, was carried by the bottom bearing sleeve and that it was equally distributed over the bearing sleeve area A, thus leading to Equation 9.3 for calculating the pressure p in the oil film. The expected pressure due to the various loads is given in Table 9.5.

$$p = \frac{F}{A} \tag{9.3}$$

The viscosity-pressure coefficient α of "medium VI spindle oil" from Table 2.3 in [1], shown in Table 9.6, was used to predict the viscosity of the oils over pressure, due to the similar viscosity values. In the case of the PAO 4 blends, the viscosity-temperature response might have been somewhat different than the actual response, since any additives in the oil are not taken into consideration by the Vogel equation. The Vogel constants for predicting the viscosity of the PAO 4 blends over temperature are shown in Table 9.7.

Table 9.5. Oil film pressure due to load

Load (N)	Area (m²)	Pressure (Pa)
500	*L* x *D*	523,013
1000	(Table 9.1)	1,046,025
1500	0.000956	1,569,038

Table 9.6. Viscosity-pressure coefficient α for medium VI spindle oil [1]

#	Viscosity measured at atmospheric pressure (cP)			Pressure viscosity coefficient α (10^{-9} m²/N)		
	30 ℃	*60 ℃*	*100 ℃*	*30 ℃*	*60 ℃*	*100 ℃*
Medium VI spindle oil	18.6	6.3	2.4	20	16	13

Table 9.7 Three known viscosity values at three temperatures (provided by Lubrizol Ltd.), which were used to calculate the Vogel constants, to predict the viscosities of the PAO 4 blends over temperature

#	*Temperature*			*Vogel constants*		
	25 °C	**40 °C**	**100 °C**	***a***	***b***	***c***
PAO 4	26.15	8	2.2	0.8705	95.5859	-3.0922
PAO 4+1%PVM	36.31	21.38	5.18	0.1013	891.239	-126.53
PAO 4+1%PAO 40	36.06	20.64	4.73	0.09	874.55	-121.03
PAO 4+1%PAO 40+1%FM	35.88	20.51	4.69	0.0917	866.08	-120.09

Figure 9.26 shows the results from the application of SH-SAWs to measure oil film viscosity in dynamic conditions, in comparison to the predicted viscosity from the combination of the Vogel and Barus equations.

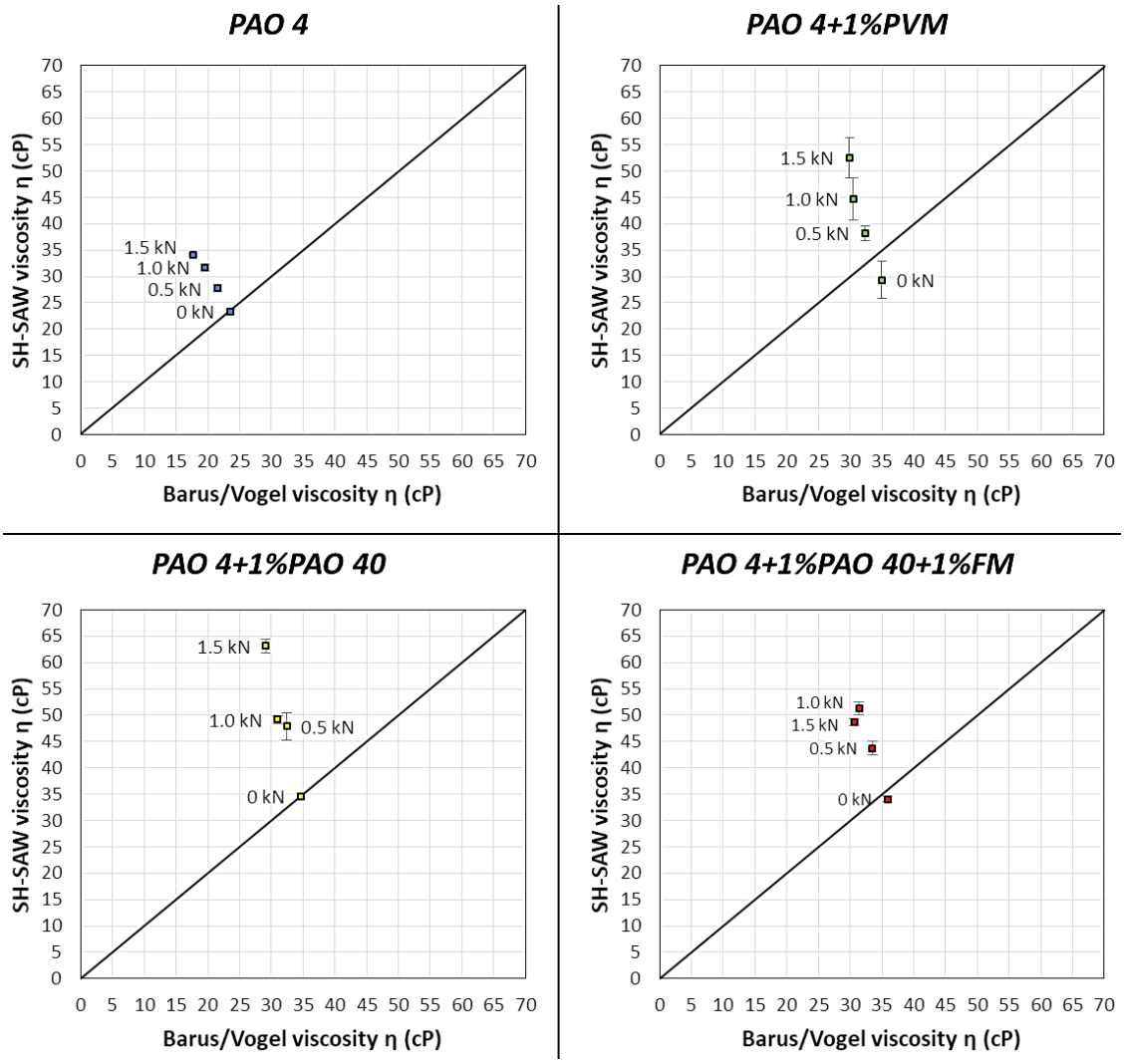

Figure 9.26 Viscosity of the PAO 4 blends, at 540 rpm and different loading conditions

According to Figure 9.26, there is a good agreement between the predicted and measured viscosities for the unloaded cases and the results show that SH-SAWs can be used to measure the oil film viscosity in-situ in a journal bearing.

However, when load was applied and pressure developed, viscosity increased rapidly as shown from the graphs in Figure 9.26, which corresponds to higher pressure than expected. Such high pressures at such low loads mean that either the loaded area must have been significantly smaller than the area calculated from the product of the bearing sleeve length and diameter, or that metal to metal contact may have occurred thus affecting the viscosity measurements. A misalignment between the bearing and journal centres would explain the formation of a thinner film along the bearing length and rise in pressure and hence the viscosity. After testing, the bearing sleeves were removed and examined for wear. Figure 9.27 clearly shows wear marks on the lower bearing sleeve due to misalignment between the journal and bearing centres. The circumferential viscosity results from the shear BAW application, are expected to provide a better understanding for the unexpected increase in pressure and viscosity, due to misalignment.

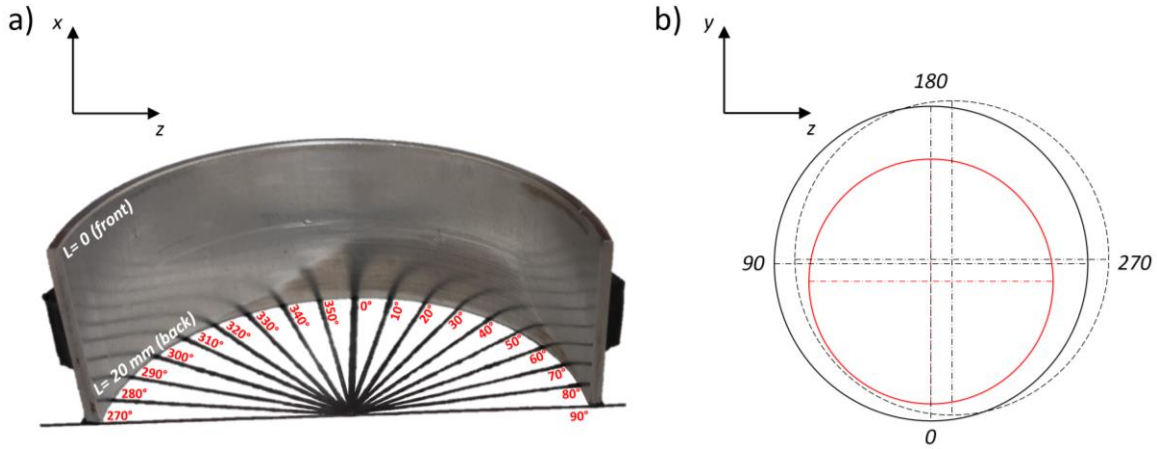

Figure 9.27 a) Lower bearing sleeve wear marks, due to b) misalignment between the journal-bearing centres

According to Figure 9.27a), the bearing sleeve was worn across its length, from L~ 10 mm to L= 20 mm, with the first wear marks appearing at 320° (L= 20 mm) and becoming more intense from 0° to 40° (up to L~ 10 mm). Wear marks also appeared from ~50° to 80° at L=0. Following the traces from the wear marks, it was assumed that misalignment most likely occurred around 80° to 90°, as shown in the schematic in Figure 9.27 b), and that it was comparable to the radial clearance c= 49.5 μm, for metal to metal contact to occur.

9.3.2 Shear BAW measurements of oil film viscosity

Viscosity was measured circumferentially with the shear BAW transducer, as the journal rotated. Firstly, the four PAO 4 blends were tested at 540 rpm, without any load on the bearing, in order to explore the accuracy of the testing method for measuring viscosity, by limiting the parameters that affect viscosity, only to the temperature effect. The results were compared with the viscosity profiles that were obtained using Vogel equation (Equation 2.4). The a, b, c constants of Vogel equation are shown in Table 9.7, for the PAO 4 blends, and the temperature t was obtained by averaging the four thermocouple readings.

Figure 9.28 shows the circumferential viscosity profiles for the tested samples, as they were obtained using the shear reflection coefficient in Equation 9.1 to calculate viscosity.

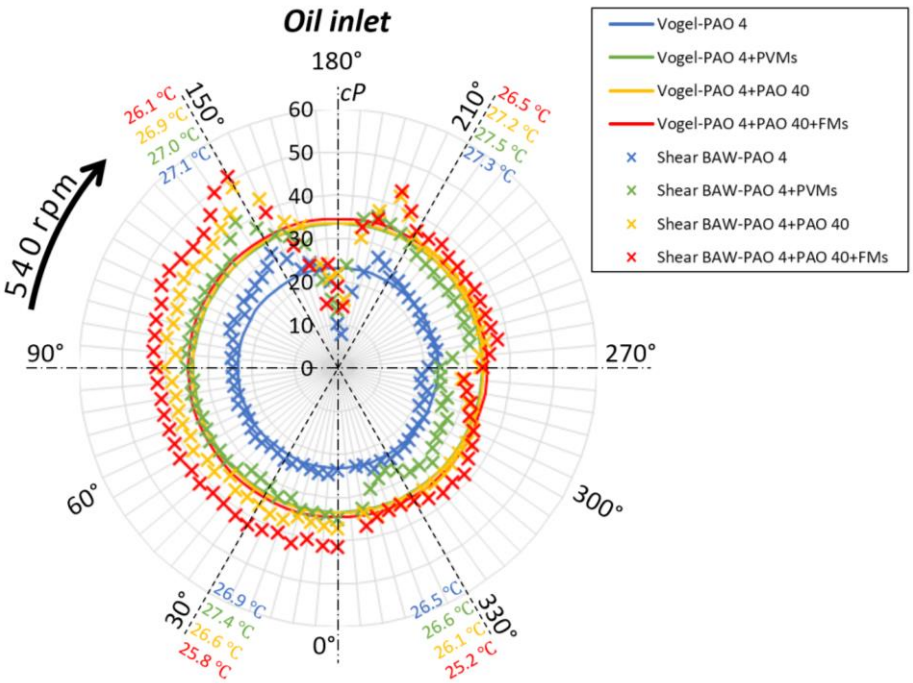

Figure 9.28 Circumferential viscosity profile of the PAO 4 blends, at 540 rpm and no load

It can be seen that, the temperature was fairly constant all around the shaft, as indicated by the thermocouple readings (coloured values at 30°, 150°, 210° and 330°), for all four samples. As a result, only temperature affected the oil film viscosity, as indicated by the viscosity profiles of the samples, which are in good agreement with the viscosity as predicted by Vogel equation over temperature, as shown in Table 9.8.

Table 9.8 Comparison between viscosities as measured with shear BAWs in-situ in a journal bearing film and predicted by Vogel equation

PAO	*Vogel*		*Shear BAWs*		Error η (%)
	t (°C)	η (cP)	t (°C)	η (cP)	
4	27.0	23.15	27.0	23.57	-0.02
4+1% PVM	27.1	33.47	27.1	31.30	0.06
4+1% 40	26.7	33.65	26.7	35.72	-0.06
4+1% 40+1% FM	25.9	35.58	25.9	37.79	-0.06

The viscosity profiles changed abruptly from 150° to 210°, close to the oil supply hole. A dip in the viscosity values appeared at the oil inlet, which more likely occurred due to the higher temperature of the entering oil and the appearance of air bubbles in the oil film. The oil temperature increased before the oil entered the film, due to friction inside the electric pump and tubes, which was reflected by the increase in the thermocouple readings, before (150°) and after (210°) the oil inlet. Air bubbles may have been created due to poor design of the supply hole. The bearing sleeves came without an oil supply hole, as in the engines they are used, the oil is supplied from the crank shaft. As a result, a supply hole was manually drilled on the upper bearing sleeve, which may have affected the oil supply in the film. When shear BAWs reflect from an air bubble, the reflection coefficient approaches 1, which leads to a decrease in the viscosity values that approach zero.

In addition to the effect of temperature, the samples were tested under the application of 0.5, 1.0 and 1.5 kN of load, normal to the journal, in order to investigate the effect of pressure on the oil film viscosity. The results were compared to the viscosity as it was determined using the combination of Reynolds equation (Equation 9.4) for hydrodynamic bearings [78] and Barus equation (Equation 2.5). Reynolds equation was used to determine the pressure distribution circumferentially, and the values were used in Barus equation to calculate the viscosity profile.

$$\frac{\partial}{\partial x}\left\{\frac{h^3}{\eta}\frac{\partial p}{\partial x}\right\} + \frac{\partial}{\partial y}\left\{\frac{h^3}{\eta}\frac{\partial p}{\partial y}\right\} = 6\left\{U\frac{\partial h}{\partial x} + V\frac{\partial h}{\partial y}\right\} + 12(W_2 - W_1) \tag{9.4}$$

In Equation 9.4, h is the oil film thickness, η is the oil viscosity, p is the oil film pressure, U and V are the components of the oil film velocity, parallel and perpendicular to the direction of the journal rotation, respectively. $W_2 - W_1$ represents the rate the oil film thickness changes, or better known as the squeeze film term.

The circumferential viscosity measurements were performed in steady state, so the term $W_2 - W_1$ in Equation 9.4, can be eliminated. Due to the configuration, the journal only rotated around its centre axis, so the oil velocity component V=0. As a result, Equation 9.4 can be written as:

$$\frac{\partial}{\partial x}\left\{\frac{h^3}{\eta}\frac{\partial p}{\partial x}\right\} + \frac{\partial}{\partial y}\left\{\frac{h^3}{\eta}\frac{\partial p}{\partial y}\right\} = 6U\frac{\partial h}{\partial x} \tag{9.5}$$

Due to the pivot and the hydraulic ram position, the load was applied normal to the bottom bearing sleeve, hence the minimum oil film was expected to occur at 0°. The oil film thickness profile can be described from Equation 9.6:

$$h = c(1 - \varepsilon cos\theta) \tag{9.6}$$

In Equation 9.6, c= ($D_{Bearing}$- $D_{Journal}$)/2 is the radial clearance, ε is the eccentricity ratio, and θ is the angular position. For θ=0°, Equation 9.6 returns the minimum film thickness, and for θ=180° it returns the maximum film thickness. A 25 to 30 µm misalignment between the journal and bearing centres was considered, occurring at 80° to 90°, so Equation 9.6 becomes:

$$h = c(1 - \varepsilon cos\theta) - \left[\left(\frac{m}{L/2}\right) x \cos\left(\theta - \widehat{m}\right)\right] \tag{9.7}$$

In Equation 9.7, the term $\left(\frac{m}{L/2}\right)$ represents the slope of the misalignment, where L is the bearing length and m= 25 to 30 µm is the misalignment, x= -L/2 to L/2 is the distance along the bearing length, and $\widehat{m}$= 80° to 90° is the misalignment angle.

The eccentricity ratio ε was obtained using the Raimondi-Boyd chart (Figure 9.29), from the intersection of the L/D= 0.42 curve with the Sommerfeld number [78]:

$$S = \frac{\left(D_{bearing}/2c\right)^2 \eta\, u}{F/LD} \tag{9.8}$$

In Equation 9.8, u is the journal rotating speed expressed in rps, F is the load expressed in Netwons, and LD is the bearing sleeve area.

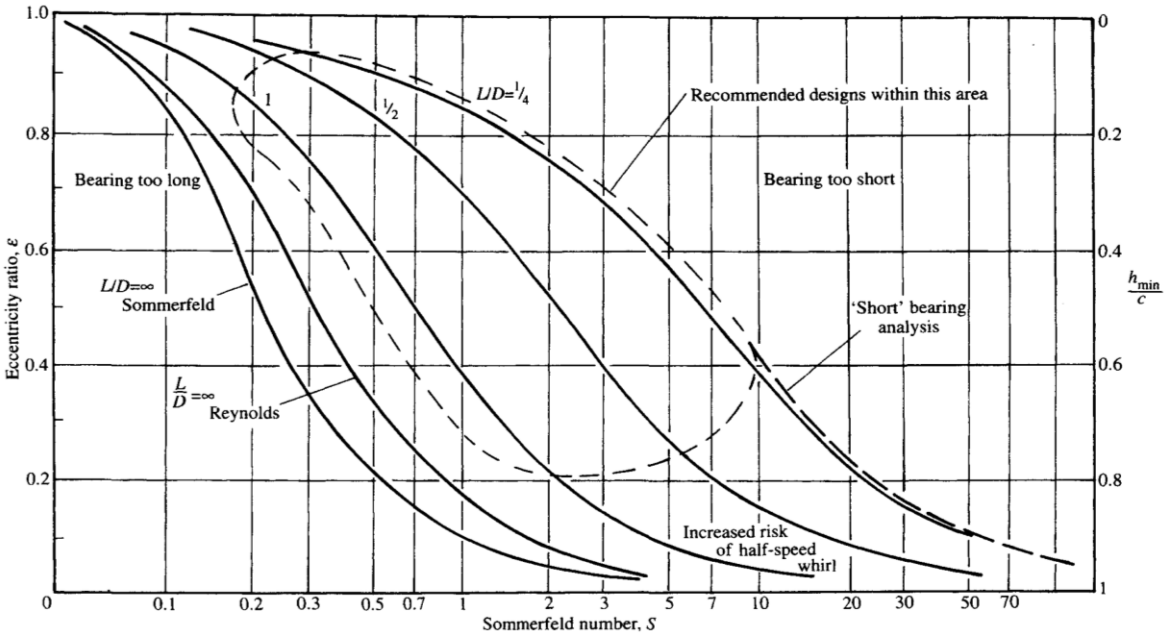

Figure 9.29 Raimondi-Boyd chart of the eccentricity ratio ε according to Sommerfeld number S, for 360° journal bearings of various L/D ratios [78]

After the eccentricity ratio was obtained, Equation 9.7 was solved to calculate the oil film thickness circumferentially.

The pressure distribution can be determined from Equation 9.5, however the equation is quite complex to solve in its current form. In order to simplify Equation 9.5, the narrow bearing solution [1] [78] was considered:

$$p = 3\frac{c\eta\omega\varepsilon sin(\theta)}{h^3}\left[\left(\frac{L}{2}\right)^2 - x^2\right] \tag{9.9}$$

In Equation 9.9, η was determined using Vogel equation (Equation 2.4) at the average temperature among the four thermocouples, and ω is the journal's angular velocity. Although the narrow bearing solution best describes the pressure profile of bearings with $L/D \leq$ 0.25 to 0.3 [1], it can also be applied to the L/D=0.42 bearing to calculate the pressure distribution with good approximation.

After the pressure profile was calculated from Equation 9.9, it was imported in Barus equation (2.5) to determine the circumferential viscosity profile. The viscosity-pressure coefficient α of "medium VI spindle oil" (Table 9.6) was used in Barus equation, to predict viscosity circumferentially.

The oil film thickness and pressure distribution were predicted for the three loading cases using Equations 9.7 and 9.9, as shown in Figure 9.30, and they were found to be very similar among the oil samples. According to the graphs in Figure 9.30, the minimum film was expected to form at 0°, since the load was normal to the bearing at 0° and the journal axis

location was fixed, causing pressure to increase at ~350° due to the journal's direction of rotation. Due to misalignment though, the film thickness was not uniform along the bearing length, leading to variations in the pressure in the same direction. For load> 1.0 kN the misalignment between the journal and bearing centres led the lower bearing sleeve closer to the journal at 30° (L =20 mm) and caused a significant increase in the pressure around that region, most likely due to metal to metal contact, which was in good agreement with the wear marks on the lower bearing sleeve in Figure 9.27.

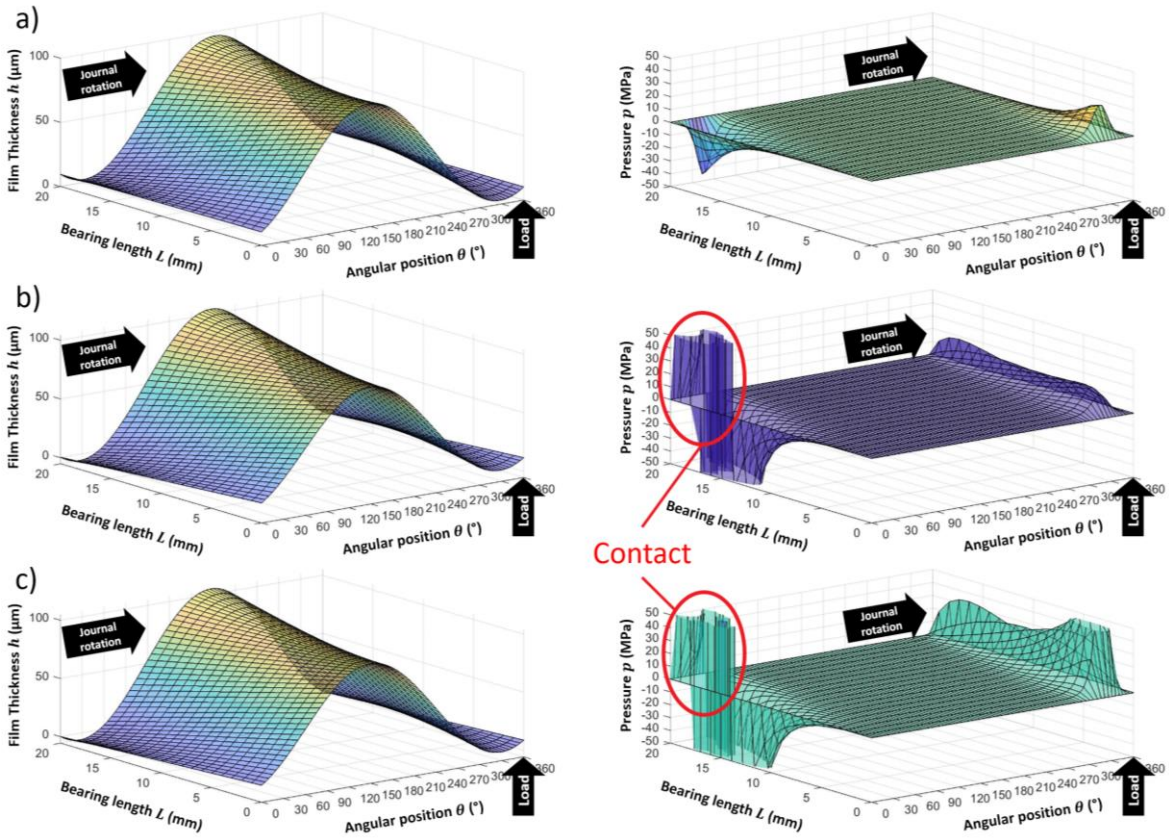

Figure 9.30 Circumferential oil film thickness and pressure distribution along the bearing length for a) 0.5 kN, b) 1.0 kN and c) 1.5 kN load

The pressure distribution along the bearing length was averaged for each loading case, from L =4 to 16 mm (same as the diameter of the shear plug), and used in Barus equation to predict the viscosity profiles of the oil samples, in comparison to the viscosity profiles as measured using the shear BAW transducer. The results can be seen in Figure 9.31, for the three loading conditions.

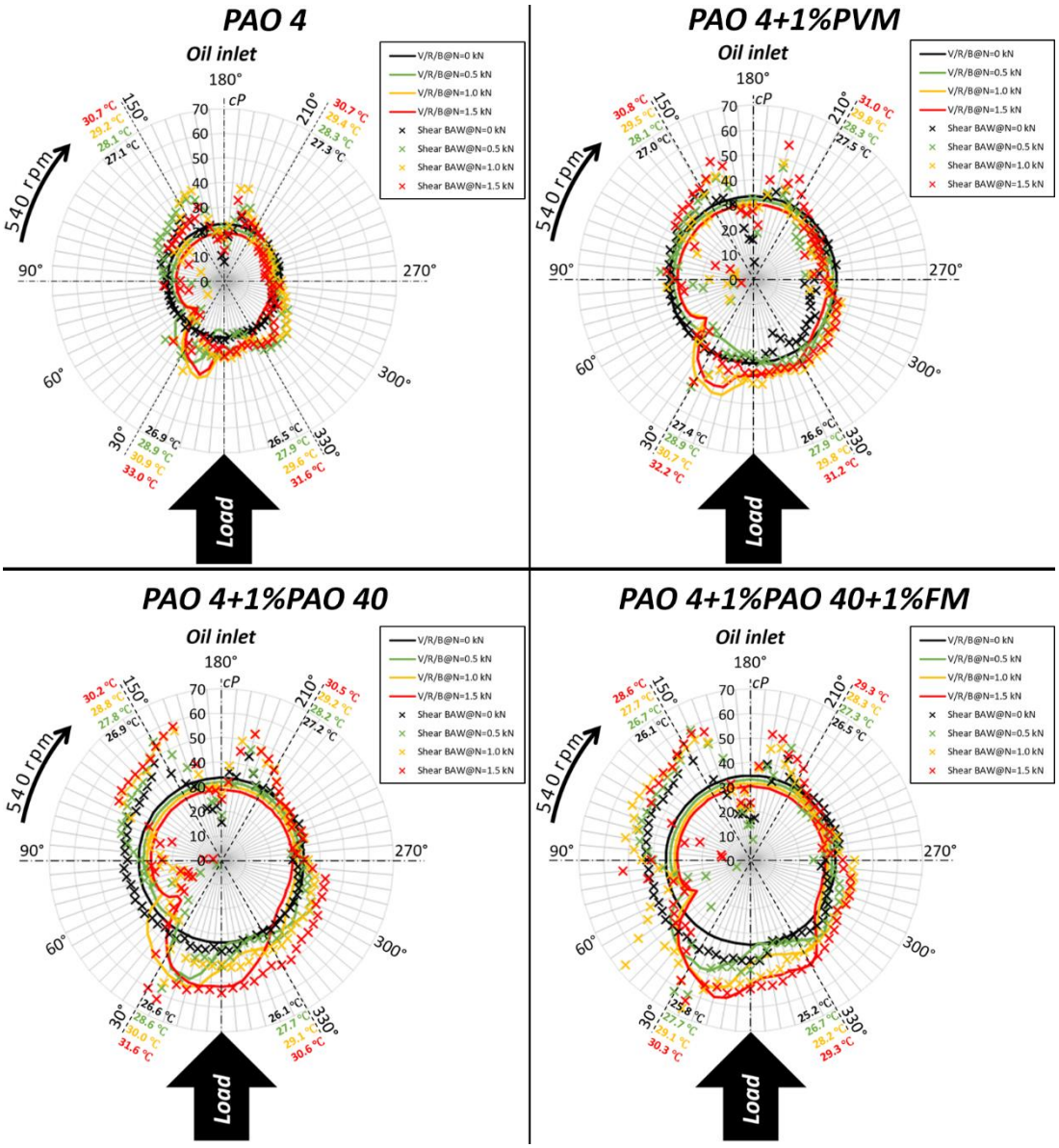

Figure 9.31 Circumferential viscosity profiles of the PAO 4 blends, at 540 rpm and different loading conditions

There are a few common features among the graphs:

- A dip always occurred at the oil inlet, as the samples were warmer before entering the film due to pumping, and the appearance of air bubbles due to the poor design of the supply hole, or lower pressure.
- The temperature readings (coloured values at 30°, 150°, 210° and 330°) varied among the thermocouples for the different loads, indicating variations of the oil film thickness and hence the oil film viscosity, around the journal. Temperature appeared to be higher at 30° angle and increased with load, which is possible

indication of metal to metal contact, due to misalignment between the journal and bearing centres.

- In addition to the increased temperature, an increase in the oil film viscosity occurred around 30° angle, which was consistent among the samples. The predicted viscosity profiles present the same behaviour as the experimental results; an increase in viscosity around 30°. According to Figure 9.27 and Figure 9.30, metal to metal contact occurred around that region, as shown by the wear marks on the lower bearing sleeve and the large increase in the film pressure, respectively, which was partially captured by the shear BAW transducer. Due to the diameter of the shear plug (12mm) and its centred position along the bearing length (L =10 mm), the shear BAW transducer was measuring from L= 4 to 16 mm, axially. As a result, the effect of the metal to metal contact on the oil film was partially captured by the shear BAW transducer, and it is shown by an increase in the oil film viscosity around 30°. Both experimental and predicted values for the viscosity found to be in good agreement in that region.
- According to the temperature readings, loading conditions and oil film viscosity, 4 regions can be distinguished as shown in Figure 9.32, the characteristics of which are summarised on Table 9.9:
    - In Region 1, oil entered the system followed by a drop in the viscosity values, as shown by the low viscosity values around 180° in Figure 9.31. This most likely occurred due to the formation of air bubbles, as a result of the poor oil supply hole design. In the presence of air bubbles, ultrasound reflects from a solid-air interface rather than solid-liquid, which leads to reflection coefficient values that approach 1 and viscosity values that approach 0.
    - In Region 2, the oil viscosity was mainly a function of temperature up to 270° angle. After that, viscosity started to increase and kept increasing due to the thickness of the oil film and the direction of journal rotation, which led pressure to develop along the bearing length, as shown in Figure 9.30. Both predicted and experimental viscosity values are in good agreement in that region.
    - Region 3 is characterised by an increased temperature (thermocouple readings), high contact pressure (Figure 9.30b,c) and high viscosity (Figure 9.31) around 30° angle, due to contact between the journal and the lower bearing sleeve. After 30°, viscosity decreased to almost 0, most likely due to cavitation. In that case, ultrasound was reflected from a solid-air interface,

leading to reflection coefficient values that approached 1 and to almost 0 viscosity.

- The cavitation region was extended halfway to Region 4, as shown by the low viscosity values in Figure 9.31. After, viscosity started to increase and maximised in Region 1 right before the oil inlet. Similar rise in viscosity was noticed after the oil inlet, before viscosity finally stabilised. As a result, the increase in viscosity in Region 4 most likely occurred due to interference between the oil in the film and the geometry of the oil supply hole.

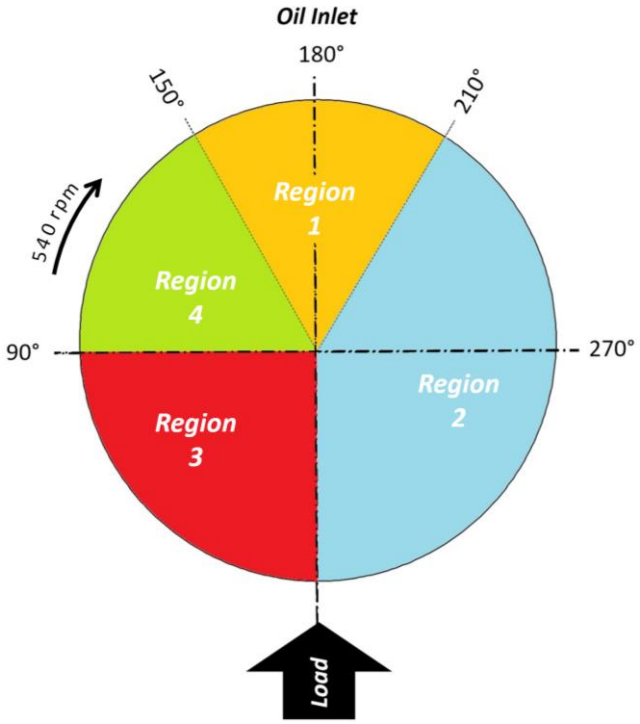

Figure 9.32 Oil film regions due to loading

There are also a few obvious differences in the viscosities among the oil samples, which can be attributed to the different additions in the PAO 4. The addition of the PAO 40, PVMs and PAO 40+FMs, respectively, has changed the behaviour of PAO 4, as it can be seen from the viscosity profiles of the blends under the same testing conditions. However, there was no sign indicating any surface layer formation, for neither the PVMs nor the FMs. Surface layer formation was expected to show presence by further increasing the oil viscosity at the minimum film thickness, but viscosity appeared to be only a function of pressure. This was somewhat expected, as the PVMs and FMs get physically adsorbed on metallic surfaces. As a result, it was very unlikely for surface layers to form on the polyimide layer the shear transducer employs. Still, the shear transducer offers a very good insight of lubricants' behaviour, from their distinguishable viscosity profiles.

Table 9.9 Oil film viscosity regions due to loading (*in the case of PAO 4 and 1.5 kN load)

Region	*Location*	*Temperature (°C)*	*Pressure*	*Viscosity (cP)*
1	150°- 210°	30.7*	Low	24.13*
2	210°- 0	31.6*	Low-High	19.45 – 25.69*
3	0- 90°	33.0*	High-Low	28.11 – 0*
4	90°- 150°	30.7*	Low	9.46*

9.3.3 Comparison of shear BAW and SH-SAW methods

In order to compare the two methods, the viscosity values from the shear BAW method were averaged between 300° to 60°, to resemble the average viscosity measured with the SH-SAW method over the same distance. The results from the comparison are shown in Figure 9.33.

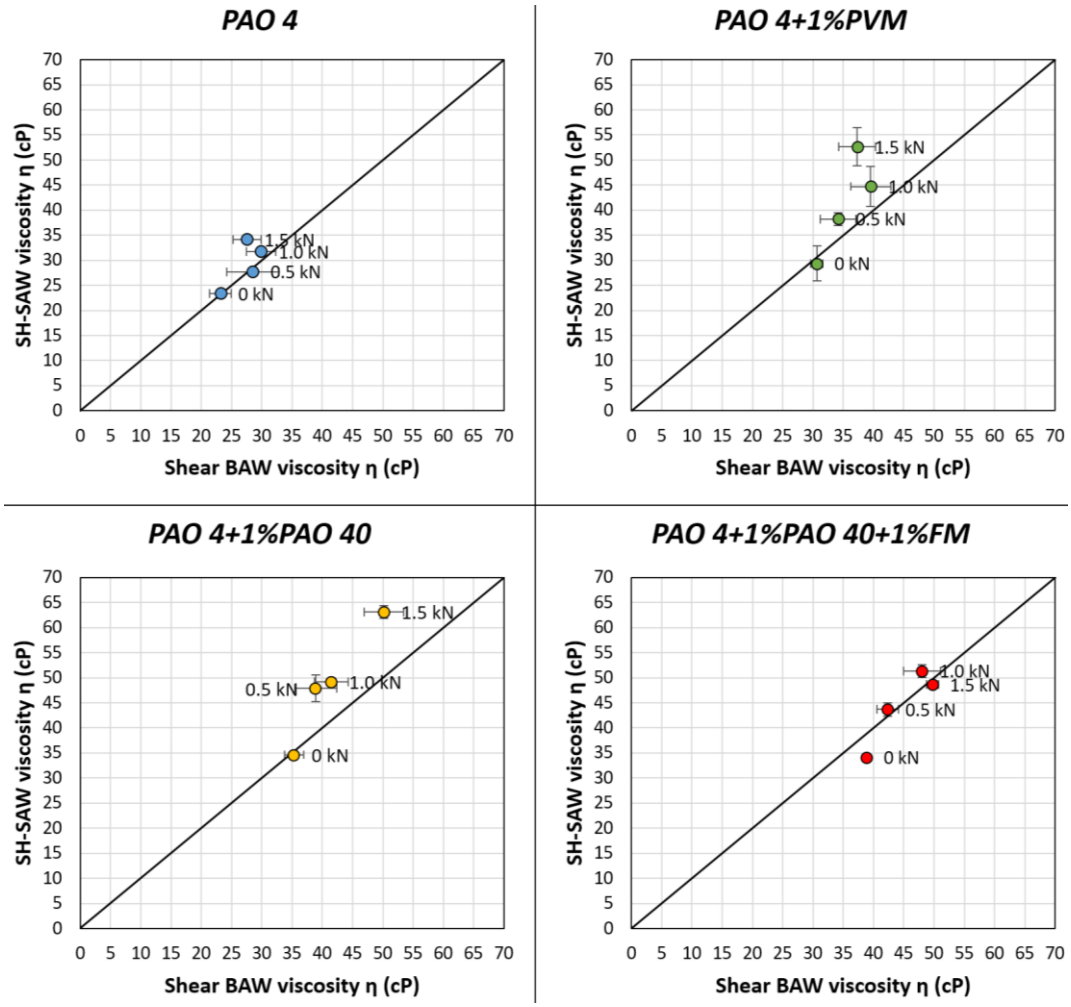

Figure 9.33 Comparison between shear BAW and SH-SAW methods for measuring oil film viscosity at the high pressure region (300° to 60°)

According to the graphs in Figure 9.33, the viscosities measured at the bearing-oil interface with the angled SH-SAW transducers, are in good agreement with those measured in the journal-oil boundary over the same region, using the ultrasonic shear transducer. In sub-Section 9.3.1, the SH-SAW viscosity results appeared to be significantly higher compared to the Vogel and Barus predictions. The pressure was considered to be uniformly distributed across the bottom bearing sleeve surface (Equation 9.3) and the bearing and journal were assumed to be concentric along their lengths. After testing, the bearing was inspected for wear. Wear indeed occurred, possibly due to misalignment between the bearing and journal centres, judging by the wear marks, which was taken into consideration when predicting the circumferential pressure distribution using Reynolds equation in sub-Section 9.3.2. The pressure profile was then used in Barus equation to predict viscosity circumferentially and it was compared to the viscosity as it was measured with the shear BAW transducer as the journal rotated. SH-SAW and shear BAW results are in good agreement, as shown in Figure 9.33, and provide evidence that misalignment should have been considered in the comparison of the viscosities as measured with SH-SAWs and predicted using Vogel and Barus equations (Figure 9.26). The results provide a form of validation for both the SH-SAW and shear BAW methods; previously, experimental results using each method were compared to numerical models. The viscosity results using the shear BAW transducer, a method already used by various authors according to Section 4.2, support the application of SH-SAWs for measuring oil viscosity in-situ in a film, and vice versa.

9.4 Conclusions

This chapter has presented the implementation of SH-SAWs for measuring viscosity of oil films, in-situ in a journal bearing application. For the purpose of the study, a rotating journal and a bearing were set up in a rig, where different loading conditions were applied to create oil films of various thickness. The minimum film thickness due to loading and rig design, was expected to occur at the lower bearing sleeve, which was instrumented with two angled SH-SAW transducers to measure the changes in oil film viscosity with pressure.

According to the results from four test samples, viscosity increased with load, as expected and it was successfully measured with the SH-SAW method. The viscosity values measured with the SH-SAW method, were compared to numerical models for predicting viscosity and found to be significantly higher for the loaded cases. After testing, the bearing sleeve was inspected and revealed wear marks, possibly due to misalignment between the journal and bearing centres. That could explain the higher viscosity values recorded with the SH-SAW method, compared to the predicted viscosity values.

An ultrasonic shear BAW transducer was used to measure the oil film viscosity in-situ in the journal bearing oil film, for comparison. The transducer was installed inside the rotating journal, which allowed measurements of the oil film viscosity circumferentially. In comparison, Reynolds equation for journal bearings was used to predict the pressure profile, which was used in Barus equation to predict the viscosity circumferentially. Misalignment between the journal and bearing centres was taken into consideration in the calculations of the pressure and viscosity profiles, and both the experimental and numerical results exhibited similar behaviour.

A third comparison between the viscosities measured with the angled SH-SAW transducers at the bearing-oil film interface and the ultrasonic shear BAW transducer at the journal-oil film boundary, found the two methods to be in good agreement. Both methods successfully distinguished differences in the test samples, according to their viscosities. The oil film viscosity at the loaded region appeared to be different among the oil samples, which was attributed to the oil composition. Viscosity appeared to be a function of only temperature and pressure, and was not further increased at the minimum film thickness to indicate the detection of a surface layer formation.

10 GENERAL DISCUSSION

This chapter presents an overall discussion of the SH-SAW method for measuring viscosity and formation of surface layers. The SH-SAW transducers, the attenuation-viscosity model, the bench-top measurements of the oil viscosity and the formation of surface layers, the oil film viscosity measurements in-situ a journal-bearing rig, as well as advantages and disadvantages of the SH-SAW method, will be discussed in the following sections.

10.1 The SH-SAW transducers

Angled transducers were used for the generation of SH-SAWs throughout the experiments, as shown in Chapters 6, 7, 8, and 9. Face-shear piezo-ceramics were also used in Chapter 5, to explore their capabilities for generating SH-SAWs, but they were abandoned due to frequency limitations. Frequency is very critical in the viscosity and surface layer formation study, especially when measuring non-Newtonian oils, as shown in sub-Sections 7.2.1 and 8.3.2.

As described in sub-Section 3.5.2, the frequency of the face-shear piezo-ceramics depends on their width; as the width increases the frequency decreases, and vice versa. As a result, the width can be reduced to a certain extent, provided that in the meantime the thickness of the ceramic must always be smaller than its width, which limits the generation of SH-SAWs to a few kHz. Thinner piezo-ceramics (hence higher frequencies) would result in a very small electrode area, which would lead to poor transduction of electrical energy to mechanical, hence weak waves. Although face-shear piezo-ceramics present limitations, they also present a few advantages over the angled sensors, amongst them being the direct coupling with the propagating medium, the small size of the transducers and the ability to couple to almost any material SH-SAWs can propagate on. The direct coupling with the propagating medium leads to the generation of stronger waves, since energy is not consumed while the wave travels through a wedge before it reaches the propagating medium. In addition, face-shear piezo-ceramics can be coupled with almost any medium, since a wedge is not required. In the angled method, the wedge material must be acoustically slower than the propagating medium, which leads to limited combinations of materials.

On the other hand, the angled method does not present any frequency limitations; it is only limited by the frequencies of the thickness-shear piezo-ceramics currently available in the market, which range from a few kHz up to 10 MHz. In addition, the same wedge geometry can be used, regardless the frequency of the piezo-ceramics, thus angled transducers offer a wider frequency range and this is the reason they were used

throughout this thesis. One major disadvantage of the angled method is the selection of an acoustically slower material for the wedge than the material of the medium, which limits the possible combinations of materials. Depending on the application, temperature, pressure and oxidation may also need to be taken into consideration for the selection of a suitable wedge material, as shown in sub-Sections 7.2.2, 8.3.3 and 9.1.2, where above a certain temperature there was a sudden decrease in the wave amplitude due to the shearing of the adhesive, caused by the different heat expansion coefficients of the wedge material and the material of the propagating medium. The shape of the propagating medium is also an important factor in the generation of SH-SAWs with angled transducers; the transducers can be coupled to flat surfaces very easily, however on curved surfaces, such as the bearing sleeve in sub-Section 9.1.2, coupling can be a challenging task. Aluminium curved wedges were originally designed for the journal-bearing application, as shown in Figure 10.1a, however the geometry led to the generation of a complex waveform due to the multiple refraction angles the curved face created (Figure 10.1b). In the end, aluminium flat wedges were mounted on the bearing sleeve, by moulding epoxy to create almost a heel that followed the contour of the bearing sleeve, and also provided a flat face for the wedge to sit on, as shown in Figure 10.2. The heel was designed to leave an air gap between the wedges and bearing sleeve, to prevent the wave to refract at the wedge-bearing sleeve interface, thus only the SH-SAW mode to be excited. Although this arrangement allowed the flat angled transducers to be mounted on the bearing sleeve, the small contact area between the wedge and the bearing sleeve, led to the generation of weaker SH-SAWs compared to the SH-SAWs generated when the wedges were mounted on a flat surface.

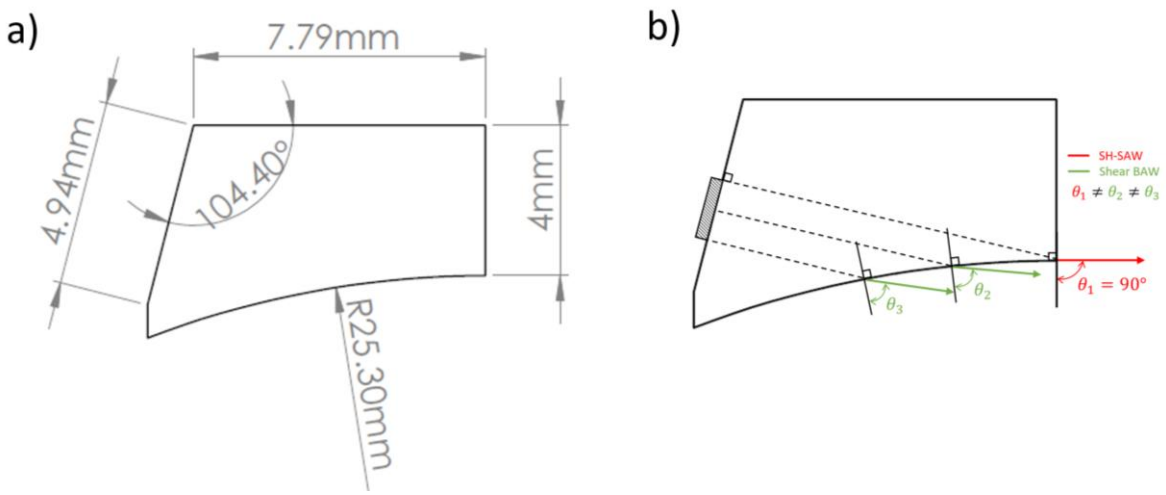

Figure 10.1 a) Schematic of the aluminium curved wedge for bearing sleeve installation, and b) the creation of multiple refraction angles, due to the curved face

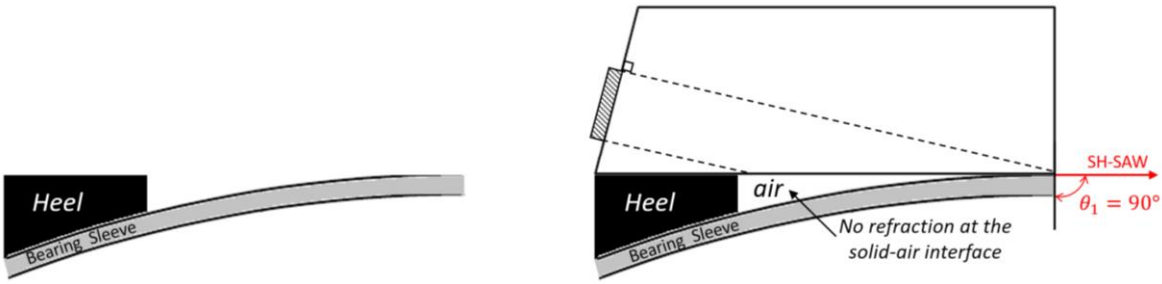

Figure 10.2 Moulded heel to allow the flat wedge to be mounted on the bearing sleeve

10.2 The attenuation-viscosity model

The SH-SAW attenuation model proposed by Martin et al. [45], for measuring the viscosity of Newtonian liquids coupled with SAW devices (piezo-electric media), was adapted for measuring the viscosity of oil on metallic media, as shown in Section 6.2. The model predicted the SH-SAW transmission coefficient very well, when the viscosity of the oil was known, as shown from the results in Sections 6.3 to 6.8. In addition, the attenuation-viscosity model also predicted the viscosity of various lubricant oils, from their transmission coefficient values, as it was shown in Section 7.2. In the model, a linear relationship between stress and strain (Newtonian liquid) was assumed, whereas in reality most engine oils exhibit a viscoelastic behaviour and perhaps a more suitable model is required to describe the relationship between stress and strain. The Newtonian assumption was considered to be a good starting point to validate the attenuation-viscosity model for Newtonian liquids, such as the Cannon viscosity standard oils, however a viscoelastic model, to describe the relationship between stress and strain such as the Maxwell model (Equation 4.3), may be more suitable for fully formulated engine oils.

Apart from flat metallic media, the attenuation-viscosity model also applies to curved metallic media coupled with a liquid, as in the case of the bearing sleeve in sub-Section 9.3.1, which was coupled with various oils. As shown by Petcher et al. [88], the bearing sleeve can be treated as a flat plate, due to its smooth curvature, without altering the SH-SAW propagation, which demonstrates the flexibility of the attenuation-viscosity model.

Furthermore, the attenuation-viscosity model is independent of the SH-SAW generation method, which allows the model to be used either with angled transducers, piezo-ceramics, EMATs or any other wave generation method. As a result, the model offers additional flexibility and can potentially cover a broader field of applications.

10.3 Bench-top testing of the oil viscosity and the formation of surface layers

A simple experimental configuration, consisting of two angled transducers, a steel plate and a data acquisition system, was presented in Section 5.2, for measuring the attenuation of SH-SAWs propagating along the steel plate, which was coupled with oil. This experimental configuration was used successfully to measure the viscosity of various oils and the formation of surface layers in Sections 7.2 and 8.3, respectively.

10.3.1 Bench-top measurements of the oil viscosity

According to Chapter 7, the viscosity of various oils was successfully measured using the SH-SAW method. As the results in sub-Section 7.2.1 has shown, the method was not limited to measuring only Newtonian oils, but it could also distinguish non-Newtonian behaviour, as in the case of PAO 100 and S600, from the viscosity they exhibited at different frequencies, hence shear rates.

Extending the frequency range of the SH-SAWs even further, by utilising different frequency piezo-ceramics bonded either on individual wedges (Figure 10.3a), or on one shared wedge (Figure 10.3b), would allow for better understanding of the oil composition and behaviour. According to Figure 3.9, if the thickness of the steel plate is selected to be such, so the product of the maximum available frequency (f_1, f_2, ..., f_n) and plate thickness is lower than ~800 kHz mm, then only the fundamental SH0 mode should be generated across the whole frequency range.

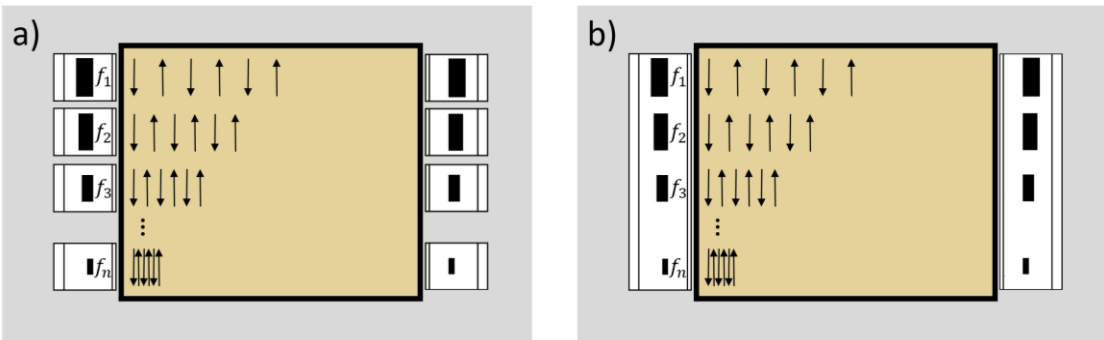

Figure 10.3 Multi-frequency set-up using different frequency piezo-ceramics bonded a) on individual wedges, and b) on one common wedge

Viscosity measurements were also performed over temperature, up to 100 °C, to investigate the capabilities of the SH-SAW bench-top configuration for measuring the effect of temperature on viscosity. The steel plate with the angled transducers and the oil

sample were placed in the oven and heated up to 100 °C, and left to gradually cool down to room temperature, while viscosity was measured every 1 °C degree. According to Figure 7.8 and Figure 8.14, the measured viscosity values were partially in agreement with the predicted viscosity values; above a certain temperature the measured viscosity suddenly decreased to almost 0. This most likely occurred due to the shearing of the adhesive, caused by the different thermal expansion coefficients of the steel plate and aluminium wedges, which needs to be taken into consideration when selecting a suitable material for the wedge and a suitable adhesive, as explained in Section 10.1, in order to improve the measurable temperature-viscosity range.

Overall, the SH-SAW method required minimum preparation and minimum engagement from the user during testing. Once the plate and the sensors were calibrated over temperature, as described in sub-Section 7.2.2, the user only had to deposit the sample on the sensing area and record the ultrasonic signal and the temperature. The temperature was acquired using three thermocouples; two installed on the steel plate, and one in contact with the oil. Once the temperature readings from all three thermocouples matched, the ultrasonic signal and temperature were automatically recorded by the acquisition system. This process was repeated every 1 °C degree, starting from the highest temperature to the lowest, both defined by the user. After testing, the user was required to remove the oil sample and clean the sensing area from any oil residue. The surface was easily accessible to clean, and it only required a few absorbing paper towels and light rubbing to ensure that the sensing area was dry. Additionally, isopropanol was sprayed on the sensing area to further clean any oil residue. This cleaning process proved to be effective enough to remove the oil sample from the sensing area, as shown from the transmission coefficient in Figure 8.5, which returned to 1, after the samples were cleaned and there was nothing but air coupled with the steel plate.

10.3.2 Bench-top measurements of surface layers

The SH-SAW bench-top configuration was also used for measuring the formation of surface layers, as shown in Chapter 8. To begin with, two base oils were formulated with two known additives that were expected to form surface layers on metal surfaces; viscosity modifiers and friction modifiers. The surface layers were expected to show presence by increasing the viscosity close to the metal surface significantly, compared to the viscosity of the bulk liquid. Figure 8.7 describes the expected viscosity change over time, as the viscosity modifiers and friction modifiers formed surface layers. As shown in the middle graph, viscosity modifiers were expected to increase the viscosity close to the surface more, since they form thicker films (~10-30 nm) compared to friction modifiers (~ 1-2 nm), due to their greater molecular size [13].

The two formulated oils were tested over time with the SH-SAW bench-top configuration, in order to measure the change in the viscosity as the additives adsorb on the steel surface. The viscosity response of the two formulated samples was compared to the response of the two base oils (no additive addition), and all four viscosities found to be constant over time. This was attributed to either no film formation or a limitation of the method.

Further investigation with model deposited layers revealed clear change in the viscosity of the base oil in the presence of a surface layer, when the surface layer thickness became comparable to the SH-SAW penetration depth in the oil sample. In the configuration described in Section 8.2, the SH-SAW penetration depth was 100 to 1000 times greater than the thickness of the layers viscosity and friction modifiers formed, respectively. As a result, their presence had negligible effect on the viscosity measured using the SH-SAW bench-top configuration, and that is the reason the viscosities of the formulated oils appeared to be constant over time. Currently, the SH-SAW bench-top configuration can successfully measure ~1 μm thick surface layers, through their effect on the viscosity of the base oil. The capabilities of the method could be further extended by reducing the SH-SAW penetration depth closer to the metal surface. According to Equation 6.26, the penetration depth is proportional to the liquid viscosity and inversely proportional to its density and SH-SAW frequency. The oil density and viscosity are beyond control, as temperature, pressure and shear can change them. The SH-SAW frequency is the only parameter in Equation 6.26 that can be controlled at a certain level.

Extremely high frequencies (~10 GHz) are required though, in order to reduce the SH-SAW penetration depth to the same scale as the surface layers friction and viscosity modifiers form. SAW devices are capable of high frequency (~ 100 to 500 MHz), as described in 4.4, however they are only suitable for bench-top testing, and they cannot be used for in-situ measurements. Other methods for generating SH-SAWs, including face-shear piezo-ceramics, angled transducers and EMATs, are currently limited to 10 MHz frequencies or lower. Once high frequency transducers become available, thinner surface layers could be detected.

10.4 Oil film viscosity measurements in-situ a journal-bearing

Chapter 9 presented the experimental rig that was designed to further investigate the capabilities of the SH-SAW method for measuring oil film viscosity at the bearing-oil boundary, under various loads and constant speed. In comparison, a second ultrasonic method employing shear BAWs was also used to measure the oil film viscosity at the journal-oil boundary, and both ultrasonic methods were compared to numerical models for the prediction of viscosity, and with each other.

The comparison between the SH-SAW and numerical models, has demonstrated a mismatch between the measured and predicted viscosities for the given conditions of load, speed and temperature. The measured values appeared to be significantly higher than the predicted values for the viscosity. On the other hand, the results from the two ultrasonic methods were found to be in good agreement and demonstrated that the SH-SAW method can be successfully used to measure oil viscosity in-situ a film. The circumferential viscosity measurements using the shear BAW transducer have revealed an abnormal increase in viscosity, which was attributed to misalignment between the journal and bearing centres. Indeed, the good agreement between the shear BAW result and the numerical results, supported the misalignment theory, which was also confirmed by wear marks on the lower bearing sleeve, where the minimum film was expected to occur.

Misalignment most likely occurred due to the way the load was applied; a hydraulic jack applied load on the one end of a lever mechanism, while the other end was on a pivot, as described in sub-Section 9.1.1. The centre axis of the pivot was designed to be parallel to the axis of the journal and bearing, in order to keep them aligned. In reality, it was found that the pivot axis was parallel to the bearing axis, but it was not parallel to the journal axis, which led to misalignment between the bearing and journal centres. For future testing, it is highly recommended to re-design the loading mechanism, to avoid any misalignment or even better, it could be designed in such way that misalignment can be controlled and measure its effect on lubrication.

Another abnormal behaviour of the oil viscosity occurred at 180° angle, as shown by the shear BAW viscosity measurements in Figure 9.28 and Figure 9.31, which was the location of the oil inlet. The oil was supplied through a hole, which was manually drilled on the top bearing sleeve. The design and location of the supply hole strongly affected the oil behaviour. As the results has shown, the oil viscosity decreased to almost 0 around that region, most likely due to the formation of air bubbles. In the future, the oil supply hole should be designed towards the minimum film location, in the convergence zone, and its geometry should be carefully selected, in order to avoid the formation of air bubbles.

Apart from the misalignment between the journal and bearing centres, and the poor oil supply hole design, the experimental rig was proved to be suitable for emulating real engine conditions. The results from the journal-bearing application support the use of the SH-SAW method for measuring the oil viscosity in-situ in films and encourage its further investigation. Compared to shear BAWs, SH-SAWs do not require the addition of a matching layer to improve the acoustic mismatch between metals and oil. The SH-SAW transducers can be installed on the bearing sleeves rather than the journal, which in most engines comes with a channel for circulating the oil to all contacts, and makes the

installation of a shear BAW transducer more complicated than it is already. However, installing SH-SAW transducers on the bearing sleeves does not offer circumferential measurements of viscosity, as a shear BAW transducer in the journal does. Instead, the SH-SAW transducers measure the average viscosity along the bearing sleeve, which still can provide valuable information about the lubrication. Potentially, the SH-SAW method could also be used to measure the formation of surface layers in-situ an oil film, once the technology allows higher frequency SH-SAWs to be generated, as explained in Section 10.1.

11 CONCLUSIONS

This thesis presents the work of developing a SH-SAW method to measure lubricant viscosity at a surface and in-situ in a bearing film. The conclusions from this study are summarised in this chapter, including modelling the SH-SAW attenuation at a solid-liquid interface for measuring oil viscosity, developing an experimental method to measure the attenuation of SH-SAWs at a solid-liquid interface, measuring oil viscosity and formation of surface layers, and implementing the method for measuring oil viscosity in-situ in a bearing film.

11.1 Modelling the SH-SAW attenuation at a solid-liquid interface

The SH-SAW attenuation at a solid-liquid interface can be utilised for measuring lubricant properties. In sub-Section 6.1, the attenuation-viscosity model that was developed by Martin et al. [45] for SH-SAW devices coupled with liquids, was adapted for SH-SAWs propagating on metallic media coupled with liquids. Viscosity and liquid path length increase the wave attenuation, as more liquid particles resist the wave oscillation. The liquid film thickness does not affect the wave attenuation, but the penetration depth of the SH-SAW oscillation inside the liquid needs to be taken into consideration, when the liquid forms a film between two solids. The SH-SAW penetration depth should always be less than the film thickness, to prevent any further wave attenuation.

Thinner and acoustically softer media increase the wave attenuation, as they present better coupling with liquids. Higher the wave frequency, greater the wave attenuation, as more energy is concentrated close to the surface, thus increases the energy lost in the liquid.

11.2 Developing an ultrasonic method for measuring the attenuation of SH-SAW

The attenuation of SH-SAWs at a solid-liquid interface can be measured experimentally using two transducers in pitch-catch mode, bonded on a medium in contact with a liquid. The pitch-catch mode allows measuring the wave attenuation through the wave transmittance at the solid-liquid interface. The wave transmittance or transmission coefficient T can be obtained from the ratio of the wave amplitudes at the solid-air and solid-liquid interfaces. The wave amplitude can be extracted by applying the fast Fourier transform to the acquired signal, after isolating the fundamental SH-SAW mode. The SH-SAW attenuation can be used in the attenuation-viscosity model to determine the viscosity of liquids.

11.3 Implementing the SH-SAW method for measuring oil viscosity at a surface

The SH-SAW method can be used for measuring viscosity of lubricant oil in contact with a metallic surface, as shown by the excellent agreement when compared to the viscosity obtained with a rotational viscometer. Viscosity can be measured accurately with the SH-SAW method over a range of temperatures, as it was proven by the good agreement between measured and predicted viscosities.

The SH-SAW method cannot be used to detect the formation of thin ($h < 30\ nm$) surface layers, as the surface layer thickness is negligible compared to the SH-SAW penetration depth. When, the surface layer thickness is comparable to the penetration depth surface layers can be detected at a solid-liquid interface, through an increase in the viscosity of the liquid, as it was shown experimental with model deposited surface layers at an oil interface.

11.4 Implementing the SH-SAW method for measuring oil viscosity in-situ in a bearing film

The SH-SAW method can be utilised for measuring oil film viscosity in-situ in a running journal bearing. The bearing sleeves can be instrumented with SH-SAW transducers and the method can successfully determine the oil film viscosity under different loading and temperature conditions, as it was shown both experimentally using a second ultrasonic method and numerically, using Vogel and Barus equations.

11.5 Future work

Further development and investigation directions are listed as follows:

- Improve the SH-SAW operating frequency range in order to reduce the wave penetration depth closer to the surface, to allow for measurements of surface layers at a solid-liquid interface. The current methods for generating SH-SAWs on metallic media, which allows surface layers to form, include piezo-ceramics, EMATs and angled transducers. Piezo-ceramics and EMATs are limited to hundreds of kHz operating frequencies, while angled transducers can generate SH-SAWs up to 10 MHz. According to literature, at least hundreds of MHz frequency is required to reduce the penetration depth of SH-SAWs to match the surface layer thickness for detection. As a result, increasing the SH-SAW frequency capabilities, by improving the existing methods should be the primary focus.

- Investigate bearing coatings for increasing the sensitivity of the SH-SAW method. Love waves, in the case of SAWs and shear waves, in the case of BAWs, have reported increased sensitivity when a "matching layer" is used to improve the acoustic mismatch between the propagating medium and tested liquid. Bearing coatings may present similar characteristics to a matching layer material, they allow adsorption of molecules to form surface layers and they can be found in most engine bearings. As a result, tuning the transducer frequency to match the resonant frequency of the coating may prove beneficial for measuring formation of surface layers, in-situ in a bearing.
- Explore the application of a continuous pulse compared to a burst pulse, to excite the transducers for generating continuous SH-SAWs. The continuous mode will allow the medium to resemble a quartz crystal microbalance. The QCM uses a continuous pulse to excite the quartz crystal. When the crystal is loaded, the amplitude and frequency of the wave changes, indicating particle adsorption on the surface. However, using a continuous pulse requires the generation of pure SH-SAWs, free of any other waves and that is exactly the reason a continuous pulse could not be used in this work.
- Extend the range of the test samples to explore any limitations of the method for measuring viscosity in dynamic oil films. In this work, four samples were tested in-situ in a bearing due to the limited capabilities of the oil pump. A larger pump is suggested to replace the current pump, to allow a wider range of oils to be tested, including fully formulated engine oils, and higher flow rates for the oil supply.
- Extend the capabilities of the angled SH-SAW transducers for measuring oil viscosity. Bonding multiple sensors of different frequencies on the wedges, would allow a more complete study of the lubricant composition and behaviour in dynamic conditions. A wide range of frequencies would allow exciting different species with different molecular weights blended inside the oil, for lubricant characterisation.
- Improve the SH-SAW attenuation-viscosity model. In this work, the oil was treated as a Newtonian liquid with an elastic behaviour. In reality due to its composition, oil presents a viscoelastic behaviour, which needs to be taken into consideration to allow more accurate predictions/measurements of viscosity. The Maxwell model for example, could be used in combination with the SH-SAW attenuation-viscosity model, to account for the viscoelasticity of the oil.

12 REFERENCES

[1] G. Stachowiak and A. W. Batchelor, Engineering Tribology, Butterworth-Heinemann, 2013.

[2] J. Fitch, "Machinery Lubrication", May 2010. [Online]. Available: https://www.machinerylubrication.com/Read/24955/current-trends-lubrication-oil-analysis. [Accessed October 2019].

[3] H. Eyring, "Viscosity, plasticity, and diffusion as examples od absolute reaction rates", *Journal of Chemical Physics,* vol. 4, pp. 283-291, 1936.

[4] R. H. Ewell and H. Eyring, "Theory of the viscosity of liquids as a function of temperature and pressure", *Journal of Chemical Physics,* vol. 5, pp. 726-736, 1937.

[5] C. Barus, "Isotherms, isopiestics and isometrics relative to viscosity", *American Journal of Science,* vol. 45, pp. 87-96, 1893.

[6] C. Roelands, "Correlational aspect of viscosity-temperature-pressure relationships of lubricating oils", PhD Thesis, Delft University of Technology, The Netherlands, 1966.

[7] G. Leblac, R. Secco and M. Kostic, "Viscosity Measurement", CLC Press LLC, 1999.

[8] N. Nassar, S. Ahmed and M. Amal, "Lubricating Oil Additives", in *Tribology-Lubricants and Lubrication*, InTech, 2011, p. 320.

[9] A. Martini, U. S. Ramasamy and M. Len, "Review of Viscosity Modifier Lubricant Additives", *Tribology Letters,* vol. 66, no. 2, pp. 1-14, 2018.

[10] Lubrizol corporation, "Lubrizol polymer chemistry", Lubrizol Corporation, 2012.

[11] S. Gunsel, M. Smeeth and H. Spikes, "Friction and wear reduction by boundary film-forming viscosity index improvers", *SAE Transactions,* vol. 105, no. 4, pp. 1831-1855, 1996.

[12] M. Müller, K. Topolovec-Miklozic, A. Dardin and H. A. Spikes, "The design of boundary flm-forming PMA viscosity modifers", *Tribology Transactions,* vol. 49, no. 2, pp. 225-232, 2006.

[13] H. Spikes, "Friction modifier additives", *Tribology Letters,* vol. 60, 2015.

[14] Finol, "The Main Causes of Oil Degradation", Finol, 2019.

[15] N. Dörr, A. Agocs, C. Besser, A. Ristić and M. Frauscher, "Engine Oils in the Field: A Comprehensive Chemical Assessment of Engine Oil Degradation in a Passenger Car", *Tribology Letters,* vol. 67, no. 68, 2019.

[16] C. Besser, N. Dorr, F. Novotny-Farkas, K. Varmuza and G. Allmaier, "Comparison of engine oil degradation observed in laboratoryalteration and in the engine by chemometric data evaluation", *Tribology International,* vol. 65, pp. 37-47, 2013.

[17] M. Soleimani, M. Sophocleous, L. Wang, J. Atkinson, I. L. Hosier, A. S. Vaughan, R. I. Taylor and R. J. Wood, "Base oil oxidation detection using novel chemical sensors and impedance spectroscopy measurements", *Sensors and Actuators B: Chemical,* vol. 199, pp. 247-258, 2014.

[18] R. S. Notay, M. Priest and M. F. Fox, "The influence of lubricant degradation on measured piston ring film thickness in a fired gasoline reciprocating engine", *Tribology International,* vol. 129, pp. 112-123, 2019.

[19] M. Kasai, N. Yoshimura and K. and Watanabe, "Evaluation of Engine Oil Deterioration Using a Comb-Shaped Electrode", *SAE International,* 2016.

[20] U. Latif and F. L. Dickert, "Conductometric sensors for monitoring degradation of automotive engine oil", *Sensors,* vol. 11, pp. 8611-8625, 2011.

[21] M. T. Devlin, "Additive Chemistry Testing Methods", in *Encyclopedia of Tribology*, Q. J. Wang and Y. Chung, Eds., Boston MA, Springer, 2013.

[22] Nanoscience Instruments, "Quartz crystal microbalance", [Online]. Available: https://www.nanoscience.com/techniques/quartz-crystal-microbalance/. [Accessed October 2019].

[23] A. Jaiswal, S. Smoukov, M. Poggi and B. Grzybowski, "Quartz crystal microbalance with dissipation monitoring (QCM-D): Real-time characterization of nano-scale interactions at surfaces", in *Nanotech*, 2008.

[24] L. Rayleigh, "On Waves Propagated along the Plane Surface of an Elastic Solid", *Proceedings of the London Mathematical Society,* Vols. s1-17, no. 1, pp. 4-11, 1885.

[25] D. P. Morgan, "History of SAW devices", in *IEEE Intl. Frequency Control Symposium*, Pasadena, 1998.

[26] X. Lu, K. Mouthaan and Y. T. Soon, "Wideband bandpass filters with SAW-filter-like selectivity using chip SAW resonators", *IEEE Transactions on Microwave Theory and Techniques,* vol. 62, no. 1, pp. 28-36, 2014.

[27] R. Brocato, E. Heller, G. Omdahl, J. Wendt, S. Jones and D. Palmer, "High frequency SAW correlator module", in *53rd Electronic Components and Technology Conference*, 2003.

[28] R. Brocato, J. Skinner, G. Wouters, J. Wendt, E. Heller and J. Blaich, "Ultra-wideband SAW correlator", *IEEE Transactions on Ultrasonics, Ferroelectrics, and Frequency Control,* vol. 53, no. 9, pp. 1554-1556, 2006.

[29] B. Lee, M. K. Song, A. Maity and D. B. Ma, "A 25MHz 4-phase SAW hysteretic DC-DC converter with 1-cycle APC achieving 190ns tsettle to 4A load transient and above 80% efficiency in 96.7% of the power range", in *IEEE International Solid-State Circuits Conference*, San Francisco, CA, USA, 2017.

[30] C. C. Ruppel, L. Reindl and R. Weigel, " SAW Devices and their Wireless Communications Applications", *IEEE microwave magazine,* pp. 65-71, June 2002.

[31] M. I. G. Rocha, Y. Jiménez, F. A. Laurent and A. Arnau, "Love Wave Biosensors: A Review", *State of the Art in Biosensors - General Aspects,* pp. 277-310, 13 March 2013.

[32] R. J. Smith, M. Hirsch, R. Patel, W. Li, A. T. Clare and S. D. Sharples, "Spatially resolved acoustic spectroscopy for selective laser melting", *Journal of Materials Processing Technology,* vol. 236, pp. 93-102, 2016.

[33] P. Benech, M. Dali-Ali and J. Keradec, "Temperature characterisation of material using SAW", in *16th IEEE Instrumentation and Measurement Technology Conference*, Venice, Italy, 1999.

[34] R. J. Smith, W. Li, J. Coulson, M. Clark, M. G. Somekh and S. D. Sharples, "Spatially resolved acoustic spectroscopy for rapid imaging of material microstructure and grain orientation", *Measurement Science and Technology,* vol. 25, no. 5, 2014.

[35] S. I. Moon, T. Kang, J. H. Lee, S. W. Han, J. S. Seo, K. H. Im, J. H. Park and J. K. Na, "Non-destructive Testing Method using Surface Acoustic Waves generated by inter-digital transducer in wall thinned pipeline", in *15th Asia Pacific Conference for Non-Destructive Testing*, Singapore, 2017.

[36] P. Aryan, S. Sampath and H. Sohn, "An overview of non-destructive testing methods for integrated circuit packaging inspection", *Sensors,* vol. 18, no. 7, 2018.

[37] V. Ferrari and R. Lucklum, "Overview of acoustic-wave microsensors", in *Piezoelectric transducers and applications*, Berlin, Springer, 2009, pp. 39-62.

[38] S. W. Jones, "Ground vibration from underground railways: how simplifying assumptions limit prediction accuracy", University of Cambridge, Cambridge, 2010.

[39] C. Willberg, S. Eisenträger, J. M. V. Perez and Z. A. B. Ahmad, "Simulation Methods for Guided Wave-Based Structural Health Monitoring: A Review", *Applied Mechanics Reviews,* vol. 67, no. 1, pp. 1-20, 2015.

[40] A. E. H. Love, "Some problems of geodynamics: being an essay to which the Adams prize in the University of Cambridge was adjudged in 1911", *Cambridge : University Press,* 1911.

[41] A. Burtin, N. Hovius and J. M. Turowski, "Seismic monitoring of torrential and fluvial processes", *Earth Surface Dynamics,* vol. 4, no. 2, pp. 285-307, 2016.

[42] P. A. Petcher and S. Dixon, "Weld defect detection using PPM EMAT generated shear horizontal ultrasound", *NDT & E International,* vol. 74, pp. 58-65, 2015.

[43] J. Krautkramer and H. Krautkramer, Ultrasonic Testing of Materials, 4th Fully Revised Edition ed., Springer-Verlag Berlin Heidelberg GmbH, 1990.

[44] Laboratory for active materials and smart structures, "Mode shape", University of South Carolina: College of Engineering and Computing,

[Online]. Available: http://www.me.sc.edu/research/lamss/html/software.html. [Accessed 2016].

[45] S. J. Martin, A. J. Ricco, T. M. Niemczyk and G. C. Frye, "Characterization of SH Acoustic Plate Mode Liquid Sensors", *Sensors and Actuators,* vol. 20, pp. 253-268, 1989.

[46] M. J. Vellekoop, "Acoustic wave sensors and their technology", *Ultrasonics,* vol. 36, pp. 7-14, 1998.

[47] M. Tyagi and G. Varde, "SAW and Interdigital Transducers", *International Journal of Scientific & Engineering Research,* vol. 3, no. 12, 2012.

[48] PI Ceramic GmbH, "Piezoelectric ceramic products; fundamentals, characteristics and applications", 2016.

[49] H. Miao, Q. Huan and F. Li, "Excitation and reception of pure shear horizontal waves by using face-shear (d24) mode piezoelectric wafers", *Smart Materials and Structures,* vol. 25, no. 11, 2016.

[50] I. A. Viktorov, Rayleigh and Lamb waves; Physical Theory and Applications, 1st ed., Springer Science and Business Media, 1967.

[51] E. S. OOI, "Rayleigh Wave Interactions with Tribological Contacts", Thesis submitted for the degree of Doctor of Philosophy, Department of Mechanical Engineering, University of Sheffield, 2015.

[52] S. Dixon and S. Palmer, "Wideband low frequency generation and detection of Lamb and Rayleigh waves using electromagnetic acoustic transducers (EMATs)", *Ultrasonics,* vol. 42, no. 10, pp. 1129-1136, 2004.

[53] T. Hiramoto, K. Okazaki and T. Sugiura, "Study on EMAT Configuration for Generating SH Waves", in *AIP Publishing*, Baltimore, Maryland, USA, 2014.

[54] Y. Cheng, Y. Deng, J. Cao, X. Xiong, L. Bai and Z. Li, "Multi-Wave and Hybrid Imaging Techniques: A New Direction for Nondestructive Testing and Structural Health Monitoring", *Sensors,* vol. 13, no. 12, 2013.

[55] R. S. Dwyer-Joyce, B. W. Drinkwater and C. J. Donohoe, "The measurement of lubricant-film thickness using ultrasound", *Proceedings of the Royal Society Series A: Mathematical Physical and Engineering Sciences,* vol. 459, no. 2032, pp. 957-976, 2003.

[56] A. Hunter, R. Dwyer-Joyce and P. Harper, "Calibration and validation of ultrasonic reflection methods for thin-film measurement in tribology", *Measurement Science and Technology*, vol. 23, 2012.

[57] R. Dwyer-Joyce, D. Green, S. Balakrishnan, P. Harper, R. Lewis, S. Howell-Smith, P. King and H. Rahnejat, "The Measurement of Liner - Piston Skirt Oil Film Thickness by an Ultrasonic Means", *SAE Technical Papers,* 2006.

[58] T. Geng, Q. Meng, Z. Chen and P. Wang, "Ultrasonic monitoring of lubricating conditions of hydrodynamic bearing", *Journal of Physics: Conference series,* vol. 305, no. 1, 2011.

[59] V. V. Shah and K. Balasubramaniam, "Measuring Newtonian viscosity from the phase of reflected ultrasonic shear wave", *Ultrasonics,* vol. 38, no. 9, pp. 921-927, 2000.

[60] M. Schirru, R. Mills, O. Smith, R. Dwyer-Joyce and M. Sutton, "In-situ measurement of journal bearing lubricant viscosity by means of a novel ultrasonic measurement technique using matching layer", *Tribology Transactions,* vol. 61, no. 1, 2017.

[61] S. Kasolang and R. Dwyer-Joyce, "Viscosity measurement in thin lubricant films using shear ultrasonic reflection", *Proceedings of the*

Institution of Mechanical Engineers, Part J: Journal of Engineering Tribology, vol. 222, no. 3, pp. 423-429, 2008.

[62] S. Kasolang, M. Ahmad and R. Dwyer Joyce, "Measurement of circumferential viscosity profile in stationary journal bearing by shear ultrasonic reflection", *Tribology International,* vol. 44, no. 11, pp. 1264-1270, 2011.

[63] N. Wilkie-Chancellier, L. Martinez, S. Serfaty and P. Griesmar, "Lamb wave sensor for viscous fluids characterization", *IEEE Sensors Journal,* vol. 9, no. 9, pp. 1142-1147, 2009.

[64] R. Kazys, L. Mazeika, R. Sliteris and R. Raisutis, "Measurement of viscosity of highly viscous non-Newtonian fluids by means of ultrasonic guided waves", *Ultrasonics,* vol. 54, no. 4, pp. 1104-1112, 2014.

[65] M. B. Gitis and V. A. Chuprin, "Application of Surface and Normal Ultrasonic Waves for Measuring the Parameters of Technical Fluids: I. Shear Viscosity Measurements", *Technical Physics,* vol. 57, no. 5, pp. 671-676, 2012.

[66] P. Kiełczyński, W. Pajewski, M. Szalewski and A. Balcerzak, "Measurement of the shear storage modulus and viscosity of liquids using the Bleustein–Gulyaev wave", *Review of Scientific Intruments,* vol. 75, no. 7, pp. 2362-2367, 2004.

[67] N. L. Bragazzi, D. Amicizia, D. Panatto, D. Tramalloni, I. Valle and R. Gasparini, "Chapter Six - Quartz-Crystal Microbalance (QCM) for Public Health: An Overview of Its Applications", *Advances in Protein Chemistry and Structural Biology,* vol. 101, pp. 149-211, 2015.

[68] K. Saha, F. Bender, A. Rasmusson and E. Gizeli, "Probing the Viscoelasticity and Mass of a Surface-Bound Protein Layer with an Acoustic Waveguide Device", *Langmuir,* vol. 19, no. 4, 2003.

[69] S. Qin, X. Tang, L. Zhu, Y. Wei, X. Du and D. M. Zhu, "Viscoelastic signature of physisorbed macromolecules at the solid–liquid interface", *Journal of Colloid and Interface Science,* vol. 383, no. 1, pp. 208-214, 2012.

[70] D. M. Zhu, J. Fang, B. Wu and X. Du, "Viscoelastic response and profile of adsorbed molecules probed by quartz crystal microbalance", *Physical Review E,* vol. 77, no. 3, 2008.

[71] J. M. Friedt and L. A. Francis, "Combined surface acoustic wave and surface plasmon resonance measurement of collagen and fibrinogen layer physical properties", *Sensing and Bio-sensing Research,* vol. 11, no. 2, pp. 60-70, 2016.

[72] I. Gendler, "Isaac's science blog", 13 08 2017. [Online]. Available: https://isaacscienceblog.com/2017/08/13/fourier-transform/. [Accessed December 2019].

[73] L. Landau and E. Lifshitz, Fluid Mechanics: Course of Theoretical Physics, 2 ed., vol. 6, Pergamon Press, 1987.

[74] Z. Shana and F. Josse, "Analysis of liquid-phase-based sensors utilizing SH surface waves on rotated Y-cut quartz", *IEEE 1988 Ultrasonics Symposium Proceedings,* vol. 1, pp. 549-554, 1988.

[75] Cannon Instrument Company, "Viscosity & flash point standards for reference, validation and calibration", Cannon Instrument Company, 2015.

[76] A. Ricco and S. Smith, "Acoustic wave viscosity sensor", *Applied Physics Letters,* no. 50, 1987.

[77] G. W. C. Kaye and T. H. Laby, Tables of Physical and Chemical Constants, 16th ed., National Physical Laboratory, 2015.

[78] J. Williams, Engineering Tribology, Cambridge: Cambridge University Press, 2005.

[79] J. Zhang and Y. Meng, "Boundary lubrication by adsorption film", *Friction,* vol. 3, no. 2, pp. 115-147, 2015.

[80] S. Hsu and R. Gates, "Boundary lubricating films: formation and lubrication mechanism", *Tribology International,* vol. 38, no. 3, pp. 305-312, 2005.

[81] P. Kapsa and J. Martin, "Boundary lubricant films: a review", *Tribology International,* vol. 15, no. 1, pp. 37-42, 1982.

[82] M. Smeeth, H. Spikes and S. Gunsel, "The formation of viscous surface films by polymer solutions: Boundary or Elastohydrodynamic lubrication? ", *Tribology Transactions,* vol. 39, no. 3, pp. 720-725, 1996.

[83] O. Furlong, B. Miller, P. Kotvis, H. Adams and W. T. Tysoe, "Shear and thermal effects in boundary film formation during sliding", *The Royal Society of Chemistry,* vol. 4, no. 46, 2014.

[84] S. M. Lundgren, K. Persson, G. Mueller, B. Kronberg, J. Clarke, M. Chtaib and P. M. Claesson, "Unsaturated fatty acids in alkane solution: adsorption to steel surfaces", *Langmuir,* vol. 23, no. 21, pp. 10598-10602, 2007.

[85] S. Qin, X. Tang, L. Zhu, Y. Wei, X. Dua and D.-M. Zhu, "Viscoelastic signature of physisorbed macromolecules at the solid–liquid interface", *Journal of Colloid and Interface Science,* vol. 383, no. 1, pp. 208-214, 2012.

[86] S. M. Campen, "Fundamentals of organic friction modifier behaviour", PhD Thesis, Imperial College London, 2012.

[87] K. Nakano and H. A. Spikes, "Process of Boundary Film Formation from Fatty Acid Solution", *Tribology Online,* vol. 7, no. 1, pp. 1-7, 2012.

[88] P. Petcher, S. Burrows and S. Dixon, "Shear horizontal (SH) ultrasound wave propagation around smooth corners", *Ultrasonics,* vol. 54, no. 4 , pp. 997-1004, 2014.